# Data Quality Bench-Marking for High Resolution Bragg Data

Dissertation

zur Erlangung des mathematisch-naturwissenschaftlichen Doktorgrades

"Doctor rerum naturalium"

der Georg-August-Universität Göttingen

im strukturierten Promotionsprogramm Chemie
der Georg-August University School of Science (GAUSS)
vorgelegt von Hilke Wolf
aus Leer/Ostfriesland

Göttingen, 2014

**Betreuungsausschuss**

Prof. Dr. D. Stalke, Institut für Anorganische Chemie, Georg-August-Universität

Prof. Dr. B. B. Iversen, Department of Chemistry, Aarhus University


**Mitglieder der Prüfungskommission**

Referent: Prof. Dr. D. Stalke, Institut für Anorganische Chemie, Georg-August-Universität

Korreferent: Prof. Dr. B.B. Iversen, Department of Chemistry, Aarhus University


**weitere Mitglieder der Prüfungskommission:**

Prof. Dr. F. Meyer, Institut für Anorganische Chemie, Georg-August-Universität Göttingen

Dr. H. Sowa, GZG, Georg-August-Universität Göttingen

Dr. F. Fabbiani, GZG, Georg-August-Universität Göttingen

Jun.-Prof. Dr. T. Waitz, Institut für Anorganische Chemie, Georg-August-Universität Göttingen

Tag der mündlichen Prüfung: 15.12.2014

# Danksagung

Der erste und größte Dank geht an meinen Doktorvater Prof. Dr. Dietmar Stalke, der mir stets das Gefühl gab, vollstes Vertrauen in meine Fähigkeiten zu haben, immer ein offenes Ohr hatte und stets mit Rat und Tat zur Seite stand, auch bei Themen, die nur entfernt mit der Promotion zu tun hatten. Ich habe große Freiheiten bei der Gestaltung meiner Forschung erhalten und gleichzeitig stets volle Rückendeckung.

My sincere thanks go to my second referee Prof. Dr. Bo B. Iversen who stepped in almost at the last minute as referee but has also previously given much fruitful advice during the course of my thesis on various CMC meetings. The collaboration with the Aarhus group was more than mere scientific get-together and has proven advantageous for all participants. It has always been a pleasure to meet on the workshops or on conferences over the world.

Des Weiteren möchte ich mich bei allen Mitgliedern meines Prüfungskomitees bedanken, dass sie die Zeit gefunden haben, meine Arbeit mit Interesse zu lesen und bei der Prüfung anwesend zu sein.

So viele Leute haben dazu beigetragen, dass ich nun am Ende tatsächlich eine Doktorarbeit schreibe, dass ich gar nicht alle auflisten kann, aber eine unvollständige Liste soll hier trotzdem erscheinen.

Mein sehr herzlicher Dank geht an die gute Fee in unserem Arbeitskreis, Heike Tappe, ohne die so manche Deadline abgelaufen wäre, ohne dass die entsprechende Arbeit/Veröffentlichung/Rechnung fristgerecht eingegangen wäre! Darüber hinaus hat Heike immer ein offenes Ohr und steht stets mit Rat und Tat zur Seite, vor allem für junge, unerfahrene (berufstätige) Mütter hat sie immer genau die richtigen Worte parat.

Ohne die diversen technischen Mitarbeiter würde kaum ein Labor richtig funktionieren und vor allem wären die meisten Praktika schon längst in undurchschaubarem Chaos versunken, deshalb möchte ich mich sehr bei „Schorse" und „Mr. Sloty" bedanken, von Euch lässt sich eine Menge lernen! Eine weitere Person, die unser Institut vor dem täglichen Chaos bewahrt, ist Frau Dr. A. C. Stückl, die unermüdlich gegen Papierberge aus der Verwaltung kämpft und nebenbei auch noch die Zeit findet, Praktika zu betreuen und Großgeräte zu bedienen. Vielen Dank für das in uns gesetzte Vertrauen beim Betreuen der MaWis.
Vor allen anderen Mistreitern möchte ich den Korrekturlesern (Lenni, Bene, Felix und Felix) dafür danken, dass sie sich die Zeit genommen haben und vor allem, dass sie so

viele Anregungsvorschläge hatten und mich vor mancher ungeschickten Formulierung bewahrt haben.

Ohne das schier unendliche kristallographische Wissen von Regine hätte so manche Servicestruktur niemals das Licht der Welt erblickt. Außerdem hätte es keinen Fokus auf Datenqualität gegeben und ich wäre bei so manchem XD Problem wahrscheinlich wahnsinnig geworden. Vielen lieben Dank Regine, dass Du immer die Ruhe gefunden hast, auch die letzte Unstimmigkeit zu entdecken und dafür, dass Du den wilden Haufen der Charge Density Subgroup gezähmt hast.

Besonders herzlich möchte ich mich bei den Programmierern aus dem ED-Zimmer bedanken, sowohl den Aktuellen (Lennard, Felix, Bene, Regine) als auch den schon längst in alle Winde zerstreuten (Bub und Bub, DrUlli und Anhang); ohne ihre Fähigkeiten würde ich heute noch Startmodelle für $R_{\text{free}}$ erstellen, mühsam alle *geo_out-files durchsuchen oder an der nächsten Verfeinerungsstrategie scheitern!

Unvergessen sind natürlich die vielen gemeinsamen Stunden im Diff-Raum (geh' machs halt einmal gescheit!)….ohne die lieben Mitschrauber, von denen ich so viel lernen durfte, wäre es doch sehr langweilig vor dem PC geworden! So konnte man sich immer aus dem Ü30-Zimmer verdrücken: „ich geh nochmal schnell an der Maschine schrauben!"

Allergrößter Dank gilt der original Ü30-Raum-Besatzung mit Sandra, Bub, Jakob und Dirk, ich habe über ED alles von Euch gelernt, was den Grundstock für diese Arbeit gelegt hat und ich hätte es mit Sicherheit nie geschafft, wenn es nicht so unglaublich nett mit Euch gewesen wäre! Nach und nach ist aus dem Ü30-Raum ein U30-Raum geworden (bis ich 30 wurde) und auch die jungen Wilden haben viel zu langen Lachsalven und allgemein guter Stimmung beigetragen!

Da der Computer mein Hauptarbeitsmittel nach den Diffraktometern war, ich aber nur bei letzteren über genug Fachwissen verfüge, es am Laufen zu halten möchte ich mich hier auch noch sehr sehr herzlich bei Bub, Felix und dem Jadmin dafür bedanken, dass sie mein Arbeitspferd immer am Laufen gehalten haben und ich so ein sorgenloses Leben hatte, selbst wenn ich im Eifer des Gefechts mal wieder einen wichtigen Ordner gelöscht habe.

Über die Jahre sind manche Kollegen zu Freunden geworden, für die hoffentlich immer ein Wochenende gefunden wird, an dem man sich treffen kann, auch wenn wir alle nicht mehr in Göttingen wohnen. Jakob, Eva und Fenna sind uns genauso ans Herz gewachsen wie Lennard und Ann-Christin! Vielen Dank für die vielen Koch- und Spieleabende und für den richtigen Rat zur rechten Zeit ☺

Vielen lieben Dank Mama und Papa, dass Ihr immer an mich glaubt und einen unglaublichen Rückhalt bietet, aber auch im richtigen Moment anspornende Worte findet! Ohne Papas Stimme im Ohr „Biegahn is half waark!" wäre hier kein Paper geschrieben und auch erst Recht keine Doktorarbeit!

Danke liebe Tina, dafür, dass man bei Dir immer ein offenes Ohr findet und für das „Rücken frei halten" und Babysitten, aber auch für den Spaß und die vielen Gespräche rund um eine Flasche Wein!

Zum Schluss möchte ich den wichtigsten Personen in meinem Leben danken, ohne die überhaupt keine Doktorarbeit möglich gewesen wäre: Danke Felix, dass Du immer da bist, wenn ich Dich am meisten brauche, dafür dass Du wie ein Fels in der Brandung allen Stress aushältst und mich immer wieder überrascht! Danke liebe Elin, dass Du unser Leben so unglaublich viel reicher gemacht hast und uns jeden Tag zum Lachen bringst!

# Table of Contents

# Abbreviations

| | |
|---|---|
| Å | Ångstrom |
| Ag | silver |
| APS | Advanced Photon Source |
| bcp | bond critical point |
| CCD | Charge Coupled Device |
| ccp | cage critical point |
| DFT | Density Functional Theory |
| HF | Hartree–Fock |
| IAM | Independent Atom Model |
| MM | Mulitpole Model |
| Mo | molybdenum |
| MP2 | Møller-Plesset-perturbation theory 2 |
| QTAIM | Quantum Theory of Atoms in Molecules |
| rcp | ring critical point |
| VSCC | Valence Shell Charge Concentration |
| λ | lambda |

# 1 SINGLE CRYSTAL X-RAY DIFFRACTION

This chapter is intended to elucidate the course from a diffraction experiment to a charge density refinement. Starting from the theory of X-ray diffraction and how structure determination is derived from it, this chapter will also deal with the structure refinement itself. An overview on the programs used within the course of this thesis for the data treatment and subsequent structure refinement will be given. Furthermore, the pitfalls in single crystal X-ray diffraction experiments will be discussed and ideas to overcome common problems will be provided.

## 1.1 Foundations of X-ray Diffraction

X-ray crystallography has been widely used for about a hundred years to unequivocally elucidate the arrangement of atoms in molecules in a single crystal. To be able to determine the molecular structure from a diffraction experiment a few requirements have to be fulfilled. The first and main characteristic that makes a single crystal is the periodic repetition of the unit cell in all three dimensions. Within the unit cell there is a specified number of atoms which are needed to represent the full structure. In order to describe each single point inside the unit cell three edges that create the unit cell are defined (a, b, and c) and each point in space can then be addressed by vectors as given in Eq. 1.

$$\mathrm{x} \cdot \vec{a} + \mathrm{y} \cdot \vec{b} + \mathrm{z} \cdot \vec{c} \qquad \text{Eq. 1}$$

X, y, and z are the fractal coordinates of the point in space and have by definition values between zero and one inside the unit cell. Exposing this periodically built structure to an X-ray beam gives rise to interference. If the beam is understood as a wave the fundamental laws of optics can be applied. In 1912 *Max von Laue*, *Walter Friedrich* and *Paul Knipping* could prove that X-rays have indeed a wave like character and that their interactions with solids follow certain rules.[1] Most famous among these are the so called *Laue equations* (Eq. 2) which combine the concept of the unit cell with the physical description of vectors being scattered at atomic positions (the scattering vector $\vec{S}$). The wave like X-ray beam is scattered at the atomic positions and is thus enhanced whenever we have positive interference, in other words when the spatial differences of the atomic positions give rise to integer multiples of the scattering vector.

$$\vec{a} \cdot \vec{S} = |\vec{a}||\vec{S}|cos(\vec{a}, \vec{S}) = \mathrm{h} \qquad \text{Eq. 2}$$

$$\vec{b} \cdot \vec{S} = |\vec{b}||\vec{S}|cos(\vec{b},\vec{S}) = k$$

$$\vec{c} \cdot \vec{S} = |\vec{c}||\vec{S}|cos(\vec{c},\vec{S}) = l$$

Only if all three Laue equations are fulfilled at the same time a reflection can be observed on the detector. The axes h, k, l are called the *Miller* indices and they are used to index the reflections observed in an experiment. In 1912 the other pioneer of X-ray crystallography *William Laurence Bragg* established a different way of describing the interaction of X-rays with crystals.[2] *Bragg* postulated that a crystal is build up from successive sheets of atoms which give rise to constructive interference if the difference between them is an integer of the wavelength (Scheme 1).
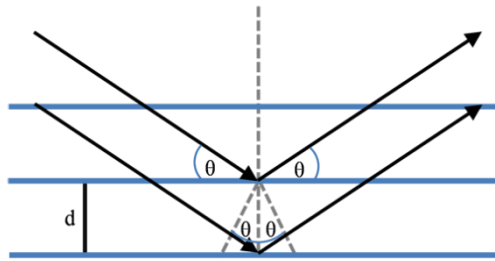


Scheme 1: A schematic visualisation of *Bragg's* law.

This results in the *Bragg* equation:

$$2d\sin(\theta) = n\lambda \qquad\qquad \text{Eq. 3}$$

With d being the lattice plane distance, λ the X-ray wavelength and θ the incident angle with respect to the lattice plane.

Considering the fact that a crystal is a three dimensional object three intersecting sheets of lattice planes - one in each dimension – are easily visualized, which characterize the crystal. The lattice distance d is a very important factor in X-ray crystallography because it defines the smallest distance that can be precisely resolved during the experiment. A comparison from day to day life is the resolution of a camera; d defines the smallest distance in between any two objects than can still be resolved without the two objects being superpositioned onto each other. In X-ray crystallography this defines the smallest distance of two lattice planes that can be resolved and the smaller this number the more features can be precisely located.

Both father and son, *William Henry* and *William Lawrence Bragg*, worked ceaselessly during 1913 on a home-made Röntgen-spectrometer to determine both diffraction wavelengths of metals and the structure of several salts.[3]

The main difference between the work of the *Braggs* and the work of *von Laue* was the used X-rays to probe the crystal. While *von Laue* used polychromatic X-rays in his

experiments the *Braggs* used monochromatic X-rays in order to determine crystal structures. This holds true until today where so called *Laue-diffraction* uses 'white beams' while it is most common to use monochromatic X-rays for standard diffraction experiments. Today *Laue* techniques are most commonly used for neutron diffraction experiments or for time resolved X-ray experiments at synchrotrons.

## 1.2    The Structure Factor

With the information in hand as to why reflections can be detected on our detector after a single crystal was hit with an X-ray beam, now is the time to explain how intense these reflection are and why they can be related to the constitution of the crystal.

The measure of intensity for a reflection is the structure factor *F* which is dependent on the scattering factors of the atoms present in the unit cell, their positions and the *Miller* indices (Eq. 4). The observed intensity is proportional to the square modulus of the structure factor *F* (Eq. 5).

$$F(\text{hkl}) = \sum_{\substack{\text{atoms j} \\ \text{in the unit cell}}} f_j e^{-2\pi^2 U_j(\theta,\lambda)} e^{2\pi^i\left(\text{hx}_j + \text{ky}_j + \text{lz}_j\right)} \qquad \text{Eq. 4}$$

$$I \propto |F^2(\text{hkl})| \qquad \text{Eq. 5}$$

To account for the different elements and their respective scattering strength, which is directly related to the number of electrons each atom possesses, the atomic scattering factor *f* is introduced. It is defined as the Fourier transformation over the electron density of a single atom and consists of three different parts that contribute differently depending on the X-ray beam (Eq. 6). If the energy of the X-ray beam lies close to the ionisation energy of an atom the energy-dependant $f'$ and $f''$ dominate the atomic scattering factor. Above and below the ionisation energy the atomic scattering factor is dominated by $f^0$.

For the Fourier transformation it is assumed that the electrons are spherically distributed around the atomic core and that no interaction between the atoms takes place.

$$f(\theta,\lambda) = f^0(\theta) + \Delta f'(\lambda) + i\Delta f''(\lambda) \qquad \text{Eq. 6}$$

The course of the atomic scattering factor is given in Figure 1 and shows that it is not only dependent on the atomic number Z, which is given as a function of *e* in Figure 1,

but also on $\sin(\theta)/\lambda$. What can also be derived from this plot is the information convoluted in the reflections at different resolutions. While the innermost reflections carry all the information about the valence electrons and thus about the bonding density, the reflections at higher angles carry the information about the positional parameters of the atoms. This is also the reason why charge density datasets have to be collected up to very high angles because only then will it be possible to accurately deconvolute the positional parameters from the information about the bonding electron density. It also means that the reflections at lowest $\theta$ values will be the most intense and the scattering strength decreases with increasing values for $\theta$.

The structure factor $F$ is the summation over all atoms and thus the Fourier transform of the total electron density of the unit cell. This means that the total electron density of a unit cell can be described by back transformation of the structure factor.
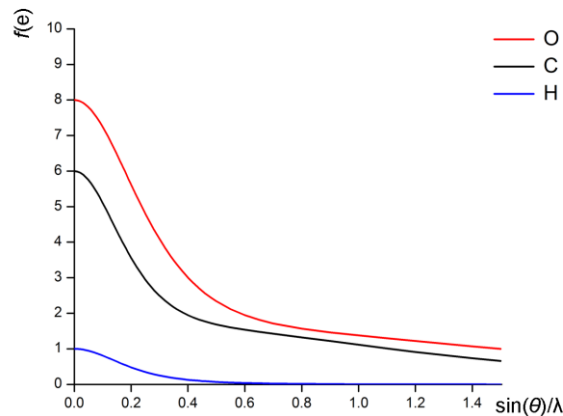


Figure 1: Atomic form factor (*f*) for hydrogen, carbon, and oxygen atoms.

Unfortunately, the phase information is not recorded during an experiment because only the intensity ($|F_{hkl}^2|$) is collected and therefore the imaginary part is lost and cannot be reconstructed during a Fourier transformation. This means that a model is needed with exemplary phases to reconstruct the electron density from the observed intensities. The computational realisation of this are the so called Direct Methods in structure solution which solve structures by trial and error of different phases based on atomic form factors that have been supplied by the user. [4]

As can be seen in Eq. 4 the structure factor $F$ is also dependent on the thermal motion of the atoms, which is part of the parameter $U_{ij}$. Despite the fact that $U_{ij}$ is sometimes still mistakenly described as the thermal motion parameter there are more effects going into this parameter than just the deviation from the position according to thermal motion (see vide infra). Hence, it should be called displacement parameter and is defined as:

$$f' = f \cdot exp\left\{-8\pi^2 U \frac{sin^2\theta}{\lambda^2}\right\} \qquad \text{Eq. 7}$$

This factor only describes an isotropic motion and is extended to describe anisotropic behaviour by a tensor that defines three perpendicular axes to fully characterize the displacement (Eq. 8).

$$f' = fexp(-2\pi^2\{U_{11}h^2a^{*2} + U_{22}k^2b^{*2} + U_{33}l^2c^{*2} + 2U_{23}klb^*c^* \\ + 2U_{13}hla^*c^* + 2U_{12}hka^*b^*\} \qquad \text{Eq. 8}$$

The value of the displacement parameter is influenced by the atomic number Z, the temperature and the bonding situation of the atom it describes. This means that different values for the same structure are expected if measured at two different temperatures or for the same atoms but in different bonding situations. However, as most diffraction experiments nowadays are done at temperatures of 100 K or below the displacement parameters are usually well defined and rather small. If this displacement parameter still becomes unusually large during the refinement progress one almost certainly has to check for disorder or a wrong atom assignment. There are however, tabulated values for displacement parameters for certain standard reoccurring bonding situations, which are very helpful if in doubt about the assignment of an atom type. During the final stages of the refinement of a structure the validation program *checkcif* (available through the PLATON program package) automatically checks if the displacement parameters are within the range of the tabulated values and sends out a warning if one of the parameters is unusually large.[5]

## 1.3    Absorption and Extinction

Based on the information given in the previous paragraphs the intensity of the incoming X-ray beam should be identical to the diffracted X-ray beam. Unfortunately, the beam does interact with the sample and is hence weakened. The most important weakening factor of the incoming beam is the absorption. As crystals do not grow in spheres but in polygonal shape the way the incoming beam passes through the crystal during the experiment is not equal for all refracted intensities. This means that the absorption is dependent on the way the beam takes through the crystal. If this absorption is elastic and thus the released energy identical to the absorbed energy, the phenomenon is called *Rayleigh* scattering and its effects are taken into account by the atomic form factors and the resulting structure factors. If this absorption is inelastic however, and thus the released energy different to the absorbed energy, the effect is called *Compton* scattering. The weakening effect of the *Compton* scattering

can be described by the linear absorption coefficient µ (Eq. 9) for which values are tabulated for each atom.[6]

$$I = I_0 e^{-\mu z}$$

<div align="right">Eq. 9</div>

The effect of absorption is also strongly dependent on the incoming beam and on the material it passes through, *e.g.* heavy elements show large absorption for softer X-rays.

In the program used for absorption correction in this thesis, *SADABS*[7], there are two ways to account for the effect of absorption. The most popular option is the semi-empirical method which describes the irradiated volume of the crystal with spherical harmonics that can be manually extended if the absorption is large. This method only works correctly if each reflection has been monitored with a high multiplicity as it scales the intensities on the mean intensities recorded for every reflection. The more accurate way is to perform a numerical absorption correction which relies on indexed faces of the used crystal and is thus able to reliably reconstruct the way the beam passed through the crystal for each single reflection. Although the two options make use of very different approaches they work equally well for small crystals that do not show large absorption effects.[8]

The other effect most prominent in crystals of highly ionic nature and great perfection is extinction. It mostly affects the very strong inner reflections and makes it especially hard to detect these with great accuracy. As *Schmøkel et al.* could show for $CoSb_3$ the best way to overcome this problem is to use a very focussed and intense beam with a very short wavelength like they are available at synchrotrons.[9-10]

## 1.4    Perils of Data Collection Strategies

Although there are many powerful tools to generate an optimal data collection strategy like the *COSMO* or *QUEEN* plugin of the APEXII suite[11] there are still certain pitfalls that these tools cannot circumvent but have to be taken care of by the crystallographer.

I.    The most important factor to guarantee excellent data is the crystal quality. It is of outermost necessity that the crystal chosen for a charge density investigation has the best quality possible. Twinning or satellite crystals can render the collected dataset useless for charge density studies and have to be avoided. As *Müller* stated in his paper from 2009 "it is much easier to refine a structure based on good data than on bad data and time invested into improving data quality is returned with interest in the refinement stage".[12]

II.   The first and most important rule concerns the crystal selection before the measurement. Especially for a charge density dataset it is always wise to

choose the size of the crystal according to the used X-ray beam as it makes scaling and absorption correction a lot more reliable if the crystal has always been completely surrounded by the beam. Another factor concerns the measured intensities. As has already been mentioned in the thesis of *Hey* the limited dynamic range of the area CCD detectors can lead to incorrectly recorded intensities.[13-15] The dynamic range of a detector is defined as the full well capacity divided by the read noise. If this value is exceeded by a single incident the detector cannot take in the information about the intensity because the CCD chip is saturated. In this case the information about the intensity is lost and even though the APEXII software automatically allows a retake with 1/8th of the exposure time, if instructed correctly by the user, the measured intensity can still exceed the dynamic range. Unfortunately, in order to collect a full charge density dataset one has to measure data up to very high resolution (d ≤ 0.5 Å). This means that a crystal is needed that can scatter up to these angles which is most often only the case if the crystal is of considerable size (approximately 0.2 x 0.2 x 0.2 mm for in-house sources), which then leads to very strong reflections in the inner shells. However, the hardware often limits the exposure time to 0.5 s. Taking all this into account the crystal has to be chosen in a manner that guarantees strong reflections up to very high resolution (with an exposure time in the range of a few minutes) and reflections that can still be taken in by the detector without saturation for the inner shells (with exposure times in the range of seconds).

III.  Even with all the abovementioned perils in mind it is sometimes simply not possible to avoid all overloads. In this case one can check the collected frames with the *summary* tool implemented in the APEXII suite.[11] This is also a very handy tool when designing and editing the data collection strategy because it helps to find the correct exposure time that is a compromise between high resolution data and little overloads.

IV.  In accordance with points I to III there is another choice that has to be made before the experiment starts and that is the one considering the wavelength of the used X-ray beam. The most widely used wavelength for in-house sources is probably molybdenum radiation ($K_{\alpha 1}$: $\lambda = 0.71073$ Å). This is the ideal wavelength for light atom structures but has its disadvantages for samples with high absorption coefficients and heavy elements. In this case it is often better to refer to silver radiation which also gives a higher maximum resolution because the reciprocal space is compressed due to higher energies ($K_{\alpha 1}$: $\lambda = 0.56086$ Å). The third option which is especially useful for salt like structures with very high absorption or extinction coefficients and therefore tiny crystal size is the synchrotron radiation. With third generation synchrotrons the produced X-ray beam is orders of magnitudes higher in intensity and has the advantage of tuneable wavelengths. On the other hand there can be detector issues as the intense beam also means very strong inner

reflections. In order to avoid the problems discussed under no. I one often has to use attenuation to collect a high quality dataset.

V.    Following all the guidelines above one can still have problems with the inner shell reflections being continuously to strong due to scattering factors that rapidly decay at higher theta angles as it is most often the case for light atom structures. In this case it can be useful to collect the innermost reflections with a so called "fast scan" which covers more degrees in the same exposure time and thus has lower intensities. With this procedure it is possible to substitute the reflections collected with too high intensities in the "normal" runs with the intensities collected in the fast scan.

Although this list is most probably incomplete it should be clear that it is by no means a simple task to collect a high quality charge density dataset. Most set-ups nowadays are optimized for high throughput standard single crystal diffraction studies so one has to take extra care when collecting data for a charge density study. It cannot be emphasized enough that in a charge density investigation it should not matter how long the data collection takes but rather how good the quality of the dataset is even if that means data collection of up to two weeks for low symmetry space groups. Once the experiment ends it is not possible to mend some flaws of the data collection which means that in extreme situations the whole experiment can turn out superfluous which of course should and can be avoided.

## 1.5    Integration Routines

After a successful experiment with the best possible data collection strategy the next step involves the data integration. Within this thesis all integrations have been performed with the program *SAINT*[16] which is a Bruker software that is based on the integration program *XDS*[17]. For routine structure refinement the standard settings which are pre-set in the APEXII software can safely be used but for charge density datasets special care has to be taken. There is more than one route to follow during an integration routine. One can chose to use the graphical user interface (GUI) that is used in the APEXII software or the command line can be used to start and set up the integration. It has to be said that some parameters can only be changed using the command line option. Whether it is wise to change these is a different story. Most of the standard settings do not have to and should not be changed at all as they are already optimized for Bruker machine set-ups. The only parameters that are routinely changed are the resolution up to which the data are integrated and the size of the integration box. To find the optimal and maximum resolution for the integration one should always consult the *SADABS* and *XPREP* statistics that are mentioned in section 1.6. This can vary substantially from the value automatically given in APEXII and should carefully be chosen for a charge density investigation.

A parameter which should also very carefully be chosen but is a lot harder to determine is the box size used for integration. For routine structure refinement one almost always uses the box size refinement strategy which is the standard setting in *SAINT*. This routine estimates the size of the integration box from a learned profile which is updated after a quick pass over the first few frames of a run.[18] This may lead to box sizes that are too large which can then lead to problems in the Multipole Model (MM) where wrong values for the observed structure factors can lead to strange features in the residual density (vide infra in chapter 1.8).[19] Within this thesis it has proven fruitful to determine the correct box size with the help of the output *\*\_ls* file, where a number of very useful statistics are provided by *SAINT*. At the end of the individual *\*\_ls* files and at the beginning of the *\*\_0m.\_ls* file there are the "Global Integration Statistics" which, among many other things, state the percent of profile used in x, y, and z and the maximum percentage of intensity on the xyz boundaries. The former value should be very close to 100 % and the latter should not exceed 10 %. Within this statistics the number of spots exceeding the dynamic range is given, these are subsequently not integrated and thus are not added to the *\*.raw* file.

## 1.6     Quality Indicators before Structural Refinement

After a successful experiment, data reduction and scaling the question about the data quality arises. There are various indicators that can help to distinguish between a promising dataset and a mediocre one.

### 1.6.1    The *SADABS* and Diederichs Plots

The most powerful tool for early stages quality assessment are the plots generated by *SADABS*[7] because up to this point all that is needed is the Laue group. Out of the many graphics *SADABS* routinely provides, the newly implemented *Diederichs* plot is also one of the most powerful diagnostic tools because it not only displays problems with the data but also flaws in the set-up of the experiment.[20] This is most useful for in-house sources where one has the chance to optimize the given set-up for the wanted research is high. In his paper *Diederichs* promotes his plot mainly for quantifying instrument errors at synchrotron sources and for macromolecules but it is also very useful for small molecule diffraction.[20-21] The generated plot shows the course of $I/\sigma(I)$ against $\log_{10}(I)$ (Figure 2, left). This curve should in theory have a sigmoidal shape as there is a limit for $I/\sigma(I)$ due to detector resolution and systematic errors.
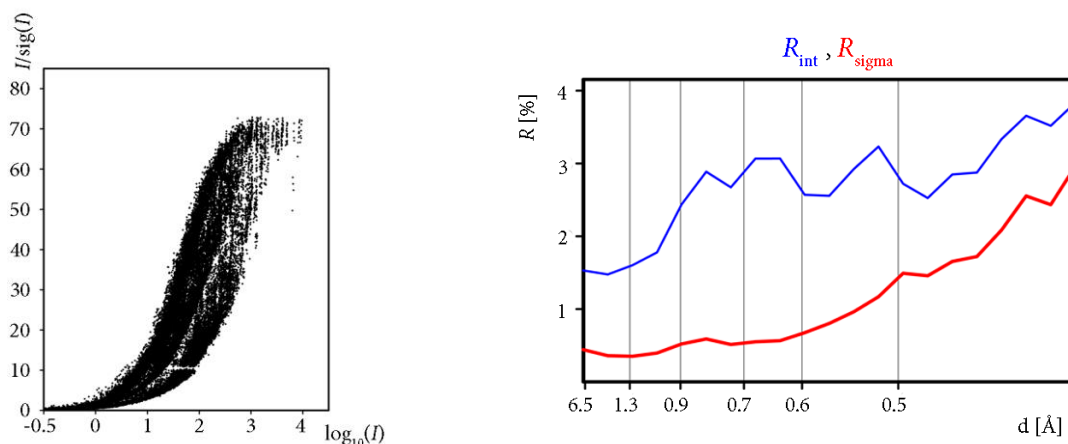
Figure 2: Exemplary *Diederichs* (left) and *SADABS* plot (right) for an in-house dataset.

A high value for the maximum indicates strong reflections with a low sigma value and thus a minimum of experimental and systematic errors in the collected data. Among many other things *SADABS* introduces a weighting scheme which minimises the differences in the standard uncertainties of all reflections and scales the intensities in a way that the weighted mean square deviation $\chi^2$ is close to unity (Eq. 10).

$$\sigma^2(I)_{\text{corrected}} = [K \cdot \sigma(I)_{raw}]^2 + [g \cdot I]^2 \qquad \text{Eq. 10}$$

Depending on the option chosen in *SADABS* individual $K$ and $g$ values for each run ca be refined or an overall $g$ and individual $K$ values. As can be seen from Eq. 10 the value of $g$ has a direct influence on the maximum $I/\sigma(I)$ value from the *Diederichs* plot.

The other graphical output from *SADABS* includes the plotting of the $R_{int}$ and $R_{sigma}$ (see 1.6.2 for definition) against the resolution (Figure 2, right). Generally, it is desirable to never exceed the value of 10 % for both $R$ values in this plot (for small molecules) as this can already indicate problems with the data. Additionally, the innermost resolution shells should not have an $R$ value larger than 5 %. Features also indicating trouble are sharp peaks which are signs for uneven data collection over the resolution shells. This can lead to trouble in scaling and error modelling.

## 1.6.2  XPREP

The next logical step in a routine structure refinement after scaling, merging and absorption correction is the use of the program *XPREP* which helps to assign the correct space group based on statistical absences in the diffraction pattern.[22] There are a lot of very useful statistics to look at in *XPREP* but the most interesting table for a data quality check is the one summarizing the intensity statistics for the given

13

dataset. It divides the dataset into resolution shells which roughly incorporate an identical number of reflections and gives the completeness, the multiplicity and intensity numbers for each. In the last two columns the historically very popular $R_{\text{merge}}$ and $R_{\text{sigma}}$ are given (Eq. 11).

$$R_{\text{int}}/R_{\text{merge}} = \frac{\sum|F_o^2 - \langle F_o^2\rangle|}{\sum[F_o^2]} \qquad\qquad R_{\text{sigma}} = \frac{\sum[\sigma(F_o^2)]}{\sum[F_o^2]}$$

$$R_{\text{r.i.m.}} = \frac{\sqrt{\frac{N}{N-1}}\sum|F_o^2 - \langle F_o^2\rangle|}{\sum[F_o^2]} \qquad\qquad R_{\text{p.i.m.}} = \frac{\sqrt{\frac{1}{N-1}}\sum|F_o^2 - \langle F_o^2\rangle|}{\sum[F_o^2]}$$

Eq. 11

Although these are useful numbers to look at the $R_{\text{merge}}$ gets artificially big if there is a high multiplicity which is almost always the case when using area detectors. *XPREP* can also calculate the multiplicity independent $R_{\text{r.i.m.}}$ and $R_{\text{p.i.m.}}$[23] factors which have an additional correction term $\left(\sqrt{\frac{N}{N-1}}\right)$ and $\left(\sqrt{\frac{1}{N-1}}\right)$ that take the number of measured equivalent reflections (N) into account (Eq. 11).

A good dataset can instantly be spotted by a high overall multiplicity (a value larger than three is the optimum) and high $I/\sigma(I)$ values up to the maximum resolution shell. For a routine crystal structure refinement $I/\sigma(I)$ larger than four are wanted in the maximum resolution shells. Below this number the uncertainties in the observed intensities become too high and thus the refinement less reliable.

## 1.7    The Independent Atom Model

For routine crystal structure refinement the used structure factors are derived from spherical atomic scattering factors. This means that the bonding electron density is not taken into account, which is feasible because data from an X-ray experiment with standard resolution (d = 0.80 Å) cannot resolve this. The term independent atom model (IAM) also implies that the atoms are treated as if they were independent, *i.e.* not involved in bonding. To gain information about coordination motives this is a correct assumption. Still a factor that cannot be ignored is the thermal vibration of the atoms which is convoluted with the electron density and has to be described adequately (Eq. 8).

By combining the spherical scattering factors with parameters for thermal motion it is possible to deconvolute the thermal motion from the information about the positional parameters. Most routine crystal structures can be solved and refined to derive wanted information like bond lengths and angles with this strategy.

Another, often desired information that can be determined making use of the IAM is the absolute structure. If the anomalous signal of selected atoms is strong enough to detect small differences in the intensities of the *Friedel* pairs it is possible to

unequivocally determine the absolute structure of a molecule.[24-26] This possible assignment is one of the main advantages of X-ray diffraction over other structure solving techniques and it has to be pointed out that single crystal X-ray diffraction is the only analytical tool that can provide this information unambiguously and without the use of comparison measurements or external standards.

## 1.8    The Multipolar Expansion

In the above mentioned IAM the atoms in a molecule are treated as independent and thus as if they were not chemically bound. This is an assumption that works very well for routine structure refinement from which structural parameters like bond lengths and angles can be derived. This model does not sufficiently describe more complex questions about the bonding situation itself. Sometimes it is essential to learn more about the nature of the bonds in a compound in order to correctly describe its reactivity. This has been proven very elegantly for the $S(NR)_3$ molecule where it could be shown that the reactivity towards facile transimidation[27] and the S-N insertion into a M-C bond[28] was due to charge depletions in the $SN_3$ plane at the bisections of the N-S-N angles.[29]

In order to be able to discuss the bonding situation there has to be an expansion model to the IAM which is able to describe the bonding electrons and does not regard the atoms as isolated spheres in a molecule. This expansion was first formulated by *Stewart*[30-33] and further developed by *Hansen* and *Coppens*[19] (Eq. 12). Their model is defined by a spherical core which holds the core electrons that cannot be removed from the nucleus ($P_c\rho_{core}(r)$) and a spherical valence shell ($P_v\kappa^3\rho_{valence}(\kappa r)$). The most important expansion is the last part of the equation which describes the valence electrons that take part in bonding.

$$\rho_{at}(\mathbf{r}) = P_c\rho_{core}(r) + P_v\kappa^3\rho_{valence}(\kappa r) + \sum_{l=0}^{l_{max}} \kappa'^3 R_l(\kappa' r) \sum_{m=-l}^{l} P_{lm\pm}d_{lm\pm}(\theta, \phi) \quad \text{Eq. 12}$$

All three parts have a population parameter $P$. $P_c$ gives the number of core electrons, *e.g.* two for neutral carbon atoms; $P_v$ and $P_{l,m}$ together give the number of valence electrons, *e.g.* four for neutral carbon atoms. As the electrons of some atoms may be more closely contracted than others the contraction/expansion parameters $\kappa$ and $\kappa'$ are introduced, which allow the radial functions to change shape accordingly. The radial functions $R_l$ are Slater-type functions which are calculated for free atoms with energy optimized orbital exponents ($\zeta_l$) (Eq. 13).

$$R_l(r) = \frac{\zeta^{n_l+3}}{(n_l + 2)!} r^{n_l} exp(-\zeta_l r)$$

<div align="right">Eq. 13</div>

The functions $d_{lm}$ are density-normalized real spherical harmonics expressed in polar coordinates.

There are several programs available that make use of the *Hansen-Coppens* formalism among the most popular are *MoPro*[34], *XD2006*[35] and *Jana*[36]. Within the frame of this thesis only *MoPro* and *XD2006* have been used, although the work with *MoPro* did not give satisfactory results. This is probably due to the fact that *MoPro* has been designed to treat macromolecules like peptides and derive their MM with the help of databanks that store information about structural features and multipole parameters for similar compounds.

It also has to be noted that the compound mainly dealt with in this thesis is of substantially higher symmetry than the usual macromolecule, which already proved a challenge for *XD2006* but probably was not accounted for in *MoPro*. *XD2006* has been written to deal with small molecules with datasets of high resolution and excellent quality as well as theoretically derived structure factors. For experimental datasets one can chose between four databanks from which the scattering factors are taken during the refinement all of which are based on theoretical wave function derived scattering factors.

During the course of the refinement the number of parameters for each atom is increased step by step in order to guarantee full convergence and to stabilize the refinement. As the number for $l_{max}$ is set to 4 in *XD2006* one can add an additional 27 parameters in a charge density refinement when compared to the IAM unless anharmonic motion is taken into account in which case this number can be even larger. This adds up to a total of 36 parameters per anisotropically refined atom. For the algorithm generate reliable results it is very important to have a high data to parameter ratio. While a ratio of about ten is desired for an IAM refinement the ratio for a charge density refinement should be above this; usually values around 20 are desired to avoid over fitting and thus introduction of model bias.

## 1.9   Quality Indicators after Structural Refinement

After the refinement of the crystal structure both with the IAM and the MM it is very important to check whether the refinement meets certain thresholds in regard to the quality of the derived model. Two values that are most common to monitor are the $R_1$ which is traditionally based on $F$ but can also be calculated based on $F^2$ and the weighted $R$ value $wR_2$ which is based on $F^2$ (Eq.14). Both $R$ values reveal how good the calculated structure factors fit the observed ones.

$$R_1 = \frac{\sum ||F_o| - |F_c||}{\sum |F_o|} \qquad\qquad wR_2 = \sqrt{\left\{\frac{\sum [w(F_o^2 - F_c^2)^2]}{\sum [w(F_o^2)^2]}\right\}} \qquad \text{Eq.14}$$

If the refined structure is a small molecule and the collected data are of average quality one would expect the value of $R_1$ below 15 % and the value for $wR_2$ below 10 %. For charge density datasets both values should be smaller than 10 % if the molecule only contains light atoms and there is no disorder involved. It has to be said however, that the absolute values of the $R$ factors have no direct meaning other than that the fitted model describes the observed density mathematically correct. This can be misleading if artefacts are modelled incorrectly and thus leading to lower $R$ values while in fact the fitted model is incorrect. It is therefore strongly recommended to also consult other ways to determine the data quality some of which will be discussed below. Overall, $R$ values are of limited use in quality control, although they provide gross numbers to judge on.

### 1.9.1   Residual Density Analysis

Even after a MM was refined and thus all electron density should be accounted for often residual electron density is still present. This is mainly due to systematic errors that arise from the experimental set-up and the way the electron density is reconstructed from the measured intensities. These are factors that we cannot account for during structural refinement even with a MM because they are intrinsic to the data. However, there is still a lot to be learned about the residual density left, most importantly whether it is randomly distributed among the unit cell or concentrated in certain areas. The first parameter to look at, regardless of the model being a simple IAM or the more detailed MM; is the highest peak and deepest hole in the residual density.
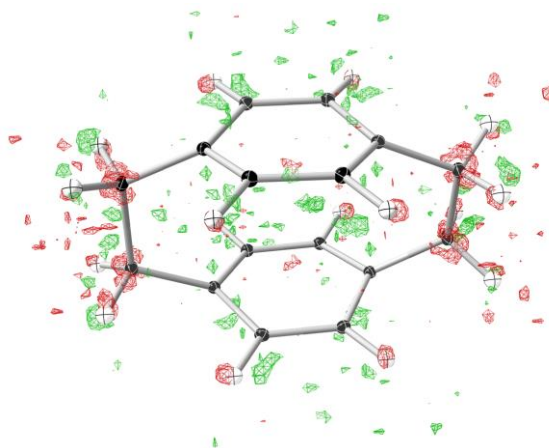


Figure 3: Residual density of paracyclophane after MM; level depicted at 0.055 eÅ$^{-3}$; positive density appears in green and negative density in red.

The calculated values should be reasonably small and should not differ much in absolute value after a multipole refinement (often referred to as a flat residual density; Figure 3).

The other descriptor usually applied in charge density studies is the absence of features in the residual density. If there are no features present the model accurately represents the measured data and there are only Poisson errors left. If however, features are present there are inaccuracies in the data modelling or at an earlier step like the data reduction and merging. *Meindl* and *Henn* published a residual data analysis tool that is very elegantly able to show both flat and featurelessness of the residual density.[37] They make use of the fractal dimension of the whole unit cell which is later analysed towards its distribution in a Gaussian shape (See Figure 4).
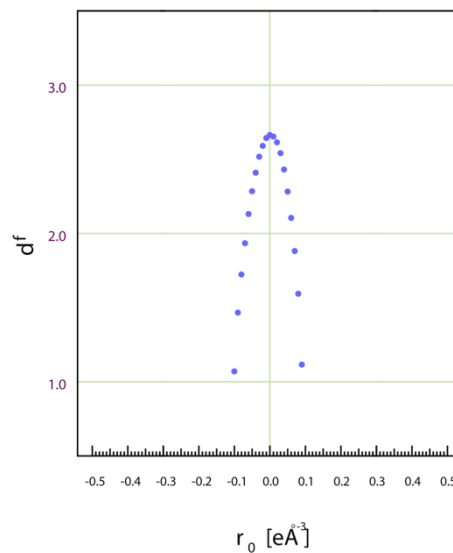


Figure 4: Fractal dimension of the residual electron density.

With an absolute flat and featureless residual density the fractal dimension would peak close to $d^f(0) = 3$ and describe a narrow parabola. Any shoulders or broad tailing of the plot indicate problems in the analysis and should warn the user to stop the refinement at this point and look for the source of potential errors. Another very important number provided by the analysis according to *Meindl* and *Henn* is the number of gross residual electrons which sums up the total error including noise (Eq. 15).

$$e_{\text{gross}} = \frac{1}{2} \int_V |\rho_0(\boldsymbol{r})| \mathrm{d}^3 \boldsymbol{r}$$

Eq. 15

18

If all electrons are accounted for correctly in the MM this value represents the noise present in the dataset and is at its minimum value. If this value is calculated over the whole unit cell it is an elegant way to compare different data processing and refinement strategies in order to find the best description for the collected intensities.

### 1.9.2 Evaluation of the Errors and Structure Factors

As with every recorded experimental value the intensities of our X-ray diffraction experiment are provided with uncertainties. This has become a point of discussion since the now routinely used area detectors provide uncertainties that can vary depending on the data reduction and scaling and sometimes result in questionable values. *Jørgensen et al.* have discussed the errors estimated by *SADABS* to result in improper values because the intensities are scaled according to an empirical formula to down weight the significance of outliers during the data reduction and scaling.[38] They promote the use of *SORTAV* to derive more reliable uncertainties. It could be shown during the course of this thesis that for small molecule data from light atom structures the absolute values for the derived parameters do not change with respect to the used data reduction software.

Nonetheless, it has proven very valuable to analyse the distribution of the standard deviations for the observed and calculated structure factors. *Zhurov et al.* were able to show that a normal probability plot[39] according to *Abrahams and Keve[40]* should follow a normal distribution. For this plot the weighted differences of the structure factors are plotted against the expected differences. If statistical weights are used, which is common for charge density refinements, the resulting plot gives an estimate for the accuracy of the determined standard uncertainties (su). As mentioned above CCD detector data are prone to underestimate the standard uncertainties and thus a weighting scheme is often used to correct the wrongly determined su's (Eq. 16).

$$w_{hkl} = \frac{1}{[\sigma(F_o^2)]^2 + \left[a\left(\frac{1}{3}F_o^2 + \frac{2}{3}F_c^2\right)\right]^2 + b\left(\frac{1}{3}F_o^2 + \frac{2}{3}F_c^2\right)}$$

Eq. 16

During an IAM and MM refinement these weighting parameters (Eq. 16) are adjusted at the very end of the refinement to give a normal distribution in the normal probability plot (Figure 5, left). The plots shown in Figure 5 are generated by the program *DRKplot* which is implemented in the *WinGX* suite.[41-42] The plot on the right in Figure 5 shows the variation of the ratio between the sum of the observed intensities and the sum of the calculated intensities plotted against the resolution. In an ideal dataset this ratio should not vary much from unity because the observed intensities should fit the calculated perfectly well if the model is adequate. There will always be a small difference because of systematic and experimental errors plus experimental noise. Additionally, to reconstruct the phases, assumptions have to be

made in order to find a model that fits best and in the course of the refinement these shortcomings lead to a small difference.
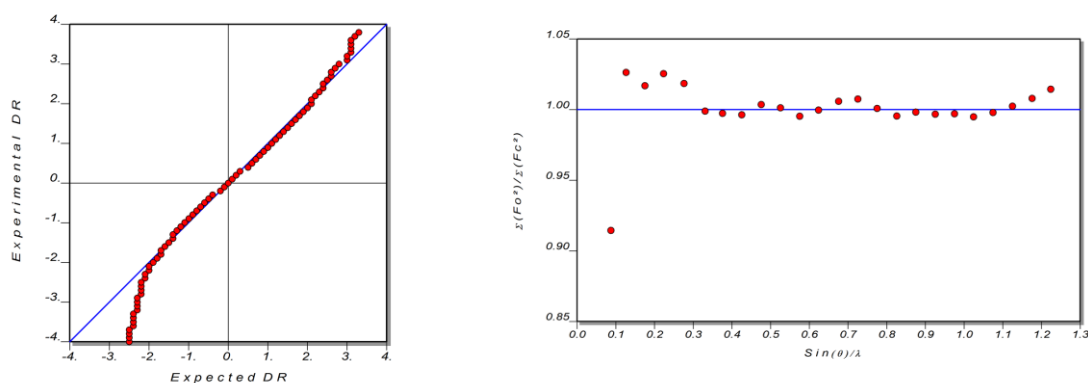


Figure 5: Normal probability plot (left) and the differences in structure factors against resolution (right).

For charge density studies a difference of about 5 % is still accepted but values above that indicate problems with either the model or the data. However, a few things about the way these plots are generated should also be carefully evaluated when studying one of them. It is in the way the program generates this plot that the resolution shells in which the structure factors are distributed are not part of the output, which means that it is not possible to determine exactly which reflections are responsible for outliers in this plot. It is also noteworthy that for samples with high symmetry the innermost resolution shells only contain very few observed reflections. As a result of this a variation greater 5 % can be the result of only one reflection that might have been collected with a wrong intensity. This fact is both an advantage and a disadvantage because it helps to identify problems with the inner data straight away but it also means that one or two bad reflections can generate large deviations. To carry out a charge density analysis it is important that the reflections hoisting all the information about the valence electron density of the atoms have been collected with great care and precision. As can be deduced from Figure 1 (p. 7) the valence electrons scatter very strongly at low angles which renders this the crucial part of the data collection. Very often a large deviation from unity observed in the plots generated by *DRKplot* coincides with high levels of both positive and negative residual density. Unfortunately, it is still not common practice to include these plots in publications dealing with charge density studies although incorrectly determined intensities have a direct influence on derived properties.

# 2 THE QUANTUM THEORY OF ATOMS IN MOLECULES (QTAIM)

The Multipole Model is able to describe the electron density distribution more accurately than the Independent Atom Model. Still, at the end of the refinement only bond lengths and angles can be extracted although with a higher precision. It is not the distribution alone that is of interest to the chemist but the quantities that can be derived from it. The most important question for synthetic chemists would probably be the one asking for a reason as to why the molecule of interest reacts in a certain manner.

Thanks to *R. W. Bader* some of the questions interesting to the wet chemist can be answered.[43-45] With a ground breaking paper in 1972 *Bader* developed the idea of QTAIM which essentially is a three dimensional curve sketching of the electron density.[46-48] This implies that the electron density $\rho(\mathbf{r})$ is a scalar vector field that can be investigated by its gradient vector field. Regarding the electron density in a mathematical way also allows partitioning of the total electron density into different basins that belong to the atoms present in the molecule but also allows the re-addition of the different parts to form the total electron density again.

## 2.1 Bond Critical Points

A chemical bond is not an observable in the density and inherently open to interpretation. Most commonly the employed measure is the distance of two atoms but of course there is no sharp dividing line. Sometimes it is not obvious from the crystal structure if two atoms share a bond or whether there is a connection which can be classified as a bond in the classical sense. With the help of QTAIM it is possible to characterize all connectivities that are based on the electron density distribution. In QTAIM these interactions are called bond paths and as *Bader* stated, if two atoms share an energy surface they will be connected through a bond path but not necessarily through a bond in the classical sense. However, if there is a bond in the classical sense there will always be a bond path between the atoms.[49-50] In order to further characterize this connection *Bader* suggests to investigate the topological features of the bond path that is the gradient of $\rho(\mathbf{r})$ (Eq. 17).

$$\nabla\rho = \mathbf{i}\frac{\partial\rho}{\partial x} + \mathbf{j}\frac{\partial\rho}{\partial y} + \mathbf{k}\frac{\partial\rho}{\partial z}$$

Eq. 17

If this derivative equals zero there is a critical point, which can be a minima, a maxima or a saddle point in the density. It is of course the sign of the second derivative that elucidates whether a minimum, a maximum, or at a saddle point of the density is

present and the curvature of this critical point can be determined by the Hessian matrix (Eq. 18).

$$H(\mathbf{r}) = \begin{pmatrix} \dfrac{\partial^2 \rho}{\partial x^2} & \dfrac{\partial^2 \rho}{\partial x \partial y} & \dfrac{\partial^2 \rho}{\partial x \partial z} \\[2ex] \dfrac{\partial^2 \rho}{\partial y \partial x} & \dfrac{\partial^2 \rho}{\partial y^2} & \dfrac{\partial^2 \rho}{\partial y \partial z} \\[2ex] \dfrac{\partial^2 \rho}{\partial z \partial x} & \dfrac{\partial^2 \rho}{\partial z \partial y} & \dfrac{\partial^2 \rho}{\partial z^2} \end{pmatrix}$$

Eq. 18

Because the Hessian matrix is real it can be diagonalized to give a set of eigenvalues. These eigenvalues give rise to the rank of the critical point ω which is equal to the number of non-zero eigenvalues. Each critical point is given a label consisting of two values, the rank and the signature σ. The signature is the sum of the signs of the eigenvalues. With these two values it is possible to deduce information about the nature of the bond, *e.g.* whether there is a chemical bond (maximum along one of the principal axes) or an interaction of more than two atoms to give a ring critical point (maximum along two of the principal axes).

The rank of the critical point in a crystal structure will in almost all cases be three as the crystal structure is the result of an energetic minimum and thus the critical point will have three non-zero curvatures. With this in mind there are four possible signatures for critical points found in crystal structures.

(3,-3) All curvatures are zero and $\rho$ is a local maximum at the critical point. This is found for atomic positions.

(3,-1) Two curvatures are negative, $\rho$ is a maximum at the critical point and a minimum along the third axis perpendicular to the first two.
This is usually found in covalent bonds.

(3,+1) Two curvatures are positive, $\rho$ is a minimum at the critical point and a minimum along the third axis perpendicular to the first two.
This is usually found inside a ring of more than two atoms and called a ring critical point.

(3,+3) All curvatures are positive and $\rho$ is a local minimum at the critical point. This is usually found inside a cage of atoms and hence called a cage critical point.

If two atoms are linked by a bond critical point then this "*atomic interaction line*" (the bond path) is defined as the path along which $\rho(\mathbf{r})$ is a maximum at all points along the bond.[51] This can be visualized easiest by the picture of a mountain ridge that

links two mountains to each other. If walking along the crest one will always be at the highest possible point in between the two mountains.

## 2.2    The Laplacian

While the connectivities between atoms can be established by looking at $\nabla\rho(\mathbf{r})$ and the classification of bond critical points, not much can be said about where the electron density is accumulated, *i.e.* whether the bond is highly polarised or if there are electrons in non-bonding regions. There is a way however, to find an answer to this questions and that is by analysis of the second derivative of $\rho(\mathbf{r})$, the Laplacian $\nabla^2\rho(\mathbf{r})$, at the bond critical point.[52-54]

Much like in a curve sketching we can deduce from the Laplacian there is charge concentration in the electron density were the Laplacian itself is negative. If a maximum is found in the Laplacian this stands for charge depletion in the density.

This gives rise to the following classifications:

$\nabla^2\rho(\mathbf{r}) < 0$      *Shared interactions*; the charge density is contracted along the bond path.

$\nabla^2\rho(\mathbf{r}) > 0$      *Closed shell interactions*; the charge density is depleted in between the atoms.

However, it has to be noted that although these criteria are almost always true they alone are not a sufficient proof for or against a certain type of bonding. The complete set of all topological descriptors has to be analysed to give a sound reasoning. Especially in regions of very flat density distributions the analysis of the second derivative might fail because there is simply not enough density to carry out the mathematical calculations behind these values.[55-57]

Although the analysis of the Laplacian at the bond critical points already gives a lot of information there is also the possibility to search for critical points in the Laplacian itself, which can then be used to identify local charge concentrations. A local charge concentration is a maximum in the negative Laplacian and is often depicted as Valence Shell Charge Concentration (VSCC).

These are especially useful when searching for electrons in non-bonding regions, which are hard to detect in the density distribution alone.

## 2.3    Ellipticity

The above mentioned characteristics depend on local concentrations or depletions of the electron density. There is one more measure which gives information about a

special concentration of charge along the bond path and that is the ellipticity $\varepsilon$ of a bond (Eq. 19). This is a value derived from the eigenvalues of the Hessian Matrix in Eq. 18 and can be used to elaborate the charge accumulation in a given plane. For a perfectly cylindrical bond like the carbon-carbon single bond in ethane the measure of $\varepsilon$ equals zero because the two eigenvalues of the Hessian Matrix perpendicular to the bond are of equal magnitude.

$$\varepsilon(r_{BCP}) = \frac{|\lambda_1|}{|\lambda_2|} - 1$$

<div align="right">Eq. 19</div>

The value of $\varepsilon$ increases with increasing deviation of cylindrical shape and can also function as an indicator for the $\pi$ character of a bond.[58] The "perfect" $\pi$ bond in the benzene molecule has an ellipticity of 0.23 whereas the isolated double bond in ethylene has an even higher value of 0.45 due to a greater charge contraction along the bond.[47] In their publication from 1983 *Bader et al.* gave standard values for carbon–carbon bonds with varying $\pi$-contribution and charge accumulation.[59]

Table 1: Selected bonds and their ellipticities observed at the bond critical point taken from [59].

| Bond | Ellipticity $\varepsilon$ |
|---|---|
| propane | 0.00 |
| butadiene | 0.72 |
| benzene | 0.23 |
| methylacetylene | 0.00 |

From the non-polar carbon–carbon single bond in propane and isobutane to the isolated carbon–carbon double bond in butadiene the value for the ellipticity increases and the isolated carbon-carbon triple bond in methylacetylene vanishes again because the two values for $\lambda$ are equal in magnitude (Table 1). The values in Table 1 nicely depict the rising ellipticity from the single bond to the conjugated or aromatic double bond in benzene to the isolated double bond in butadiene. The isolated triple bond in acetylene has a the same value as the single bond because it is again built symmetrically with respect to the bond. In order to give rise to positive values for $\varepsilon$ the eigenvalue of smallest magnitude has to be $\lambda_2$.

# 3 PAIRED REFINEMENT AND $R_{free}$

While there are a number of indicators to judge about the quality of the data there are only very limited indexes published to deal with model quality in a charge density refinement. There are a number of questions to answer during a charge density refinement the most important being those about the number of parameters to be refined and the refinement strategy itself. Furthermore, a decision has to be made about the resolution limit of the data and about other data truncation procedures like outlier rejection.

One relatively new method to monitor the quality of a refinement is the paired refinement as introduced by *Diederichs* and *Karplus*.[21,60] With this model it is possible to link the model with the data quality. In a paired refinement a model derived with a certain dataset is refined against a different dataset with the same refinement protocol. The resulting models are then compared by means of standard $R$ values to judge which data result in the better model. Although this method was presented for macromolecular refinements it is also applicable to charge density studies. It is common practice in both fields to truncate the data at a certain resolution to ensure accurately measured intensities or to perform a rigorous outlier rejection in terms of $I/\sigma(I)$ values. Until *Karplus* and *Diederichs* published their paired refinement approach it was accepted to discriminate against certain datasets solely by means of merging $R$ factors. During the course of this thesis it became obvious that the paired refinement approach is superior to the simple $R$ value approach. Furthermore, it makes it facilities the justification for a certain dataset even though the intuitive choice would have been different. In macromolecular X-ray crystallography the determination of the correct crystal structure almost always involves the testing of different models. Instinctively, one would expect to have the best model to describe the experimental data when the $R$ values are at their lowest. Unfortunately, artificially low $R$ factors can also be generated by increasing the number of parameters without actually improving the model. This procedure is called over fitting. As an indicator towards over fitting of the data our work group has only recently started to use a procedure that has been common practice in the macromolecular world for quite some time. To avoid an over fitting *Brünger* developed "a reliable and unbiased indicator of the accuracy of such models", the so called $R_{free}$.[61-62] In order to validate a certain model against over fitting the reflection dataset is divided into a *working* and a *validation* set. Macromolecular datasets can be divided quite easily as the molecules in question almost exclusively crystallize in non-centrosymmetric space groups of low symmetry which result in a high number of independent reflections. Certain extra criteria have to be fulfilled when dividing a dataset, *i.e.* the *Friedel* pairs both have to be either in the *working* or the *validation* set.
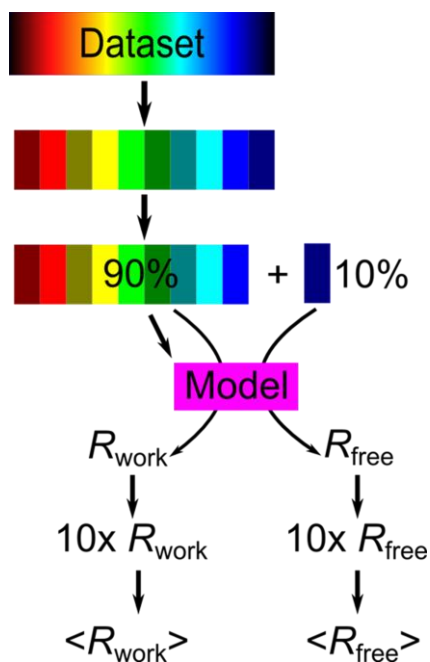
Scheme 1: Working scheme for an $R_{free}$ analysis.

The *validation* set must not be biased by any model before it is used to calculate the $R_{free}$; it is simply left untouched. The *working* set is then refined against a certain model which is subsequently used to derive the $R_{free}$ value against the *validation* set. If the $R_{free}$ value is higher than the $R_{work}$ this is a sign for over fitting. While it is already common to use this indicator to avoid over fitting in the macromolecular community only very few reports are published for charge density investigations.[63] Despite this, the option to monitor the course of a charge density refinement with $R_{free}$ has been implemented into the *MoPro* software.[34,64] Within the *Stalke* group we have developed a slightly different procedure (Scheme 2).

The full dataset is divided into ten subsets of roughly equal size and the *Friedel* pairs are always in the same set. Subsequently, ten different refinements with ten independent *training* sets are performed. The ten different models derived by this method are used to calculate ten different $R_{free}$ values with the ten *validation* sets. Additionally, another $R$ value is calculated, the $R_{cross}$ (Eq. 20), which is derived using all calculated intensities (*xd.fco*) of the validation sets.[62]

$$R_{cross} = \frac{\sum |F_o^2 - F_c^2|}{\sum F_o^2}$$

Eq. 20

With this method it is possible to monitor the course of $R_{free}$ depending on the number of parameters that are refined. It is possible to discriminate against certain parameters to be refined and thus avoid strong model bias in the derived parameters.

26

# 4     [2,2]-Paracyclophane

After the previous chapters gave an introduction to the methods that will be used and the pitfalls that lurk on the way the following subchapters will present the use of the described methods. Within this chapter two main questions will be answered. Firstly, there had been an ongoing discussion about the two possible conformers of [2,2]-paracyclophane at low and elevated temperature. After a brief introduction to the molecule itself and its importance in both synthetic and theoretical chemistry the two conformers are established unequivocally.

In the following chapters, the aspect of data quality is dicussed. To solve the problem of correct space group assignment and possible phase transitions many different single crystal X-ray datasets have been recorded at various temperatures and diffractometers. In order to find the best data various quality indicators and their role in charge density data are investigated.

## 4.1     [2,2]-Paracyclophane in Synthetic Chemistry

After [2,2]-paracyclophane (the compound will be referred to as paracyclophane in the following text) was discovered in 1949 by *Brown* and *Farthing* as a side product in a polymerization reaction it has played a large role in synthetic chemistry. Because the parent compound can be easily substituted and thus derivatized, the family of cyclophanes has intrigued experimental chemists. These highly strained molecules consist of very reactive aromatic ring systems that undergo substitutions much quicker than unbridged aromatics. Because the aromatic rings are forced together closer than they would normally pack they also experience significant repulsion interactions which means that they have a higher affinity to electron withdrawing substituents to ease the repulsion forces.[65] These π-π interactions are often denoted transannular interactions and the cyclophane family is a perfect group to study them. Various theoretical investigations have been conducted mostly together with spectroscopic measurements.[66-71]

What is probably a direct result of these interactions is the ability to readily undergo Diels-Alder-Additions.[72] While paracyclophane as the smallest member of the family only reluctantly undergoes a Diels-Alder-Addition (six days at room temperature) this reactivity is drastically enhanced if more and longer bridges are introduced (order of a few seconds).[65]

when an electron withdrawing group is introduced the aromatic rings tend to move even closer together, which can be due to the strain relieve when electron density is withdrawn from the ring system. This has been thoroughly studied for the reactivity of paracyclophane towards $Cr(CO)_6$.[73-74] *Dyson et al.* compared the reactivity of paracyclophane with that of *p*-xylene both experimentally and theoretically. They

found the rate constants for the rate determining step to be $1.6 \cdot 10^{-6}$ for paracyclophane and $1.2 \cdot 10^{-6}$ for *p*-xylene. What does not seem to make much of a difference becomes more impressing when both ligands are made available to $Cr(CO)_6$ at the same time, the formed product is dominated by the paracyclophane reaction with a ratio of 10:1.[73]

While the effect of transannular interactions in paracyclophane has been discussed and investigated on a theoretical level and with spectroscopic experimental results only one charge density investigation based on an X-ray diffraction dataset collected at 100 K has been published.[75] It was also the goal of this thesis to investigate the transannular interactions for a low-temperature dataset in order to characterize the reactivity of paracyclophane at reduced temperature.

## 4.2     A Short History of Paracyclophane

Paracyclophane has been first discovered as a side product of di-*p*-xylylene polymerization and its first crystal structure was determined in 1949 by *Brown* and *Farthing* who were intrigued by its structural features.[76] This small but very interesting molecule consists of two benzene rings stacked on top of each other linked by an ethylene bridge each on two adjacent carbon atoms (Figure 6). Due to these two ethylene moieties the benzene rings are held closer than their *van der Waals* radii would allow them to be packed (>3.4 Å). *Brown* and *Farthing* reported an inter ring distance of 3.10 Å which is significantly shorter than the distance in graphite for example which is 3.35 Å.
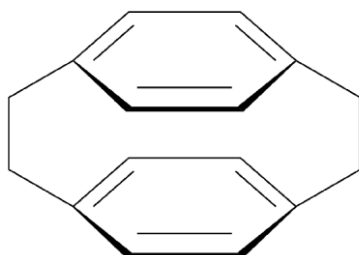


Figure 6: Sketch of paracyclophane.

Another interesting feature is the non-planarity of the aromatic rings which is necessary to accommodate the short linkers. Interestingly, the aromatic system does not seem to be disturbed by this deformation as the inner ring bond lengths are still reported to be equal (1.4 Å) as would be expected for an aromatic system. In a follow-up publication *Brown* and *Farthing* report difficulties in assigning the correct space group having to choose between the non-centro symmetric $P\bar{4}n2$ and the centro symmetric $P4_2/mnm$. In the course of their refinement it became obvious that the

centro symmetric space group was the correct one. As was usual at this time the X-ray diffraction experiment was done on a powder sample at room temperature.[77]



Figure 7: Non-centro symmetric $D_2$ (left) and centro symmetric $D_{2h}$ (right) structure of paracyclophane.

When *Lonsdale et al.* published an article on paracyclophane in 1960 they compared the results of single crystal X-ray diffraction experiments performed at 93 and 291 K.[78] Having worked as a research assistant with *Bragg* and establishing the nature of benzene molecules in a crystal by X-ray diffraction, *Lonsdale* was one of the pioneers of X-ray diffraction and was constantly working on improving the method. The work published on paracyclophane deals with the anisotropy of thermal expansion coefficients of atoms in a crystal structure and its effect on the bond lengths. This study resulted in strong vibrational movements of the molecule namely two strong ones characteristic for a "concertina-like vibration of the two benzene rings towards and away from each other (…) and a twisting of the benzene rings out of parallelism with one another(…)".[78] To the best of our knowledge this is the first time this twisting motion has been mentioned in literature and it is this twisting motion that would be the center of discussions about paracyclophane for the following 50 years. If frozen out at low temperature this twisting motion would result in a symmetry that would be described in the non-centro symmetric space group $P\bar{4}n2$ (Figure 7).



Figure 8: Eclipsed and staggered position of the hydrogen atoms due to the twist.

Although the study of *Lonsdale et al.* used data collected at liquid nitrogen temperature this was not cold enough to justify a change in space group, the structure refined still perfectly in $P4_2/mnm$. *Ron* and *Schnepp* were the first to investigate paracyclophane at a temperature as low as 20 K when they collected an electronic spectrum plus absorption and fluorescence spectra in 1962.[79] They noticed a very weak peak in their spectra that should have been forbidden in a centro symmetric structure. This peak could be assigned to a motion which would result from a $D_2$
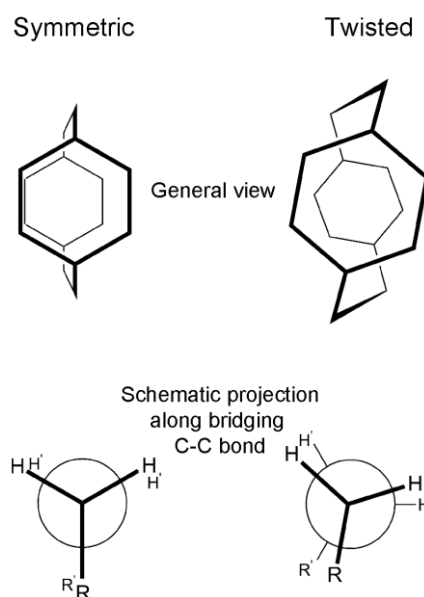
symmetric structure and a resulting twist of the ethylene bridges of about 3°. Although only visible for the excited state this feature was reproducible and follow-up experiments as well as theoretical calculations backed the small twist of the ethylene bridges.[66,80]

Further evidence of a phase transition at low temperatures even in the ground state was published by *Andrews* and *Westrum* in 1970 when they could show that the heat capacity of paracyclophane had an unsteady region around 50 K.[81] Due to the fact that no crystal structure was available for these temperatures they speculated about a twisted form which would also be energetically favourable as it relieves the strain on the molecule due to eclipsed hydrogen positions (Figure 8).

Following this publication *Hope, Bernstein* and *Trueblood* reported a reinvestigation of the structure of paracyclophane in 1972.[82] A feature that experienced special attention was the strong thermal motion of the bridging carbon atoms. *Trueblood* and co-workers tried to delineate this motion with a disordered model which is essentially a description of the two enantiomers of the twisted structure in the low-temperature phase. They refer to *Westrums* publication to further promote a dynamic disorder present at room temperature to account for the strong thermal motion. This crystal structure was used as a base for further theoretical and experimental investigations although the experiment was conducted at room temperature and thus nowhere near the phase transition region. It has to be said however, that it was not common to use low-temperature devices during X-ray experiments until the early 90ies and most experiments were conducted at room temperature. This means it is not surprising that the determination of the low-temperature crystal structure was not feasible for a long time simply because there was no suitable hardware. For almost 30 years after the reinvestigation of *Hope, Bernstein,* and *Trueblood* a lot of spectroscopic experiments were performed which further fuelled the discussion about a symmetry change at low temperatures but no experiment ultimately proving the existence of the twisted structure was reported.

At the end of the 90ies, computational methods reached a new level of accuracy due to stronger computational power, which promoted the rapid expansion of energies and interactions that could be taken into account when calculating an energetic minimum structure. In the course of this expansion a fierce discussion started between *Walden* and *Glatzhofer* on one side and *Henseler* and *Hohlneicher* on the other. It started with a publication of *Walden* and *Glatzhofer* in which they promoted the hybrid HF/DFT hybrid functional B3LYP to be able to correctly describe the minimum structure of the highly strained paracyclophane. They calculated a twisting angle of 3.9°.[83]

Not a year later a second paper was published by *Henseler* and *Hohlneicher* dealing with the same problem also using HF/DFT B3LYP hybrid functionals but also a split valence basis set (MP2/6-31G(d)) which includes polarization and diffuse functions at all atoms.[84] With this method they calculated a twisting angle of about 16°. It seems to be that this apparent dissimilarity which goes along with a difference in the

stability of the minimum structure revived the paracyclophane research on a structural level.

After low-temperature devices for X-ray diffractometers had been made available for a wider community and slowly established as routinely used devices, more and more crystals that were excluded from X-ray diffraction due to their thermal instability could be analysed. Among the first in Germany to make use and improve the low-temperature devices was *Stalke* who designed a low-cost low-temperature device and most importantly designed an apparatus that allowed crystal handling at low temperatures under inert conditions.[85-87] Using these devices it became feasible to manipulate crystals that melted at room temperature and were sensitive to air and moisture and for the first time it was possible to determine the crystal structures of compounds such as *t*BuLi and other lithium organyles.[85-86] It was in 1997 that *Leusser* from the *Stalke* group first conducted single crystal X-ray diffraction experiments at very low temperatures (19 K) of paracyclophane and was thus, to the best of my knowledge, the first to unambiguously determine the low-temperature crystal structure of paracyclophane. [88] Based on the data of this measurement it became clear that the low-temperature phase was indeed twisted and that the symmetry was lower than in the high-temperature phase resulting in the non-centrosymmetric space group $P\bar{4}$n2. The twist in the ethylene bridges was described with a value of 12.6° which is very close to the calculated value by *Henseler* and *Hohlneicher* (16°). The geometry of the 19 K experiment was used to do a geometry optimization by *Grimme* in 2004 which, for the first time, was able to reproduce the experimental results and correctly predict the bond lengths and angles.[89] *Grimme* used a newly developed spin-component-scaled MP2-method (SCS-MP2) which is also a hybrid density functional. He calculated the $D_2$-$D_{2h}$ barrier to be as low as 0.2 kcal/mol. Even though this result was based on our experimental results and was meant to settle a decade's long debate the opposite was the result. While most theoretical publications cite the twisting angle and result in minimum structures with $D_2$ symmetry and a considerable twist some experimental publications still doubt a twisted minimum structure. Among the most fierce opponents against the twist angle is a publication from *Dodziuk et al.* from 2011 in which they even argue that the experimental results from *Leusser* were plain wrong.[90] In this publication they arrive at the conclusion that there is no minimum structure with a considerable twist based on NMR experiments which are conducted well above the postulated phase transition region. They calculated geometry optimized structures using DFT calculations and arrive at a very small twist angle of less than 5 °.[90] Although they mention the phase transition published by *Westrum et al.* they do not seem to believe in a twisted minimum structure.

In pursuance of the correct description of the low-temperature phase and the phase transition region and to end the dispute about the twist angle single crystal X-ray diffraction data up to high resolution (d ≤ 0.45 Å) has been collected for 15, 45, 50, and 55 K. In addition the heat capacity as a function of the temperature from 4 to 70 K

31

was measured (Scheme 3). It was the aim of this thesis to do a full aspherical charge density refinement of the low-temperature phase based on the results from the diploma thesis by *Leusser*.[88] Additionally, the nature of the phase transition and its exact location was to be determined.

## 4.3    Phase Transitions in Paracyclophane

Based on the heat capacity measurement of *Westrum et al.* high resolution single crystal X-ray diffraction datasets were collected both on our in-house diffractometer and at a synchrotron beam-line (for further information about the data collection see 10.1.1). Several datasets were collected over a temperature range from 15 K to 300 K allowing us to detect structural changes within the phase transition region. From the publication of *Westrum et al.* we expected the phase transition to take place between 40 and 70 K; a temperature range that is hard to probe with the standard cooling devices for X-ray diffractometers. This is due to limitation to either liquid helium or liquid nitrogen as a cooling gas which are not able to stabilize temperatures around 60 K. For our data collection an open stream *Oxford Helijet* was used to generate stable temperatures in the range from 15 K to 50 K, by pushing the hardware to its absolute limit we were able to generate 60 K warm gas flow of helium but the temperature is not stable in this range. With a standard liquid nitrogen cooling device like the *Bruker Kryoflex2,* which was used for the elevated temperature measurement the temperature scale ranges from roughly 90 K to room temperature.

### 4.3.1    Phase Transitions Studied by X-ray Diffraction

Based on the work of *Leusser* the structure solution for the low-temperature datasets was straight forward and resulted in the non-centro symmetric space group $P\bar{4}n2$ which gives rise to a twist of the ethylene bridges and the aromatic carbon rings as described in Figure 7 and Figure 8. There were no signs of disorder along the aliphatic carbon bond but only one discrete position for the bridging carbon atom (Figure 9).

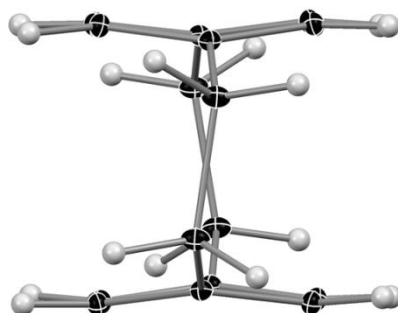

Figure 9: Single crystal structure of paracyclophane at 15 K.

It was also not possible to refine the structure in the higher symmetrical space group $P4_2/mnm$ as has been done in previous crystal structure determinations at temperatures above 80 K. This result was an early sign that the nature of the twist is dynamic and that it freezes out below 45 K. Spectroscopic results from experiments

conducted below 30 K support this assumption as well as theoretical calculations which predict an energetic barrier of only a few kcal/mol between $D_2$ and $D_{2h}$ symmetry.[79,89,91-92]

The properties derived from the crystal structure are in excellent agreement with the theoretical values available for the low-temperature phase and the values derived by *Leusser* in an earlier study.[88-89,93] To extend the characterisation of the structural features beyond mere bond lengths and angles *Hope et al.* and *Grimme* defined the angles *alpha* and *beta* (Figure 10).
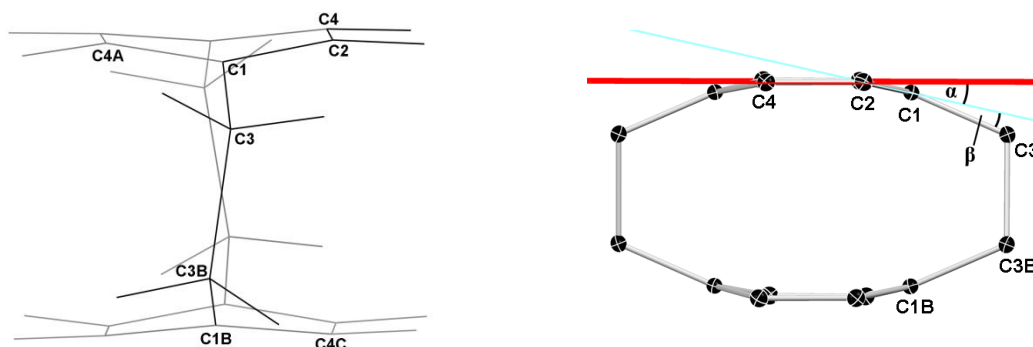


Figure 10: Sketch of paracyclophane (left); definition of the angles *alpha* and *beta* (right).

The angle *alpha* is enclosed by a plane defined by C2, C4, C2A and C4A and a second plane defined by C2, C4 and C1. It describes the distortion out of planarity for the benzene rings. The angle *beta* is enclosed by the plane going through C2, C4 and C1 and the bond C1–C3. Although there is a substantial bend of the aromatic ring out of planarity (*alpha* = 12.5°) the aromatic ring system is still intact demonstrated by the almost equal bond lengths C1–C2 and C2–C4 (Table 2). The value for *alpha* is in good agreement with the one calculated by *Grimme*.[89] Rather interestingly the two angles *alpha* and *beta* seem to be temperature independent as they do not change much over a temperature range of almost 300 K (Table 2). This results in an almost equal interring distance (C1–C1B) which varies only within 0.01 Å over the same temperature range. The only distance which changes significantly is the distance of the bridging unit C3–C3B which is not surprising as the system tries to lower its energy by avoiding eclipsed formation in the low-temperature phase and the bond is thus stretched by 0.02 Å below 45 K. The most striking difference to previously published crystal structures is the twisting or torsion angle of the aliphatic bridge which is zero in the high-temperature phase but has a value of 12.83(4)° in our 15 K experimental data (Table 2).

34

Table 2: Selected bond lengths and angles.

| | 15 K exptl.[a] | calc.[b] | 19 K exptl.[c] | 45 K exptl.[a] | 55 K exptl.[a] | 120 K exptl.[d] | 100 K exptl.[e] | 291 K exptl.[f] |
|---|---|---|---|---|---|---|---|---|
| C1—C3 | 1.5084(5) | 1.506 | 1.5080(5) | 1.5128(16) | 1.5108(17) | 1.5084(9) | 1.509 | 1.547 |
| C1—C2 | 1.3993(4) | 1.401 | 1.3992(6) | 1.401(2) | 1.3978(10) | 1.3980(6) | 1.384 | 1.380 |
| C2—C4 | 1.3942(5) | 1.394 | 1.3953(5) | 1.3947(16) | 1.3913(18) | 1.3925(10) | 1.386 | 1.415 |
| C1—C4A | 1.3993(4) | 1.400 | 1.3995(6) | 1.398(2) | 1.3978(10) | 1.3980(6) | | |
| C3—C3B | 1.5927(6) | 1.594 | 1.5931(8) | 1.592(2) | 1.584(2) | 1.5737(14) | 1.562 | 1.630 |
| C1—C1B | 2.7837(8) | 2.772 | 2.7825(11) | 2.785(2) | 2.785(2) | 2.7812(12) | 2.76 | 2.751 |
| C2—C4C | 3.0990(9) | 3.080 | 3.0978(10) | 3.1012(16) | 3.1004(16) | 3.0956(11) | 3.09 | 3.087 |
| $\varphi$[g] | 12.83(4) | 17.6 | 12.69(8) | 10.7(3) | 0 | 0 | | |
| $\alpha$ | 12.5 | 12.2 | 12.5 | 12.6 | 12.5 | 12.4 | 12.6 | 14 |
| $\beta$ | 11.1 | 11.5 | 11.1 | 10.9 | 10.9 | 11.2 | 11.2 | n.a. |

[a]15 K data collected at the APS [b] SCS-MP2 level of theory, taken from [89] [c] 19 K data taken from [88] [d] 120 K data collected with Mo-Kα radiation [e] taken from [82] [f] taken from [78] [g] torsion angle defined by C1—C3—C3B—C1B.

The twisting or torsion angle has been described by *Hope et al.* as well but it was calculated for a disordered model in the higher symmetrical space group $P4_2$/mnm and has thus a considerably lower value.[82] The theoretical value obtained by *Grimme* is somewhat larger than the experimental value but his results were the first that were able to predict a value close to the experimental one founding his calculations on the geometry of the 19 K dataset collected by the *Stalke* group.[89] A value close to *Grimmes* was later also reported by *Bachrach* who also used DFT functionals and various basis sets with different expansion parameters taking molecular forces into account but did not have access to the experimental geometry.[93] It also has to be pointed out that although the 19 K dataset was collected using Ag-Kα radiation and a point detector and is thus of considerably lower multiplicity than the 15 K dataset the number of independent reflections is very high for the point detector dataset and the geometrical parameters are therefore reliable (Table 3). They do not vary within the given standard deviations for the two datasets which clearly shows that the low-temperature phase is indeed the most stable and energetically most favourable minimum structure and no polymorph that crystallized by accident.

Table 3: Crystallographic data after IAM.

| Parameters | 15 K | 19 K | 120 K |
|---|---|---|---|
| Crystal System | tetragonal | tetragonal | tetragonal |
| Space group | $P\bar{4}n2$ | $P\bar{4}n2$ | $P4_2/mnm$ |
| Wavelength λ | 0.39360 | 0.56086 | 0.71073 |
| $\theta$ range for data collection [°] | 1.917 to 31.188 | 2.731 to 49.307 | 3.446 to 49.116 |
| Limiting indices | $-19 \leq h \leq 19$ | $-13 \leq h \leq 20$ | $-16 \leq h \leq 16$ |
| | $-20 \leq k \leq 15$ | $-13 \leq k \leq 17$ | $-16 \leq k \leq 13$ |
| | $-24 \leq l \leq 24$ | $-6 \leq l \leq 24$ | $-19 \leq l \leq 19$ |
| Reflections collected | 49429 | 5172 | 30579 |
| Independent reflections | 5147 ($R_{int}$ = 7.05 %) | 4359 | 1530 ($R_{int}$ = 4.22 %) |
| Completeness to $\theta$ | 98.6 % ($\theta$ = 13.660°) | 100 % ($\theta$ = 19.665°) | 99.3 % ($\theta$ = 25.242°) |
| Data/restraints/parameters | 5147 / 0 / 53 | 4359 / 0 / 49 | 1530 / 0 / 30 |
| Goodness – of – fit on $F^2$ | 1.104 | 0.986 | 1.180 |
| Final $R$ indices [$I > 2\sigma(I)$] | $R1$ = 2.60 %, $wR2$ = 6.88 % | $R1$ = 4.10 %, $wR2$ = 10.62 % | $R1$ = 4.60 %, $wR2$ = 14.99 % |
| $R$ indices (all data) | $R1$ = 2.72 %, $wR2$ = 6.98 % | $R1$ = 6.68 %, $wR2$ = 11.22 % | $R1$ = 4.98 %, $wR2$ = 15.67 % |
| Largest diff. peak and hole | 0.753 and -0.224 eÅ$^{-3}$ | 0.782 and -0.366 eÅ$^{-3}$ | 0.462 and -0.290 eÅ$^{-3}$ |

For temperatures above 90 K it becomes apparent that the displacement parameter for C3 is considerably larger orthogonal to the C-C bond compared to the other carbon atoms (Figure 11). This has been observed in all earlier crystal structure determinations and was the reason *Hope et al.* refined a disordered model which essentially models the two enantiomers of the low-temperature phase. The refinement of a similar model for our data was not feasible as the refinement got unstable and convergence was not reached even if restraints or constraints were applied.
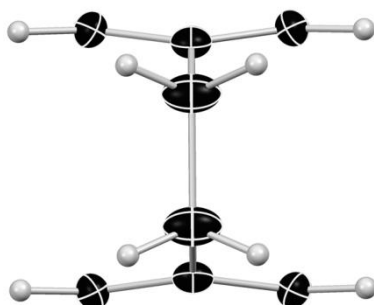


Figure 11: Single crystal structure of paracyclophane at 120 K.

It was therefore decided to favour a model which does not account for the presence of disorder. This is supported by a charge density study reported by *Lyssenko et al.* showing that the paracyclophane molecule at 100 K satisfies the Hirshfeld rigid-bond criterion.[94] Within this publication it was also stated that the disorder in solid paracyclophane is of dynamic nature and can thus probably not be resolved by X-ray crystallography at this temperature.[75] To gain more insight into the nature of the structural phase transition heat capacity ($C_p$) measurements were performed in the work group of *Scherer* in Augsburg. The cooling and heating $C_p/T$ sequences consistently revealed a sharp anomaly at 45.2 K with a full width at half maximum of 0.7 K and a secondary $C_p/T$ feature (shoulder) at 60 K (Scheme 3). This is a more detailed result than from the earlier study by *Westrum et al.* who reported only one broad "rounded" $C_p$ maximum between 50 and 70 K.[81] The resolution of this study was not sufficient enough to provide a microscopic picture of the transition.
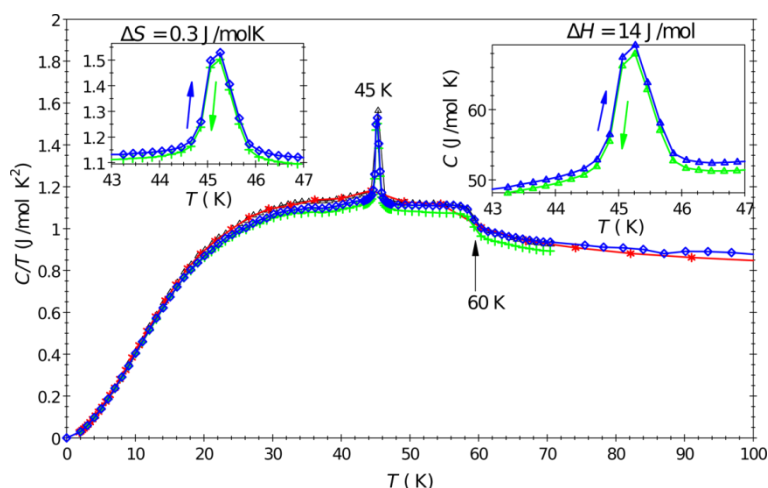


Scheme 3: Temperature dependent specific heat divided by temperature ($C_p/T$) of paracyclophane. The inserts show an enhanced view of the λ-type shape at 45.2 K in $C_p$ *vs. T*.

The observed course of the specific heat resembles the one of the λ-type transition in ferrocene at 163.9 K which is connected with a rotational order disorder transition involving the cyclopentadienyl rings. For this structure the features were explained by the presence of a mixed phase formed by the ferrocene conformers (staggered/eclipsed).[95] This could also be the case in our experiment for the shoulder at 60 K being formed by the coexistence of $D_{2h}$ and $D_2$ symmetric molecules. The X-ray single crystal diffraction data collected at 45 K, 50 K and 55 K support this interpretation as the $D_{2h}$ model fits the data more accurately the higher the temperature. Accordingly, the broad $C_p/T$ shoulder at 60 K might simply reflect the small variation of the cell parameters as a consequence of a temperature dependent change of the ratio of $D_{2h}$ and $D_2$ symmetric molecules.

Furthermore, analysis of the symmetry relationship between the crystal structures above and below the phase transition reveals that the formation of the low-temperature modification of paracyclophane (space group $P\bar{4}n2$) below 45.2 K

proceeds via a continuous *translationengleiche* phase transition of index t2 from the centro symmetric high-temperature (space group $P4_2/mnm$) towards the acentric low-temperature modification. A phase transition is often related to twinning. After careful investigation of the collected data we did not observe any signs of twinning. There was no splitting of the reflection profiles and there remained no unindexed spots. This excludes non-merohedral twinning. For pseudo-merohedral twinning a transformation into a higher symmetry crystal class needs to be possible. This is not the case in our study. The only twinning possible in this compound would be merohedral twinning which would show as a twinning by inversion. The mirror plane that exists in space group $P4_2/mnm$ of the high-temperature phase is related to the inversion center in space group $P\bar{4}n2$. This kind of twinning is thus the most favourable one. However, the anomalous dispersion of carbon at the used wavelengths is not large enough to decide about the absolute structure or chirality. This renders a decision about twinning by inversion impossible but the structure determination would remain untouched in any case as the systematic absences are the same in both cases.

The enthalpy change of $\Delta H = 14$ J/mol and the entropy change of $\Delta S = 0.3$ J/mol K at 45.2 K can thus be classified as an order disorder transition. More evidence for an order disorder transition is gained from the lack of hysteretic behaviour between cooling down and warming up cycles.

Although we had proof for the first phase transition already in hand from X-ray diffraction experiments it was unclear what really happened in the phase transition region. Based on the specific heat measurement over a broad temperature range three more single crystal X-ray diffraction datasets were collected at the APS beam-line. To unequivocally establish the structural changes in the phase transition region, high resolution datasets at 45 K, 50 K, and 55 K were collected. Despite the high resolution and the excellent data quality the third phase or a change in structural parameters around 60 K was not observed.

There is, however, further proof for the phase transition at and slightly above 45 K. Within the region from 45 K to 60 K neither model within the two known space groups describes the data perfectly. The only difference of symmetry in both space groups is the absence of an additional mirror plane in $P\bar{4}n2$. If in doubt about the correct space group assignment it is important to carefully evaluate the weaker reflections especially so as they bear the most crucial information when deciding for or against a centro symmetric setting.[96-99]

Table 4: Crystallographic data for 45 K.

| Parameters | 45 K | | | |
|---|---|---|---|---|
| Crystal System | tetragonal | | | |
| Wavelength $\lambda$ | 0.41328 | | | |
| $\theta$ range for data collection [°] | 2.532 to 20.164 | | | |
| Reflections collected | 13952 | | | |
| Completeness to $\theta$ | 97.6 % ($\theta = 14.357°$) | | | |
| Limiting indices | $-12 \leq h \leq 10$ | | | |
| | $-10 \leq k \leq 12$ | | | |
| | $-13 \leq l \leq 15$ | | | |
| Space group | $P\bar{4}n2$ | | $P4_2/mnm$ | |
| Independent reflections | 1309 ($R_{int} = 6.80$ %) | | 738 ($R_{int} = 6.93$ %) | |
| Data/restraints/parameters | 1309 / 0 / 53 | | 738 / 0 / 30 | |
| Goodness – of – fit on $F^2$ | 1.043 | | 1.381 | |
| Final $R$ indices [$I > 2\sigma(I)$] | $R1 = 4.17$ %, | | $R1 = 8.17$ %, | |
| | $wR2 = 10.92$ % | | $wR2 = 19.10$ % | |
| R indices (all data) | $R1 = 4.75$ %, | | $R1 = 8.57$ %, | |
| | $wR2 = 11.24$ % | | $wR2 = 19.25$ % | |
| Largest diff. peak and hole | 0.551 and -0.210 eÅ$^{-3}$ | | 0.638 and -0.478 eÅ$^{-3}$ | |
| $F_c/F_{c(max)}$ | 0.000 -0.040 | 0.040 - 0.064 | 0.000 - 0.023 | 0.023 - 0.049 |
| Number of reflections in group | 132 | 135 | 76 | 72 |
| $K$ | 1.117 | 1.030 | 10.503 | 2.684 |

A figure which gives information about the goodness of fit for reflection intensities is $K = \frac{|[F_o^2]|}{|[F_c^2]|}$ calculated for the reflections with the lowest intensity. For a high quality crystal these factors should not deviate much from unity as the model should fit the collected data well. Every error due to the model and/or the data would affect the weakest reflections most and thus this $K$ value is a reliable indicator for problems either with the model or the data quality. Not being in doubt about the quality of the crystal or the way the data were collected high $K$ values will only monitor model deficiencies in this case.

For the dataset collected at 45 K refinement in both symmetry settings is feasible but a distinct preference for the lower symmetry setting can be observed. This becomes obvious when the resulting $R$ values for both space groups are compared because the $R1$ almost doubles for the high symmetry setting compared to the non-centro symmetric space group. The resulting residual density also clearly shows a preference of the low symmetry setting as we see well defined residuals on the bonds which are expected for a high resolution dataset that has only be modelled with the IAM (Figure 12).

The refinement in $P\bar{4}n2$ results in a $K$ value for the weakest reflections of 1.117 while the refinement in $P4_2/mnm$ results in $K = 10.503$ which clearly indicates that the weakest reflections do not fit the model. This is in very good agreement with the idea that we enter the phase transition region at this temperature; therefore the low symmetry setting should still be the favourable one.



Figure 12: Residual density after IAM refinement for 45 K; left: space group $P\bar{4}n2$ (level depicted at ±0.12e Å$^{-3}$); right: space group $P4_2/mnm$ (level depicted at ±0.31 eÅ$^{-3}$); green colour indicates positive and red colour negative residual density.

Increasing the temperature to 50 K it becomes more apparent that there will ultimately be a change from a structure without the additional mirror plane below 45 K to a structure with that mirror plane above 60 K. Similar to the refinement at 45 K both symmetry settings converge nicely but unlike at lower temperature there is no strong bias towards one or the other space group. Both refinements lead to reasonable values ($R1 = 5.85\,\%$, $K = 1.686$ for $P\bar{4}n2$ and $R1 = 6.16\,\%$, $K = 3.656$ for $P4_2/mnm$) which do not allow a clear discrimination (Table 5).

Table 5:Crystallographic data for 50 K.

| Parameters | 50 K | |
|---|---|---|
| Crystal System | Tetragonal | |
| Wavelength $\lambda$ | 0.41328 | |
| $\theta$ range for data collection [°] | 2.531 to 18.559 | |
| Reflections collected | 12514 | |
| Completeness to $\theta$ | 97.6 % ($\theta = 14.357°$) | |
| Limiting indices | $-9 \leq h \leq 11$ | |
| | $-10 \leq k \leq 11$ | |
| | $-12 \leq l \leq 14$ | |
| Space group | $P\bar{4}n2$ | $P4_2/mnm$ |
| Independent reflections | 1032 ($R_{int} = 7.43$ %) | 587 ($R_{int} = 7.54$ %) |
| Data/restraints/parameters | 1032 / 0 / 53 | 587 / 0 / 30 |
| Goodness – of – fit on $F^2$ | 1.083 | 1.123 |
| Final $R$ indices [$I > 2\sigma(I)$] | $R1 = 4.63$ %, $wR2 = 10.86$ % | $R1 = 5.44$ %, $wR2 = 12.31$ % |
| R indices (all data) | $R1 = 5.85$ %, $wR2 = 11.54$ % | $R1 = 6.16$ %, $wR2 = 12.70$ % |
| Largest diff. peak and hole | 0.349 and -0.208 eÅ$^{-3}$ | 0.350 and -0.224 eÅ$^{-3}$ |
| $F_c/F_{c(max)}$ | 0.000 -0.026     0.026 - 0.045 | 0.000 - 0.022     0.023 - 0.041 |
| Number of reflections in group | 106          103 | 62          58 |
| $K$ | 1.686        1.103 | 3.656        1.490 |

An indicator for poor model quality is the peculiar angle found at the benzene hydrogen atoms in the non-centro symmetric structure. All hydrogen atoms have been found in the difference density map and their coordinates have been refined freely. This proposes no apparent problem but leads to one very strange angle at C4 which is symmetry generated in the centro symmetric setting but an independent atom in the lower symmetry. Comparing the bond angles at C2–H2–C4 and C4–H4–C2 in $P\bar{4}n2$ (119.7(6)° and 121.3(6)° in the 15 K data) one does not expect these values to differ much for the structure solution at higher temperatures. However, this only holds true for the centro symmetric setting (119.3(8)°) but not for the refinement in $P\bar{4}n2$ (C2–H2–C4 112.7(1.9)° and C4–H4–C2 125.0(1.6)°).
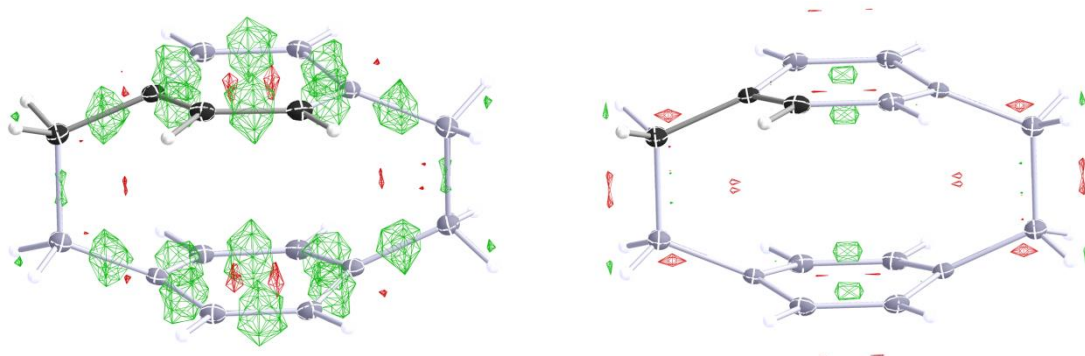
Figure 13: Residual density after IAM refinement for 50 K; left: space group $P\bar{4}$n2 (level depicted at $\pm0.12$ eÅ$^{-3}$); right: space group $P4_2$/mnm (level depicted at $\pm0.14$ eÅ$^{-3}$); green colour indicates positive and red colour negative residual density.

Table 6: Crystallographic Parameters for 55 K.

| Parameters | 55 K | | | |
|---|---|---|---|---|
| Crystal System | Tetragonal | | | |
| Wavelength $\lambda$ | 0.41328 | | | |
| $\theta$ range for data collection [°] | 2.531 to 18.571 | | | |
| Reflections collected | 12590 | | | |
| Completeness to $\theta$ | 97.6 % ($\theta = 14.357°$) | | | |
| Limiting indices | $-11 \leq h \leq 10$ | | | |
| | $-10 \leq k \leq 11$ | | | |
| | $-12 \leq l \leq 14$ | | | |
| Space group | $P\bar{4}$n2 | | $P4_2$/mnm | |
| Independent reflections | 1038 ($R_{int} = 6.76$ %) | | 591 ($R_{int} = 6.88$ %) | |
| Data/restraints/parameters | 1038 / 0 / 53 | | 591 / 0 / 30 | |
| Goodness – of – fit on $F^2$ | 1.098 | | 1.122 | |
| Final $R$ indices [$I > 2\sigma(I)$] | $R1 = 3.95$ %, | | $R1 = 4.16$ %, | |
| | $wR2 = 10.12$ % | | $wR2 = 11.31$ % | |
| $R$ indices (all data) | $R1 = 5.10$ %, | | $R1 = 4.97$ %, | |
| | $wR2 = 10.72$ % | | $wR2 = 11.79$ % | |
| Largest diff. peak and hole | 0.307 and -0.153 eÅ$^{-3}$ | | 0.337 and -0.156 eÅ$^{-3}$ | |
| $F_c/F_{c(max)}$ | 0.000 - 0.024 | 0.024 - 0.043 | 0.000 - 0.022 | 0.023 - 0.043 |
| Number of reflections in group | 104 | 105 | 60 | 60 |
| $K$ | 0.940 | 0.918 | 1.469 | 1.027 |

In contrast to the structures at 45 K both IAM models at 50 K lead to a similar residual density distribution. As expected the highest positive residual density is concentrated on the bonds (Figure 13). A different picture emerges for the crystal structure refinement at 55 K. Although refinement in both space groups readily converges and leads to reasonable $R$ and $K$ values ($R1 = 5.10$ %, $K = 0.940$ for $P\bar{4}$n2

and $R1 = 4.97$ %, $K = 1.469$ for $P4_2$/mnm) it is this negligible difference that holds the key to a correct space group assignment. As it is always better to describe the structure in the higher symmetry if possible the centro symmetric space group is the correct model for this temperature.

Further indicators are again peculiar bond angles this time at C3 in the non-centro symmetric space group. While the bond angle C1–C3–H31 equals 117.5(1.2)° the angle C1–C3–H32 equals 104.1(1.2)° which indicates problems as both these angles should be at least similar. Comparing these values to the ones found in the 15 K IAM model (110.1(5)° and 113.5(6)°, respectively) it seems more reasonable to use the higher symmetric space group for the 55 K dataset.

Refinement in $P4_2$/mnm results in a bond angle of 110.5(8)° which is a lot more reasonable. None of these features show in the residual density which is essentially the same for both space groups.
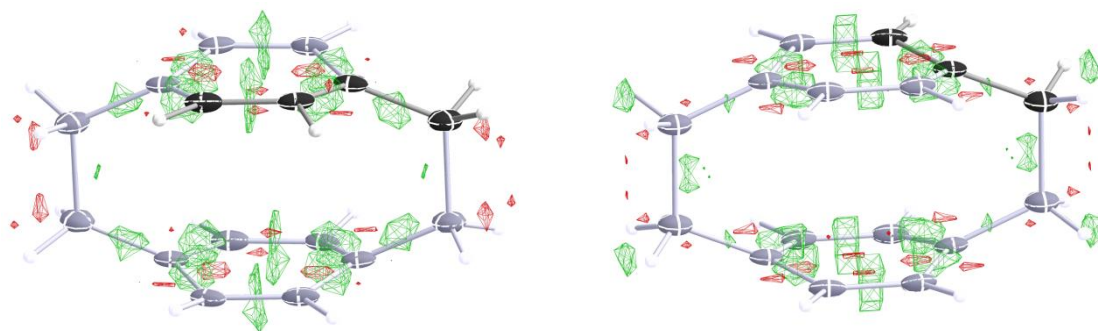


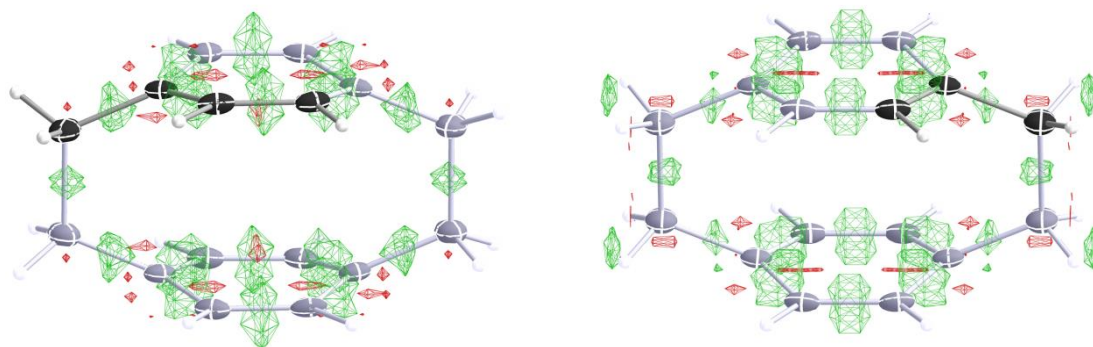Figure 14: Residual density after IAM refinement for 55 K; left: space group $P\bar{4}$n2 (level depicted at ±0.09 eÅ$^{-3}$); right: space group $P4_2$/mnm (level depicted at ±0.11 eÅ$^{-3}$); green colour indicates positive and red colour negative residual density.

### 4.3.2 Conclusion

Summing up all the results presented above it becomes clear that there is only one model to accurately describe the low-temperature structure of paracyclophane and that is by solving the structure in the non-centro symmetric space group $P\bar{4}n2$. It also is beyond doubt that the phase transition at 45.2 K is driven by the structural change in the ethylene bridges which manifests in the change in space group and symmetry. It remains to find an answer as to whether the high symmetry phase is indeed a disordered model of the low symmetry/low-temperature phase and is highly dynamic in nature and can thus not be separated by X-ray crystallography. To gain more insight into the nature of this phase transition and the energies involved an Inelastic Neutron Scattering (INS) experiment was performed.

### 4.3.3 Simultaneous Raman and Inelastic Neutron Scattering

In the last paragraphs it could very impressively be shown where the use of single crystal X-ray diffraction has its shortcomings. A crystal structure is always a merged picture of all molecules in the crystal and because a diffraction experiment takes at least a couple of hours it will also always be an average over time as well. It also means that we will never be able to unambiguously prove that the high-temperature phase really is the low-temperature phase but with a dynamically disordered ethylene bridge which causes the space group change by X-ray diffraction experiments alone. The dynamics of the disorder are simply too fast to be separated by X-ray crystallography. There is however, a very elegant way to investigate the nature of the phase transition with a different technique and that is spectroscopy. The interaction of light with an energy range equivalent to that of molecular vibrations is a very powerful tool to characterize bonding situations and possible changes in structural features due to vibrational excitation.

#### 4.3.3.1 Inelastic Neutron Scattering and Raman Spectroscopy

Because this thesis is mainly based on X-ray crystallography and spectroscopic techniques are only used as a complimentary analytical tool its principles will only be described on a very basic level and the reader is referred to more detailed literature for a deeper understanding.[100-102]

All spectroscopic methods are based on the emission or absorption of radiation by the molecules of a sample. It is only possible to record a spectrum at all if the probed material has a dipole moment $\mu_{fi}$ even if it is very short lived (Eq. 21).[101]

$$\mu_{fi} = \int \varphi_f^* \hat{\mu} \varphi_i d\tau$$

$$\mu_{fi} \neq 0$$

Eq. 21

44

This dipole moment has to change during the interaction with the photon to give a detectable signal. Among the very many spectroscopic techniques available we chose Inelastic Neutron Scattering (INS) combined with *Raman* spectroscopy for the following reasons:

Both techniques are so called inelastic techniques, *i.e.* the probe can gain or lose energy during the interaction with the sample. In every *Raman* experiment there will be three types of radiation that can be detected. As only one of $10^7$ photons collides with the molecules in the sample a very considerable part of the radiation will pass the sample unchanged in energy. This radiation is called *Rayleigh* scattering and does not give any information about the energy states of the molecules and is thus subsequently filtered out.

The second type of radiation is the so called *Stokes* scattering which is of lower energy than the incoming beam. The lost energy has been transferred to the molecules in terms of absorption through excitation. This can be easily visualized by considering that the energy has now been transferred to a vibration or rotation and thus the outgoing beam is of lower intensity than the incoming beam.
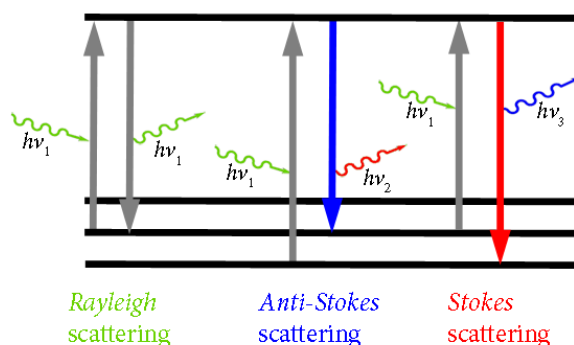


Scheme 4: Energy level diagram displaying the different types of scattering present in a *Raman* experiment.

If the incoming beam gains energy from the sample the outgoing beam will be of higher energy and is called *Anti-Stokes* scattering. In this case the beam interacts with already excited vibrational or rotational states and gains energy from them (Scheme 4).

In general *Raman* experiments give information about rotational and vibrational modes in a given system. For every spectroscopic technique there are certain selection rules that have to be obeyed in order to detect a signal. There are general selection rules to describe which property has to be present in the molecule to allow a transition. To fully analyse a recorded spectrum there are more detailed selection rules to derive allowed transitions by the change in quantum numbers.[101] In the case of diatomic molecules like $N_2$ or even $CO_2$ it is rather easy to derive the allowed

transitions because not many motions are possible. It becomes more tedious to decide on the number of expected *Raman* active modes if a larger molecule is analysed. The one rule that has to be fulfilled in order to record a rotational spectrum concerns the moment of inertia. Only if this changes during the rotation is it possible to detect a rotational mode. A nonlinear molecule with N (number of) atoms has 3N-6 degrees of freedom for all its motions. This rule is derived from the fact that N atoms have three coordinates each (3N), which each of N atoms can change by a motion resulting in 3N possible delocalisations. To describe a movement three coordinates are necessary again which leaves 3N-3 coordinates. Additionally, the orientation of the molecule in space has to be defined if the motion is to be described adequately for which three more coordinates relative to the main molecular axes are needed resulting in 3N-6 coordinates or motions for the molecule. Not every vibration or rotation that is possible for the molecule to perform is necessarily *Raman* active, only the ones where the polarisation of the molecule changes give rise to a signal in the spectrum. Furthermore, not all motions are independent from each other but can in contrast influence each other quite strongly. The set of modes that are independent from each other are called normal modes. Their number can be derived using group theory and the symmetry class of the molecule. For *Raman* spectra the normal mode is active if it has the same symmetry as one of its squared form.

*Raman* spectroscopy uses monochromatic light like that of a laser diode in the visible, near infrared or near ultraviolet range because the changes in energy are very subtle and hence, highly coherent light is needed. The wavelength used also decides about the information gained from the experiment since the input energy is responsible for the excitation of a rotation or vibration.

INS is a very powerful technique because there are no selection rules, *i.e.* the recorded spectra will display all possible vibrational modes irrespective of symmetry. Much like with *Raman* spectroscopy the neutron beam can lose or gain energy when passing through the sample and a similar spectrum is recorded. Unlike X-rays, which interact with the electrons, neutrons interact with the nuclei of the probed atoms. In contrast to electrons, which can be accelerated and manipulated quite easily because they bear a charge, neutrons are much harder to control. This is one of the reasons that the intensity and the flux of a neutron beam are orders of magnitude smaller than that of an electron beam at a synchrotron. Their neutrality is also a reason why these particles do not interact very strongly which makes the detection of the scattered beam difficult. A beneficial result of the abovementioned characteristics is that most neutron diffractometers are built as *time-of-flight* (TOF) machines which allow the characterization of every single neutron in the beam. Each neutron gets a time stamp when it is released through the chopper and if the length of the flight path is known it is possible to calculate the energy the neutron had before it hit the sample and how much energy it lost or gained after passing through the sample. The resulting spectrum looks much the same as the *Raman* spectrum and they can be superimposed to analyse the absence of certain peaks in the *Raman* spectrum due to

selection rules. If little is known about the probe but its composition *Raman* and INS can be used to gain a lot of information about the nature of the bonds.

### 4.3.3.2 Experimental Set-up at ISIS

The ISIS Neutron and Muon Source, which is part of the Rutherford Appleton Laboratory, is a pulsed spallation neutron source. The neutrons are produced by firing a high-energy proton beam into a tungsten target. The protons are accelerated in a synchrotron booster ring which circumferences 163 m. The neutrons released from the tungsten target are subsequently channelled along the beam-lines of the target stations. There are two target stations at ISIS, target station one has been operating since 1985 and target station two produced its first neutrons in 2008.
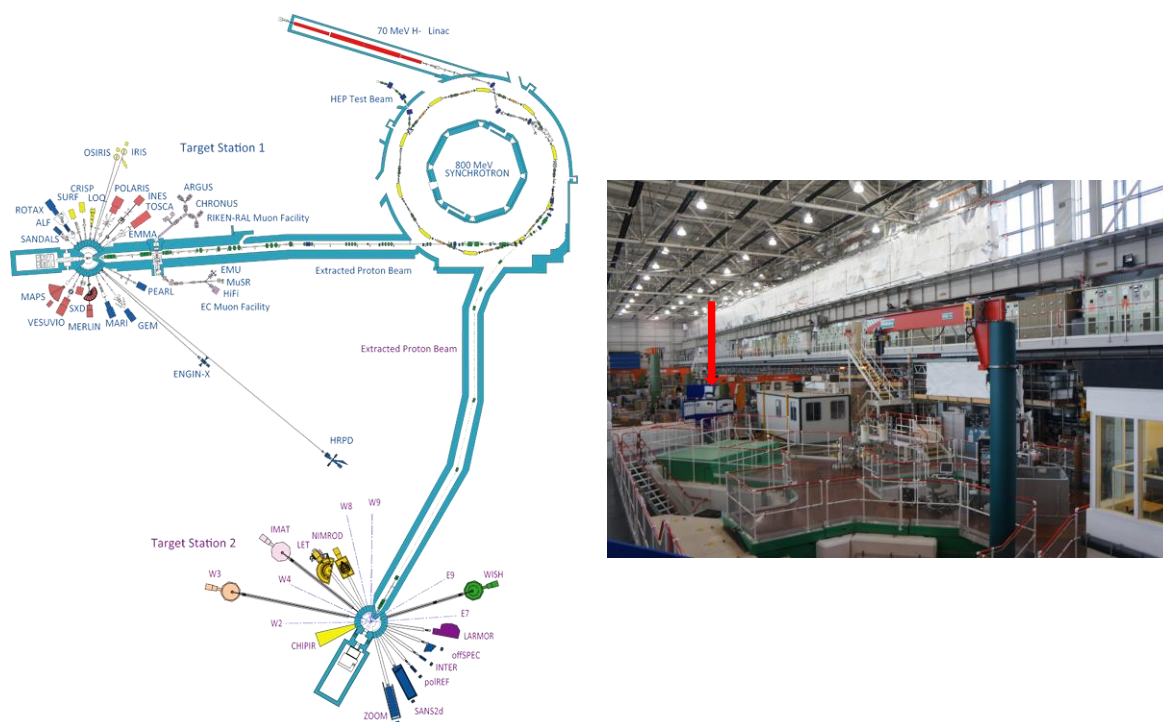


Figure 15: Map of the target stations and neutron source (left), inside the target station one: location of TOSCA beam-line (right).

The experimental set-up at the TOSCA beam-line at ISIS Rutherford Appleton Laboratory in Didcot, UK is rather unique and combines the two aforementioned techniques of *Raman* spectroscopy and inelastic neutron scattering. The instrument has an indirect geometry that allows the detection of forward and backward scattering at the same time. The pulsed neutron beam is of similar energy than atomic and electronic processes and the TOSCA beam-line allows the characterisation of the whole range of molecular vibrations with energies ranging from 0 - 4000 $cm^{-1}$. The spectrometer is equipped with a custom made center stick which holds the sample chamber and allows *Raman* and INS spectra to be recorded simultaneously (Scheme 5).[103]
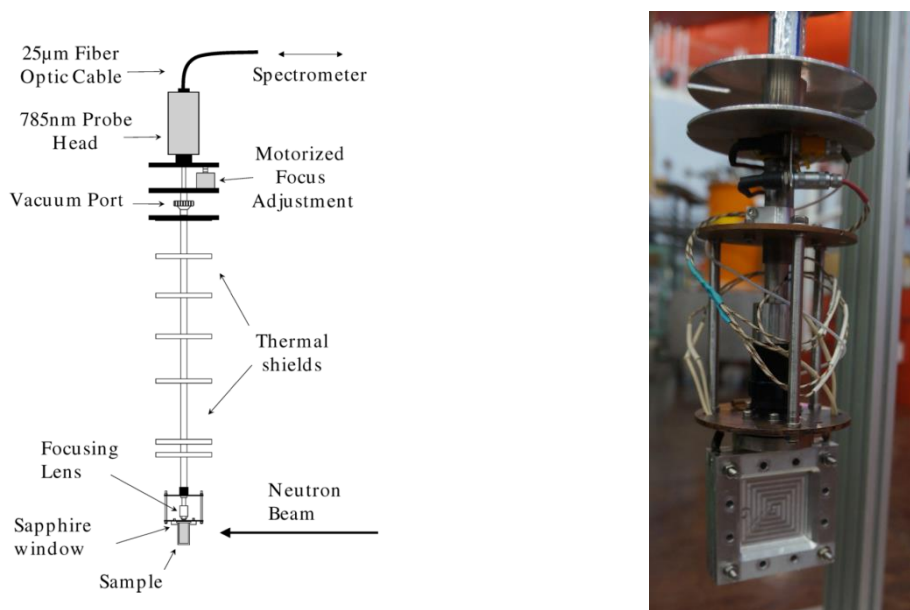
Scheme 5: INS/*Raman* center stick[103] (left) and the attached experimental chamber (right).

To record the *Raman* spectra the stick is coupled to a *Renishaw inVia* spectrometer incorporating a *Toptica* 785 nm wavelength stabilized diode laser. The spectra were recorded with 100 % laser power and *confocal* mode collecting signals every 30 seconds for the duration of the neutron exposure. The sample consisted of 2.1 g finely ground single crystals of paracyclophane that was packed into aluminium foil which was secured into the aluminium sample holder. The custom made sample holder was lowered into the neutron beam and irradiated for approximately 4 h at each temperature. The temperature was controlled via a closed cycle refrigerator (CCR). Simultaneous *Raman* and INS data were collected at 12 K, 45 K, 55 K, 60 K, and 70 K to learn more about possible participation of vibrational modes in the phase transition.

### 4.3.3.3  Experimental Results

Based on the results presented in section 4.3.1 it was not possible to unquestionably determine the driving force behind the phase transitions of paracyclophane. However, it was very likely that the twisting motions of the ethylene bridges responsible for the phase transition at 45 K. Once this energetic barrier is overcome the movement about the ethylene bridge averages out to give a broad end elongated atomic displacement parameter for the bridging carbon atom in the crystallographic analysis (Figure 16).
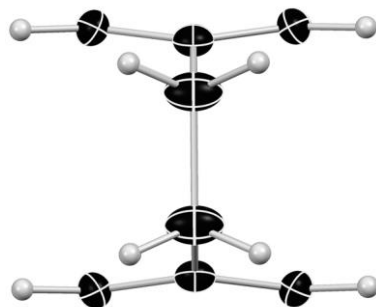
Figure 16: Single crystal x-ray structure of paracyclophane at 120 K. Thermal ellipsoids have been depicted at the 50 % probability level.

Over the last 40 years there have been quite a few spectroscopic studies on paracyclophane and its derivatives, however, none of them specially dealt with the characterization of the phase transition region. On the other hand, there have been results dealing with the twist angle in the low-temperature phase and whether the minimum structure has $D_2$ or $D_{2h}$ symmetry.[91-92,104] To the best of our knowledge there is no report of an INS experiment on paracyclophane in the literature even though there have been discussions about symmetry forbidden and *Raman* inactive modes. This gap was attempted to be closed with the abovementioned experiment. The relatively high symmetry of paracyclophane in the solid state limits the number of *Raman* allowed transitions and additionally the symmetry of the low- and the high-temperature phase only differs by an additional mirror plane. Thus, the differences in the observed spectra were expected to be very subtle and in the low energy region of the spectra because they are expected to be dominated by lattice modes. Earlier spectroscopic studies often failed to measure spectra of high enough accuracy especially in this region.[79-80,91]

With the help of the beam-line scientist *Parker* and co-worker *Lock* simultaneous *Raman* and INS spectra were collected at 12 K, 45 K, 55 K, 60 K, and 70 K. *Parker* also very kindly performed the theoretical calculations to compare the experimental results with. Additional *Raman* spectra were recorded by *S. F. Parker* with a more powerful laser and the temperature range was extended to room temperature (additional experiments were performed at 16, 30, 45, 46, 50, 54, 59, 61, 71, 150, 152, and 300 K). While the whole spectrum covers a range from roughly 20 to 3300 cm$^{-1}$ for the INS and from 40 to 3300 cm$^{-1}$ for the *Raman* spectra, the most important part is the low energy region due to the reasons given above.

Periodic DFT calculations were carried out using a plane wave basis-set and pseudo potentials as implemented in the CASTEP code.[105] The refined crystal structures at 15 K and 120 K were used as the initial input structures. Phonon modes were calculated using density-functional perturbation theory.[106] As a prerequisite to any lattice dynamics calculation a full geometry optimization of the internal atomic coordinates was performed.

Both calculations depict excellent agreement with the experimental INS spectra (Figure 17).
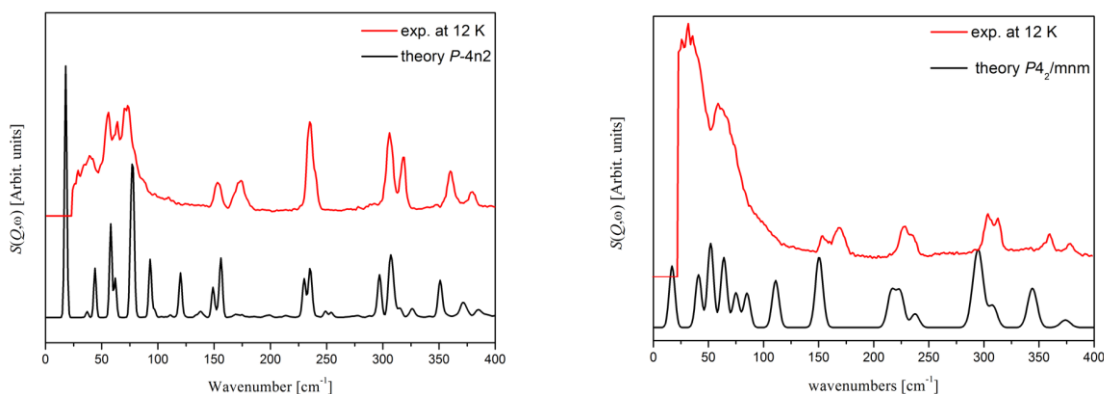


Figure 17: Theoretical and experimental INS spectra. Left: low-temperature phase T = 12 K; right: high-temperature phase T = 70 K.

There are only minor shifts in energies and the lack of agreement for both spectra at values below 100 wavenumbers is due to the bad resolution of the experimental spectra. For the high-temperature phase the calculations resulted in four imaginary modes at low wavenumbers which correspond to the twisting of the ethylene bridge and the pumping motion of the benzene rings. The resulting imaginary modes are due to the fact that these are 0 K calculations and that the high-temperature phase is not stable at this temperature. However, this is also a very strong sign that it is indeed this twisting motion which is responsible for the phase change. The calculated wavenumbers for the higher energy modes are not affected by this and can be correctly assigned.

Comparing the theoretical and the experimental spectra going from the low energy part of the spectra to higher wavenumbers the first difference occurs at 165 cm$^{-1}$. Both the experimental *Raman* and INS spectra depict a signal at this position (Figure 19) but there is no direct match in theoretical energies for the low-temperature phase. In a publication of theoretically derived normal vibrations *Walden* and *Glatzhofer* assigned this peak to a 'ring rock around (the) y-axis clamshell'.[83] For temperatures above 54 K this peak disappears from the *Raman* spectra but is still clearly visible in the INS spectra (Figure 18). Interestingly, this peak shows up in both the INS and the *Raman* spectra, which is a strong indicator that it is not an artefact. It is also very interesting that the peak at 165 cm$^{-1}$ is only very subtle in the *Raman* spectra but clearly visible in the INS. Furthermore, since it does not disappear in the INS spectra above 55 K this peak might have its origin in a change of symmetry during the second phase transition at 60 K.
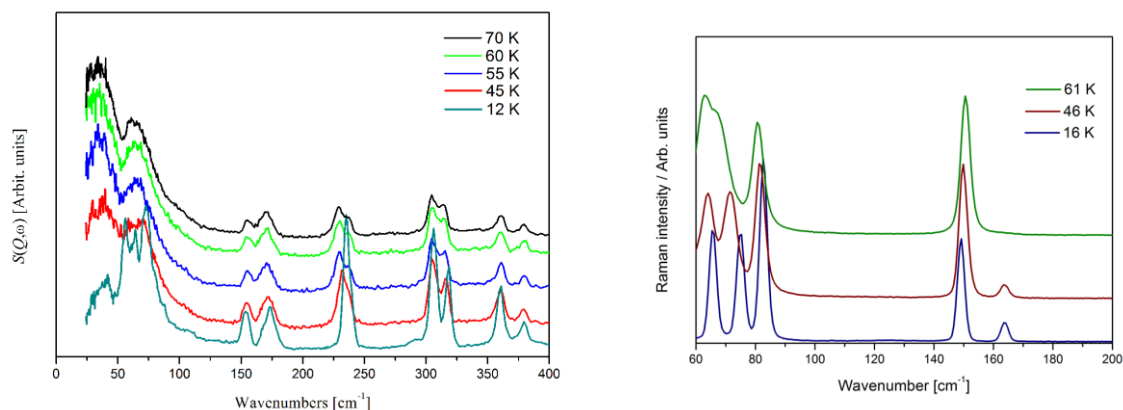
Figure 18: Enlarged temperature dependent INS and Raman spectra of paracyclophane from 0 to 400 cm$^{-1}$.

For the experimental spectra recorded at 12 K a number of modes are *Raman* silent but INS active (Figure 19). There is also a difference in intensities but this is mainly due to scaling issues and is not related to the molecule responding to the energies in question in a different manner for the two different probes. Apart from the peak at 165 cm$^{-1}$ there are no more obvious differences between the experimental and theoretical spectra.
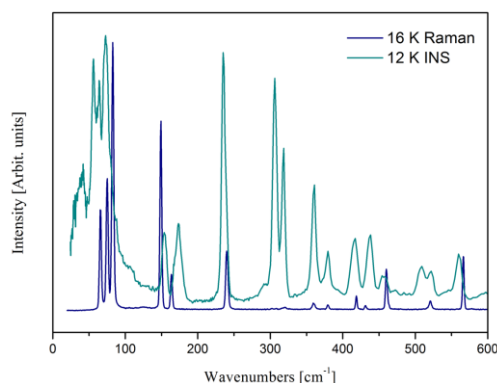


Figure 19: Enlarged experimental INS and *Raman* spectrum of paracyclophane at 12 K (left) and experimental together with theoretical INS spectrum (right) from zero to 600 wavenumbers.

Hence, the following differences are found in the temperature dependent *Raman* and INS spectra to give evidence for the force behind the phase transitions.

If the phase transition at 45.2 K is indeed driven by the twisting motion of the ethylene bridges as has been proposed, this should be visible in the INS and *Raman* spectra going from the low-temperature to the high-temperature phase. Comparing a 12 K spectrum to one collected at 70 K, where the high-temperature phase is solely present, there is a significant difference in the signals recorded for the small wavenumbers. The broad peak at the very low energy region (60-100 cm$^{-1}$) of the INS spectrum weakens and loses its sharp features (Figure 18, left). With the stronger

*Raman* laser it was possible to collect the peaks in the very low energy region with great precision (Figure 18, right). At the very low energy part of the spectrum three well resolved peaks coincide at higher temperatures to form one broad and one sharp peak in the *Raman* spectra (Figure 18, right). The two peaks at 65 and 75 cm$^{-1}$ coincide above 58 K, indicating that these peaks might hold a reason for the second discontinuity at 60 K in the heat capacity measurement. In a very recent publication *Li et al.* observed a similar splitting when paracyclophane is subjected to high pressure at room temperature.[107]

Another difference in the INS spectra recorded at different temperatures concerns a well-defined peak at roughly 750 cm$^{-1}$, which slowly disappears if the temperature is increased (Figure 20). These two peaks around 75 and at 750 cm$^{-1}$ nicely match the calculated energies for twisting motions of the CH$_2$-moieties at the ethylene bridges in the low-temperature phase (calc.: 76, 78 and 749 cm$^{-1}$). Apart from these signals more discrepancies between low and high-temperature phase are visible around 240 cm$^{-1}$ in the *Raman* and INS spectra. Quite surprisingly the peak at 240 cm$^{-1}$ splits up into a doublet at higher temperatures, *i.e.* at higher symmetry, according to both *Raman* and INS (Figure 18, Figure 21).
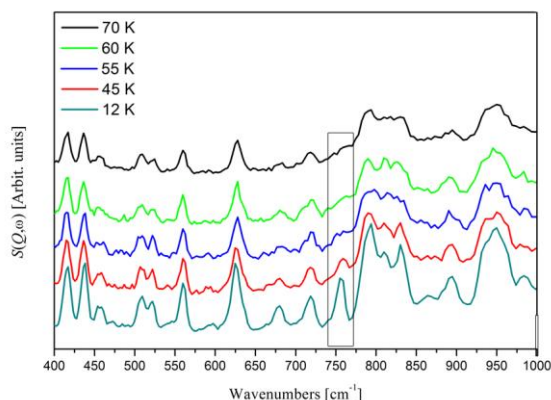


Figure 20: Enlarged temperature dependent INS spectrum of paracyclophane from 400 to 1000 cm$^{-1}$.

In fact, a doublet is present in the calculated spectrum as well (Figure 21) corresponding to a number of motions in this energy region. For the low-temperature phase there are two peaks predicted for twisting motions of the CH$_2$-groups (230 and 235 cm$^{-1}$). Moreover, two pumping motions for the benzene rings towards and away from each other (236 and 237 cm$^{-1}$) are also predicted at similar energies. In the high-temperature phase there is only one predicted peak for the CH$_2$-group twist (224 cm$^{-1}$) and two for the pumping motion (237 and 238 cm$^{-1}$). Although this feature is more prominent in the *Raman* spectra it can also be observed in the INS spectra. The same feature but in the reversed direction is observed by *Li et al.* for their high pressure study.[107] The peak at ~240 cm$^{-1}$ splits up above pressures of 3.9 GPa, thus forming only one peak for the high-symmetry phase. Apart from this discrepancy our

results are in excellent agreement with theirs and it cannot be said why this difference occurs. They speculate about a phase transition towards the low symmetry phase with $D_2$ symmetry induced by high pressure above 3.9 GPa, which would explain their spectra. As their spectra are in excellent agreement less the discussed peak, with our study, just using pressure instead of temperature as a probe, this seems indeed to be the case.
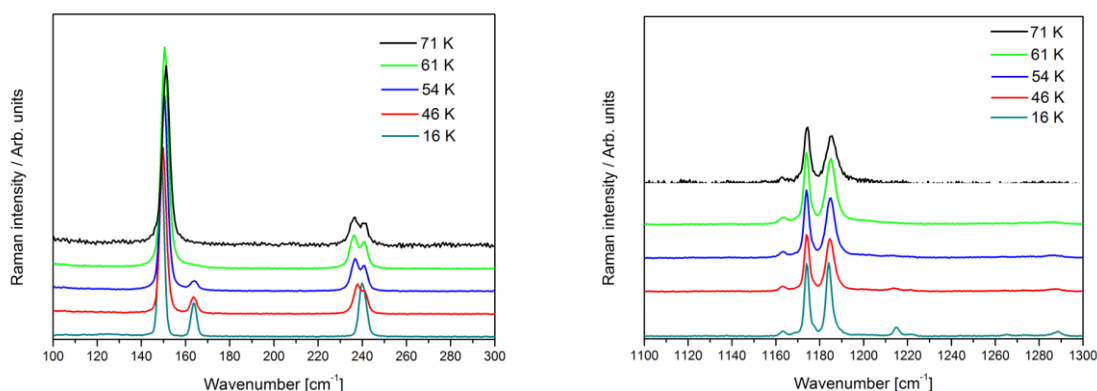


Figure 21: Enlarged temperature dependent *Raman* spectra of paracyclophane from 100 to 300 cm$^{-1}$(left) and from 1100 to 1300 cm$^{-1}$.

A difference which is also puzzling is a small sharp peak at around 1220 cm$^{-1}$ which also disappears at elevated temperatures (Figure 21, right). Again, there is no exact match for this peak in the calculated energies. For the low-temperature phase *Raman* active modes were calculated at 1202-1207 cm$^{-1}$ and at 1242 to 1255 cm$^{-1}$. Furthermore, *Li et al.* also report this peak for pressures above 3.9 GPa. Unfortunately, they are also not able to explain the physical origin of this peak. *Walden* and *Glatzhofer* assign this peak to a stretching motion of the bridging carbon to the ring carbon and a bending of the aromatic hydrogen atoms.[83] Unfortunately, the INS spectra are already too noisy in this energy region so it is impossible to say for sure that this peak is also present here.

### 4.3.4   Conclusion

One of the main questions for this experiment was the nature of the possible disorder at high-temperatures. With the spectroscopic data in hand now it seems clear that a twisting motion of the bridges can indeed be observed in both the low and the high-temperature phase. This supports the idea of a dynamic disorder of the *ipso*-carbon in the high-temperature phase. The motion simply averages out to give a higher symmetry in the crystal structure and a large displacement parameter for the bridging carbon atom. Although there are minute changes in the spectroscopic data in between 55 and 65 K (peaks at 165 cm$^{-1}$ and 240 cm$^{-1}$) there are no obvious changes in the observed spectra once we surpass 55 K. It can be safely said that from the spectroscopic view the phase above 55 K already resembles the high-temperature phase.

## 4.4 Charge Density Investigation on Paracyclophane and Data Quality Analysis

After the two different space groups for the two phases have been unequivocally established using single crystal X-ray diffraction and combined *Raman* spectroscopy and inelastic neutron scattering, a charge density investigation of the low-temperature phase was carried out. To record a full dataset with sufficient resolution for the investigation was by no means a routine task. Paracyclophane has very strong reflections up to a resolution of $d = 0.7$ Å but only comparably weak Bragg maxima after that. This is mainly due to the atomic form factors of carbon and hydrogen (Chapter 1.2, Figure 1) which fall off rapidly at higher angles. This makes data collection very challenging because one has to compromise between sample size and exposure time. Choosing a large crystal to collect data up to very high resolution as is necessary in a charge density experiment very often leads to saturation of the detector for the low angle reflections. Collecting data on a smaller crystal to avoid overloads in the low order region can result in a resolution too low for a charge density experiment. The use of synchrotron radiation should be beneficial for this type of crystal because the high intensity and energy supports more powerful scattering for a smaller crystal.

The datasets presented below were collected on our in-house diffractometer and on a similar machine at the Advanced Photon Source (APS) in Chicago, USA. The in-house diffractometer is equipped with a Bruker molybdenum rotating anode ($\lambda = 0.71073$ Å) and Incoatec mirror optics on a Bruker D8 goniometer with a Smart APEXII CCD detector. The hardware limit for the resolution on the in-house machine is $d = 0.4$ Å. The diffractometer at the APS is of a similar set-up with a Bruker D8 goniometer equipped with a Smart APEXII CCD detector. The phosphor of the synchrotron detector has been modified to yield higher light output for the high energy synchrotron radiation. Data were collected with a wavelength of $\lambda = 0.3936$ Å and attenuated beam for some of the runs in order to avoid overloads on the detector. The temperature was controlled with an open stream *Oxford Helijet* operating with liquid Helium both in-house and at the APS. The temperature control was set to 15 K but the temperature at the crystal was probably a little higher for the in-house data collection since no calibration was performed before the experiment. The temperature control at the APS has been calibrated using a crystal that undergoes a phase transition at 15 K so the temperature is a little more precise than in-house.

## 4.4.1  Data Collection and Processing

The datasets from our in-house source were collected on the same crystal (0.163 x 0.202 x 0.225 mm) and using the same strategy. In order to measure up to high resolution a combination of 90° and 180° ω scans using three different $2\theta$ settings (-32°, -50°, -90°) were performed. (More detailed information is available from 10.1.1.1 and 10.1.1.2)

At the synchrotron the data were collected combining 360° φ scans with different $2\theta$ settings (-10°, -20°, -30°). Unlike for the in-house data it was not possible to collect both datasets on the same crystal because the first crystal was lost during temperature change and was replaced by a similar crystal out of the same batch (0.120 x 0.100 x 0.110 mm).

Data reduction was carried out using *SAINT-8.30C* with enabled automatic box size refinement. The synchrotron data were integrated using individually made integration masks to cover the beam stop and the shadow from the Helijet as well as some damaged pixels from the detector. Each run was integrated separately and merged in *SADABS*. The phosphor modification within the synchrotron CCD detector was taken into account by scaling the phosphor efficiency to tabulated values for the respective wavelength in the *saint.ini* file. Absorption correction, scaling and merging was done using *SADABS 2014/2* in expert mode. The weighting $g$ value has been refined using individual $K$ for each run but an overall $g$ until it converged. Since $P\bar{4}n2$ is a non-centro symmetric space group the *Friedel* pairs have not been merged for both the IAM and the MM *\*.hkl* file but negative intensities and systematic absences have been discarded for the *xd.hkl* file.

Following the advice given in the introduction there are some early stages quality indicators to check. One of these are the so called *Diederichs* plots which show significantly different maximum values for $I/\sigma(I)$ for the two different sources. Both in-house datasets show values around 70 while the synchrotron datasets only reach maximum values of 30 (Figure 22.)
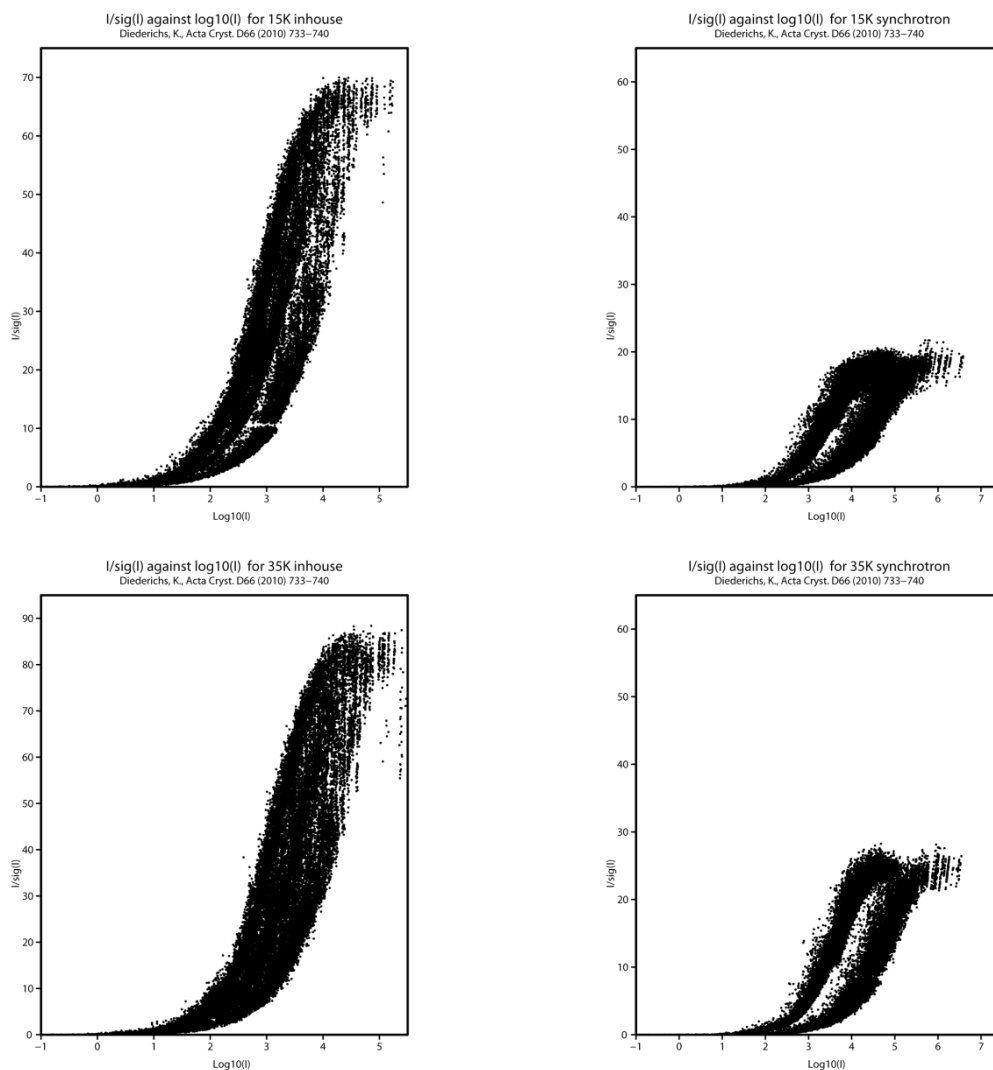
Figure 22: Diederichs plots generated by *SADABS* for synchrotron and in-house datasets.

These plots already show that there are some systematic errors in the way the synchrotron data were collected. This is due to the fact that our in-house source is optimized for charge density investigations while synchrotron sources are optimized to suit various experiments. Another very useful plot generated by *SADABS* is $R_{int}$ and $R_{merge}$ plotted against the resolution. This is most helpful in making an early decision about the maximum resolution possible with the data in hand. The in-house datasets depict values for both $R$ factors below 4 % throughout the resolution range indicating well detected intensities both in the low and in the high order region. The synchrotron data follow a flatter course but start at slightly higher $R$ values. However, the values reached are clearly below 10 % over the whole resolution range which is within the range usually seen for charge density datasets (Figure 23).
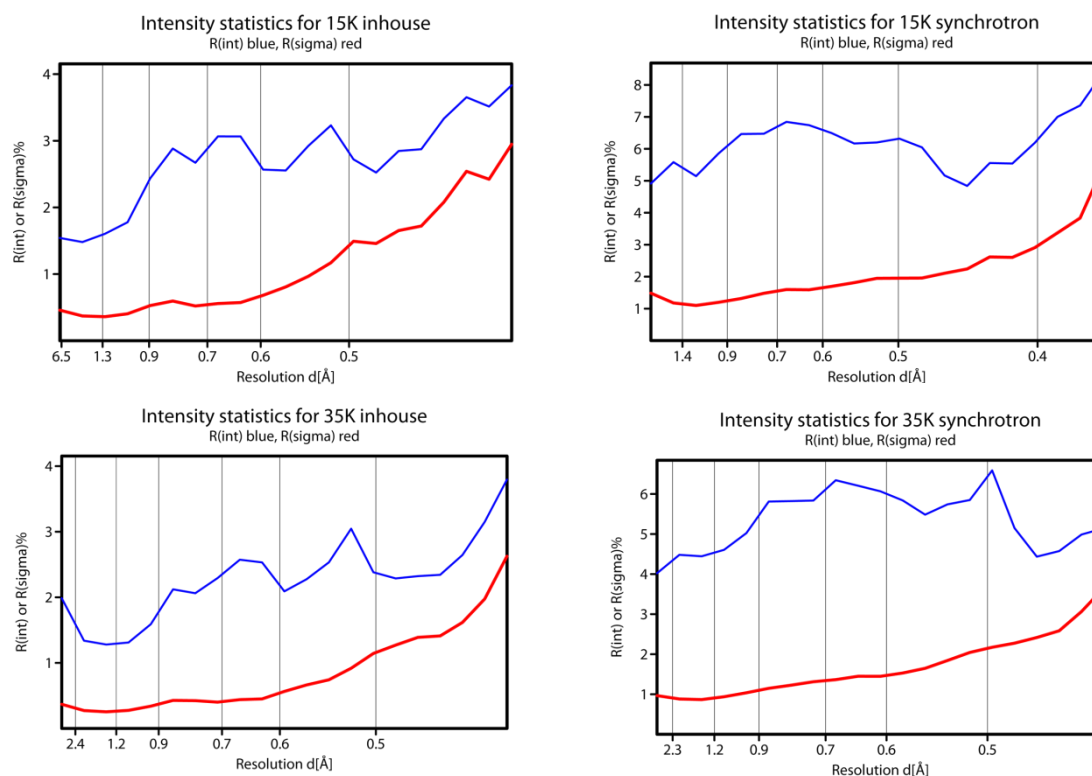
Figure 23: Course of $R_{int}$ and $R_{merge}$ over the resolution range plotted by *SADABS*.

Up to this point the datasets do not show large deviations in quality although the *Diederichs* plots suggest that there are problems with systematic errors for the synchrotron data. The next step to evaluate the data quality are the statistics provided by *XPREP* which give information about the completeness, the multiplicity, the mean $I/\sigma(I)$ values and a number of $R$ values calculated for different resolution shells as well as for the whole dataset. Based on these statistics a more reliable decision can be made about the maximum resolution. In theory the high energy and high flux of the synchrotron radiation should allow for a higher resolution as the in-house source. Surprisingly, this was not the case for these experiments. The in-house datasets have been integrated to the maximum hardware limit of d = 0.40 Å (15 K) and to a slightly lower level of d = 0.42 Å for 35 K. Although the *XPREP* statistics still show high $I/\sigma(I)$ values for the outermost resolution shells the multiplicity and completeness dropped. It became clear after MM that the weakest outermost reflections simply were not measured with the required accuracy (Figure 24).
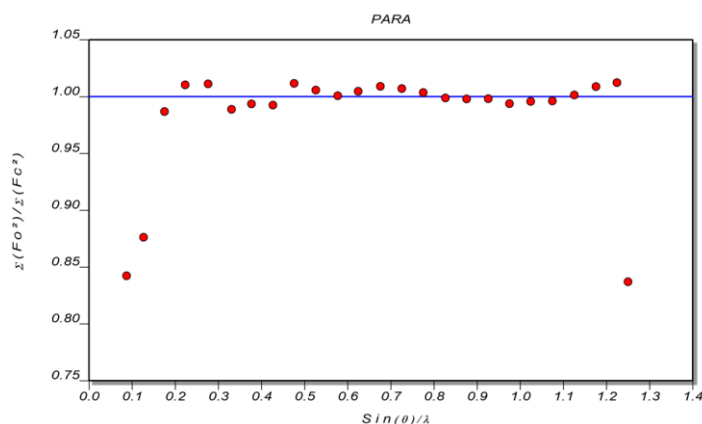
Figure 24: Variance of the ratio $F_o^2/F_c^2$ against resolution after MM; d = 0.40 Å.

Both in-house datasets also display high intensities up to high resolution (mean $I/\sigma(I)$ 58.03 (15 K) and 79.80 (35 K)) with a completeness higher than 99 % and an overall multiplicity of 9.19 (15 K) and 8.73 (35 K).

The maximum resolution for the APS datasets did not surpass 0.40 Å for the 15 K data and even less for the 35 K data, which could only be integrated up to d = 0.43 Å. Although the multiplicity and the completeness dropped in the outermost shells the $I/\sigma(I)$ values are still well above ten. Unfortunately, these data did not lead to a better model after the XD refinement, probably due to the low multiplicity and completeness. The overall completeness is around 99 % for both datasets and they also display high intensities up to the full resolution (mean $I/\sigma(I)$ 32.21 and 40.21 for 15 K and 35 K respectively).

*XPREP* also calculates a number of different merging $R$ factors, most useful among them are the $R_{\text{r.i.m.}}$ [23] which is a multiplicity independent $R$ factor and the $R_{\text{merge}}$ and $R_{\text{sigma}}$.
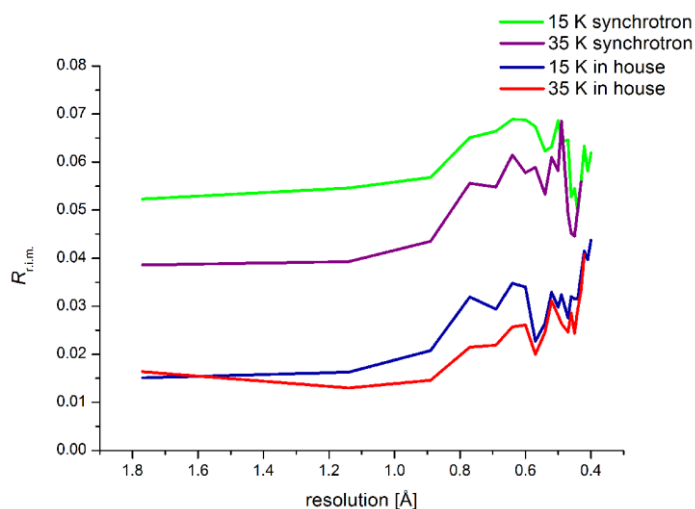


Figure 25: $R_{\text{r.i.m.}}$ plotted against the resolution for all four datasets.

All four datasets display small $R$ values in the whole resolution range, but the values for the two synchrotron datasets are significantly higher. This is especially pronounced for the lower resolution shells (Figure 25). The low overall $R_{r.i.m.}$ values for all four datasets (15 K in-house: $<R_{r.i.m.}> = 3.33$ %; 15 K synchrotron: $<R_{r.i.m.}> = 5.92$ %; 35 K in-house: $<R_{r.i.m.}> = 2.80$ %; 35 K synchrotron: $<R_{r.i.m.}> = 5.47$ %) representing high precision could lead to anticipate a reliable charge density model. As the differences of the $R_{r.i.m.}$ values between the innermost and the outermost reflections are so small for the synchrotron data, although on a low level, one can conclude that the high order data are of excellent quality, while the low order data have their deficiencies. Unfortunately, detection of the innermost data is prone to errors.[9-10,108]

### 4.4.2   Independent Atom Model (IAM)

The structures were solved using *SHELXS*[4] and structure refinement was done using *SHELXL*[109] within the GUI *ShelXle*[110]. For a charge density refinement it is important to carefully set up a model from which to start the multipole expansion. The asymmetric unit of paracyclophane consist of four carbon and four hydrogen atoms on general positions. The atomic positions and displacement parameters for the carbon atoms have been refined using only high angle data (d = 0.7 to 0.4 Å). The hydrogen atom positions have been taken from the Fourier-density-difference map using only low angle data (d = inf. to 1.0 Å) and their $U_{iso}$ values have been constrained to 1.5 $U_{eq}$ of their pivot atom for sp$^3$ hybridized carbon and 1.2 $U_{eq}$ for sp$^2$ hybridized carbon atoms. The carbon hydrogen distances were set to average distances determined from neutron diffraction.[111] For the starting model only experimental weights have been applied. For a standard IAM refinement weighting has been applied leading to the results summarized in Table 7. After the IAM refinement all positive residual density was concentrated on the bonds, which is not surprising since it only refines the model based on scattering factor derived for spherical atoms.

Table 7: Experimental details after IAM refinement.

| | in-house | | synchrotron | |
|---|---|---|---|---|
| | 15 K | 35 K | 15 K | 35 K |
| space group | | $P\bar{4}$n2 | | |
| theta range | 3.459° to 62.653° | 3.457° to 57.883° | 1.917° to 29.441° | 1.916° to 27.235° |
| maximum resolution | 1.25 Å$^{-1}$ | 1.19 Å$^{-1}$ | 1.25 Å$^{-1}$ | 1.16 Å$^{-1}$ |
| reflections collected/independent | 32293/4407 | 34569/3834 | 41593/4407 | 29629/3544 |
| completeness | 100.0 % ($\theta = 25.242°$) | 99.7 % ($\theta = 25.242°$) | 100.0 % ($\theta = 13.660°$) | 100.0 % ($\theta = 13.660°$) |
| data/restraints/parameters | 4407 / 0 / 49 | 3834 / 0 / 49 | 4407 / 0 / 49 | 3544 / 0 / 49 |
| Goof | 1.110 | 1.087 | 1.080 | 1.082 |
| weighting scheme | 0.0529/0.0061 | 0.0589/0.0062 | 0.0525/0 | 0.0609/0 |
| $R$ indices [I>2σ(I)] | $R1 = 0.0226$, w$R2 = 0.0745$ | $R1 = 0.0238$, w$R2 = 0.0783$ | $R1 = 0.0252$, w$R2 = 0.0726$ | $R1 = 0.0275$, w$R2 = 0.0793$ |
| $R$ indices (all data) | $R1 = 0.0236$, w$R2 = 0.0754$ | $R1 = 0.0243$, w$R2 = 0.0788$ | $R1 = 0.0260$, w$R2 = 0.0734$ | $R1 = 0.0287$, w$R2 = 0.0805$ |
| largest diff. peak and hole | 0.590 and -0.17 e Å$^{-3}$ | 0.490 and -0.241 e Å$^{-3}$ | 0.768 and -0.241 e Å$^{-3}$ | 0.733 and -0.233 e Å$^{-3}$ |

### 4.4.3 Multipole Modelling (MM)

The charge density refinements were performed against $F^2$ and the convergence criterion was set to $1 \times 10^{-8}$ as the allowed maximum shift over standard uncertainties for each refined parameter. All refinement steps readily converged. The $I/\sigma(I)$ cut off of 2 was slowly reduced to zero in the final steps of the refinement. It has to be noted at this point that it is still common practice not to reduce the default value in the instruction file which is set to 3 in order to avoid taking data into account that has not been measured accurately. All four datasets have been refined using the same refinement strategy (0). The investigations to back up this observation were carried out with using the paired refinement strategy as introduced in chapter 3 which calculates the $R$ values for a given model a with a dataset b and vice versa.
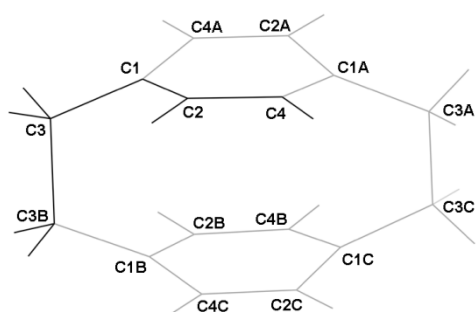
| | Symmetry operation |
|---|---|
| A | -½+y, ½+x, 3/2-z |
| B | -x, 1-y, +z |
| C | ½-y, ½-x, 3/2-z |

Scheme 6: General view of paracyclophane including symmetry generated parts.

All crystallographically independent atoms have been refined using scattering factors derived from wave functions fitted to a relativistic Dirac-Fock solution from the *SCM* databank in the *XD2006* program package.[112] Dispersion corrections were taken from tabulated values[113] for synchrotron radiation and manually adjusted in the *\*.mas* file. The local coordinate system for the unique atoms has been set up according to Table 8.

Table 8: Local coordinate systems for the XD refinement.

| Atom | Atom/Axis 1 | Atom/Axis2 | R/L |
|------|-------------|------------|-----|
| C1   | C3/z        | C2/y       | R   |
| C2   | C4/x        | C1/y       | R   |
| C3   | C1/z        | DUM2/y     | R   |
| C4   | C2/x        | DUM1/y     | L   |
| H2   | C2/z        | C1/x       | R   |
| H4   | C4/z        | C2/y       | R   |
| H31  | C3/z        | C1/x       | R   |
| H32  | C3/z        | C1/x       | R   |

DUM 2 is positioned on the symmetry equivalent C3B; DUM 1 is positioned on the symmetry equivalent C1A.

For all non-hydrogen atoms multipole parameters to $l = 4$ were refined; for the hydrogen atoms only the populations for the monopole and bond directed dipoles were refined. Chemically equivalent atoms were refined with the same *kappa* parameter. The *kappa* parameters for the hydrogen atoms were kept fixed to values derived by *Volkov et al.* throughout the refinement after initially manually resetting them.[114]

The bond distances were reset to neutron values for the hydrogen atoms after each refinement of the coordinates since X-ray data do not give reliable values for these. The isotropic thermal parameters were refined fixed to the $U_{eq}$ of their pivot atoms. It was chosen not to use anisotropic displacement parameters derived by the *SHADE* server[115] for two reasons. Firstly, the server needs at least five heavy atoms in the asymmetric unit to derive reliable values for the hydrogen atoms. Unfortunately, paracyclophane only contains four independent carbon atoms in the asymmetric unit and the *SHADE* server is not capable of generating symmetry equivalent atoms to complete the full molecule. If less than five heavy atoms are present *SHADE* automatically generates thermal displacement parameters for the hydrogen atoms constraining them to the pivot atom as describes above. For paracyclophane the values derived by this method resulted in a model inferior to the model without anisotropic displacement parameters.
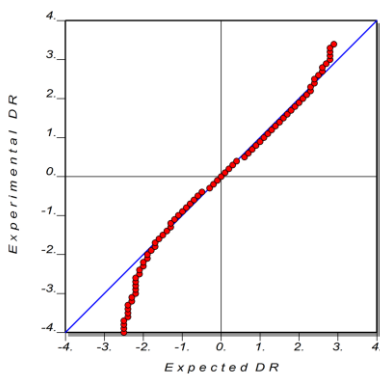
|  |  |
|---|---|
| 15 K in-house data | 35 K in-house data |
| weighting parameters: | weighting parameters: |
| a = 0.01          b = 0.005 | a = 0.01          b = 0.005 |
| 15 K synchrotron data | 35 K synchrotron data |
| weighting parameters: | weighting parameters: |
| a = 0.009          b = 0.003 | a = 0.017          b = 0.003 |
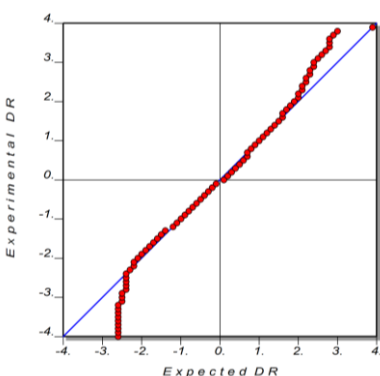
Scheme 7: Graphical output from the *DRKplot* program for the normal probability plot.

Hence, no anisotropic thermal parameters have been used in the refinement. In order to avoid problems with convergence and/or over fitting of the data a conservative refinement strategy with chemical constraints in place has been used. Chemical constraints were used for C2 and C4 as well as for H2 and H4 plus H31 and H32, respectively. This constraint defines the shifts in multipole parameters to be identical for the given atoms. If the atoms have the same starting value for the population parameters this means that their population parameters are kept identical throughout the refinement. Since all atoms are crystallographically independent and do not lie on a special position no symmetry restrictions were applied and all multipole populations were refined (Scheme 12).

After a complete refinement the weighting scheme was adapted using the *DRKplot* program to give normal probability plots (Scheme 7). The formula for the weighting scheme is the same as used in *SHELXL* and is given in Eq. 16. A complete refinement of all parameters was performed with the derived values. The weighting parameters differ slightly for the four datasets but not significantly (Scheme 7).

The refinement readily converged for all datasets and the residual density maps appear almost flat and featureless for the in-house data. For the synchrotron data it becomes obvious that there are severe problems in the data as the level of residual density is considerably higher (maximal hole is -0.28 compared to -0.16 e/Å³) and there is still a significant amount of undescribed density left on the carbon-carbon bonds and on the carbon atoms themselves (Figure 26). Despite this, the 35 K synchrotron data show less residual density compared to the 15 K synchrotron data but still considerably more than the in-house data. Although the residual density shows negative features especially in the case of the 35 K in-house data, the level is still very low considering that no resolution and/or $I/\sigma(I)$ cut off was used for generating these maps. It is still common practice to limit the data used for the residual density plots to a resolution of $d = 0.8$ Å arguing that data above this limit would not provide additional information on the bonding density which is modelled by a multipolar expansion. Cutting the data to generate the residual density plots always results in a map with less features and lower contours but has to be regarded as a cosmetic tool to artificially lower the residual density level. Furthermore, it is still common practice to only provide 2D representations of the residual density.
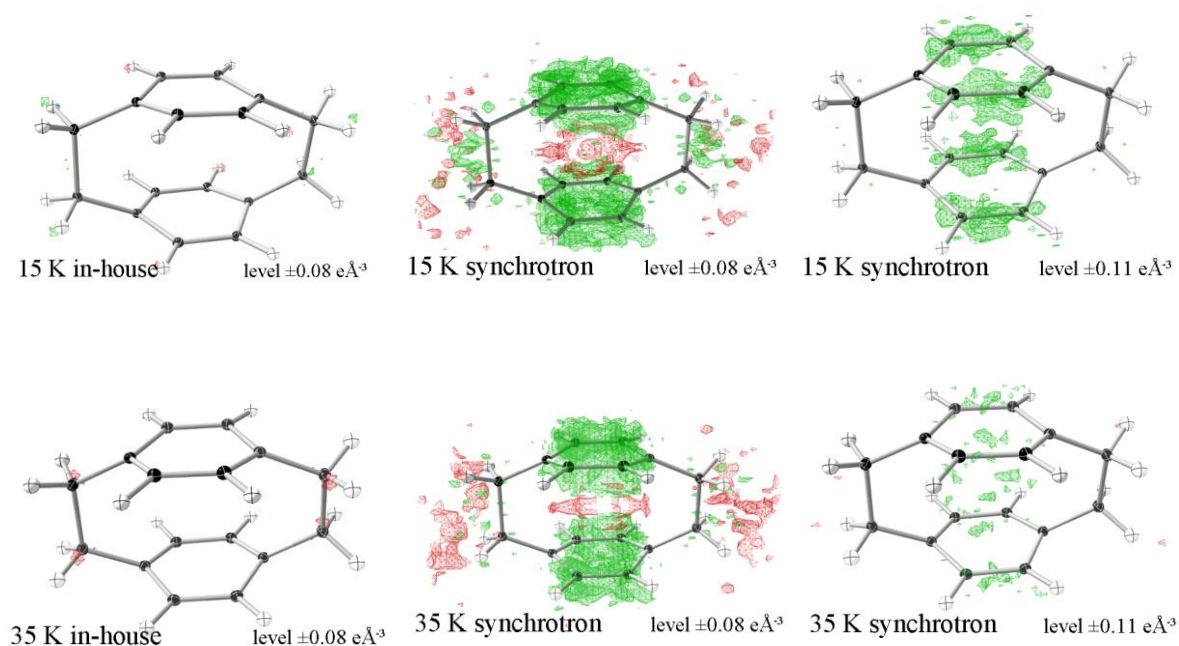


Figure 26: Residual density after XD refinement including all data. Positive density appears in green and negative density in red.

Using this technique it is very easy to choose a 2D plane with little residual density for these maps. The representations generated by the program *MoleCoolQT*[116] are three dimensional and can be interpreted quite easily and without the limitations of a 2D maps. Analysis of the residual density according to *Meindl* and *Henn* results in a Gaussian distribution for the 15 K in-house dataset.[37]

All plots have been derived using the same resolution for all datasets (d = 1.16Å$^{-1}$) for comparison reasons (Figure 27). Plots for the full resolution range can be found in appendix 10.1.4.1. The so called *Henn-Meindl plot* is a very elegant way to describe both flat- and featurelessness of the residual density. Both the 3D-plots generated by *MoleCoolQT*[116] in Figure 26 and the *Henn-Meindl plots* can be generated easier than using the program implemented in *XD* (*XDgraph*) and they are also more informative and should thus be made compulsory for the publication of a charge density study. The *Henn-Meindl plots* are available through the *WinGX*[41] suite, which is installed on almost every computer used by a crystallographer and the program *MoleCoolQT* is available free of charge from the programmer's homepage.

While the interpretation of the 3D-visualisation of the residual density is straight forward and does not need further elucidation the analysis of the *Henn-Meindl plot* takes a little more consideration. The narrower the parabolic curve the flatter the residual electron density and the higher the fractal dimension of its peak the less features are present.[37] The residual density of the 15 K in-house data results in a narrow parabolic curve with a maximum $d^f(0) = 2.6265$ which is quite close to the maximum possible $d^f(0) = 3$ and thus indicates both a flat and featureless residual electron density. All other plots are broader and display shoulders. While the 35 K in-house data give rise to a still narrow curve with a maximum $d^f(0) = 2.4169$, both plots for the synchrotron data only show resemblance to a parabolic curve. They are very broad and display maxima of $d^f(0) = 2.4823(15 K)$ and $d^f(0) = 2.4585$ (35 K), respectively. The 35 K in-house density plot has a little shoulder in the negative range showing the negative residual density that is obvious in Figure 26.
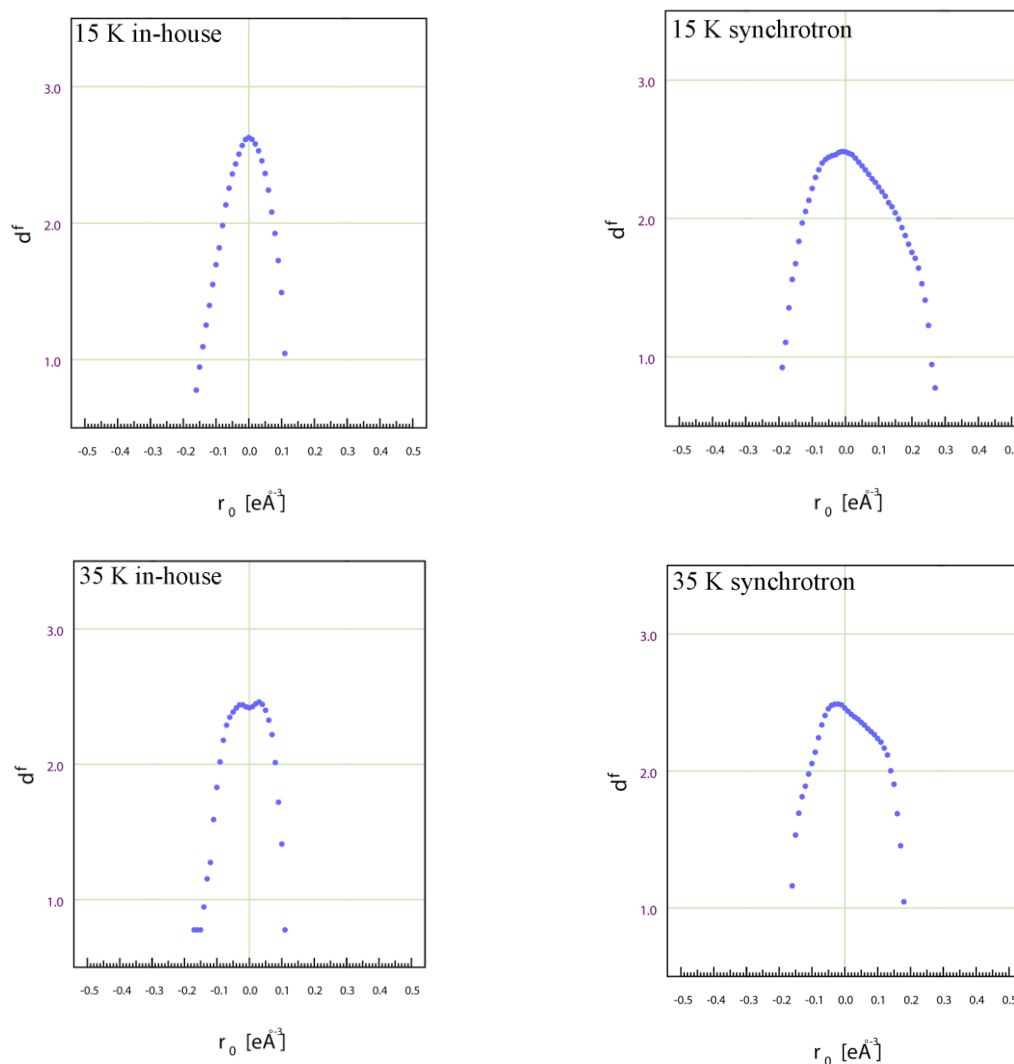
Figure 27: Residual density analysis according to *Meindl* and *Henn*; d = 0.43 Å.

A value also worth monitoring is the value of $e_{gross}$, which states the sum of the gross residual electrons.[37] This values states the total error including noise. For the in-house datasets these values add up to 7.3515 e for the 15 K dataset and to a significantly higher value of 10.1996 e for the 35 K data. It can be safely concluded that there are still features present in the residual density but these have to be very subtle as both curves resemble a parabola without any broad shoulder or tails at the bottom. Both synchrotron datasets have a values for $e_{gross}$ larger than 10 (15 K $e_{gross}$ = 15.2754 e; 35 K $e_{gross}$ = 13.6089 e), which only back up what was also visible from the residual density graphics in Figure 26. Together with the aforementioned values for $d^f(0)$ this indicates a much more featured residual density. Features in the residual density can be triggered by various causes. One of them can be a mismatch between calculated and experimental structure factors. As the calculated structure factors are derived from the model that is generated by the crystallographer this is also a treasure trove for model inefficiencies. In 2008 *Zhurov et al.* introduced the above mentioned *DRKplot* which was also used to adapt the weighting scheme during

68

the charge density refinement.[39] Together with the normal probability plots this program also calculates the variation of the ratio between $\Sigma(F_o^2)/\Sigma(F_c^2)$ with respect to resolution. For a perfect match between collected and calculated data this factor should not vary much from unity. As there are always shortcomings in an experiment (and in any model) that cannot be overcome one does expect small variances but a ratio of more than 5 % difference implies that there is something wrong with either the model or the data. The variation in the ratio shows a smooth course and a close match to unity even for the high angle data but a significant deviation for the innermost reflections (Figure 28).
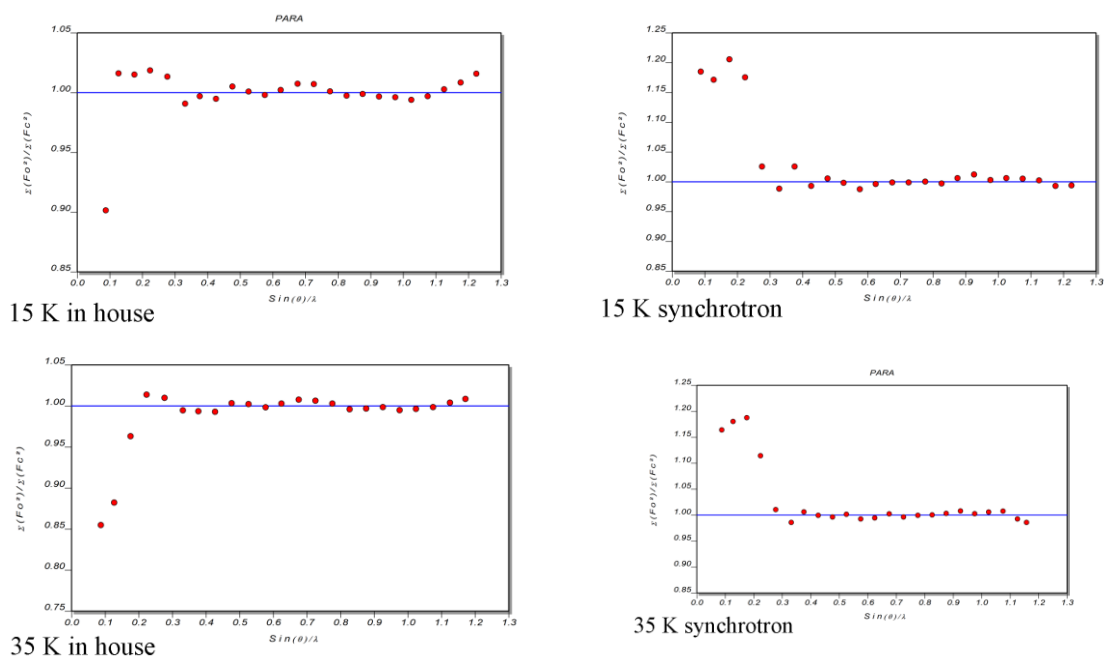


Figure 28: Variation of the ratio $\Sigma(F_o^2)/\Sigma(F_c^2)$ with respect to resolution.

Careful inspection of these reflections shows that for the 15 K in-house data it is only the (110) reflection that is responsible for the mismatch. There are two main reasons for the problems with the collection of the innermost data. One of them is the fact that paracyclophane crystallizes in a tetragonal space group and has a very small cell with only very few reflections present in the inner shells. This results in very few reflections with wrongly determined intensities being responsible for the stark deviation. The second reason is the course of the atomic form factor of carbon and hydrogen. These give rise to strong scattering up to a resolution of about d = 0.7 Å but only very weak Bragg maxima after that limit. To detect data up to a resolution required for a charge density refinement the crystal has to be selected carefully. Unfortunately, the innermost reflections could not be measured with enough multiplicity without surpassing the upper limit of the dynamic range of the detector. For the 15 K in-house data it was possible to trace the mismatch back to only one

reflection. All other datasets revealed more than one reflection responsible for the mismatch and it was not possible to determine the exact number.

The APEXII software package provides the ability to search for each indexed reflections and its position on the recorded frames. With the help of this tool it was possible to carefully inspect all occurrences of the (110) reflection and its symmetry equivalents individually. Comparing the list of indexed reflections provided by APEXII with the *.raw* file of the final integration it was possible to identify the gross outliers. For most of these outliers the dynamic range of the detector was surpassed resulting in poor spot shapes and incorrectly determined intensities. As is depicted in Table 2 the raw intensities for all symmetry equivalents of the (110) reflection have been measured with extremely high values and thus have been given high error values as well.

Table 9: Raw intensities for exemplary reflections from the 15 K in-house dataset.

| Reflection | raw intensity | raw error |
| --- | --- | --- |
| -110 | 107380 | 1610 |
| 1-10 | 110512 | 2194 |
| 1-10 | 117213 | 1942 |
| 110 | 100222 | 2179 |
| 110 | 112170 | 2004 |
| 110 | 110831 | 1708 |
| 110 | 142536 | 817 |
| -10-1 | 72076.3 | 378.4 |

For comparison reasons the (-10-1) reflection was chosen to show the raw intensity with error recorded for an also bright reflection that has not reached the limit of the CCD detector. It was very carefully tested if there were any differences in the charge density refinement results if the (110) reflection was deleted from the *.hkl* file. The outcome of the refinement is almost untouched by this modification for the pole populations or the course of the bond path. The *DRKplot*, on the other hand, does not show any variation large than a few percent any more (Figure 29).
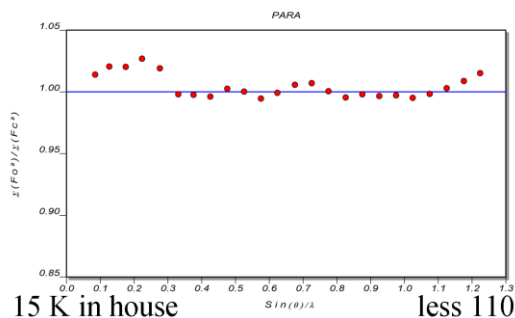
Figure 29: Variation of the ratio $\Sigma(F_o^2)/\Sigma(F_c^2)$ with respect to resolution for the in-house data at 15 K without the (110) reflection.

In a paired refinement approach it was tested whether this data lead to a better model but this was not the case. As can be seen from Table 10, the $R$ value for the model derived with the full *.hkl file is significantly smaller than the value for the model derived with the trimmed *.hkl file. It was thus concluded to keep the reflection and use the full dataset for the charge density refinement.

Table 10: Paired refinement of the full *.hkl and an *.hkl without the (110) reflection.

| $R$(all)$F^2$ | | model | |
|---|---|---|---|
| | | full *.hkl | less (110) |
| **data** | full *.hkl | 2.71 | 2.78 |
| | less (110) | 2.37 | 1.67 |

This quite impressively shows that it is sometimes not necessary to remove reflections that have not been measured with the necessary precision for cosmetic reasons. It is also true that this is only correct if just a minor percentage of reflections have been incorrectly determined. When a similar approach was tested for the 35 K in-house dataset it became obvious that too many incorrectly determined reflections had to be removed from the dataset.

Table 11: Refinement results after the Multipole Modelling.

| | 15 K in-house | 15 K synchrotron | 35 K in-house | 35 K synchrotron |
|---|---|---|---|---|
| data / parameters | 4389 / 127 | 5388 / 127 | 3822 / 127 | 3525 / 127 |
| Goof | 1.4662 | 1.1978 | 1.5995 | 1.1362 |
| weighting scheme | 0.01/0.005 | 0.009/0.003 | 0.007/0.006 | 0.017/0.003 |
| $R1$(F$^2$) | 0.0206 | 0.0523 | 0.0263 | 0.0484 |
| $wR1$(F$^2$) | 0.0319 | 0.0351 | 0.0268 | 0.0347 |
| largest diff. peak and hole [eÅ$^{-3}$] | 0.125 and -0.155 | 0.251 and -0.280 | 0.118 and -0164 | 0.210 and -0.191 |

The problem with the dynamic range only increases for the synchrotron data because the radiation is orders of magnitude more intense than the in-house source. Thus, it

becomes even harder to collect the innermost reflections with great precision because they are also the most intense. The exposure time for the inner reflections was already lowered to 0.3 s for the synchrotron data and the beam was attenuated but there was still too much intensity for the detector to cope with. The gross variation in the ratio between observed and calculated structure factors is certainly the reason for the large amount of positive residual electron density still present after the MM for the synchrotron data.

Sadly, it is the innermost reflections that bear most of the information about the valence density which is to be modelled in a charge density refinement. The figures in Figure 28show unacceptable variation of the ratio of $\Sigma(F_o^2)/\Sigma(F_c^2)$ for the low angle synchrotron data (up to 17 %). Furthermore, the calculated $R1(F^2)$ values are significantly higher for the synchrotron data (Table 11). They are almost twice as high indicating low accuracy for the experimental structure factors. This should render the two datasets useless for a charge density refinement and the related results have to be inspected critically.

### 4.4.4 QTAIM Analysis of Paracyclophane

The most common way to analyse the results of a charge density refinement using the *Hansen-Coppens* formalism is the Quantum Theory of Atoms in Molecules (QTAIM)[51] as promoted by *Bader* and described in chapter 2. Given the problems with the synchrotron data stated above the most reliable results are expected for the 15 K in-house data. Therefore, the results following are presented in comparison to the ones derived from the 15 K in-house data.

The first features usually analysed are the bond paths and bond critical points (bcp) and their position or absence compared to the classical Lewis-bonds drawn in an IAM. For paracyclophane bond paths and critical points were found at all expected positions. Additionally, two ring critical points in the middle of the aromatic six membered ring and in the center of the 12-membered ring of one half of the paracyclophane molecule were found (Figure 30). These results nicely match the observations reported by *Lyssenko et al.* who analysed the electron density of paracyclophane in the high-temperature phase. [75]
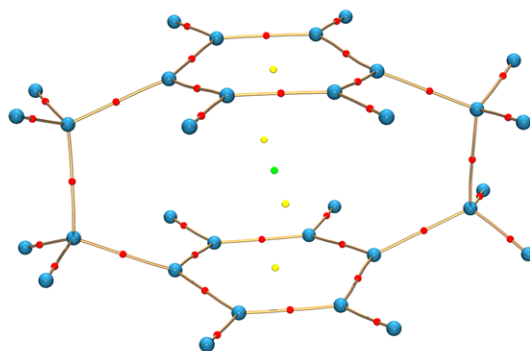
Figure 30: Molecular graph for paracyclophane; bond critical points are marked in red, ring critical points are marked in yellow, cage critical points are marked in green.

The absence of bond critical points between carbon atoms from different aromatic rings back up the lack of transannular effects. The interring distance is smaller than in graphite (3.10 Å in paracyclophane vs. 3.35 Å in graphite) and thus one would expect some weak interactions between the two strained aromatic rings. It should be noted that the bond paths in this molecule may not totally be predictable because the staggered low-temperature form generated a narrow and shallow area of low density, which is close to a catastrophe situation.[56-57] The absence of any bond critical point between carbon atoms from adjacent rings are in contrast to possible interactions. The same absence of bond critical points was also found in a theoretical investigation which analysed the electron density derived from wave functions for the low-temperature phase.[70] The cage critical point in the center of the molecule is also reported by *Caramori and Galembeck*[70] and *Lyssenko et al.*, it is thus present in both phases.

## 4.4.5 Properties Along the Bond Path

The topological parameters for the carbon-carbon bonds are depicted in Table 12 together with the theoretical and experimental values *Lyssenko et al.* gained from their charge density analysis of the high-temperature phase. Additionally, the values derived from theory for the low-temperature phase by *Caramori and Galembeck* have been added for comparison.

Table 12: Topological parameters for the carbon-carbon bonds at the bond critical points for the 15 K in-house dataset. Values: [theory], *exptl.* from Lyssenko et al.[75]; [theory] from Caramori and Galembeck [70]; {theory} from Grimme. [89]

| | $\rho(r)$ [eÅ$^{-3}$] | $\nabla^2\rho(r)$ [eÅ$^{-5}$] | $\varepsilon$ | bond length [Å] |
|---|---|---|---|---|
| C1–C2 | 2.150 | -18.406 | 0.12 | 1.40087(16) |
| | [2.06] | [-19.66] | [0.205] | {1.401} |
| | *2.24* | *-19.56* | *0.18* | |
| | [2.07] | [-19.74] | [0.21] | |
| C1–X7_C4 | 2.132 | -19.205 | 0.16 | 1.40168(16) |
| | [2.06] | [-19.78] | [0.20] | {1.40} |
| | *2.24* | *-19.56* | *0.18* | |
| | [2.07] | [-19.74] | [0.21] | |
| C2–C4 | 2.193 | -19.348 | 0.21 | 1.39515(14) |
| | [2.07] | [-19.81] | [0.22] | {1.394} |
| | *2.26* | *-20.49* | *0.20* | |
| | [2.07] | [-19.86] | [0.23] | |
| C3–C1 | 1.776 | -14.799 | 0.03 | 1.50901(15) |
| | [1.71] | [-14.54] | [0.03] | {1.506} |
| | *1.84* | *-11.43* | *0.01* | |
| | [1.79] | [-14.59] | [0.03] | |
| C3–X3_C3 | 1.392 | -8.484 | 0.03 | 1.59497 |
| | [1.46] | [-10.72] | [0.01] | {1.594} |
| | *1.52* | *-6.29* | *0.07* | |
| | [1.43] | [-10.17] | [0.02] | |

The values for $\rho(\mathbf{r})$ and the Laplacian ($\nabla^2\rho(\mathbf{r})$) at the bond critical points nicely agree with the values reported by *Lyssenko et al.* even though these were derived from a different phase and space group. This also means that paracyclophane essentially keeps its properties over a large temperature range (15-300 K) even though it undergoes a phase transition. The results published by *Caramori and Galembeck* support this as well as their values have been derived for a twisted paracyclophane

body as present in the low-temperature phase.[70] In a publication on the phase transition[117] we could show that almost all intramolecular distances are kept similar over a temperature range of 300 K and the phase transition, which is in nice agreement with the results from this paper. There really is only one distance that changes and that is the length of the aliphatic bridge which is elongated in the low-temperature phase to account for the twisting motion.

The values for the ellipticity ($\varepsilon$) at the bond critical point nicely display the different bonds present in paracyclophane (Table 12). All bonds in the six-membered-ring clearly display values expected for aromatic bonds (around 0.2) the two bonds connected to the aliphatic bridge show values expected for single non-polar carbon-carbon bonds (around 0).[51]

If the four datasets are compared between each other it is obvious again that the synchrotron data are inferior to the in-house data. This is already visible in the bond lengths as can be seen from Table 13. There seem to be two blocks with consistent lengths and angles between each other.

Table 13: Bond lengths for carbon-carbon distances in paracyclophane after MM. Marked in bold are the distances that vary more than 3σ from the 15 K in-house values.

| Bond [Å] | 15 K in-house | 15 K synchrotron | 35 K in-house | 35 K synchrotron |
|---|---|---|---|---|
| C1–C2 | 1.40087(16) | **1.39869(15)** | 1.40054(17) | **1.39859(18)** |
| C1–C3 | 1.50901(15) | **1.50809(12)** | 1.50907(15) | **1.50751(16)** |
| C1–C4 | 1.40168(16) | 1.39991(15) | 1.40144(16) | **1.39934(18)** |
| C2–C4 | 1.39515(14) | **1.39382(12)** | 1.39523(14) | **1.39370(15)** |
| C3–X3_C3 | 1.59465 | 1.59215 | 1.59336 | 1.59118 |
| | | | | |
| Angle [°] | | | | |
| C2–C1–C3 | 121.113(10) | 121.1202(9) | 121.153(11) | 121.135(12) |
| C2–C1–C4 | 117.210(9) | 117.195(8) | 117.204(9) | 117.192(9) |
| C3–C1–C4 | 120.368(10) | 120.391(9) | 120.338(11) | 120.363(12) |
| C1–C2–C4 | 120.358(10) | 120.380(9) | 120.392(10) | 120.386(11) |
| C1–C4–C2 | 120.783(11) | 120.780(9) | 120.756(10) | 120.777(11) |

The two synchrotron datasets give similar bond lengths and the same is true for the two in-house datasets. The values marked in bold show that both synchrotron datasets result in bond lengths that deviate more than 3σ from the in-house data for most of the bonds. This points towards a hardware specific systematic error in the synchrotron data that cannot be corrected for by the software. The bond angles do not seem to be as affected by this source of error. Only the angles involving hydrogen atoms deviate in the synchrotron data which is not unusual as the hydrogen atom positions can only be derived inadequately by X-rays anyhow (See Appendix 10.1.5).

Table 14: Topological parameters along the bond path at the bond critical point of the carbon-carbon bonds for all four datasets.

| BCP between the atoms | Property | 15 K in-house | 15 K synchrotron | 35 K in-house | 35 K synchrotron |
|---|---|---|---|---|---|
| C1–C2 | $\rho(\mathbf{r})$ [eÅ$^{-3}$] | 2.150 | 2.103 | 2.149 | 2.169 |
| | $\nabla^2 \rho(\mathbf{r})$ [eÅ$^{-5}$] | -18.406 | -18.740 | -19.069 | -19.386 |
| | $\varepsilon$ | 0.12 | 0.18 | 0.18 | 0.13 |
| C3–C1 | $\rho(\mathbf{r})$ [eÅ$^{-3}$] | 1.776 | 1.814 | 1.729 | 1.786 |
| | $\nabla^2 \rho(\mathbf{r})$ [eÅ$^{-5}$] | -14.799 | -15.389 | -13.477 | -14.093 |
| | $\varepsilon$ | 0.03 | 0.18 | 0.01 | 0.07 |
| C1–X7_C1 | $\rho(\mathbf{r})$ [eÅ$^{-3}$] | 2.132 | 2.090 | 2.130 | 2.106 |
| | $\nabla^2 \rho(\mathbf{r})$ [eÅ$^{-5}$] | -19.205 | -19.168 | -18.821 | -18.493 |
| | $\varepsilon$ | 0.16 | 0.18 | 0.16 | 0.13 |
| C2–C4 | $\rho(\mathbf{r})$ [eÅ$^{-3}$] | 2.193 | 2.130 | 2.163 | 2.237 |
| | $\nabla^2 \rho(\mathbf{r})$ [eÅ$^{-5}$] | -19.348 | -18.475 | -18.591 | -18.930 |
| | $\varepsilon$ | 0.21 | 0.22 | 0.21 | 0.20 |
| C3–X3_C3 | $\rho(\mathbf{r})$ [eÅ$^{-3}$] | 1.392 | 1.482 | 1.404 | 1.374 |
| | $\nabla^2 \rho(\mathbf{r})$ [eÅ$^{-5}$] | -8.484 | -12.094 | -8.116 | -7.461 |
| | $\varepsilon$ | 0.03 | 0.14 | 0.00 | 0.01 |

Plotting the Laplacian along the bond path does not give rise to any new surprising elements. The bonds forming the aromatic ring do not show any polarisation towards one of the atoms. For the bond between the *ipso*-atom and the aliphatic bridge (C1–C3) the expected slight polarisation towards the aromatic carbon atom can be detected. This holds true for all four datasets. The variation is only minute in absolute numbers but not in the qualitative course of the Laplacian along the bond paths (See Appendix 10.1.6).

Apart from the ring strain in this compound there is no other effect that could influence the bond polarity or ellipticity of the bonds. Hence, according to *Bader* at the bond critical points ellipticities close to zero are expected for carbon-carbon single bonds and values around 0.23 for aromatic double bonds.[51] It is worth looking at these numbers, because the ellipticity is one of the most sensitive properties responding to data quality. As could be shown in Table 12 and Table 14 the values derived for the 15 K in-house data reasonably match the anticipated values for non-polar C–C single and aromatic bonds. The failure of the synchrotron data is also

visible in the topological parameters at the bond critical point (Table 14). A value of more than 0.10 for the ellipticity at the bond critical point of a carbon-carbon single bond is unacceptable. The same failure is visible if the ellipticity is plotted along the bond path; both graphs for the single carbon-carbon bonds of paracyclophane show a clearly different course than the other three datasets (Figure 31).
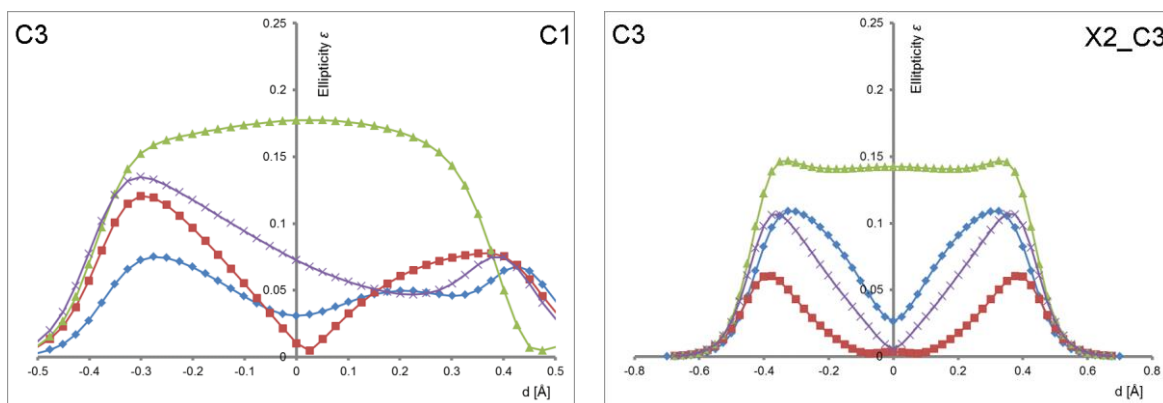


Figure 31: Colour-code: blue diamonds: 15 K in-house; green triangle: 15 K synchrotron; red squares: 35 K in-house; purple cross: 35 K synchrotron.

These findings underline that it is extremely important to carefully check on the results from the bond path analysis. Additionally, the ellipticity at the bond critical point can be influenced quite a lot by data quality issues as it is calculated from the Laplacian. Quite surprisingly, the 35 K synchrotron data do give sensible values both for the ellipticity at the bcp and along the bond path even though they show the same quality issues as the 15 K data.

### 4.4.6 Static Deformation Electron Density and Laplacian

Just like *Lyssenko et al.* in their charge density study of the high-temperature phase no charge concentration could be detected inside the paracyclophane cage in the low-temperature phase. The Laplacian and deformation density very clearly show no charge concentration to be present between the two rings which was a necessary prerequisite for the above mentioned transannular effects. Quite in contrast charge depletion is observed further substantiating the absence of bond paths between the aromatic rings (Figure 32). This is in good agreement with the cage critical point found in the center of the molecule since it always sits on a local minimum of the charge density.

static deformation electron density in the plane of C1 and its symmetry mates

Laplacian distribution in the plane of C1 and its symmetry mates
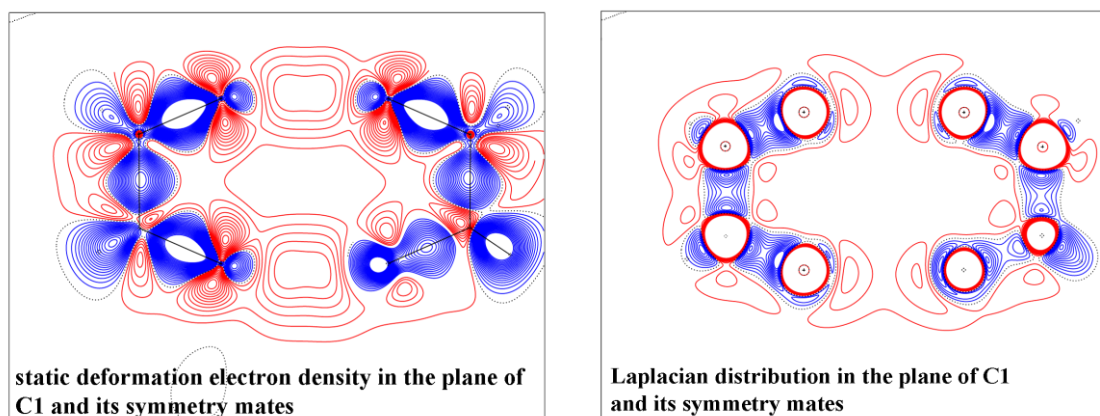
Figure 32: Static deformation density and Laplacian distribution inside the paracyclophane cavity. Contour lines are drawn at $\pm 0.02, \pm 0.04, \pm 0.06, ...$ eÅ$^{-3}$ interval levels for the deformation density and $\pm 2, \pm 4, \pm 6,...$ eÅ$^{-5}$ interval levels for the Laplacian distribution. Blue: positive; red: negative.

The static deformation density in the ring plane and the aliphatic bridge depict a distribution of the electron density as expected (Figure 32, Figure 33). As all plots look essentially the same neither the Laplacian nor the static deformation density is particularly indicative to data quality. The plots in the plane of the aromatic ring underline the fact that the aromatic ring system is kept intact even though the *ipso*-carbon atom (C1) is considerably dislocated from the ring plane.

### Laplacian Maps



15 K in house

15K synchrotron

35 K in house

35 K synchrotron

### Deformation Density Maps



15 K in house

15K synchrotron

35 K in house

35 K synchrotron
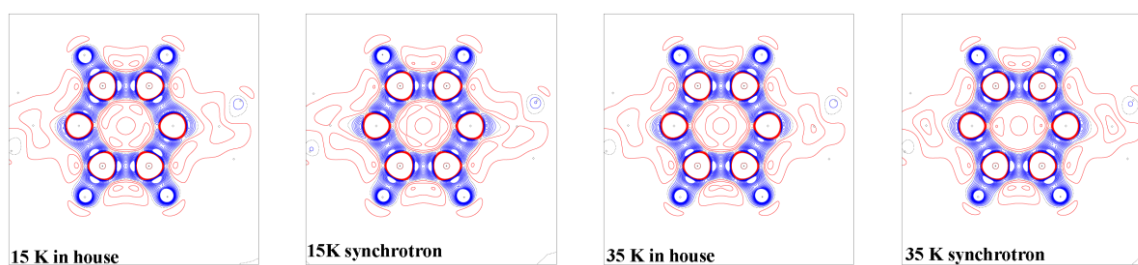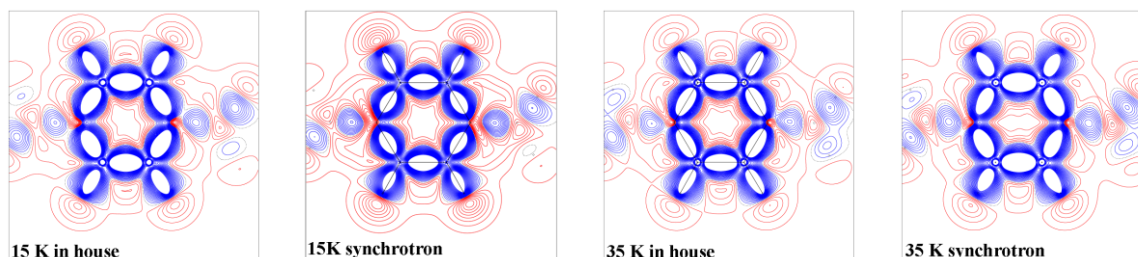
Figure 33: Laplacian and static deformation density maps for all datasets in the ring plane. Contour step size and colour coding is the same as in Figure 32.

This is also displayed in the bond lengths which are almost the same within the ring (C2–C4 1.39529(11) Å; C1–C2 1.40088(13) Å and C1–C4 1.40160(13) Å), with only the C2–C4 bond being a little shorter as this bond experiences less strain than the other two. Taking a closer look at the synchrotron datasets it becomes clear that even though they are inferior in quality little to no qualitative difference could be seen between the four datasets.

### 4.4.7   Net and Bader Charges

Resulting from the refined multipole parameters a charge density refinement also gives information about the Net charges of an atom. These are simply derived from the monopole populations and state the loss or gain of electrons compared to the starting model. There is another way of determining a charge on an atom after the multipolar modelling. It is in the heart of QTAIM that it is possible to divide the total electron density of a molecule into atomic basins. This is possible by means of the first derivative of the electron density $\nabla\rho(\mathbf{r})$, which defines a field of gradient vectors. The nuclei serve as attractors of the gradient vectors defining a basin in which all gradient paths terminate. Each basin only contains one attractor, the atomic nucleus. The surface of a basin is not crossed by any gradient line and is called the surface of zero flux. The total boundary of the surface of the basin (or integrated atomic charge) is defined as $\nabla\rho(\mathbf{r})\mathbf{n}(\mathbf{r}) = 0$ with $\mathbf{n}(\mathbf{r})$ defining each point on the normal of the surface. The integrated charges derived from atomic basin integration can differ significantly from the Net charges. This phenomena is also visible in the analysed data that give a Net charge of +0.18(3) for C1 but an integrated Bader charge of -0.0267 (Table 15). Generally, for the given molecule all charges are very small, which is not unexpected given the fact that the main body only consists of carbon-carbon bonds.

Table 15: Integrated Bader and Net charges for the carbon backbone of paracyclophane.

|  | 15 K in-house | 15 K synchrotron | 35 K in-house | 35 K synchrotron |
|---|---|---|---|---|
| **C1** |  |  |  |  |
| Net charge | +0.18(3) | -0.01(3) | +0.19(3) | +0.10(3) |
| Bader charge | -0.0267 | -0.1775 | -0.0128 | -0.0515 |
| **C2/C4** |  |  |  |  |
| Net charge | -0.148(15) | -0.106(5) | -0.128(13) | -0.160(16) |
| Bader charge | -0.1558/ -0.1862 | -0.1633/ -0.1775 | -0.1515/ -0.1664 | -0.2067/ -0.2186 |
| **C3** |  |  |  |  |
| Net charge | -0.40(3) | -0.51(3) | -0.43(3) | -0.48(3) |
| Bader charge | -0.1236 | -0.2669 | -0.1764 | -0.2760 |

It is noteworthy however, that the two in-house datasets give rise to chemically reasonable Bader and Net charges while the synchrotron datasets show significantly different values for the integrated charges.[118] This is most pronounced for the bridging carbon atom C3. While the Net charges do not differ more than 3σ, the Bader charges are significantly different for the synchrotron data using esd's derived by *Kaminski et al.*.[118] The same is visible for C1 where even the Net charges differ substantially. The gross mismatch between the in-house and the synchrotron data does not come unexpected as it only supports what was already visible from the residual densities. What is also very nicely deducible from the charges is the fact that both in-house datasets give very similar values, which is in good agreement with the other quality indicators marking these as the best datasets. The 35 K synchrotron dataset did show lower residual density and better agreement in the bond path analysis but gives rise to significantly different charges. The 15 K synchrotron data fail topological characteristics and it is thus not surprising that it also gives rise to meaningless charges.

### 4.4.8 Conclusion

Despite the fact that all four datasets have their shortcomings if the most prominent quality indicators are monitored, a clear discrepancy between the synchrotron and the in-house data is visible. Even for a small hydrocarbon compound, with an advantageous suitability factor[119] of 4.2 for a charge density investigation, excellent data are essential. It became obvious that collecting data of a quality high enough for a charge density investigation is not trivial at all and has to be monitored very closely during data collection. For data collected on Bruker diffractometers it is very easy to monitor the collected data by use of the *summary* tool which gives information about pixel overload on the recorded frames. It would be feasible to adapt the exposure time during the experiment to avoid gross overload.

Although for some of the data it only became obvious that they were absolutely useless for a charge density refinement after the MM in hindsight these problems were already detectable in the $R_{int}$ and $R_{r.i.m.}$ values of the *XPREP* statistics. Although the synchrotron data do have very low total $R_{int}$ and $R_{r.i.m.}$ values, especially the values for the low order shells are still significantly higher than for the in-house data. It seems that values above 5 % in $R_{int}$ for the innermost reflections are too high. For a high quality dataset we would expect a stronger increase with rising resolution as was given for the in-house data. The difference of the $R_{int}$ values between the innermost and the outermost reflections are so small for the synchrotron data, although on a low level, that it is save to conclude that the high order data are of excellent quality, while the low order data have their deficiencies. As these data are of crucial importance for a charge density investigation the synchrotron data fail. A very

useful tool to monitor data quality during a refinement is *DRKplot*. In the case of the 15 K in-house data the spike in this plot could be related to just one reflection, but it was still important to check on this reflection very carefully. The next hint on the reliability of the derived properties was found in the residual density. Therefore, it is absolutely necessary to monitor it in the whole resolution range and to use all information from the *Henn-Meindl-plot*. This was most elegantly shown for the 35 K synchrotron data where the residual density does look promising even though the *DRKplot* shows significant problems with the inner data. Although the properties along the bond path are in agreement with the in-house data the Net and Bader charges calculated for C1 and C3 are out of range for both synchrotron datasets. The variance in the values derived for the bcps and the atoms themselves is a warning that these values should be taken with great care and unexpected results should be carefully evaluated. All this does not seem to affect the outcome of this study if only structural parameters are taken into account. Paracyclophane is a relatively simple molecule and the observed differences in the topological parameters are subtle. But these problems will become more obvious if more complex compounds are investigated. Therefore, the use of simple molecules like urea and oxalic acid as benchmark systems as is the practice of the IUCr is not feasible any longer. Instead of these small molecules with mostly covalent bonds there should be benchmark systems involving ionic bonds and/or heavier atoms like sulphur and phosphorous.

# 5 CHARGE DENSITY INVESTIGATIONS OF 7,7,8,8-TETRACYNOQUIODIMETHANE

Tetracyanoquinodimethane (TCNQ; Scheme 8) has been in the center of research ever since it was first reported in the late 1950s.[120-121] This was mainly due to the fact that TCNQ easily undergoes reduction processes to form the radical anions TCNQ−and (TCNQ)$_2$−, which are remarkably stable.[122] Shortly after those radical anions were first mentioned in literature some of them were also reported to show semi-conducting solid-state properties.[122-123] Amongst the most famous complexes is tetrathiafulvalene-tetracyanoquinodiemthane (TTF) (Scheme 8), which has been studied extensively since its first preparation by *Ferraris et al.* in 1973.[124] TTF acts as the electron donor and TCNQ as the electron acceptor in this complex.
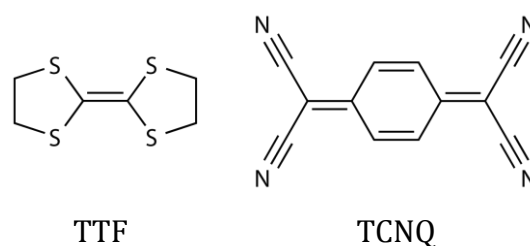


TTF                 TCNQ

Scheme 8: Chemical structures of TTF and TCNQ.

Showing superb potential for industrial use in the semi-conducting industry TTF-TCNQ and its derivatives have been subject of various publications.[125-130] Since conductivity always involves the migration of electrons, charge density investigations are the consequent steps to further elucidate how the electrons move in the complexes. Unfortunately, most of these complexes show a lack of stability under cooling.[131] This makes a charge density investigation even more challenging as cooling to at least 100 K is essential to collect a high quality dataset.[132-134]To the best of our knowledge the only charge density investigations dealing with TTF-TCNQ or any complex containing TCNQ have been published by *Coppens et al.* , *Cole et al.* and *Espinosa et al.*.[131,135-136]

Although it is substantial to investigate the physical properties of the semiconducting substances themselves, it is also of outermost importance to understand the involved substances before they form the complex. When *Trueblood* published the crystal structure of TCNQ in 1965 he already mentioned its importance to provide "a standard for comparison" purposes in future studies involving the radical anions TCNQ− and (TCNQ)$_2$−.[137] Regarding the amount of articles involving those anions that have been published since, it is astonishing that there is no charge density investigation published yet that deals with the ground state of TCNQ and could thus make a more elaborate standard for theoretical investigations. The following

subchapters will show the results on charge density investigations carried out on four different datasets. The four datasets have been collected at different temperatures, different radiation types and unfortunately, on different crystals. Despite this, the agreement in parameters is surprisingly good although the datasets are of significantly different quality.

## 5.1    Data Collection and Processing

Dataset 1 has been collected on our in-house Bruker D8 diffractometer with a Mo rotating anode ($\lambda = 0.71073$ Å) equipped with mirror optics and an ApexII CCD detector. The data were collected using ω scans and four different 2θ settings (chapter 10.2.1). The exposure time was adapted to give high $I/\sigma(I)$ values up to high resolution.

Dataset 2 was collected at Bruker headquarters in Madison, USA on a D8 diffractometer also equipped with a Mo rotating anode and an ApexII CCD detector. Thus, the set-up for dataset 1 and 2 is similar but different collection strategies as well as different crystals were used for the two datasets (chapter 10.2.2). The data in Madison were collected at the same temperature as the in-house data (100 K).

Dataset 3 was collected at the 15-ID-B beam-line at the Advanced Photon Source (APS) in Chicago. The set-up at the APS is similar to the in-house source used for dataset 1 but the ApexII detector has a modified phosphor to yield higher light output for the high energy synchrotron radiation. The data were collected using 360° φ scans with three different 2θ settings. The temperature was set to 15 K and controlled with an Oxford Open Stream Helijet operated with liquid helium. The wavelength was set to 31.5 keV ($\lambda = 0.39360$ Å).

Dataset 4 was also collected at the 15-ID-B beam-line at the APS but on a different crystal and with a different energy (30 keV, $\lambda = 0.41328$ Å). Two different 2θ settings were used together with 360° φ scans. Based on the experiences with the 31.5 keV data the low order data were recorded with maximum attenuation. The high order data were collected both with maximum and with no attenuation.

All four datasets have been integrated and reduced with *SAINT-8.30C*. For the synchrotron data all runs have been integrated separately and with individual integration masks to cover the beam stop and damaged pixels. The individual *\*.raw* files were merged in *SADABS-2014/2*. The phosphor efficiency was taken from a calibration curve for the synchrotron data. For the in-house data the phosphor efficiency was set to the value recommended by Bruker (0.92). Absorption correction and scaling has been done using *SADABS-2014/2* using the expert mode. The weighting $g$ value has been refined using an individual $K$ for each run but an overall $g$ and repeated until it converged.

## 5.2   XPREP and IAM

TCNQ crystallizes in the monoclinic space group $C2/c$ and contains half a molecule in the asymmetric unit. There were no problems assigning a space group in *XPREP*. Based on the results from chapter 4.4.1 (pp. 56), the course of $R_{\text{r.i.m.}}$ against the resolution is very informative concerning data quality. Looking at Figure 34 it is obvious that the synchrotron data have considerably higher $R$ values for the innermost resolution shells. Interestingly, the data collected in Madison (100 K Bruker) give rise to the highest $R$ values for the highest resolution shells. The data collected at the APS with 31.5 keV radiation show an inacceptable course of the $R_{\text{r.i.m.}}$ against resolution. Not only do the data start at the highest values for the innermost data but also have a spike at the resolution values routinely used for structure determination (d = 0.8 Å).
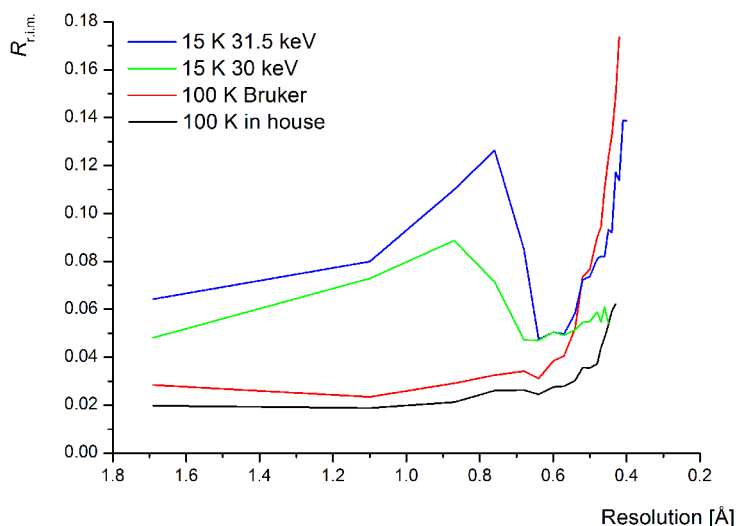


Figure 34: $R_{\text{r.i.m.}}$ plotted against the resolution for all four datasets.

The second dataset collected at the APS shows an expected course up d = 0.8 Å but the $R$ value drops at higher resolution and stays surprisingly small even at maximum resolution. This is somewhat surprising as the usual course depicts an increase in $R$ value with an increase of resolution. Following the argument in chapter 4.4.8 (pp. 79) this clearly shows that the data quality of the inner data is poor despite the fact that it was collected with the highest possible attenuation. The most promising course is depicted by the data collected on our in-house diffractometer at 100 K. The starting $R$ value is around 2 % and it does not change drastically until very high resolution is reached (d ≥ 0.5 Å). Even at maximum resolution the $R_{r.i.m.}$ stays below 6 %.

The maximum resolution reached for the individual datasets has been determined using the XPREP statistics. The maximum resolution and crystallographic details have been summarized in Table 16. Despite the high energy radiation used for the two

synchrotron datasets the attenuation used for the 30.0 keV data has cut off the high resolution data since integration to higher θ values was not feasible. Nevertheless, all datasets reach the necessary resolution for a charge density refinement and fulfil standard criteria.[138] It is also interesting that the synchrotron data have the lowest $R$ values although Figure 34 would lead to a different assumption

Table 16: Crystallographic details after the IAM refinement for all four datasets.

|  | 100 K in-house | 100 K Bruker | 15 K APS 30.0 keV | 15 K APS 31.5 keV |
|---|---|---|---|---|
| θ range [°] | 2.508 to 55.742 | 2.510 to 57.876 | 1.460 to 27.340 | 1.392 to 29.530 |
| maximum resolution [Å] | 0.43 | 0.42 | 0.45 | 0.40 |
| reflections collected / independent | 38421 / 6499 | 52999 / 6962 | 115727 / 5641 | 116425 / 8025 |
| completeness to θ max | 99.3 % | 98.7 % | 99.2 % | 99.8 % |
| data / restraints / parameters | 6499 / 0 / 79 | 6962 / 0 / 79 | 5641 / 0 / 79 | 8025 / 0 / 79 |
| Goof | 1.125 | 1.065 | 1.094 | 1.037 |
| $R$ indices [$I > 2\sigma(I)$] | $R1 = 0.0313$ w$R2 = 0.1148$ | $R1 = 0.0358$ w$R2 = 0.1108$ | $R1 = 0.0249$ w$R2 = 0.0857$ | $R1 = 0.0293$ w$R2 = 0.0838$ |
| $R$ indices (all data) | $R1 = 0.0339$ w$R2 = 0.1177$ | $R1 = 0.0441$ w$R2 = 0.1187$ | $R1 = 0.0268$ w$R2 = 0.0883$ | $R1 = 0.0335$ w$R2 = 0.0872$ |
| largest diff. peak and hole [e$Å^{-3}$] | 0.767 and - 0.233 | 0.894 and - 0.209 | 0.924 and - 0.295 | 1.044 and - 0.231 |

The structures were solved with *SHELXT*[139] and refined in a full matrix least squares procedure against $F^2$ using *SHELXL*[109] implemented in the GUI *ShelXle*[110]. The displacement and positional parameters for the heavy atoms (C and N) were refined against high resolution data (d ≤ 0.7 Å). The hydrogen atoms positional parameters were refined against low resolution data (d ≥ 1.0 Å) and their displacement parameters were constrained to the $U_{eq}$ of their pivot atom. The carbon-hydrogen distances were set to averaged distances derived from neutron diffraction experiments[114] using the HIMP command in XP.[22]

## 5.3 Multipole Modelling with XD2006

The starting model was generated as described above for all four datasets and the starting files for the *XD2006* refinement were generated by the program *XDINI*. The aspherical scattering factors were taken from the *SCM*[112] databank in the *XD2006* program package. Subsequently, all datasets have been refined with the same strategy (see chapter 10.2.5). For the synchrotron datasets dispersion corrections

were taken from tabulated values [113] for the respective wavelength and manually adjusted in the *.mas* file. The charge density model was refined against $F^2$ and the convergence criterion was set to $1x10^{-8}$ allowed maximum shift over esd's for each refinement step. Convergence was reached for all refinement steps. The standard $I/\sigma(I)$ cut off (three) was used for stabilization purpose in the early stages of the refinement but was reduced to zero in the course of the refinement.
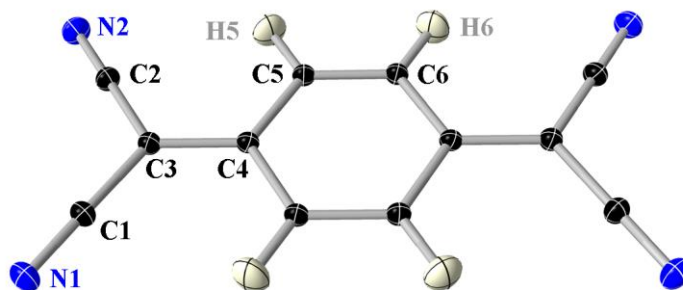


Figure 35: Tetracyanoquiodimethane (TCNQ) numbering scheme as applied in the *XD2006* refinement.

TCNQ consists of twelve carbon, four nitrogen and four hydrogen atoms but one half is built by symmetry (Figure 35). Hence, only half the atoms have to be assigned multipole parameters in an *XD* refinement. Since all atoms lie on general positions there are no restrictions to the number of refined parameters according to symmetry. However, in the beginning of the refinement local symmetry was imposed to stabilize the refinement but was later released and all multipole parameters have been subsequently refined. All non-hydrogen atom multipole parameters have been refined to $l_{max} = 4$. For the hydrogen atoms only the populations for the monopole and the dipole directed along the bond axis were refined. The $\kappa$ parameters for the hydrogen atoms have been kept fixed at the values reported by *Volkov et al.*[114] ($\kappa = 1.10$ and $\kappa' = 1.18$).

In order to find a refinement strategy with the maximal number of parameters without over fitting of the data an $R_{free}$ and $R_{cross}$ (see chapter 3 for definition) were calculated for all four datasets. Since all datasets were to be refined using the same strategy the results of cross validation from the 100 K in-house dataset were taken as measure for all other datasets. This dataset looked the most promising after inspection of the *XPREP* statistics and was thus decided to serve as a reference.
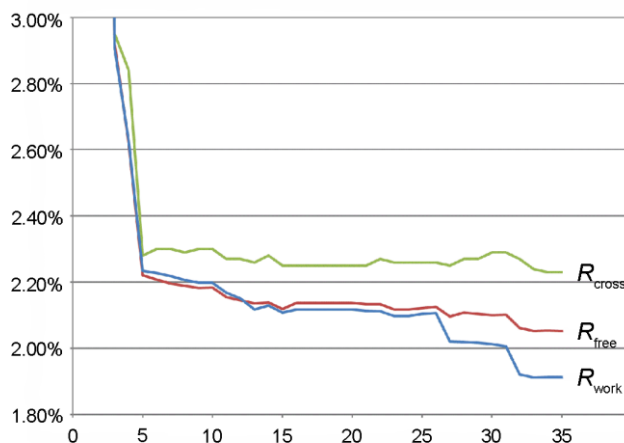
Figure 36: Course of cross validation $R$ factors over the number of refinement steps.

It becomes obvious from Figure 36 that there are signs of over fitting around refinement step 28. The values for $R_{cross}$ and $R_{free}$ are increasing while the values for $R_{work}$ are decreasing. In the refinement strategy applied for the cross validation the chemical constraints are released after refinement step 30. Chemical constraints force chemically equivalent atoms to have the same shift in multipole parameters. If they are applied from the beginning this implies identical pole populations. From the cross validation it is obvious that the release of these constraints is not feasible for this molecule and should thus be avoided. Hence, the final refinement strategy mentioned above does not include the release of chemical constraints applied for N1/N2, C1/C2, C5/C6 and H5/H6 (Figure 35). All refinement steps readily converged for all four datasets. After refinement of the full set of parameters the weighting scheme was adapted using the *DRKplot* program to give a normal distribution of the standard uncertainties of the intensities.
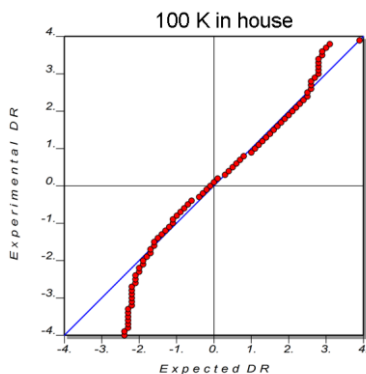
weighting scheme: a = 0.02; b = 0.006
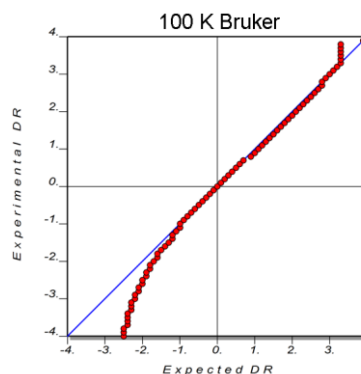
weighting scheme: a = 0.01; b = 0.02
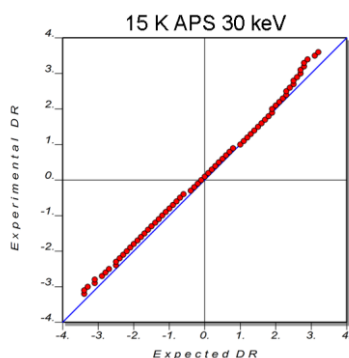
weighting scheme: a = 0.007; b = 0.022
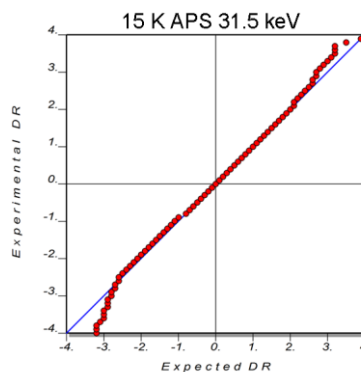
weighting scheme: a = 0.01; b = 0.02

Scheme 9: Normal probability plot for all four datasets with adjusted weighting scheme.

All four datasets show a normal distribution and the parameters *a* and *b* do not vary much for the different datasets. Another most informative plot generated by *DRKplot* is the variation of $\Sigma(F_o^2)/\Sigma(F_c^2)$ with respect to resolution (Scheme 10). For all four datasets little variance is observed despite the shortcomings visible for the synchrotron data in the *XPREP* statistics (Figure 34). Only the data collected with 30.0 keV radiation at the APS show a deviation of larger than 5 % for the innermost data.

Although these two plots do not provide any hint for obvious data problems the residual density looks significantly different for the individual datasets. For the two datasets collected at 100 K residual density around the nitrogen atoms shows an alternating pattern of positive and negative residual density as described for anharmonic motion (Figure 37).[140-141]
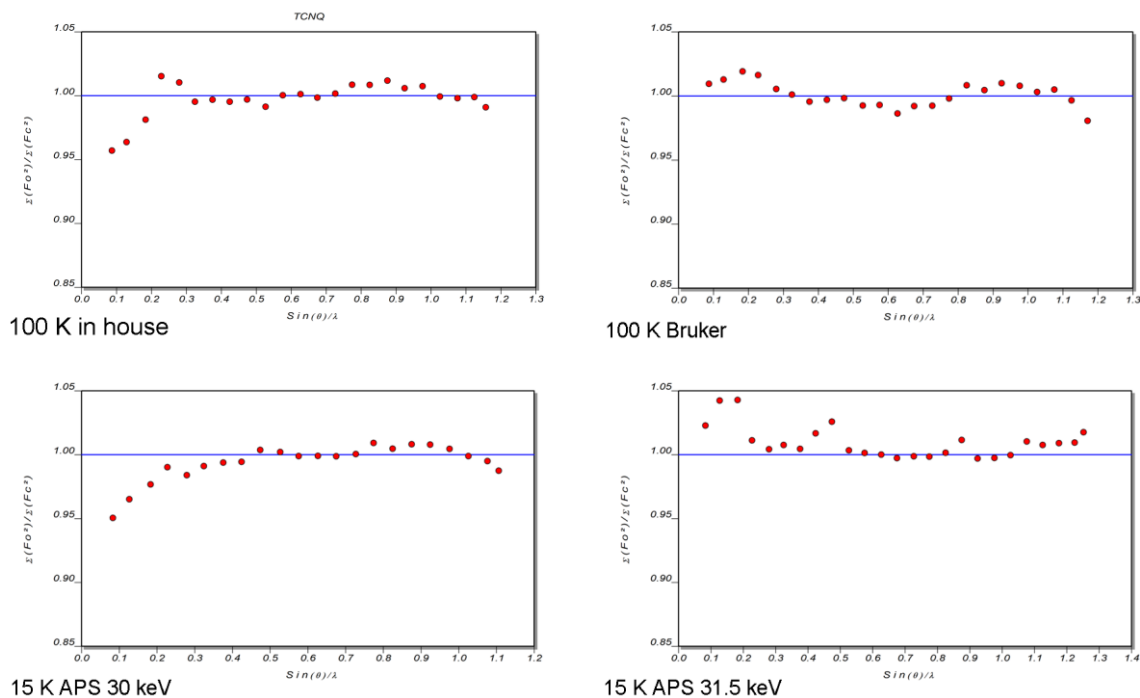
Scheme 10: Variation of $(F_o^2)/\Sigma(F_c^2)$ with respect to resolution for all four datasets.

Since no other obvious reason behind this pattern was found 3rd order Gram Charlier expansion[142] was included in the charge density refinement for the 100 K data. After the expansion the characteristic residual density pattern around the nitrogen atoms was no longer visible and reduced to only little positive density (Figure 37).
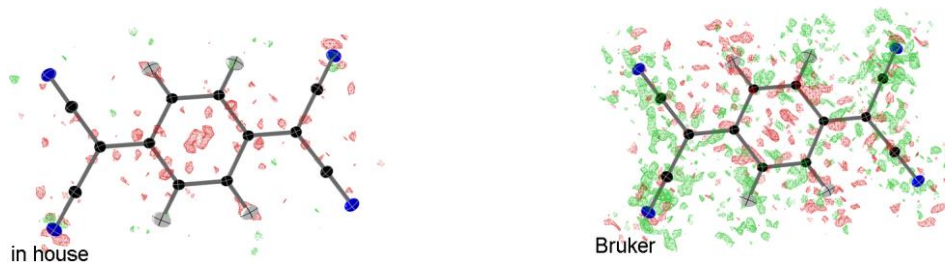


Residual difference density map without Gram Charlier expansion; level depicted at ±0.066 eÅ-3
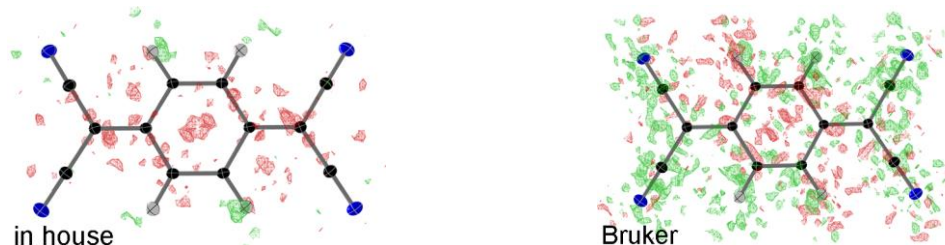


Residual difference density map including Gram Charlier expansion; level depicted at ±0.066 eÅ-3

Figure 37: Fourier difference density map for the in-house and Bruker data before (top) and after (bottom) Gram Charlier expansion.

If Gram Charlier expansions are included in the XD refinement it is necessary to carefully check whether the additional parameters are fitting anharmonic motion or

simply mopping up residual density.[141] There are a number of parameters that have to be checked individually to confirm anharmonic motion. The first hint towards anharmonic motion is the characteristic residual density pattern of alternating negative and positive residual density about the atom in question after a conventional charge density refinement. If a characteristic pattern is observed the next step is to expand the multipole model via the Gram Charlier parameters. Implemented into XD2006 is the option to expand the usual six variables for the displacement parameters to third and fourth order Gram Charlier exponents. Based on the paper by *Herbst-Irmer et al.* stepwise addition of the third and fourth order coefficients is the best option.[141] After the additional ten variables have been added to the atom in question and the convergence of the refinement a probability density function (pdf) can be calculated for the atom in question.[143-144] The shape of the pdf should resemble that of the thermal ellipsoid and be elongated along the largest axis of the ellipsoid. No nodes or holes should be visible and the pdf should also not resemble a doughnut. For the nitrogen atoms in TCNQ which were refined with 3rd order Gram Charlier expansion the pdfs look reasonable (Figure 38).
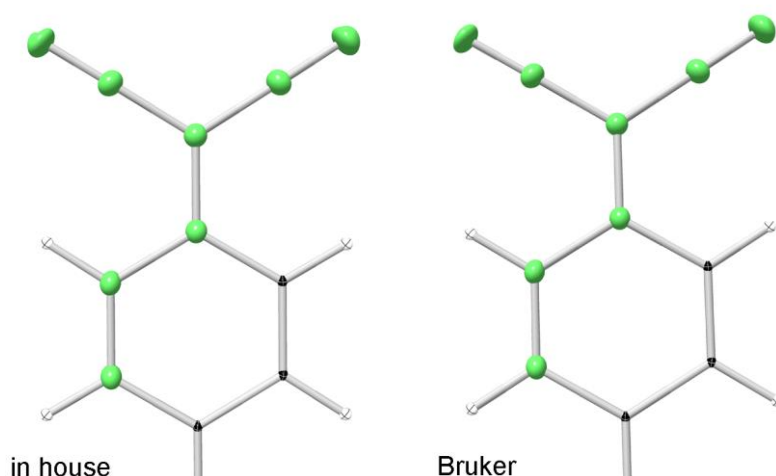


Figure 38: Probability density function calculated for N1/N2. Left: in-house data; right: Bruker data

Additionally, the characteristic pattern of alternating positive and negative residual density has disappeared from the difference density map around the nitrogen atoms (Figure 39).

These three criteria for anharmonic motion in the crystal structure are fulfilled for the two datasets collected at 100 K. Still it is clearly visible from the difference density maps that the data collected on our in-house diffractometer are superior to the data collected by Bruker. The level of residual density is significantly lower for the in-house data. In comparison to the synchrotron data, which did not depict any anharmonic motion, the residual density of the in-house data collected at 100 K is still on the lowest level (Figure 39).
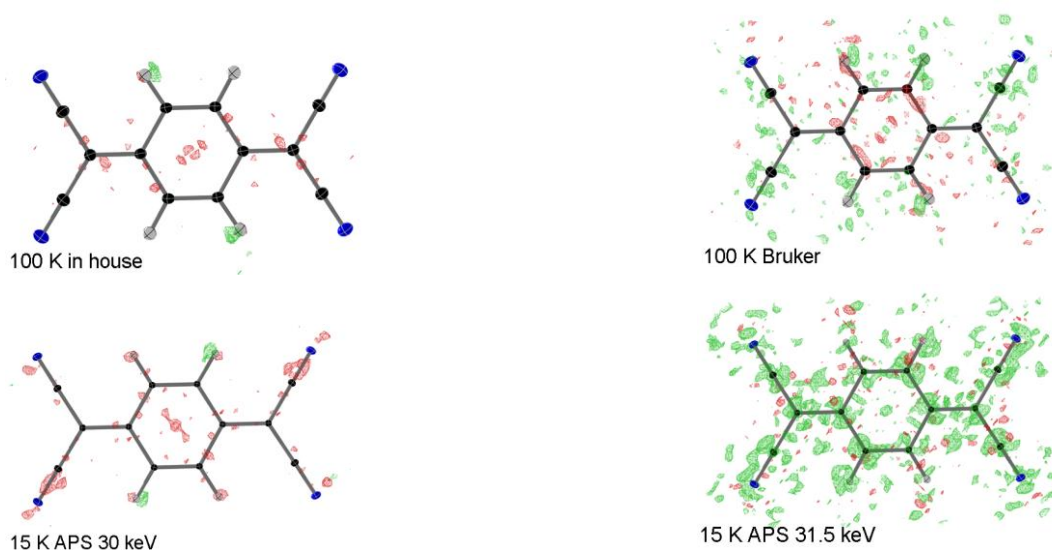
Figure 39: Residual density maps for all four datasets after final refinement. The level is depicted at ±0.08 eÅ⁻³. Positive density appears in green and negative density appears in red.

The highest level of residual density is present in the synchrotron dataset collected with the 31.5 keV radiation. This is traced back to the inacceptable values in $R_{int}$ and $R_{r.i.m.}$ for the lower resolution data. Surprisingly, this does not show up in the *DRKplot* analysis, which only underlines the importance to check on the *XPREP* statistics carefully when in doubt about the data quality.

Table 17: Refinement results after MM

|  | 100 K in-house | 100 K Bruker | 15 K 30 keV | 15 K 31.5 keV |
|---|---|---|---|---|
| data / parameters | 6294 / 228 (+kappa') | 6543 / 228 | 5537 / 208 | 7805 / 208 |
| Goof | 1.3553 | 1.0403 | 0.8675 | 0.08898 |
| weighting scheme a / b | 0.02 / 0.006 | 0.01 / 0.02 | 0.007 / 0.022 | 0.01 / 0.02 |
| $R1$ ($F^2$) | 0.0204 | 0 0227 | 0.0206 | 0.0270 |
| $wR1$ ($F^2$) | 0.0498 | 0 0415 | 0.0254 | 0.0364 |
| largest diff. peak and hole [eÅ⁻³] | 0.113 and -0.117 | 0.142 and -0.128 | 0.122 and -0.143 | 0.215 and -0.126 |

Analysis of the residual density according to *Meindl* and *Henn*[37,45] shows that all four datasets depict a Gaussian shape in the fractal dimension plot. The residual density depicted in Figure 39 for the synchrotron data collected with 31.5 keV radiation is also visible in the fractal dimension as this plot is considerably broader on the positive axis. Apart from the shape of the parabola there are two other numbers worth looking at derived from these plots. The value for $d^f(0)$ is an indicator for the featurelessness of the residual density, the closer to three the better the model

describing the data.[37] All plots have been derived with the same resolution and using the same grid for comparison purpose. Plots for the individual maximum resolution can be found in chapter 10.2.6. The highest value from the four datasets for $d^f(0)$ is derived from the Bruker data with $d^f(0) = 2.73205$ followed by the 30 keV data from the synchrotron ($d^f(0) = 2.7160$).



100 K in house    $r_0$ [eÅ$^{-3}$]

100 K Bruker    $r_0$ [eÅ$^{-3}$]

15 K APS 30 keV    $r_0$ [eÅ$^{-3}$]

15 K APS 31.5 keV $r_0$ [eÅ$^{-3}$]
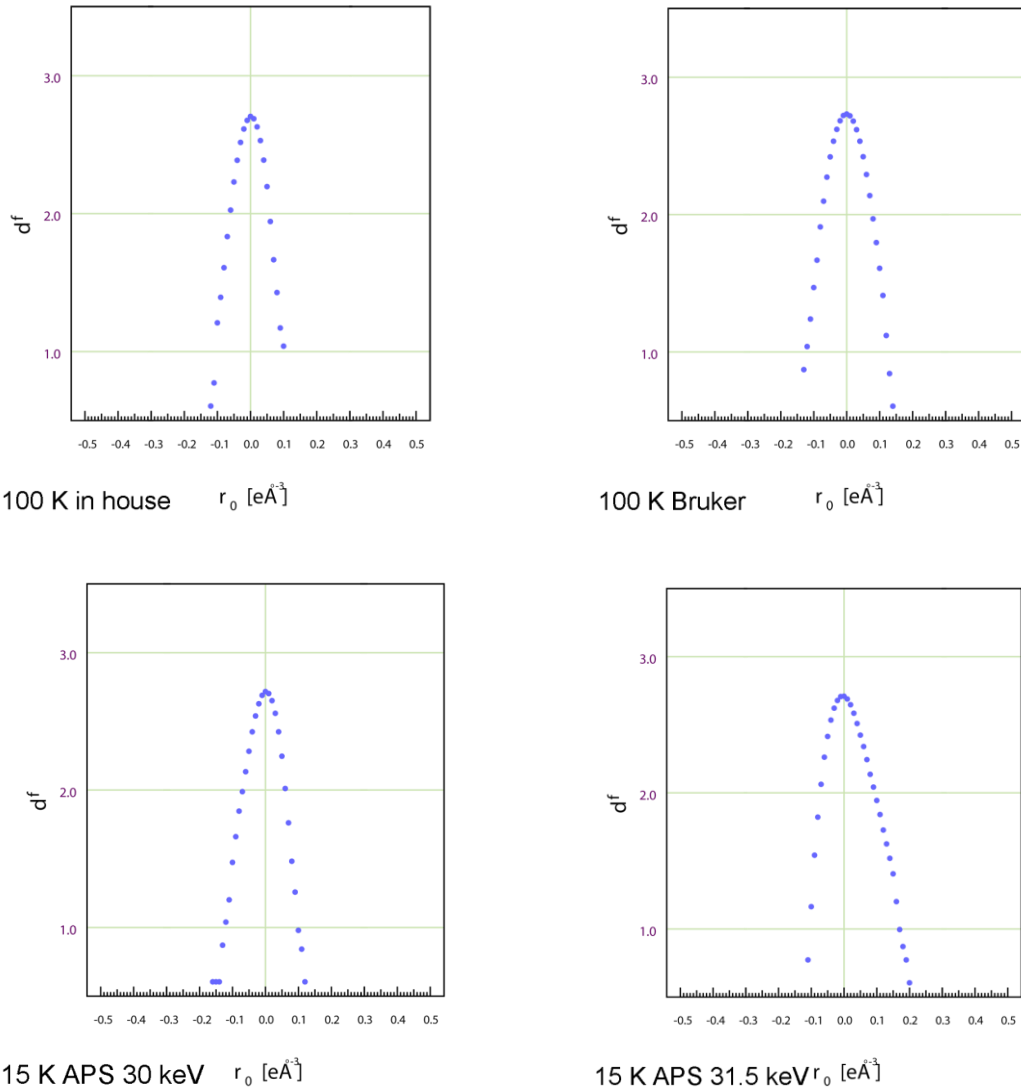
Scheme 11: Fractal dimension plot of the residual density according to *Meindl* and *Henn*.

The in-house dataset reached a maximum of $d^f(0) = 2.7040$ and the synchrotron data collected with 31.5 keV radiation depict a similar value with $d^f(0) = 2.7093$.

If only these numbers are taken into account the model fits the Bruker data best and thus result in the highest value for $d^f(0)$. However, there is a second number derived in the *Meindl* and *Henn* analysis and that is the value stating the gross residual electrons including noise $e_{gross}$. Analysing the values derived for the four datasets a different outcome is depicted. The lowest $e_{gross}$ and thus the model with the lowest gross residual electrons and noise is derived from the 100 K in-house data

($e_{gross}$ = 10.1403 e). The data with the highest $d^f(0)$ (100 K Bruker) give rise to $e_{gross}$ = 12.9650 e, thus reflecting the residual density left in the difference density map. The two synchrotron datasets depict values around ten (30 keV: $e_{gross}$ = 10.5410 e), the data collected with 31.5 keV radiation resulting in the highest value of $e_{gross}$ = 13.3869 e. Based on these numbers it is obvious why no quality indicator should be evaluated on its own because they may be misleading. All values should be considered together and only if all are taken into account a clear decision for the best dataset should be made.

From the results presented above the 100 K in-house data have the best data quality, hence all following results from the QTAIM analysis[51] are referenced to this dataset.

## 5.4    QTAIM Analysis of TCNQ

All four datasets have been analysed according to *Bader's* QTAIM and the 100 K in-house data are used as reference for all others. The following results are all derived from the in-house 100 K data if not stated otherwise.

All bond paths and critical points were found at the expected positions. There is one ring critical point inside the six-membered carbon ring. This is in accordance with results published by *Espinosa et al.* who reported on a charge density investigation of bis(thiodimethylene)-tetrathiafulvalene    tetracynaoquinodimethane    (BTDMTTF-TCNQ) in 1997.[131] Although TCNQ is serving as an electron acceptor in this complex and is thus reduced, the overall molecular features are kept intact.
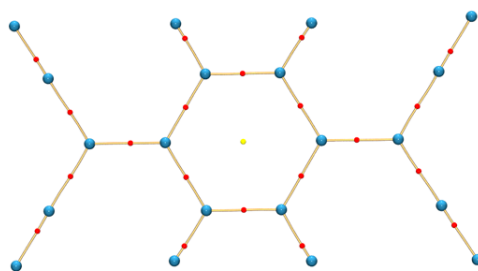


Figure 40: Molecular graph of TCNQ. Bond critical points are marked in red and ring critical points in yellow.

The interesting feature about the TCNQ molecule in the ground state is the bonding situation as provoked by the four cyanide groups. The six membered carbon ring in the center of the molecule has alternating double and single bonds. The bond to the *ipso*-carbon is characterized as a double bond and the carbon-carbon bond to the cyanide groups is a single bond again. This means that the molecule is built by alternating double and single bonds, which is also nicely represented by the bond lengths (Table 18).
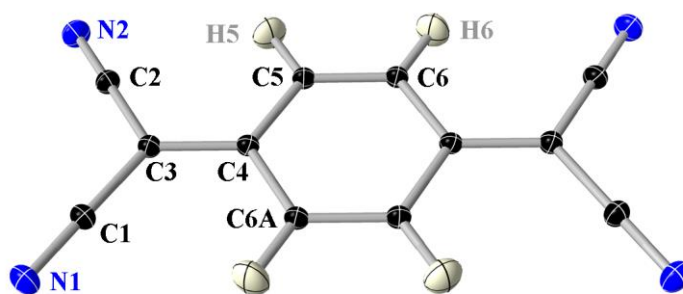
Figure 41: Numbering scheme of TCNQ.

The double bonds C5–C6 and C3–C4 refine to bond lengths of similar values (1.35706(18) Å and 1.38214(18) Å, respectively). The single bonds C5–C4 and C3–C2 refine to lengths of 1.44590(17) Å and 1.42721(18) Å, respectively. All these values are in good agreement with the values derived by *Espinosa et al.* although they were looking at TCNQ embedded into a charge transfer complex and thus at the reduced molecule (Table 18). There is another publication by *Cole et al.* which presents the charge density investigation of a nonlinear optical precursor {4-[bis(diethylamino)-methylium]phenyl}dicyanomethanide (DED-TCNQ) which is a derivate of TCNQ.[136] The presented study is based on data collected at 20 K. Since the TCNQ derivative is not involved in any charge transfer complex or any complex at all this crystal structure should reveal an even closer resemblance to the study presented within this thesis. Despite this, the carbon-nitrogen bonds are significantly longer in DED-TCNQ which is traced back to the chemically different environment. The alterations made on the parent molecule TCNQ break up the conjugated double bonds and thus result in different bond lengths.

Table 18: Selected bond lengths and angles.

|        | BTDMTTF TCNQ | DED-TCNQ    | TCNQ 100 K   | TCNQ 15 K    |
|--------|--------------|-------------|--------------|--------------|
| N1–C1  | 1.1593(5)    | 1.1720(16)  | 1.1587(5)    | 1.15685(12)  |
| N2–C2  | 1.1593(5)    | 1.1724(24)  | 1.1594(5)    | 1.15683(11)  |
| C1–C3  | 1.4176(4)    | 1.4100(14)  | 1.42715(18)  | 1.42553(11)  |
| C2–C3  | 1.4176(4)    | 1.4072(14)  | 1.42721(18)  | 1.42541(11)  |
| C3–C4  | 1.3998(7)    | 1.4426(12)  | 1.38214(18)  | 1.38008(11)  |
| C4–C5  | 1.4363(4)    | 1.4204(13)  | 1.44590(17)  | 1.44345(11)  |
| C4–C6  | 1.4363(4)    | 1.4211(13)  | 1.44545(18)  | 1.44433(10)  |
| C5–C6  | not given    | 1.3870(12)  | 1.35706(18)  | 1.35505(11)  |

*Espinosa et al.* collected their data at 130 K and on the reduced molecule but despite this, the bond lengths are remarkably similar. The addition of electrons into a given system usually results in a change in bond lengths as they sometimes force the population of energetically disfavoured orbitals. Despite the fact that all four datasets have been collected at a different temperature and show derivatives or reduced TCNQ bodies in two cases, the bond lengths stay almost unchanged.

### 5.4.1 Properties Along the Bond Path

The topological parameters for all bonds at the bond critical point containing heavy atoms are depicted in Table 19. Where available the corresponding values reported by *Espinosa et al.* are given in *italic* and the values reported by *Cole et al.* are given in **bold** letters.

Table 19: Topological parameters at the bond critical points. *Italic* values are taken from[131]; **bold** values are taken from [136] and plain values are derived from the 100 K data.

|  | $\rho(r)$ [eÅ$^{-3}$] | $\nabla^2 \rho(r)$ [eÅ$^{-5}$] | $\varepsilon$ |
|---|---|---|---|
| N1–C1 | 3.276 | -22.156 | 0.08 |
|  | *3.58* | *-29.44* | *0.05* |
|  | **3.292** | **-25.425** | **0.06** |
| N2–C2 | 3.273 | -22.267 | 0.08 |
|  | *3.58* | *-29.44* | *0.05* |
|  | **3.442** | **-26.168** | **0.03** |
| C1–C3 | 1.887 | -15.148 | 0.06 |
|  | *1.91* | *-11.64* | *0.10* |
|  | **1.963** | **-13.616** | **0.22** |
| C2–C3 | 1.881 | -14.355 | 0.10 |
|  | *1.91* | *-11.64* | *0.10* |
|  | **2.00** | **-14.772** | 0.16 |
| C3–C4 | 2.199 | -22.379 | 0.30 |
|  | *2.01* | *-14.36* | *0.17* |
|  | **1.868** | **-13.552** | **0.17** |
| C4–C5 | 1.911 | -15.833 | 0.08 |
|  | *1.98* | *-14.60* | *0.11* |
|  | **1.990** | **-14.502** | **0.18** |
| C4–C6 | 1.915 | -15.867 | 0.05 |
|  | *1.98* | *-14.60* | *0.11* |
|  | **2.113** | **-18.355** | **0.15** |
| C5–C6 | 2.297 | -24.818 | 0.31 |
|  | *2.25* | *-19.91* | *0.23* |
|  | **2.090** | **-17.818** | **0.19** |

Overall the values are in good agreement although the ellipticity of the C3−C4 and C1−C3 bond differs significantly in our study. Still the values derived from our experiment show the expected low value for a non-polar carbon-carbon single bond for the C1−C3 bond (around zero). The value derived for C3−C4 is a little lower than expected for an isolated carbon-carbon double bond (around 0.7) depicting a value higher than for an aromatic double bond, which is sensible as these bond is involved in a conjugated system and thus lies between both. Based on this table it is fair to

assume the alternating double and single bonds to be present within the TCNQ molecule in the ground state since the ellipticities as well as the bond lengths support this.

If the ellipticity is plotted along the bond path it becomes obvious that the two supposed double bonds display the highest ellipticities by far (Figure 42). The carbon-carbon double bond inside the six membered ring in the centre of the molecule follows the course of a classic carbon-carbon double bond (C5–C6). The double bond going out to the *ipso*-carbon (C4–C3) displays slightly higher ellipticities towards the *ipso*-carbon but fits the course of a double bond as well. The course of the Laplacian along the bond path nicely displays rather covalent bonds between the carbon atoms and a strongly polarized bond for the nitrogen carbon bond.
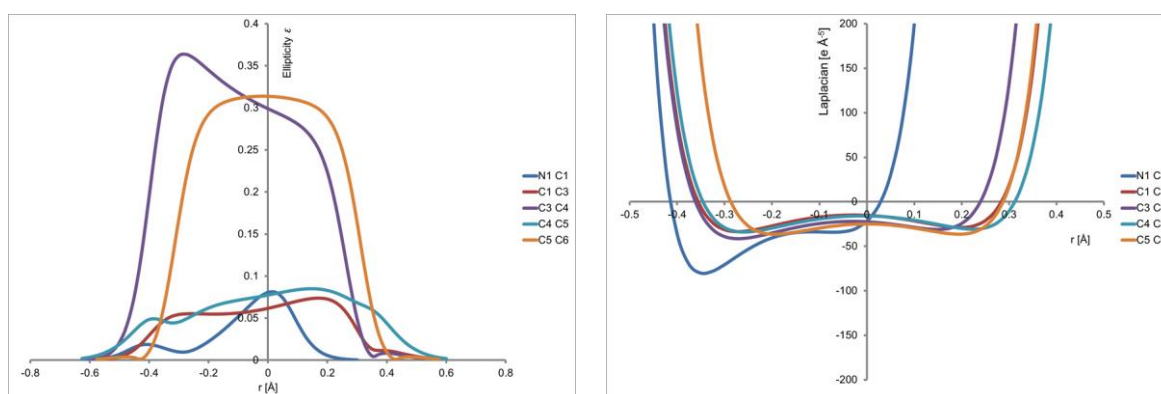


Figure 42: The ellipticities and Laplacian plotted against the bond path for all bonds derived from the 100 K in-house data.

For the other three datasets it becomes obvious that the data quality problems reveal themselves again in the course of the ellipticy along the bond path for single carbon-carbon bonds (Figure 43). This was also visible for the paracyclophane data. The synchrotron data reveal a significantly different course for C1−C3. The differences in course are even more pronounced for the bond between C4 and C5 where the synchrotron data collected with 31.5 keV radiation show a completely different course compared to all other datasets.
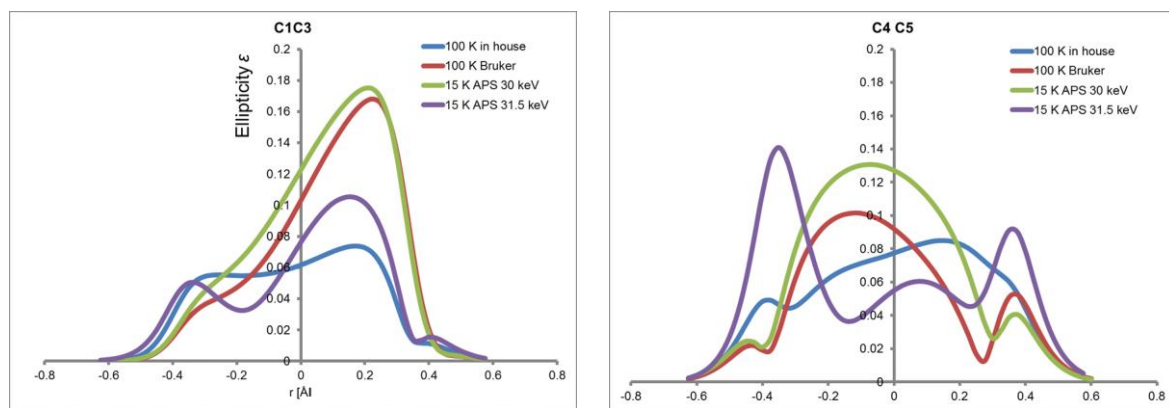
Figure 43: Ellipticity along the bond path for all four datasets for C1−C3 and C4−C5.

Although the differences may seem small if displayed graphically over the whole bond path the values at the bond critical point differ significantly especially for the 100 K Bruker and the 30 keV data (Figure 43). The gross deviations are depicted for the double bond C3–C4 and the two single bonds C1–C3 and C4–C5. Again, it is the ellipticity that reveals the problems with data quality.

Table 20: Properties at the bond critical points for all four datasets.

| Bond: | Property | 100K in-house | 100K Bruker | 15K 30keV | 15K 31.5keV |
|---|---|---|---|---|---|
| N1-C1 | $\rho(\mathbf{r})$ [eÅ$^{-3}$] | 3.276 | 3.370 | 3.362 | 3.466 |
| | $\nabla^2(\mathbf{r})$ [eÅ$^{-5}$] | -22.156 | -25.822 | -30.946 | -35.628 |
| | $\varepsilon$ | 0.08 | 0.06 | 0.01 | 0.10 |
| C1-C3 | $\rho(\mathbf{r})$ [eÅ$^{-3}$] | 1.887 | 1.947 | 1.929 | 1.932 |
| | $\nabla^2(\mathbf{r})$ [eÅ$^{-5}$] | -15.148 | -15.268 | -16.155 | -13.800 |
| | $\varepsilon$ | 0.06 | 0.10 | 0.12 | 0.08 |
| C3-C4 | $\rho(\mathbf{r})$ [eÅ$^{-3}$] | 2.199 | 2.160 | 2.154 | 2.233 |
| | $\nabla^2(\mathbf{r})$ [eÅ$^{-5}$] | -22.379 | -19.169 | -19.104 | -18.924 |
| | $\varepsilon$ | 0.30 | 0.09 | 0.19 | 0.22 |
| C4-C5 | $\rho(\mathbf{r})$ [eÅ$^{-3}$] | 1.911 | 1.952 | 1.960 | 1.932 |
| | $\nabla^2(\mathbf{r})$ [eÅ$^{-5}$] | -15.833 | -16.196 | -17.256 | -14.350 |
| | $\varepsilon$ | 0.08 | 0.09 | 0.13 | 0.06 |
| C5-C6 | $\rho(\mathbf{r})$ [eÅ$^{-3}$] | 2.297 | 2.264 | 2.281 | 2.388 |
| | $\nabla^2(\mathbf{r})$ [eÅ$^{-5}$] | -24.818 | -21.888 | -23.090 | -22.729 |
| | $\varepsilon$ | 0.31 | 0.26 | 0.24 | 0.21 |

### 5.4.2 Deformation Density and Laplacian Distribution

The static deformation density and the Laplacian distribution show nicely modelled bonds for the TCNQ molecule.
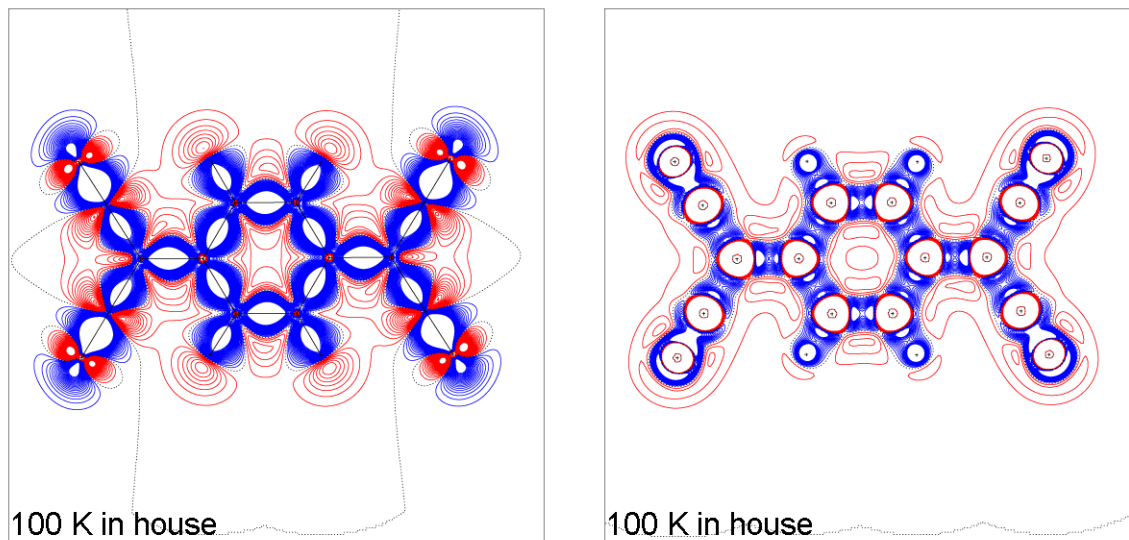


Figure 44: Left: Deformation density and right: Laplacian distribution in the plane of the TCNQ molecule. Contour lines are drawn at $\pm 0.02, \pm 0.04, \pm 0.06,...$e$\text{Å}^{-3}$ interval levels for the deformation density and $\pm 2, \pm 4, \pm 6,...$ e$\text{Å}^{-5}$ interval levels for the Laplacian distribution. Blue: positive; red: negative.

The highly polarized triple bond between C1 and N1 is nicely depicted in the deformation density as well as the lone pair at the nitrogen atom. The proposed single bonds between C3 and C1 and C4 and C5 are a little more cylindrical in shape as would be expected in comparison to the double bonds between C3 and C4 and C5 and C6. The plots for the remaining three datasets look the same.

### 5.4.3 Net and Bader Charges

In MM it is also possible to derive the charge of the atoms inside the molecule. Since the molecule as a whole is constrained to remain neutral the derived charges can be traced back to charge transfer between the atoms in the molecule and thus give valuable information about the nature of a bond. For the given compound there are the highly polarized triple bonds between C1 and N1 (C2 and N2 as well) and the rather covalent double bonds between C5 and C6 and C3 and C4.

Table 21: Net and integrated Bader charges for TCNQ. *Italic* values are taken from [131], **bold** values are taken from [136] and regular values are derived from the 100 K dataset.

| | Net Charge | Bader Charge |
|---|---|---|
| N1/N2 | -0.057(23) | -0.959/-0.958 |
| | *-0.139(19)* | |
| | **-0.17(12)** | |
| C1/C2 | +0.005(29) | +0.824/+0.833 |
| | *-0.075(23)* | |
| | **-0.13(13)** | |
| C3 | -0.149(40) | -0.023 |
| | *-0.074(30)* | |
| | **-0.09(9)** | |
| C4 | +0.169(39) | +0.108 |
| | *+0.088(31)* | |
| | **0.07(7)** | |
| C5/C6 | -0.131(21) | -0.161/-0.171 |
| | *-0.045(19)* | |
| | **0.00(7)** | |

All values derived from our data are in good agreement with the published charges. Only the Net charge for C1/C2 is slightly positive but also has a large standard deviation and is thus not very reliable. The integrated Bader charges for the nitrogen atoms both depict a negative charge with in good agreement with chemical intuition. The neighbouring atoms C1 and C2 both depict positive integrated Bader charges, which is the logical consequence to a negatively charged nitrogen atom. The slightly positive charge at C4 also follows chemical intuition given its bonding situation.

Based on the results obtained with the paracyclophane data the Net and Bader charges are also sensitive to data quality. Thus, the charges obtained from all four datasets are summarized and compared in Table 22. Since TCNQ does not undergo a phase transition or a change in geometry over the given temperature range there is no reason for a significant change in pole populations. This makes all values comparable between the individual datasets and can give information about the data and derived model reliability.

Table 22: Net and Bader Charges from all four TCNQ datasets.

|  | 100 K in-house | 100 K Bruker | 15 K APS 30 keV | 15 K APS 31.5 keV |
|---|---|---|---|---|
| **N1/N2** | | | | |
| Net Charge | -0.057(23) | -0.106(20) | +0.015(12) | -0.071(16) |
| Bader Charge | -0.959/-0.958 | -0.910/-0.910 | -0.875/-0.876 | -0.798/-0.799 |
| **C1/C2** | | | | |
| Net Charge | +0.005(29) | +0.032(26) | -0.081(17) | -0.005(21) |
| Bader Charge | +0.824/+0.833 | +0.760/+0.757 | +0.745/+0.748 | +0.669/+0.663 |
| **C3** | | | | |
| Net Charge | -0.149(40) | -0.137(38) | -0.041(25) | -0.012(30) |
| Bader Charge | -0.023 | +0.018 | +0.074 | +0.106 |
| **C4** | | | | |
| Net Charge | +0.169(39) | +0.189(38) | +0.105(25) | +0.092(31) |
| Bader Charge | +0.108 | +0.010 | +0.030 | +0.030 |
| **C5/C6** | | | | |
| Net Charge | -0.131(21) | -0.101(20) | -0.109(10) | -0.091(17) |
| Bader Charge | -0.161/-0.171 | -0.132/-0.143 | -0.131/-0.131 | -0.154/-0.157 |

Interestingly the Net charges do not vary as much for the four different datasets as the Bader charges. Only the 30 keV data from the APS show a slightly positive value for the nitrogen atoms. Considering the large standard deviation given for all charges this is still not significant. Since the Net charges are simply based on the monopole population these do also not differ more than 3σ. This is also true for most of the multipoles. Only the synchrotron data have a larger number of populations that deviate more than 3σ from the 100 K in-house data (chapter 10.2.7). Furthermore, the 100 K in-house data depict values for the multipole populations which are in good agreement with the values derived from the Invariom database.[145-147] The Bader charges do not differ much as well, apart from the charge on C3 which is positive for all but the in-house data. Since all charges are rather small in absolute values this might also be due to the shape of the atomic basin being different for the different datasets. Only the 31.5 keV data do give rise to a significantly different charge of +0.106 compared to -0.023 for the in-house data. This is in good agreement with the other indicators, which depict this dataset to be of lowest quality.

# 6    FRONTIERS OF EXPERIMENTAL CHARGE DENSITY STUDIES

At the beginning of this thesis a high resolution charge density dataset of a gold complex of sulphur oxidized phosphanylanthracene (Figure 45) was recorded at liquid helium temperature with the help of *Leusser, Hey*, and *Kratzert*.
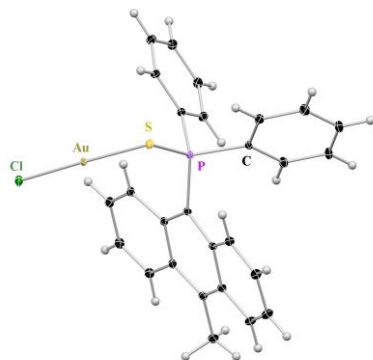


Figure 45: Gold complex of sulphur oxidized phosphanylanthracene.

The compound was synthesized in our work group by *N. Finkelmeier* who investigated the fluorescence properties of anthracene derivatives and their metal complexes in his PhD thesis. During his work *N. Finkelmeier* was able to detect a significant shift in the emission spectra if the parent compound phosphanylanthracene was oxidized. It was also unclear if the additional complexation of a metal to the sulphur would change the electronic structure of the athracene body to explain the shift in emission energies. We therefore decided to perform an experimental charge density analysis of several anthracene compounds in order to establish possible differences that could explain the shift. The gold complex is by far the most ambitious molecule to study because it not only involves three atoms which are already considered heavy atoms in charge density studies (P, S, and Cl) but also the transition metal gold. This metal would have been considered impossible to deal with in a charge density investigation only a few years ago. These very heavy elements only came within reach of a charge density investigation with the ability to collect highly redundant datasets in very little time with the introduction of CCD area detectors and with greater computational power to calculate accurate scattering factors.[148] One strategy to deal with very heavy elements in a charge density investigation is to divide the core electron density into more than one shell.[149] This procedure requires an additional set of monopole and kappa parameters to correctly describe the so called core polarisation. It is necessary to take the polarisation into account because for transition metals even the core electrons are subject to deformations caused by bonding effects. This has been shown for uranium but also for light atomic structures.[148-150] In order to properly describe the core polarisation excellent resolution is necessary the more so if light atoms like

102

silicon or carbon are studied.[149-150] For most of the cited studies the advantages of highly intense synchrotron radiation were used, among these reduced absorption and extinction effects. Still, there are not many examples of charge density studies involving heavy elements because the data acquisition is still very challenging and prone to errors.[9-10,108]

## 6.1 Data Acquisition and IAM

The gold complex crystallizes in the orthorhombic space group $Pbca$ and contains one molecule and one solvent molecule (acetone) in the asymmetric unit. The data were collected on a Bruker D8 diffractometer equipped with a molybdenum rotating anode and an APEXII CCD detector. The temperature was controlled by the use of an open stream *Oxford Helijet* and kept fixed at 15 K for the experiment. The frames were collected at three different $2\theta$ settings and 180° ω scans. Different exposure times were used for the different settings in order to guarantee optimal signal to noise ratios throughout the whole resolution range. The data were reduced with the program *SAINT 8.30C* in a straight forward procedure keeping to the standard settings of the program. Different integration routines were tried, for instance integration with a fixed box size and the individual integration of the different two theta settings, but gave no improvement in data quality. The data were integrated up to a maximum resolution of d = 0.45 Å based on the statistics given in *XPREP*. The resolution was chosen to give high multiplicity, I/σ(I) values and completeness. For a routine charge density refinement this is the minimum resolution required but for the treatment of heavy elements this is challenging at least. The raw intensities were scaled and corrected for absorption using *SADABS 2014/2* treating the crystal as a heavy absorber. From the diagnostic plots generated by *SADABS* the almost typical course of the $R_{int}$ became visible with two mountain-like spikes around 0.74 Å and 0.55 Å (Figure 46). With values starting at roughly 2 % but rising to above 12 % for the maximum resolution shells the $R_{int}$ values are higher than usual for a charge density refinement.
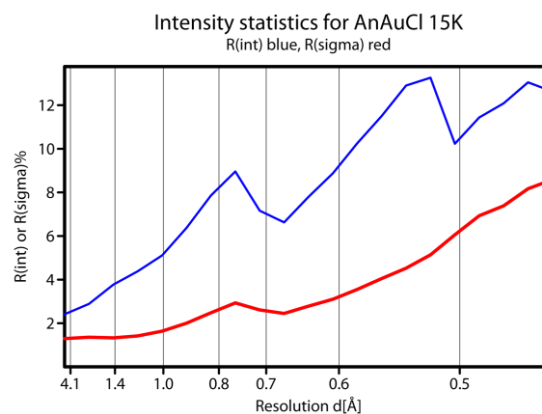


Figure 1: $R_{int}$ and $R_{sigma}$ plotted against the resolution.

103
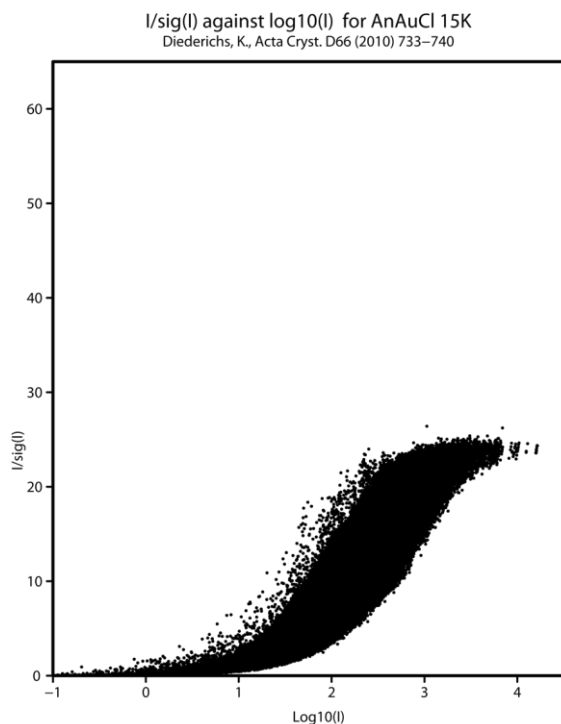
Figure 2: *Diederichs* plot for the gold complex.

Furthermore, the diagnostic *Diederichs* plot which is also generated by *SADABS* shows an $I/\sigma(I)$ limit of only 25 (Figure 47).

This is a value usually reached for synchrotron data and indicates serious data problems for in-house data. In comparison to the in-house datasets recorded for the lighter atom structure paracyclophane (>70) this value is considerably lower and is already a warning sign towards the quality of the data.

The statistics generated by *XPREP* show excellent multiplicity and completeness up to the highest resolution shell but also show the spikes in the *R* values (Appendix). Structure solution was straight forward and done with *SHELXT*[139] indicating no problems with the space group assignment.

Table 23: Experimental details after IAM refinement.

| Structure code | AnAuCl | Z | 8 |
|---|---|---|---|
| Empirical formula | $C_{27} H_{21}$ Au Cl P S, $C_3 H_6$ O | $\rho_{calcd.}$ [g cm$^{-3}$] | 1.742 |
| Formula weight [g mol$^{-1}$] | 698.96 | $\mu$ [mm$^{-1}$] | 5.782 |
| Sample temperature [K] | 15(2) | F(000) | 2736 |
| Wavelength [Å] | 0.71073 | $\theta$ range [°] | 1.793 to 52.398 |
| Crystal system | Orthorhombic | Reflections collected / independent | 301485 / 30705 |
| Space group | $P$bca | Max. resolution [Å$^{-1}$] | 1.11 |
| Unit cell dimensions [Å] | a=15.856(8) | Completeness ($\theta$=25.242°) | 100 % |
| | b=14.799(7) | Goof | 1.002 |
| | c=22.7100(10) | weighting scheme a/b | 0.0283 / 2.4753 |
| | α=β=γ = 90 | $R$ indices [I>2σ(I)] | $R1$=2.80 %, $wR2$=5.69 % |
| Volume [Å$^3$] | 5329(4) | $R$ indices (all data) | $R1$=4.68 %, $wR2$=6.27 % |
| crystal size [mm] | 0.07 x 0.07 x 0.05 | max. diff. peak/hole [e Å$^{-3}$] | 5.953 / -4.031 |

The structure was refined using *SHELXL* implemented in the *ShelXle GUI* against $F^2$ in a full matrix least squares refinement and readily converged. It became obvious that the crystal was heavily absorbing emerging through high residual density concentrated around the gold atom (Table 23). The hydrogen atoms were treated as described in more detail in chapter 4.4.2 and set to neutron distances using the HIMP command in XP.

## 6.2    Multipole Refinement with XD2006

The starting model for *XD2006* was generated with *XDINI* and standard refinement strategy was carried out as given in 0. To guarantee convergence the first refinement steps were carried out forcing the pole populations to be equal for chemically equivalent atoms. This constraint was loosened in the course of the refinement. Additionally, local symmetry was taken into account in the first refinement steps and was also abandoned in the final steps of the refinement. This was possible since all atoms lie on general positions.

All non-hydrogen atom multipole parameters have been refined to $l = 4$, the hydrogen atom parameters have been refined to $l = 2$. The kappa parameters for the hydrogen atoms have been set to optimum values ($\kappa = 1.10$; $\kappa' = 1.18$) and have been kept fixed during the refinement.[114] The hydrogen atom displacement parameters were constrained to the displacement parameters of their pivot atoms (1.5 eq for terminal carbon atoms and 1.2 eq for all others). For the final refinement steps anisotropic displacement parameters have been used for the hydrogen atoms, derived by the *SHADE* server. The weighting scheme has been adapted using the *DRKplot* tool to give a normal distribution (Figure 48).
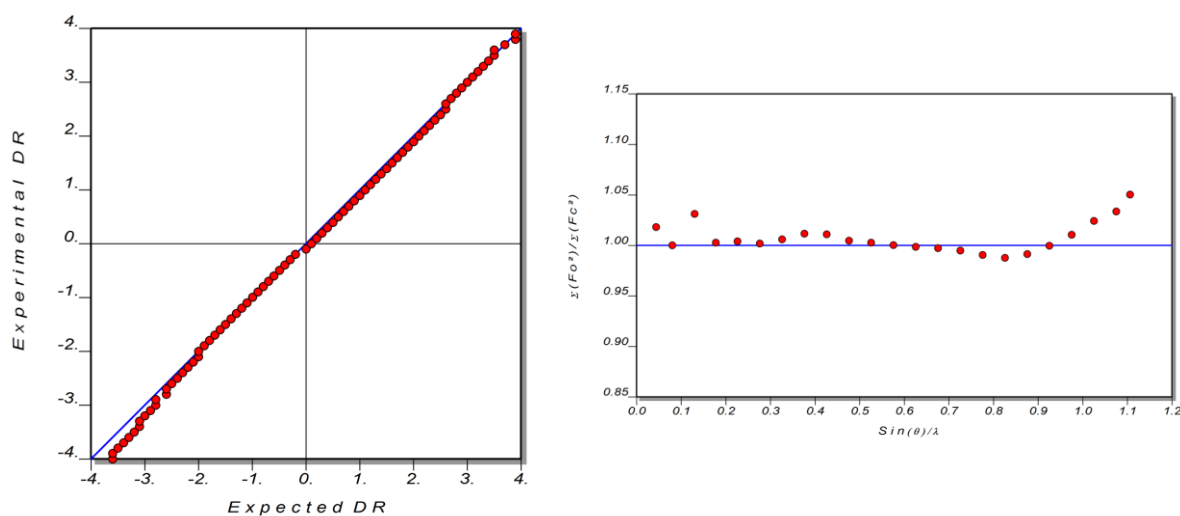


Figure 48: Normal probability plot (left) and the ratio of $F_o^2/F_c^2$ against the resolution.

Although the refinement readily converged and the plots generated by the *DRKplot* tool do not show gross mismatches for the calculated and experimental intensities (Figure 48), the residual density is enormous (Figure 49). Analysis of the residual density according to *Meindl* and *Henn* clearly shows that the charge density refinement fails (Figure 49).[37] Most of the residual density is located around the gold atom much like in the IAM. This residual density is most likely caused by high absorbance and cannot be accounted for by a refinement.

106
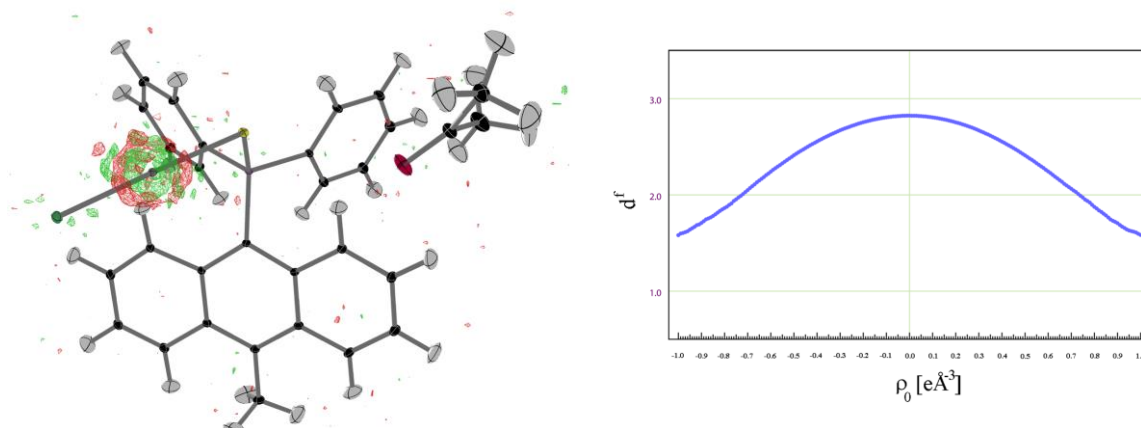
Figure 49: Residual density after the MM (left), level depicted at ±0.8 eÅ⁻³; Fractal dimension of the residual density according to *Meindl* and *Henn* (right).

To accurately describe the electron density of this molecule kappa and kappa' values derived from theory could be advantageous. Additionally, a shorter wavelength and a smaller crystal would also be necessary for a successful refinement. *Schmøkel et al.* have proven very elegantly that the choice of crystal and beam is crucial when dealing with heavy elements.[9-10] Considering all these criteria it seems little surprising that the conventional charge density refinement fails. For future projects dealing with heavy elements and thus potential core polarisation theoretical calculations and different wavelengths seem to be essential.

# 7 SUMMARY AND OUTLOOK

This thesis is based on the detailed charge density analysis of two small molecules (paracyclophane and TCNQ), which have been of great interest to both theoretical and experimental chemists for over 50 years. In order to perform a high quality charge density investigation on both compounds the quality of the data has been analysed extensively. This was done on several different datasets for both compounds collected on different crystals, at different temperatures and different radiation sources.

The first molecule which was studied (chapter 4) is the hydrocarbon paracyclophane. This compound has been used as a standard for theoretical calculations over the last 40 years, despite the fact that there were still ongoing discussions about a possible phase transition at low temperatures.[69,81,83-84,89-90,93,104,151-153] It could be unambiguously proven by low-temperature X-ray crystallography that paracyclophane crystallizes in the non-centro symmetric space group $P\bar{4}$n2 below 45 K and has thus a twist angle of the bridging ethylene bridges of 12.83(4)°.[117] It could also be proven that the phase transition at 45 K is driven by this twisting motion (chapter 4.3.3). Above 60 K the system can no longer stabilize the twisting effect but shows a dynamic disorder of the ethylene bridge. This was proved by means of simultaneous *Raman* spectroscopy and inelastic neutron scattering over a temperature range from 12 K to 300 K. The crystal structure of paracyclophane above 60 K is refined in the centro symmetric space group $P4_2/mnm$, which does not depict a twist angle. Since the crystal structure is a measure over time and space the disorder cannot be resolved by this and averages out to give a non-twisted structure with elongated ADPs perpendicular to the bond.

The second molecule studied (chapter 5) is tetracynaoquiodimethane (TCNQ), which is famous for its reduction to radical anions TCNQ$^-$ and (TCNQ)$_2{}^-$.[127,131,136-137,154-157] Since this molecule is also used as a standard reference because of its simplicity in theoretical calculations a charge density investigation of the ground state was in demand. The charge density investigation supports the idea of alternating double and single bonds in the molecule which are the reason for its great stability. The study presented in this thesis also show excellent agreement with parameters derived from charge density studies of reduced or modified TCNQ. According to this, the molecule absorbs the additional electrons into is system without changing the conjugated double bonds.

On the way to the charge density investigations on these two molecules it became obvious that collecting datasets of a high enough quality was not trivial for these two compounds. Although they are suited well for a charge density study the course of atomic scattering factors make it hard to detect both inner and outer resolution shells with the same accuracy. It could be shown that the $R_{int}$ of the innermost resolution shells (inf. to 1.1 Å) should not exceed 5 % in the raw data for a charge density refinement. Based on the results from this thesis this value is more important for the reliability of the charge density investigation than the overall $R_{int}$, which is usually given in publications. The derived parameters such as ellipticity and charges are very sensitive to data quality and meaningless if the data are bad. Based on the results from this thesis the careful evaluation of all quality indicators over the course of the charge density investigation should be followed and made compulsory for publication. Among the indicators that should be added routinely to a charge density investigation are:

a) Statistics plots generated by *SADABS* or *SORTAV*
b) *XPREP* statistics for the whole resolution range
c) Statistics plots generated by *DRKplot*
d) XD2006 refinement strategies
e) 3D representations of the residual density derived from all data
f) Fractal dimension plots according to *Henn* and *Meindl* for all data
g) Ellipticity and Laplacian along the bond path

The use of high brilliance synchrotron radiation is of limited use if the dynamic range of the detector is not suited to deal with very bright and weak Bragg maxima simultaneously.[10,15] For the datasets collected at the 15-ID-B beam-line at the APS it could be shown that the simple modification of in-house detectors does not provide data of enough accuracy for a charge density investigation due to limitations in discrimination. The challenges of data collection on both in-house sources and synchrotron radiation should be further evaluated, especially for detection capacities. The use of fast scans to avoid overloads on the detector for the inner data should be addressed in further studies.

Not only the dynamic range is of outermost importance for a good detector but also the way radiation is converted into a signal. Over the last twenty years the charge density community has made use of the advantages of area CCD detectors over the old point detectors in terms of higher multiplicity and larger detection space. Due to the limitation in dynamic range the CCD detectors have been given a rival in pixel detectors and hybrid pixel area detectors.[14,158] Together with the image plate these detectors seem superior over the CCD detectors because they do have almost no limitation in the dynamic range and low background noise. Additionally, they have a very fast readout time. Although most of these pixel detectors were optimized to deal with synchrotron radiation there are developments to mount them on in-house

diffractometers, hence making them available for routine experiments.[158] Despite these developments in detection power charge density optimized in-house diffractometers equipped with a CCD detector are still able to produce excellent data if handled correctly. It cannot be stressed enough that time should never be the limiting factor in a charge density data collection. If the crystal under investigation is stable for an unlimited timespan in the X-ray beam and does not suffer from icing or temperature change it is still possible to collect perfect data on an in-house machine. Until the integration routine and data reduction of the newly developed detectors have not proven to be of similar accuracy and precision like *SAINT* they cannot become the systems of choice.

As a final remark it shall be noted that for the compounds studied in this thesis problems with data quality did not reveal themselves for most of the derived parameters. This is due to the simplicity of the bonding situation in both compounds. Unfortunately, most of the standards used in crystallography to check on crystal and data quality are of similar simplicity. They can no longer be regarded as the optimal choice but should be replaced by molecules that involve ionic bonds and heavier elements like sulphur and phosphorous.

It would be a key to better data and improved experimental set-up to change the approach from experimental data with a fixed model to high-level theoretical calculations with a flexible model. In such a procedure the theoretically derived data would be altered by introduction of different errors such as low resolution, missing or wrong intensities, high background noise, and anharmonic motion. It would be possible to monitor the influence of these errors on the results of the QTAIM analysis. This would link data quality issues to results from a QTAIM analysis unequivocally. It opens the opportunity to avoid the misinterpretation of derived values and thus incorrectly determined properties. The probability to link certain errors directly to miscalculated properties like the ellipticity or the charge of an atom is a powerful tool to control high quality charge density investigation. A similar approach has already been established by *Henn* for the residual density and has found its way into modern charge density analysis.[37,159-160] Henn was able to depict the influence of certain flaws of either model or data on the residual density. Extending this feature to the QTAIM analysis according to Bader would enhance the trust in results obtained from experimental data.

# 8 CRYSTAL STRUCTURE DETERMINATION IN COLLABORATIONS

## 8.1 Crystal Selection and Manipulation

Crystals suitable for single crystal X-ray diffraction were selected under inert conditions and if necessary at low temperatures using the X-temp device[86-87]. In order to extract the crystals from their mother liquor *Schlenk*-technique was used so the crystals could be extracted under an argon atmosphere. The crystals were placed on a glass object slide in drops of per fluorinated polyether oil. Selection of suitable crystals was carried out with the help of a polarisation filter incorporated into a microscope. The crystals were mounted on MiTeGens Kryoloops or glass fibre and quickly placed into the nitrogen cold stream of the diffractometer.

## 8.2 Data Acquisition

Diffraction data were collected on three different diffractometers with different radiation and or beam size and energies in order to collect the best data possible. All machines are Bruker D8 three circle diffractometers equipped with focusing mirror optics and CCD detectors. The radiation source is either a rotating Mo-Anode or an Incoatec IµS with either Mo or Ag radiation.

The data acquisition strategy was planned with the APEXII[11] plugin *COSMO* or *QUEEN*. If not specified otherwise the frame width was 0.5°.

## 8.3 Data Processing

The diffraction raw data were integrated with *SAINT* 7.68A and 8.30C [16,161]and data reduction and scaling was done using *SADABS*.[7-8] The space group was chosen according to the systematic absences with the program *XPREP*[22] and structure solution was done using direct methods in *SHELXS*[4] or *SHELXT*[139]. The structure refinement was done by full-matrix least-squares methods on $F^2$ using *SHELXL*[109] inside the *GUI ShelxLe*[110] against all data. If not stated otherwise the hydrogen atoms have been refined using a riding model which fixes the isotropic displacement parameters to 1.5 $U_{eq}$ of their pivot atom for terminal sp$^3$ carbon atoms and 1.2 times for all other carbon atoms. All non-hydrogen atoms have been refined anisotropically. Disorder was treated using restraints and if necessary constraints and by refining the site occupation factor with a free variable.

If not stated otherwise the atomic displacement parameters have been displayed at the 50 % probability level. Most hydrogen atoms are omitted for clarity.

# 9 SINGLE CRYSTAL STRUCTURES DETERMINED IN COLLABORATION WITH SERVICE PARTNERS

## 9.1 Collaboration with Dr. Ramachandran Azhakar (Prof. Roesky)
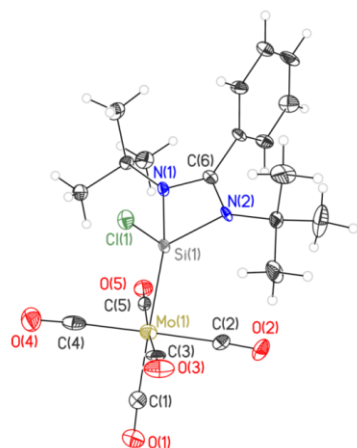


| Structure code | HW_Az_LSiCl_MoCO | Z | 4 |
|---|---|---|---|
| Empirical formula | $C_{20} H_{23} Cl Mo N_2 O_5 Si$ | $\rho_{calc}$ [g cm$^{-3}$] | 1.468 |
| Formula Weight [g mol$^{-1}$] | 530.88 | $\mu$ [mm$^{-1}$] | 2.044 |
| Temperature [K] | 100 | F(000) | 1080 |
| Wavelength [Å] | 0.5608 | Crystal Size [mm] | 0.20 x 0.20 x 0.15 |
| Crystal System | Orthorhombic | $\theta$ range [°] | 1.74 to 20.09° |
| Space Group | $P2_12_12_1$ | Reflections Collected | 17349 |
| Unit cell dimensions [Å] | | Unique reflections | 4609 |
| | a = 9.791 (2) | Completeness to $\theta_{max}$: | 99.8 % |
| | b = 13.307 (2) | Data/Restrains/Parameters | 4609 / 0 / 278 |
| | c = 18.432 (2) | $R_{int}$ | 0.1123/ |
| | $\alpha$ = 90 ° | $R1$ [I>2$\sigma$(I)] | 0.0472 |
| | $\beta$ = 90 ° | $wR2$ (all data) | 0.1208 |
| | $\gamma$ = 90 ° | GooF | 1.042 |
| Volume [Å$^3$] | 2401.5 (7) | Largest Diff. peak and hole [e Å$^{-3}$] | 1.001 and -1.021 |

The crystal consisted of two domains of which only one was used for scaling and absorption correction. The structure was refined against HKLF 4 data. Only the reflections of the stronger domain were used for refinement.

The structure is published in: Ramachandran Azhakar, Rajendra S. Ghadwal, Herbert W. Roesky, Hilke Wolf and Dietmar Stalke „Stabilization of Low Valent silicon Fluorides in the Coordination Sphere of Transition Metals" *JACS*, **2011**, *134*, 2423 – 2428.

Structural Information is also deposited in the CSD under: **851189.**
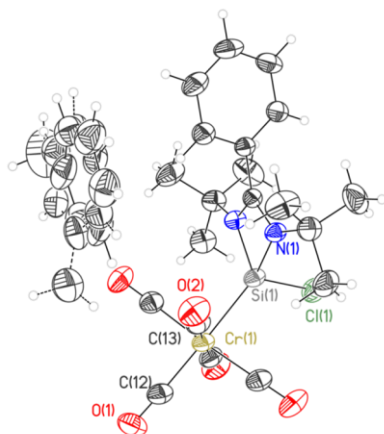
| Structure code | HW_Az_LSiCl_CrCO | Z | 2 |
|---|---|---|---|
| Empirical formula | $C_{27} H_{31} Cl Cr N_2 O_5 Si$ | $\rho_{calc}$ [g cm$^{-3}$] | 1.300 |
| Formula Weight [g mol$^{-1}$] | 579.08 | $\mu$ [mm$^{-1}$] | 0.292 |
| Temperature [K] | 100 | F(000) | 604 |
| Wavelength [Å] | 0.56086 | Crystal Size [mm] | 0.30 x 0.21 x 0.13 |
| Crystal System | Monoclinic | $\theta$ range [°] | 1.40 to 20.28° |
| Space Group | $P2_1$/m | Reflections Collected | 13702 |
| Unit cell dimensions [Å] | | Unique reflections | 3068 |
| | a = 9.896(3) | Completeness to $\theta_{max}$: | 99.6 % |
| | b = 13.060(5) | Data/Restrains/Parameters | 3068 / 363/ 284 |
| | c = 11.577(4) | $R_{int}$ | 0.0229 |
| | $\alpha$ =90 ° | $R1$ [I>2$\sigma$(I)] | 0.0313 |
| | $\beta$ = 98.60(2) ° | $wR2$ (all data) | 0.0917 |
| | $\gamma$ = 90 ° | GooF | 1.062 |
| Volume [Å$^3$] | 1479.4(9) | Largest Diff. peak and hole [e Å$^{-3}$] | 0.307 and -0.443 |

The Toluene moiety is disordered over two positions while sitting on a mirror plane. The positional parameters have been refined using a free variable for the site occupation factor. 1,2 and 1,3 distance similarity restraints had to be employed as well as thermal parameter restraints to stabilize the refinement of the solvent molecule.

The structure is published in: Ramachandran Azhakar, Rajendra S. Ghadwal, Herbert W. Roesky, Hilke Wolf and Dietmar Stalke „Stabilization of Low Valent silicon Fluorides in the Coordination Sphere of Transition Metals" *JACS*, **2011**, *134*, 2423 – 2428.

Structural Information is also deposited in the CSD under: **851187.**
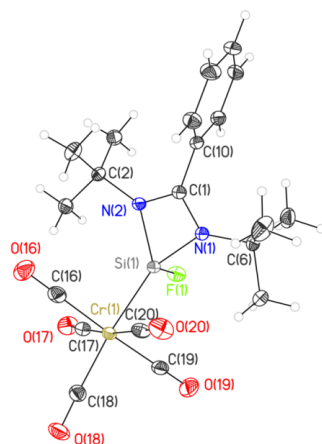
| Structure code | HW_Az_LSiF_CrCO | Z | 4 |
|---|---|---|---|
| Empirical formula | $C_{20} H_{23} Cr F N_2 O_5 Si$ | $\rho_{calc}$ [g cm$^{-3}$] | 1.403 |
| Formula Weight [g mol$^{-1}$] | 470.49 | μ [mm$^{-1}$] | 0.322 |
| Temperature [K] | 100 | F(000) | 976 |
| Wavelength [Å] | 0.56086 | Crystal Size [mm] | 0.20 x 0.15 x 0.12 |
| Crystal System | Monoclinic | θ range [°] | 1.63 to 21.35° |
| Space Group | $P2_1/n$ | Reflections Collected | 36069 |
| Unit cell dimensions [Å] | | Unique reflections | 5057 |
| | a = 10.538(2) | Completeness to θ$_{max}$: | 99.1 % |
| | b = 18.0290(10) | Data/Restrains/Parameters | 5057 / 0 / 277 |
| | c = 12.411(3) | $R_{int}$ | 0.0285 |
| | α = 90 ° | $R1$ [I>2σ(I)] | 0.0253 |
| | β = 109.130 (2) ° | $wR2$ (all data) | 0.0684 |
| | γ = 90 ° | GooF | 1.039 |
| Volume [Å$^3$] | 2227.7(7) | Largest Diff. peak and hole [e Å$^{-3}$] | 0.352 and -0.370 |

The structure is published in: Ramachandran Azhakar, Rajendra S. Ghadwal, Herbert W. Roesky, Hilke Wolf and Dietmar Stalke „Stabilization of Low Valent silicon Fluorides in the Coordination Sphere of Transition Metals" *JACS*, **2011**, *134*, 2423 – 2428.

Structural Information is also deposited in the CSD under: **851188.**
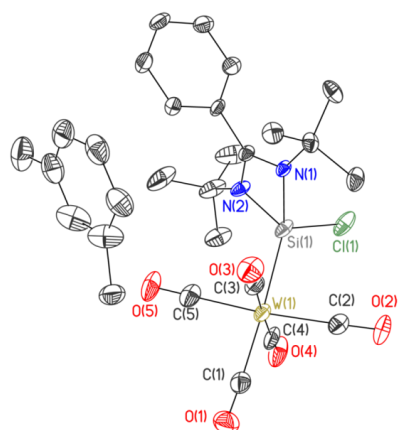
| Structure code | HW_Az_LSiCL_WCO | Z | 2 |
|---|---|---|---|
| Empirical formula | $C_{27} H_{31} Cl N_2 O_5 Si W$ | $\rho_{calc}$ [g cm$^{-3}$] | 1.591 |
| Formula Weight [g mol$^{-1}$] | 710.93 | $\mu$ [mm$^{-1}$] | 2.187 |
| Temperature [K] | 100(2) | F(000) | 704 |
| Wavelength [Å] | 0.56086 | Crystal Size [mm] | 0.18 x 0.16 x 0.10 |
| Crystal System | Triclinic | $\theta$ range [°] | 1.23 to 20.81 |
| Space Group | $P\bar{1}$ | Reflections Collected | 62539 |
| Unit cell dimensions [Å] | | Unique reflections | 6280 |
| | a = 9.873(2) | Completeness to $\theta_{max}$: | 99.2 % |
| | b = 11.621(2) | Data/Restrains/Parameters | 6280 / 111 / 353 |
| | c = 13.126(2) | $R_{int}$ | 0.0303 |
| | $\alpha$ = 94.91(2)°. | $R1$ [I>2$\sigma$(I)] | 0 0205 |
| | $\beta$ = 93.04(2)°. | $wR2$ (all data) | 0 0514 |
| | $\gamma$ = 97.56(2)°. | GooF | 1.087 |
| Volume [Å$^3$] | 1484.4(5) | Largest Diff. peak and hole [e Å$^{-3}$] | 1.965 and -1.182 |

The crystal was non-merohedrally twinned with two domains. The data reduction and scaling was done using TWINABS, structure solution was done using a HKLF4 file with only the reflections of the strong domain while the refinement was done using the HKLF5 file which includes the reflections of both domains. The batch scale factor refined to 0.493. The Toluene solvent molecule is disordered onto two positions and was refined using 1,2- and 1,3-distance similarity restraints as well as thermal displacement restraints.

The structure is published in: Ramachandran Azhakar, Rajendra S. Ghadwal, Herbert W. Roesky, Hilke Wolf and Dietmar Stalke „Stabilization of Low Valent silicon Fluorides in the Coordination Sphere of Transition Metals" *JACS*, **2011**, *134*, 2423 – 2428.
Structural Information is also deposited in the CSD under: **851190.**
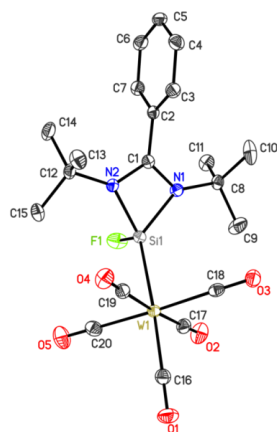
| Structure code | HW_Az_LSiF_WCO | Z | 2 |
|---|---|---|---|
| Empirical formula | $C_{20} H_{23} F N_2 O_5 Si W$ | $\rho_{calc}$ [g cm$^{-3}$] | 1.744 |
| Formula Weight [g mol$^{-1}$] | 602.34 | $\mu$ [mm$^{-1}$] | 2.765 |
| Temperature [K] | 100(2) | F(000) | 588 |
| Wavelength [Å] | 0.5608 | Crystal Size [mm] | 0.20 x 0.20 x 0.15 |
| Crystal System | Triclinic | $\theta$ range [°] | 1.32 to 20.91 |
| Space Group | $P\bar{1}$ | Reflections Collected | 68180 |
| Unit cell dimensions [Å] | | Unique reflections | 4949 |
| | a = 9.203(3) | Completeness to $\theta_{max}$: | 99.6 % |
| | b = 10.280(1) | Data/Restrains/Parameters | 4949 / 0 / 277 |
| | c = 13.187(2) | $R_{int}$ | 0.0419 |
| | $\alpha$ = 110.72(1)°. | $R1$ [I>2$\sigma$(I)] | 0.0139 |
| | $\beta$ = 99 33(2)°. | $wR2$ (all data) | 0.0352 |
| | $\gamma$ = 91.24(4)°. | GooF | 1.065 |
| Volume [Å$^3$] | 1147.2(4) | Largest Diff. peak and hole [e Å$^{-3}$] | 1.098 and -0.861 |

The structure is published in: Ramachandran Azhakar, Rajendra S. Ghadwal, Herbert W. Roesky, Hilke Wolf and Dietmar Stalke „Stabilization of Low Valent silicon Fluorides in the Coordination Sphere of Transition Metals" *JACS*, **2011**, *134*, 2423 – 2428.

Structural Information is also deposited in the CSD under: **851191.**
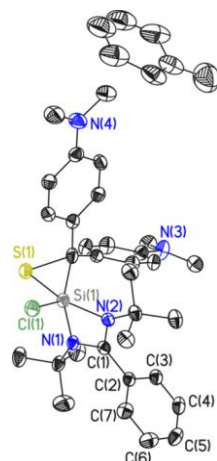
| Structure code | HW_Az_SiSC_Cl | Z | 2 |
|---|---|---|---|
| Empirical formula | $C_{35.50} H_{47} Cl N_4 S Si$ | $\rho_{calc}$ [g cm$^{-3}$] | 1.233 |
| Formula Weight [g mol$^{-1}$] | 625.37 | $\mu$ [mm$^{-1}$] | 0.242 |
| Temperature [K] | 100(2) | F(000) | 670 |
| Wavelength [Å] | 0.71073 | Crystal Size [mm] | 0.20 x 0.20 x 0.15 |
| Crystal System | Triclinic | $\theta$ range [°] | 1.51 to 23.29°. |
| Space Group | $P\bar{1}$ | Reflections Collected | 24098 |
| Unit cell dimensions [Å] | | Unique reflections | 4840 |
| | a = 11.073(5) | Completeness to $\theta_{max}$: | 99.7 % |
| | b = 12.294(6) | Data/Restrains/Parameters | 4840 / 92 / 425 |
| | c = 13.696(6) | $R_{int}$ | 0.0565 |
| | $\alpha$ = 97.980(10)°. | $R1$ [I>2$\sigma$(I)] | 0.0462 |
| | $\beta$ = 93.88(2)°. | $wR2$ (all data) | 0.1065 |
| | $\gamma$ = 112.96(9)°. | GooF | 1.024 |
| Volume [Å$^3$] | 1684.9(13) | Largest Diff. peak and hole [e Å$^{-3}$] | 0.296 and -0.299 |

The Toluene solvent molecule is disordered on an inversion center and was refined using 1,2- and 1,3-distance similarity restraints as well as thermal displacement restraints. The site occupation factor was set to 0.5.

The structure is published in: Ramachandran Azhakar, Rajendra S. Ghadwal, Herbert W. Roesky, Ricardo Mata, Hilke Wolf, Regine Herbst-Irmer and Dietmar Stalke „Reaction of N-Heterocyclic Silylenes with Thioketone: Formation of Silicon-Sulfur Three-(Si-C-S) amd Five-(Si-C-C-C-S) Membered Ring Systems" *Chem. Eur. J.* **2013**, *19*, 3715 – 3720.

Structural Information is also deposited in the CSD under: **889037**
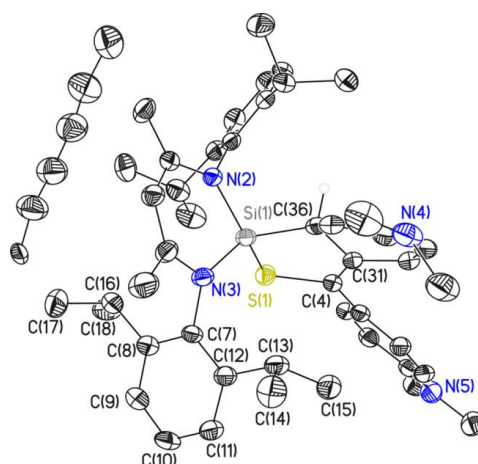
| Structure code | HW_Az_SiCCCS | Z | 4 |
|---|---|---|---|
| Empirical formula | $C_{49} H_{67} N_4 S Si$ | $\rho_{calc}$ [g cm$^{-3}$] | 1.133 |
| Formula Weight [g mol$^{-1}$] | 772.22 | $\mu$ [mm$^{-1}$] | 0.135 |
| Temperature [K] | 100(2) | F(000) | 1676 |
| Wavelength [Å] | 0.71073 | Crystal Size [mm] | 0.20 x 0.20 x 0.20 |
| Crystal System | Monoclinic | $\theta$ range [°] | 1.33 to 23.30°. |
| Space Group | $P2_1$/c | Reflections Collected | 63635 |
| Unit cell dimensions [Å] | | Unique reflections | 6532 |
| | a = 15.696(8) | Completeness to $\theta_{max}$: | 99.8 % |
| | b = 16.291(6) | Data/Restrains/Parameters | 6362 / 67 / 550 |
| | c = 18.109(9) | $R_{int}$ | 0.0509 |
| | $\alpha$ = 90° | $R1$ [I>2$\sigma$(I)] | 0.0521 |
| | $\beta$ = 102.05(2)°. | $wR2$ (all data) | 0.1410 |
| | $\gamma$ = 90°. | GooF | 1.064 |
| Volume [Å$^3$] | 4529(4) | Largest Diff. peak and hole [e Å$^{-3}$] | 0.625 and -0.358 |

The Hexane solvent molecule is disordered on a special position and was refined using 1,2- and 1,3-distance similarity restraints as well as thermal displacement restraints. The site occupation factor was set to 0.5.

The structure is published in: Ramachandran Azhakar, Rajendra S. Ghadwal, Herbert W. Roesky, Ricardo Mata, Hilke Wolf, Regine Herbst-Irmer and Dietmar Stalke „Reaction of N-Heterocyclic Silylenes with Thioketone: Formation of Silicon-Sulfur Three-(Si-C-S) amd Five-(Si-C-C-C-S) Membered Ring Systems" *Chem. Eur. J.* 2013, *19*, 3715 – 3720.

Structural Information is also deposited in the CSD under: **889038.**

| Structure code | HW_Az_SiN | Z | 4 |
|---|---|---|---|
| Empirical formula | $C_{24} H_{28} Cl F_6 N_3 Si$ | $\rho_{calc}$ [g cm$^{-3}$] | 1.399 |
| Formula Weight [g mol$^{-1}$] | 536.03 | $\mu$ [mm$^{-1}$] | 0.259 |
| Temperature [K] | 100(2) | F(000) | 1112 |
| Wavelength [Å] | 0.71073 | Crystal Size [mm] | 0.10 x 0.10 x 0.05 |
| Crystal System | Monoclinic | $\theta$ range [°] | 1.867 to 25.358°. |
| Space Group | $P2_1$/n | Reflections Collected | 18144 |
| Unit cell dimensions [Å] | | Unique reflections | 4661 |
| | a = 10.617(2) | Completeness to $\theta$ (25.242): | 100.0 % |
| | b = 16.479(3) | Data/Restrains/Parameters | 4661 / 0 / 322 |
| | c = 14.578(2) | $R_{int}$ | 0.0441 |
| | $\alpha$ = 90° | $R$1 [I>2$\sigma$(I)] | 0.0399 |
| | $\beta$ = 93.59(2)°. | $wR$2 (all data) | 0.0904 |
| | $\gamma$ = 90°. | GooF | 1.042 |
| Volume [Å$^3$] | 2545.5(8) | Largest Diff. peak and hole [e Å$^{-3}$] | 0.251 and -0.311 |

The structure is published in: Ramachandran Azhakar, Herbert W. Roesky, Hilke Wolf and Dietmar Stalke „Metal free and selective activation of one C-F bond in a bound CF$_3$ group" *Chem. Commun.* **2013**, *49*, 1841 – 1843.

Structural Information is also deposited in the CSD under: **912595.**

| Structure code | HW_Az_SiN | Z | 4 |
|---|---|---|---|
| Empirical formula | $C_{24} H_{28} Cl F_6 N_3 Si$ | $\rho_{calc}$ [g cm$^{-3}$] | 1.399 |
| Formula Weight [g mol$^{-1}$] | 536.03 | $\mu$ [mm$^{-1}$] | 0.259 |
| Temperature [K] | 100(2) | F(000) | 1112 |
| Wavelength [Å] | 0.71073 | Crystal Size [mm] | 0.10 x 0.10 x 0.05 |
| Crystal System | Monoclinic | $\theta$ range [°] | 1.867 to 25.358°. |
| Space Group | $P2_1/n$ | Reflections Collected | 18144 |
| Unit cell dimensions [Å] | | Unique reflections | 4661 |
| | a = 10.617(2) | Completeness to $\theta$ (25.242): | 100.0 % |
| | b = 16.479(3) | Data/Restrains/Parameters | 4661 / 0 / 322 |
| | c = 14.578(2) | $R_{int}$ | 0.0441 |
| | $\alpha$ = 90° | $R1$ [I>2$\sigma$(I)] | 0.0399 |
| | $\beta$ = 93.59(2)°. | $wR2$ (all data) | 0.0904 |
| | $\gamma$ = 90°. | GooF | 1.042 |
| Volume [Å$^3$] | 2545.5(8) | Largest Diff. peak and hole [e Å$^{-3}$] | 0.251 and -0.311 |

The molecule crystallizes with half a molecule in the asymmetric unit. The crystallographic mirror plane through the molecule leads to disorder between the $CF_2$ and the $CF_3$ group and between a $CCH_3$ and a $C=CH_2$ group in the *nacnac* ligand. This disorder was treated using 1,2- and 1,3-distance similarity and thermal displacement restraints.

The structure is published in: Ramachandran Azhakar, Herbert W. Roesky, Hilke Wolf and Dietmar Stalke „Metal free and selective activation of one C-F bond in a bound $CF_3$ group" *Chem. Commun.* **2013**, *49*, 1841 – 1843.

Structural Information is also deposited in the CSD under: **912594.**
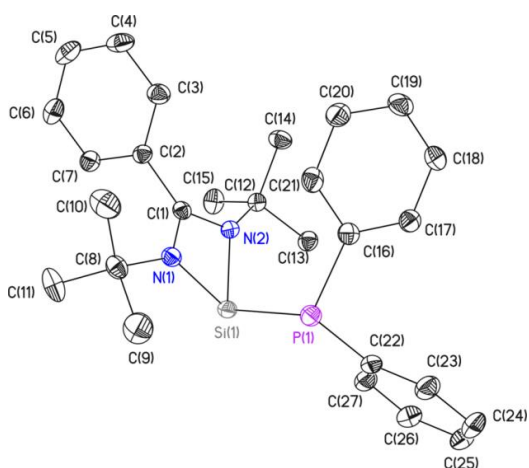
| Structure code | HW_Az_SiPPh2 | Z | 2 |
|---|---|---|---|
| Empirical formula | $C_{27} H_{33} N_2 P Si$ | $\rho_{calc}$ [g cm$^{-3}$] | 1.183 |
| Formula Weight [g mol$^{-1}$] | 444.61 | $\mu$ [mm$^{-1}$] | 0.175 |
| Temperature [K] | 100(2) | F(000) | 476 |
| Wavelength [Å] | 0.71073 | Crystal Size [mm] | 0.10 x 0.10 x 0.10 |
| Crystal System | Triclinic | $\theta$ range [°] | 1.18 to 28.30°. |
| Space Group | $P\bar{1}$ | Reflections Collected | 42389 |
| Unit cell dimensions [Å] | | Unique reflections | 6185 |
| | a = 8.384(3) | Completeness to $\theta_{max}$: | 99.7 % |
| | b = 9.073(3) | Data/Restrains/Parameters | 6185 / 0 / 286 |
| | c = 17.254(4)) | $R_{int}$ | 0.0192 |
| | $\alpha$ = 89.190(10)° | $R1$ [I>2$\sigma$(I)] | 0.0311 |
| | $\beta$ = 86.06(2)°. | $wR2$ (all data) | 0.0841 |
| | $\gamma$ = 72.470(10) | GooF | 1.061 |
| Volume [Å$^3$] | 1248.5(7) | Largest Diff. peak and hole [e Å$^{-3}$] | 0.355 and -0.259 |

The structure is published in: Ramachandran Azhakar, Rajendra S. Ghadwal, Herbert W. Roesky, Hilke Wolf and Dietmar Stalke „Facile Access to the Functionalized N-Donor Stabilized Silylenes PhC(N$t$Bu)$_2$SiX (X = PPh$_2$, NPh$_2$, NCy$_2$, N$i$Pr$_2$, NMe$_2$, N(SiMe$_3$)$_2$, O$t$Bu)" *Organometallics* 2012, *31*, 4588 – 4592.

Structural Information is also deposited in the CSD under: **878553.**
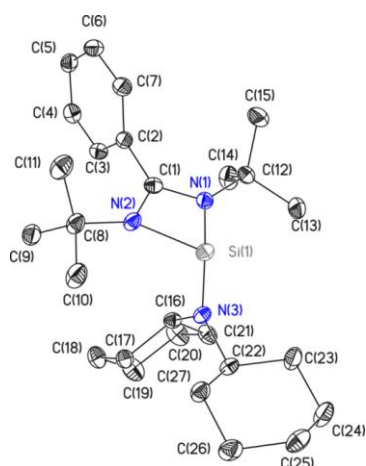
| Structure code | HW_Az_SiNCy2 | Z | 4 |
|---|---|---|---|
| Empirical formula | $C_{27} H_{45} N_3 Si$ | $\rho_{calc}$ [g cm$^{-3}$] | 1.096 |
| Formula Weight [g mol$^{-1}$] | 439.75 | μ [mm$^{-1}$] | 0.106 |
| Temperature [K] | 100(2) | F(000) | 968 |
| Wavelength [Å] | 0.71073 | Crystal Size [mm] | 0.20 x 0.10 x 0.02 |
| Crystal System | Monoclinic | θ range [°] | 1.46 to 26.35° |
| Space Group | $P2_1$/c | Reflections Collected | 60239 |
| Unit cell dimensions [Å] | | Unique reflections | 5422 |
| | a = 15.040(4) | Completeness to θ$_{max}$: | 99.5 % |
| | b = 11.542(4) | Data/Restrains/Parameters | 5422 / 0 / 286 |
| | c = 16.516(6) | R$_{int}$ | 0.0398 |
| | α = 90° | R1 [I>2σ(I)] | 0.0379 |
| | β = 111.70(2)° | wR2 (all data) | 0.0921 |
| | γ = 90° | GooF | 1.043 |
| Volume [Å$^3$] | 2663.9(15) | Largest Diff. peak and hole [e Å$^{-3}$] | 0.291 and -0.264 |

The structure is published in: Ramachandran Azhakar, Rajendra S. Ghadwal, Herbert W. Roesky, Hilke Wolf and Dietmar Stalke „Facile Access to the Functionalized N-Donor Stabilized Silylenes PhC(N*t*Bu)$_2$SiX (X = PPh$_2$, NPh$_2$, NCy$_2$, N*i*Pr$_2$, NMe$_2$, N(SiMe$_3$)$_2$, O*t*Bu)" *Organometallics* 2012, *31*, 4588 – 4592.

Structural Information is also deposited in the CSD under: **878554.**
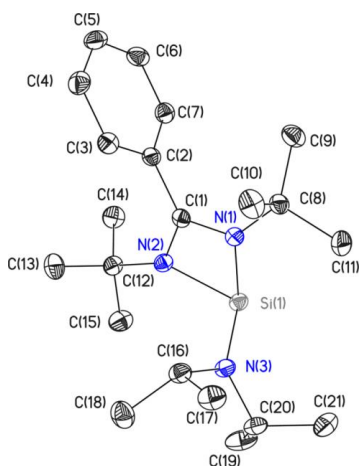
| Structure code | HW_Az_SiNiPr2 | Z | 8 |
|---|---|---|---|
| Empirical formula | $C_{21} H_{37} N_3 Si$ | $\rho_{calc}$ [g cm$^{-3}$] | 1.079 |
| Formula Weight [g mol$^{-1}$] | 359.63 | $\mu$ [mm$^{-1}$] | 0.114 |
| Temperature [K] | 100(2) | F(000) | 1584 |
| Wavelength [Å] | 0.71073 | Crystal Size [mm] | 0.15 x 0.10 x 0.02 |
| Crystal System | Monoclinic | $\theta$ range [°] | 1.48 to 27.58° |
| Space Group | $C2/c$ | Reflections Collected | 39498 |
| Unit cell dimensions [Å] | | Unique reflections | 5111 |
| | a = 27.820(2) | Completeness to $\theta_{max}$: | 99.9 % |
| | b = 8.447(3) | Data/Restrains/Parameters | 5111 / 0 / 236 |
| | c = 19.099(2)) | $R_{int}$ | 0.0492 |
| | $\alpha$ = 90° | $R1$ [I>2$\sigma$(I)] | 0.0416 |
| | $\beta$ = 99.35(2)° | $wR2$ (all data) | 0.1002 |
| | $\gamma$ = 90° | GooF | 1.047 |
| Volume [Å$^3$] | 4428.6(17) | Largest Diff. peak and hole [e Å$^{-3}$] | 0.299 and -0.263 |

The structure is published in: Ramachandran Azhakar, Rajendra S. Ghadwal, Herbert W. Roesky, Hilke Wolf and Dietmar Stalke „Facile Access to the Functionalized N-Donor Stabilized Silylenes PhC(N*t*Bu)$_2$SiX (X = PPh$_2$, NPh$_2$, NCy$_2$, N*i*Pr$_2$, NMe$_2$, N(SiMe$_3$)$_2$, O*t*Bu)" *Organometallics* **2012**, *31*, 4588 – 4592.

Structural Information is also deposited in the CSD under: **878555.**
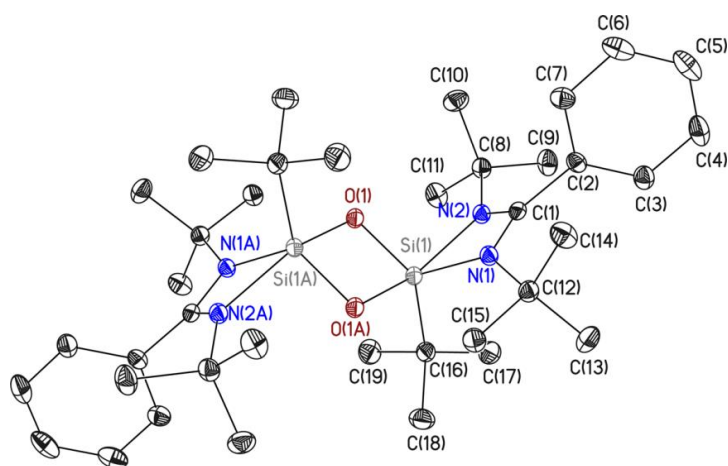
| Structure code | HW_Az_SitBuOx | Z | 1 |
|---|---|---|---|
| Empirical formula | $C_{38} H_{64} N_4 O_2 Si_2$ | $\rho_{calc}$ [g cm$^{-3}$] | 1.167 |
| Formula Weight [g mol$^{-1}$] | 665.11 | μ [mm$^{-1}$] | 0.131 |
| Temperature [K] | 100(2) | F(000) | 364 |
| Wavelength [Å] | 0.71073 | Crystal Size [mm] | 0.5 x 0.5 x 0.3 |
| Crystal System | Triclinic | θ range [°] | 1.98 to 28.35° |
| Space Group | $P\bar{1}$ | Reflections Collected | 27594 |
| Unit cell dimensions [Å] | | Unique reflections | 4682 |
| | a = 9.878(3) | Completeness to θ$_{max}$: | 99.5 % |
| | b = 10.371(4) | Data/Restrains/Parameters | 4682 / 0 / 217 |
| | c = 11.472(5) | $R_{int}$ | 0.0284 |
| | α = 110.480(10)°. | $R$1 [I>2σ(I)] | 0.0327 |
| | β = 94.95(2)°. | $wR$2 (all data) | 0.0918 |
| | γ = 116.21(2)°. | GooF | 1.060 |
| Volume [Å$^3$] | 946.3(6) | Largest Diff. peak and hole [e Å$^{-3}$] | 0.450 and -0.216 |

The molecule crystallizes with one half in the asymmetric unit.

The structure is published in: Ramachandran Azhakar, Rajendra S. Ghadwal, Herbert W. Roesky, Hilke Wolf and Dietmar Stalke „A début for base stabilized monoalkylsilylenes" *Chem. Commun.* **2012**, *48*, 4561 – 4563.

Structural Information is also deposited in the CSD under: **866117.**
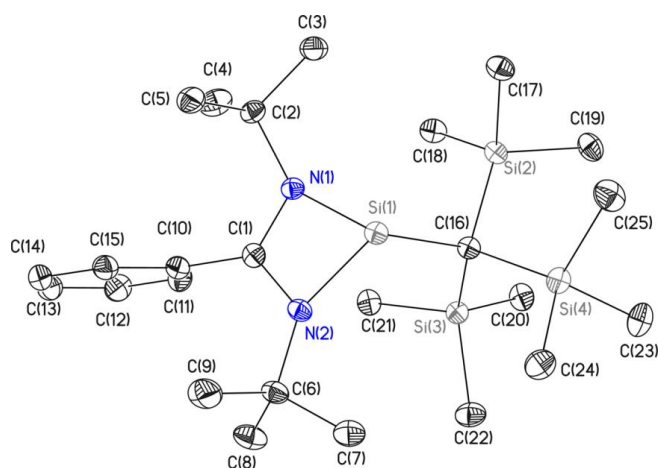
| Structure code | HW_Az_SiNSiMe3 | Z | 4 |
|---|---|---|---|
| Empirical formula | $C_{25} H_{50} N_2 Si_4$ | $\rho_{calc}$ [g cm$^{-3}$] | 1.103 |
| Formula Weight [g mol$^{-1}$] | 491.03 | $\mu$ [mm$^{-1}$] | 0.216 |
| Temperature [K] | 100(2) | F(000) | 1080 |
| Wavelength [Å] | 0.71073 | Crystal Size [mm] | 0.2 x 0.2 x 0.2 |
| Crystal System | Monoclinic | $\theta$ range [°] | 1.54 to 27.11° |
| Space Group | $P2_1$/n | Reflections Collected | 50349 |
| Unit cell dimensions [Å] | | Unique reflections | 6530 |
| | a = 14.760(1) | Completeness to $\theta_{max}$: | 99.9 % |
| | b = 12.202(1) | Data/Restrains/Parameters | 6530 / 0 / 295 |
| | c = 17.706(2) | $R_{int}$ | 0.0277 |
| | $\alpha$ = 90° | $R1$ [I>2$\sigma$(I)] | 0.0278 |
| | $\beta$ = 112.04(2)°. | $wR2$ (all data) | 0.0740 |
| | $\gamma$ = 90°. | GooF | 1.046 |
| Volume [Å$^3$] | 2955.8(5) | Largest Diff. peak and hole [e Å$^{-3}$] | 0.354 and -0.200 |

The structure is published in: Ramachandran Azhakar, Rajendra S. Ghadwal, Herbert W. Roesky, Hilke Wolf and Dietmar Stalke „A début for base stabilized monoalkylsilylenes" *Chem. Commun.* **2012**, *48*, 4561 – 4563.

Structural Information is also deposited in the CSD under: **866116.**
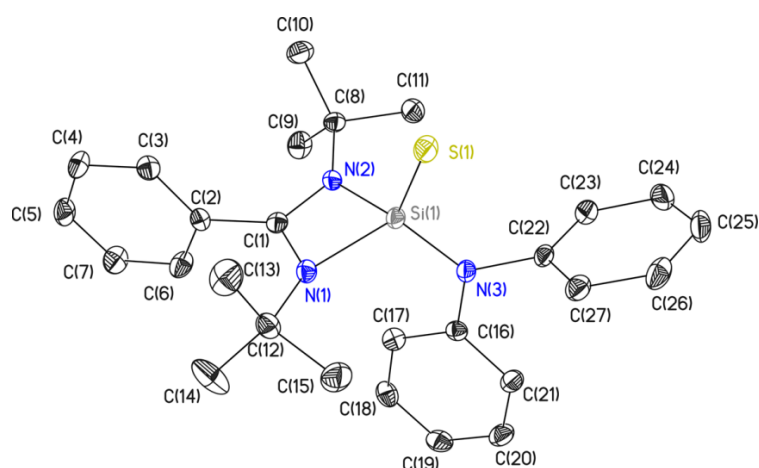
| Structure code | HW_Az_SiSNph2 | Z | 4 |
|---|---|---|---|
| Empirical formula | $C_{27} H_{33} N_3 SiS$ | $\rho_{calc}$ [g cm$^{-3}$] | 1.202 |
| Formula Weight [g mol$^{-1}$] | 459.71 | $\mu$ [mm$^{-1}$] | 0.194 |
| Temperature [K] | 100(2) | F(000) | 984 |
| Wavelength [Å] | 0.71073 | Crystal Size [mm] | 0.2 x 0.2 x 0.2 |
| Crystal System | Monoclinic | $\theta$ range [°] | 1.44 to 26.37° |
| Space Group | $P2_1$/c | Reflections Collected | 25948 |
| Unit cell dimensions [Å] | | Unique reflections | 5201 |
| | a = 15.190(5) | Completeness to $\theta_{max}$: | 99.9 % |
| | b = 10.883(4) | Data/Restrains/Parameters | 5201 / 0 / 295 |
| | c = 16.458(3) | $R_{int}$ | 0.0479 |
| | $\alpha$ = 90° | $R1$ [I>2σ(I)] | 0.0426 |
| | $\beta$ = 110.96(2)°. | $wR2$ (all data) | 0.1036 |
| | $\gamma$ = 90°. | GooF | 1.060 |
| Volume [Å$^3$] | 2540.7(13) | Largest Diff. peak and hole [e Å$^{-3}$] | 0.327 and -0.354 |

The structure is published in: Ramachandran Azhakar, Herbert W. Roesky, Hilke Wolf and Dietmar Stalke „On the Reactivity of the Silylene PhC(N*t*Bu)$_2$SiNPh$_2$ toward Organic Substrates" *Z. Anorg. Allg. Chem.* 2013, *639*, 934 – 938.

Structural Information is also deposited in the CSD under: **924135.**
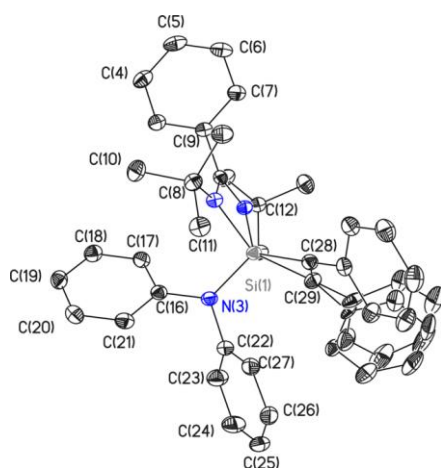
| Structure code | HW_Az_SiPh2Nph2 | Z | 8 |
|---|---|---|---|
| Empirical formula | $C_{48} H_{51} N_3 Si$ | $\rho_{calc}$ [g cm$^{-3}$] | 1.162 |
| Formula Weight [g mol$^{-1}$] | 698.00 | μ [mm$^{-1}$] | 0.095 |
| Temperature [K] | 100(2) | F(000) | 2992 |
| Wavelength [Å] | 0.71073 | Crystal Size [mm] | 0.2 x 0.1 x 0.05 |
| Crystal System | Monoclinic | θ range [°] | 1.479 to 28.312° |
| Space Group | $C2/c$ | Reflections Collected | 122463 |
| Unit cell dimensions [Å] | | Unique reflections | 9932 |
| | a = 31.623(4) | Completeness to θ (25.242°): | 100 % |
| | b = 16.340(7) | Data/Restrains/Parameters | 9932 / 135 / 596 |
| | c = 19.088(9) | $R_{int}$ | 0.0432 |
| | α = 90° | $R1$ [I>2σ(I)] | 0.0392 |
| | β = 125.97(2)°. | $wR2$ (all data) | 0.1035 |
| | γ = 90°. | GooF | 1.038 |
| Volume [Å$^3$] | 7982(5) | Largest Diff. peak and hole [e Å$^{-3}$] | 0.336 and -0.307 |

Two toluene solvent molecules are disordered and have been refined using 1,2- and 1,3-distance similarity as well as thermal displacement restraint. Additionally, one of the benzene rings in the main structure is disordered as well and has been modelled similar to the solvent molecules. The toluene moieties are hidden for clarity.

The structure is published in: Ramachandran Azhakar, Herbert W. Roesky, Hilke Wolf and Dietmar Stalke „On the Reactivity of the Silylene PhC(N$t$Bu)$_2$SiNPh$_2$ toward Organic Substrates" *Z. Anorg. Allg. Chem.* **2013**, *639*, 934 – 938.

Structural Information is also deposited in the CSD under: **924136.**
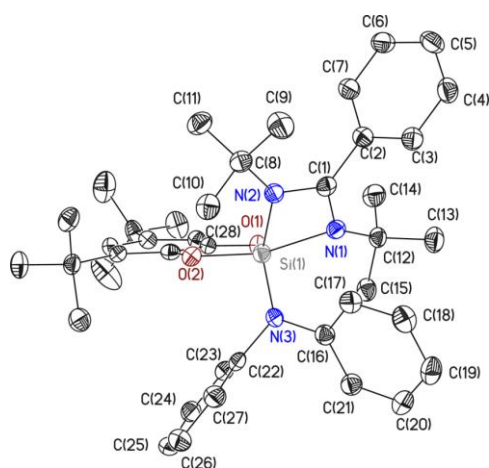
| Structure code | HW_Az_SibenzNph2 | Z | 4 |
|---|---|---|---|
| Empirical formula | $C_{41} H_{53} N_3 Si O_3$ | $\rho_{calc}$ [g cm$^{-3}$] | 1.138 |
| Formula Weight [g mol$^{-1}$] | 647.95 | $\mu$ [mm$^{-1}$] | 0.099 |
| Temperature [K] | 100(2) | F(000) | 1400 |
| Wavelength [Å] | 0.71073 | Crystal Size [mm] | 0.15 x 0.15 x 0.08 |
| Crystal System | Monoclinic | $\theta$ range [°] | 1.553 to 22.485° |
| Space Group | $P2_1/n$ | Reflections Collected | 51825 |
| Unit cell dimensions [Å] | | Unique reflections | 4936 |
| | a = 10.012(4) | Completeness to $\theta$ (20.706°): | 100 % |
| | b = 26.226(8) | Data/Restrains/Parameters | 4936 / 0 / 436 |
| | c = 14.407(5)) | $R_{int}$ | 0.0657 |
| | $\alpha$ = 90° | $R1$ [I>2$\sigma$(I)] | 0.0442 |
| | $\beta$ = 90.14(2)°. | $wR2$ (all data) | 0.0987 |
| | $\gamma$ = 90°. | GooF | 1.089 |
| Volume [Å$^3$] | 3783(2) | Largest Diff. peak and hole [e Å$^{-3}$] | 0.199 and -0.281 |

The structure is published in: Ramachandran Azhakar, Herbert W. Roesky, Hilke Wolf and Dietmar Stalke „On the Reactivity of the Silylene PhC(N*t*Bu)$_2$SiNPh$_2$ toward Organic Substrates" *Z. Anorg. Allg. Chem.* **2013**, *639*, 934 – 938.

Structural Information is also deposited in the CSD under: **924137.**
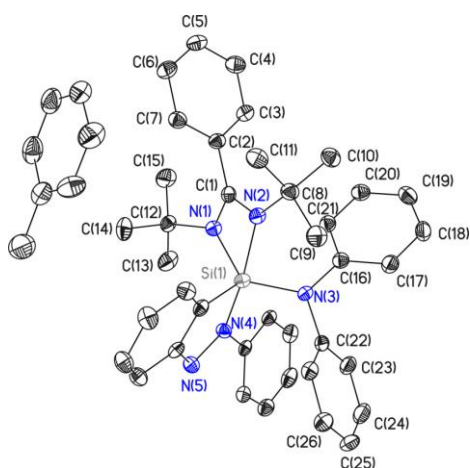
| Structure code | HW_Az_SiN2Ph_Nph2 | Z | 4 |
|---|---|---|---|
| Empirical formula | $C_{46} H_{51} N_5 Si$ | $\rho_{calc}$ [g cm$^{-3}$] | 1.198 |
| Formula Weight [g mol$^{-1}$] | 702.01 | $\mu$ [mm$^{-1}$] | 0.100 |
| Temperature [K] | 100(2) | F(000) | 1504 |
| Wavelength [Å] | 0.71073 | Crystal Size [mm] | 0.15 x 0.10 x 0.02 |
| Crystal System | Monoclinic | $\theta$ range [°] | 1.56 to 23.28° |
| Space Group | $P2_1$/n | Reflections Collected | 29310 |
| Unit cell dimensions [Å] | | Unique reflections | 5599 |
| | a = 11.129(5) | Completeness to $\theta_{max}$ : | 99.9 % |
| | b = 16.631(7) | Data/Restrains/Parameters | 5599 / 0 / 481 |
| | c = 21.2720(10) | $R_{int}$ | 0.0769 |
| | $\alpha$ = 90° | $R1$ [I>2$\sigma$(I)] | 0.0444 |
| | $\beta$ = 98.68(2)°. | $wR2$ (all data) | 0.1036 |
| | $\gamma$ = 90°. | GooF | 1.036 |
| Volume [Å$^3$] | 3892(2) | Largest Diff. peak and hole [e Å$^{-3}$] | 0.241 and -0.337 |

The structure is published in: Ramachandran Azhakar, Herbert W. Roesky, Hilke Wolf and Dietmar Stalke „Reactivity of Stable Heteroleptic Silylene PhC(N*t*Bu)$_2$SiNPh$_2$ toward Diazobenzene and *N*-Benzylidineaniline" *Organometallics* **2012**, *31*, 8608 – 8612.

Structural Information is also deposited in the CSD under: **900930.**
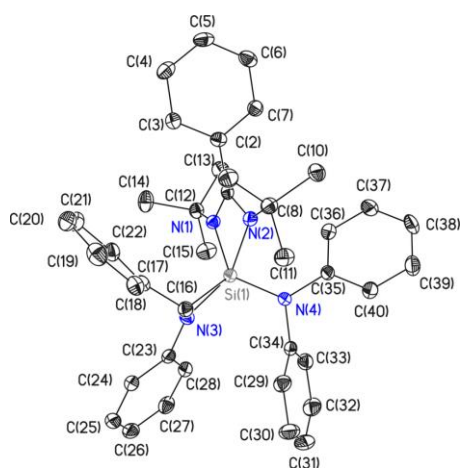
| Structure code | HW_Az_SiNCPh_Nph2 | Z | 4 |
|---|---|---|---|
| Empirical formula | C$_{40}$ H$_{44}$ N$_4$ Si | $\rho_{calc}$ [g cm$^{-3}$] | 1.195 |
| Formula Weight [g mol$^{-1}$] | 608.88 | μ [mm$^{-1}$] | 0.104 |
| Temperature [K] | 100(2) | F(000) | 13004 |
| Wavelength [Å] | 0.71073 | Crystal Size [mm] | 0.10 x 0.08 x 0.08 |
| Crystal System | Monoclinic | θ range [°] | 1.69 to 26.40° |
| Space Group | $P2_1$/c | Reflections Collected | 43791 |
| Unit cell dimensions [Å] | | Unique reflections | 6921 |
| | a = 11.486(4) | Completeness to θ$_{max}$ : | 99.7 % |
| | b = 15.541(5) | Data/Restrains/Parameters | 6921 / 0 / 412 |
| | c = 19.133(6) | R$_{int}$ | 0.0519 |
| | α = 90° | $R$1 [I>2σ(I)] | 0.0440 |
| | β = 97.84(2)°. | $wR$2 (all data) | 0.1126 |
| | γ = 90°. | GooF | 1.058 |
| Volume [Å$^3$] | 3383.4(19) | Largest Diff. peak and hole [e Å$^{-3}$] | 0.240 and -0.405 |

The structure is published in: Ramachandran Azhakar, Herbert W. Roesky, Hilke Wolf and Dietmar Stalke „Reactivity of Stable Heteroleptic Silylene PhC(N*t*Bu)$_2$SiNPh$_2$ toward Diazobenzene and *N*-Benzylidineaniline" *Organometallics* **2012**, *31*, 8608 – 8612.

Structural Information is also deposited in the CSD under: **900931.**

## 9.2    Collaboration with Martin Kuß-Petermann (Prof. Wenger)
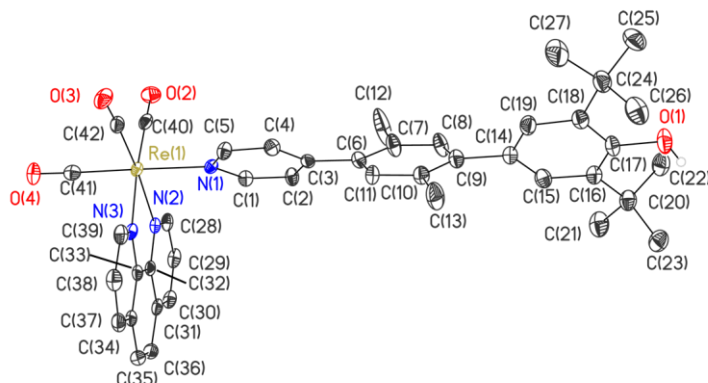


| Structure code | MKP 02 | Z | 4 |
|---|---|---|---|
| Empirical formula | $C_{92} H_{96} Cl_4 F_6 N_6 O_{15} Re_2 S_2$ | $\rho_{calc}$ [g cm$^{-3}$] | 1.562 |
| Formula Weight [g mol$^{-1}$] | 2218.06 | $\mu$ [mm$^{-1}$] | 2.799 |
| Temperature [K] | 100(2) | F(000) | 4456 |
| Wavelength [Å] | 0.71073 | Crystal Size [mm] | 0.07 x 0 06 x 0 02 |
| Crystal System | Monoclinic | $\theta$ range [°] | 1.153 to 26.394 |
| Space Group | C2/c | Reflections Collected | 88421 |
| Unit cell dimensions [Å] | | Unique reflections | 9663 |
| | a = 38.135(3) | Completeness to $\theta$ (25.242) : | 100 % |
| | b = 10.364(2) | Data/Restrains/Parameters | 9663 / 124 / 652 |
| | c = 25.782(2) | $R_{int}$ | 0.0464 |
| | $\alpha$= 90°. | $R$1 [I>2$\sigma$(I)] | 0.0279 |
| | $\beta$= 112.20(2)° | $wR$2 (all data) | 0.0548 |
| | $\gamma$ = 90°. | GooF | 1.032 |
| Volume [Å$^3$] | 9434(2) | Largest Diff. peak and hole [e Å$^{-3}$] | 1.020 and -0.677 |

Disordered diethylether has been refined using 1,2- and 1,3-distance similarity as well as thermal displacement restraints. Dichloromethane and triflate molecules as well as the diethylether moiety have been omitted for clarity. The hydrogen atom attached to O1 has been found in the difference Fourier density map.
The structure is published in: Martin Kuss-Petermann, Hilke Wolf, Dietmar Stalke, Oliver Wenger "Influence of donor-Acceptor Distance Variation on Photoinduced Electron and Proton Transfer in Rhenium(I)-Phenol Dyads" *J. Am. Chem. Soc.* **2012**, *134*, 12844 – 12854.

Structural information is also deposited in the CSD under: **838939**.

## 9.3    Collaboration with Markus Scheibel      (Prof. Schneider)
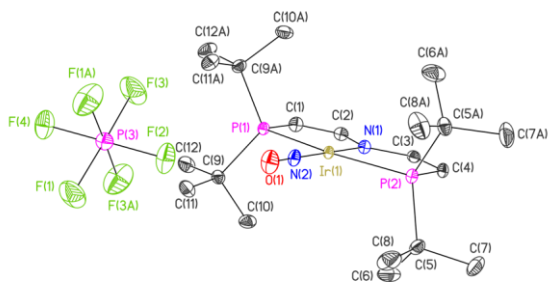


| Structure code | MS_NO | Z | 2 |
|---|---|---|---|
| Empirical formula | $C_{20} H_{40} F_6 Ir N_2 O P_3$ | $\rho_{calc}$ [g cm$^{-3}$] | 1.840 |
| Formula Weight [g mol$^{-1}$] | 723.65 | $\mu$ [mm$^{-1}$] | 2.862 |
| Temperature [K] | 100(2) | F(000) | 716 |
| Wavelength [Å] | 0.56086 | Crystal Size [mm] | 0.15 x 0.10 x 0.05 |
| Crystal System | Monoclinic | $\theta$ range [°] | 1.436 to 21.996 |
| Space Group | P2$_1$/m | Reflections Collected | 40707 |
| Unit cell dimensions [Å] | | Unique reflections | 3458 |
| | a = 9.948(5) | Completeness to $\theta$ (19.665) : | 100 % |
| | b = 11.929(6) | Data/Restrains/Parameters | 3458 / 13 / 175 |
| | c = 11.396(5) | R$_{int}$ | 0.0473 |
| | $\alpha$= 90°. | $R$1 [I>2$\sigma$(I)] | 0.0162 |
| | $\beta$= 101.00(2)° | $w$R2 (all data) | 0.0359 |
| | $\gamma$ = 90°. | GooF | 1.042 |
| Volume [Å$^3$] | 1327.5 (11) | Largest Diff. peak and hole [e Å$^{-3}$] | 0.612 and -0.878 |

The PF$_6$ moiety is placed on a special position and has been refined using 1,2- and 1,3- distance similarity restraints.

The structure is published in: Markus G. Scheibel, Isabel Klobsch, Hilke Wolf, Peter Stollberg, Dietmar Stalke, Sven Schneider "Thionitrosyl- and Selenonitrosyliridium Complexes" *Eur. J. Inorg. Chem.* **2013**, *22 - 23*, 3836 – 3839.

Structural information is also deposited in the CSD under: **930521**.

# 10 APPENDIX

## 10.1 Additional information on [2,2]-Paracyclophane

### 10.1.1 Data Collection Strategies

#### 10.1.1.1 In-house Data Collection on the Molybdenum Rotating Anode

Image width: 0.4°

Detector Distance: 4 cm

| run | exposure time | 2 theta value |
|-----|---------------|---------------|
| 1   | 5             | -32           |
| 2   | 5             | -32           |
| 3   | 5             | -32           |
| 4   | 5             | -32           |
| 5   | 30            | -50           |
| 6   | 30            | -50           |
| 7   | 30            | -50           |
| 8   | 100           | -90           |
| 9   | 100           | -90           |
| 10  | 100           | -90           |
| 11  | 100           | -90           |
| 12  | 100           | -90           |

Data collection strategy for 15, 35 and 60 K

Image width: 0.4°

Detector Distance: 5 cm

| run | exposure time | 2 theta value |
|-----|---------------|---------------|
| 1   | 4             | -20           |
| 2   | 3             | -10           |
| 3   | 2             | 0             |
| 4   | 3             | -20           |
| 5   | 60            | -52.5         |
| 6   | 4             | -20           |
| 7   | 4             | -20           |
| 8   | 110           | -75           |
| 9   | 120           | -77.5         |
| 10  | 120           | -85           |
| 11  | 2             | -2.5          |
| 12  | 120           | -87.5         |
| 13  | 3             | -22.5         |

| | | |
|---|---|---|
| 14 | 120 | -82.5 |

Data collection strategy for 120 K

## 10.1.1.2        Data Collection at the 15-ID-B beam-line at the APS

| | 15 K | | | 35 K | |
|---|---|---|---|---|---|
| run | exposure time | 2 theta value | run | exposure time | 2 theta value |
| 1 | 0.5 | -30 | 1 | 0.5 | -30 |
| 2 | 0.5 | -30 | 2 | 0.5 | -30 |
| 3 | 0.3 | -10 | 3 | 0.5 | -35 |
| 4 | 0.5 | -20 | 4 | 0.3 | -10 |
| 5 | 0.5 | -35 | 5 | 0.3 | -10 |
| 6 | 0.3 | -10 | 6 | 1 | -20 |

Image width: 0.3°

Detector Distance: 5 cm

| | 45 K | | | 50 K | | | 55 K | |
|---|---|---|---|---|---|---|---|---|
| run | exposure time | 2 theta value | run | exposure time | 2 theta value | run | exposure time | 2 theta value |
| 1 | 0.3 | -10 | 1 | 0.3 | -10 | 1 | 0.3 | -10 |
| 2 | 0.3 | -10 | 2 | 0.3 | -10 | 2 | 0.3 | -10 |
| 3 | 0.3 | -10 | 3 | 0.3 | -10 | 3 | 0.3 | -10 |

## 10.1.2  XPREP statistics

### 10.1.2.1　　　In-house data collection

15 K

| Resolution | %Complete | Multiplicity | Mean I/s | $R_{merge}$ | $R_{sigma}$ | $R_{rim}$ |
|---|---|---|---|---|---|---|
| Inf - 1.77 | 100.0 | 11.32 | 149.41 | 0.0144 | 0.0053 | 0.0156 |
| 1.77 - 1.14 | 100.0 | 16.96 | 153.25 | 0.0155 | 0.0047 | 0.0155 |
| 1.14 - 0.89 | 100.0 | 15.49 | 116.30 | 0.0189 | 0.0059 | 0.0187 |
| 0.89 - 0.77 | 100.0 | 13.83 | 85.69 | 0.0282 | 0.0083 | 0.0282 |
| 0.77 - 0.69 | 99.6 | 14.98 | 103.61 | 0.0265 | 0.0070 | 0.0274 |
| 0.69 - 0.64 | 100.0 | 14.62 | 91.53 | 0.0305 | 0.0076 | 0.0319 |
| 0.64 - 0.60 | 100.0 | 11.86 | 84.90 | 0.0300 | 0.0086 | 0.0296 |
| 0.60 - 0.57 | 100.0 | 8.01 | 71.58 | 0.0223 | 0.0104 | 0.0252 |
| 0.57 - 0.54 | 100.0 | 7.58 | 59.44 | 0.0259 | 0.0126 | 0.0258 |
| 0.54 - 0.52 | 100.0 | 7.12 | 48.88 | 0.0318 | 0.0150 | 0.0299 |
| 0.52 - 0.50 | 99.6 | 4.54 | 43.44 | 0.0276 | 0.0183 | 0.0348 |
| 0.50 - 0.49 | 98.7 | 3.11 | 34.90 | 0.0279 | 0.0231 | 0.0292 |
| 0.49 - 0.47 | 99.7 | 3.10 | 37.38 | 0.0225 | 0.0215 | 0.0304 |
| 0.47 - 0.46 | 98.9 | 2.96 | 30.22 | 0.0264 | 0.0262 | 0.0283 |
| 0.46 - 0.45 | 100.0 | 2.87 | 31.80 | 0.0265 | 0.0241 | 0.0316 |
| 0.45 - 0.44 | 99.6 | 2.76 | 30.04 | 0.0261 | 0.0258 | 0.0317 |
| 0.44 - 0.43 | 100.0 | 2.65 | 26.51 | 0.0305 | 0.0298 | 0.0369 |
| 0.43 - 0.42 | 100.0 | 2.47 | 21.50 | 0.0341 | 0.0371 | 0.0418 |
| 0.42 - 0.41 | 99.7 | 2.29 | 25.17 | 0.0314 | 0.0341 | 0.0400 |
| 0.41 - 0.40 | 93.7 | 1.89 | 19.40 | 0.0322 | 0.0444 | 0.0448 |
| | | | | | | |
| 0.50 – 0.40 | 98.8 | 2.54 | 28.17 | 0.0271 | 0.0281 | 0.0334 |
| Inf – 0.40 | 99.4 | 9.19 | 58.03 | 0.0212 | 0.0100 | 0.0222 |

35 K

| Resolution | %Complete | Multiplicity | Mean I/s | $R_{merge}$ | $R_{sigma}$ | $R_{rim}$ |
|---|---|---|---|---|---|---|
| Inf - 1.87 | 100.0 | 13.27 | 187.43 | 0.0164 | 0.0047 | 0.0197 |
| 1.87 - 1.19 | 100.0 | 19.95 | 213.49 | 0.0121 | 0.0033 | 0.0124 |
| 1.19 - 0.93 | 100.0 | 19.40 | 178.56 | 0.0135 | 0.0040 | 0.0130 |
| 0.93 - 0.81 | 99.5 | 16.93 | 115.83 | 0.0210 | 0.0060 | 0.0193 |
| 0.81 - 0.73 | 100.0 | 16.82 | 129.58 | 0.0198 | 0.0057 | 0.0211 |
| 0.73 - 0.67 | 99.6 | 17.49 | 126.96 | 0.0248 | 0.0058 | 0.0238 |
| 0.67 - 0.63 | 100.0 | 16.15 | 111.99 | 0.0245 | 0.0060 | 0.0254 |
| 0.63 - 0.60 | 100.0 | 12.46 | 102.89 | 0.0252 | 0.0073 | 0.0268 |
| 0.60 - 0.57 | 100.0 | 8.27 | 88.07 | 0.0188 | 0.0082 | 0.0208 |
| 0.57 - 0.55 | 100.0 | 7.77 | 76.29 | 0.0222 | 0.0099 | 0.0228 |
| 0.55 - 0.53 | 100.0 | 7.50 | 65.11 | 0.0257 | 0.0111 | 0.0277 |
| 0.53 - 0.51 | 100.0 | 6.38 | 57.79 | 0.0297 | 0.0133 | 0.0318 |
| 0.51 - 0.50 | 98.6 | 3.27 | 45.84 | 0.0198 | 0.0176 | 0.0236 |
| 0.50 - 0.48 | 99.7 | 3.11 | 41.48 | 0.0218 | 0.0195 | 0.0262 |
| 0.48 - 0.47 | 99.5 | 2.95 | 42.95 | 0.0192 | 0.0187 | 0.0235 |
| 0.47 - 0.46 | 100.0 | 2.90 | 32.36 | 0.0244 | 0.0240 | 0.0286 |
| 0.46 - 0.45 | 98.6 | 2.80 | 38.18 | 0.0183 | 0.0208 | 0.0244 |
| 0.45 - 0.44 | 99.1 | 2.64 | 32.32 | 0.0233 | 0.0239 | 0.0294 |
| 0.44 - 0.43 | 98.5 | 2.66 | 29.42 | 0.0260 | 0.0267 | 0.0333 |
| 0.43 - 0.42 | 94.1 | 2.26 | 23.19 | 0.0333 | 0.0341 | 0.0411 |
| | | | | | | |
| 0.52 – 0.42 | 98.5 | 2.99 | 36.65 | 0.0234 | 0.0213 | 0.0280 |
| Inf – 0.42 | 99.2 | 8.73 | 79.80 | 0.0172 | 0.0070 | 0.0180 |

35 K in-house data integrated up to d = 0.4 Å

| Resolution | %Complete | Multiplicity | Mean I/s | $R_{merge}$ | $R_{sigma}$ | $R_{rim}$ |
|---|---|---|---|---|---|---|
| Inf - 1.77 | 100.0 | 13.64 | 200.09 | 0.0150 | 0.0045 | 0.0180 |
| 1.77 - 1.14 | 100.0 | 20.38 | 210.19 | 0.0127 | 0.0034 | 0.0125 |
| 1.14 - 0.89 | 99.6 | 18.63 | 160.47 | 0.0142 | 0.0042 | 0.0140 |
| 0.89 - 0.77 | 100.0 | 16.61 | 116.29 | 0.0208 | 0.0061 | 0.0211 |
| 0.77 - 0.70 | 99.6 | 17.54 | 136.03 | 0.0208 | 0.0054 | 0.0209 |
| 0.70 - 0.64 | 100.0 | 16.79 | 117.72 | 0.0252 | 0.0060 | 0.0267 |
| 0.64 - 0.60 | 100.0 | 13.15 | 104.46 | 0.0254 | 0.0069 | 0.0245 |
| 0.60 - 0.57 | 100.0 | 8.28 | 88.66 | 0.0188 | 0.0082 | 0.0207 |
| 0.57 - 0.55 | 100.0 | 7.77 | 76.49 | 0.0223 | 0.0099 | 0.0229 |
| 0.55 - 0.52 | 100.0 | 7.36 | 62.02 | 0.0272 | 0.0117 | 0.0277 |
| 0.52 - 0.50 | 99.2 | 4.46 | 53.04 | 0.0254 | 0.0150 | 0.0318 |
| 0.50 - 0.49 | 99.4 | 3.08 | 41.90 | 0.0223 | 0.0195 | 0.0248 |
| 0.49 - 0.47 | 99.7 | 3.05 | 42.43 | 0.0200 | 0.0190 | 0.0260 |
| 0.47 - 0.46 | 100.0 | 2.89 | 32.42 | 0.0242 | 0.0240 | 0.0255 |
| 0.46 - 0.45 | 98.6 | 2.80 | 38.46 | 0.0183 | 0.0208 | 0.0243 |
| 0.45 - 0.44 | 99.1 | 2.64 | 32.50 | 0.0232 | 0.0239 | 0.0292 |
| 0.44 - 0.43 | 98.5 | 2.66 | 29.59 | 0.0256 | 0.0267 | 0.0327 |
| 0.43 - 0.42 | 98.9 | 2.40 | 23.49 | 0.0322 | 0.0337 | 0.0399 |
| 0.42 - 0.41 | 96.5 | 2.36 | 27.61 | 0.0287 | 0.0313 | 0.0372 |
| 0.41 - 0.40 | 89.8 | 1.81 | 21.16 | 0.0320 | 0.0401 | 0.0433 |
| | | | | | | |
| 0.50 – 0.40 | 97.5 | 2.59 | 31.76 | 0.0234 | 0.0248 | 0.0294 |
| Inf – 0.40 | 98.7 | 7.89 | 73.26 | 0.0172 | 0.0075 | 0.0181 |

### 10.1.2.2    Synchrotron data collection

15 K

| Resolution | %Complete | Multiplicity | Mean I/s | $R_{merge}$ | $R_{sigma}$ | $R_{rim}$ |
|---|---|---|---|---|---|---|
| Inf - 1.62 | 98.9 | 19.54 | 51.19 | 0.0524 | 0.0217 | 0.0546 |
| 1.62 - 1.05 | 100.0 | 23.75 | 58.40 | 0.0512 | 0.0148 | 0.0528 |
| 1.05 - 0.82 | 100.0 | 19.82 | 49.54 | 0.0593 | 0.0173 | 0.0589 |
| 0.82 - 0.71 | 100.0 | 16.09 | 45.17 | 0.0624 | 0.0208 | 0.0641 |
| 0.71 - 0.64 | 100.0 | 13.38 | 39.93 | 0.0662 | 0.0246 | 0.0704 |
| 0.64 - 0.59 | 100.0 | 11.65 | 38.21 | 0.0651 | 0.0242 | 0.0668 |
| 0.59 - 0.56 | 100.0 | 8.98 | 33.70 | 0.0627 | 0.0279 | 0.0662 |
| 0.56 - 0.53 | 100.0 | 7.80 | 30.86 | 0.0598 | 0.0309 | 0.0631 |
| 0.53 - 0.50 | 100.0 | 7.48 | 30.06 | 0.0618 | 0.0308 | 0.0650 |
| 0.50 - 0.48 | 100.0 | 6.84 | 28.59 | 0.0618 | 0.0297 | 0.0649 |
| 0.48 - 0.47 | 100.0 | 6.13 | 26.61 | 0.0567 | 0.0312 | 0.0642 |
| 0.47 - 0.45 | 99.7 | 4.88 | 24.99 | 0.0480 | 0.0341 | 0.0531 |
| 0.45 - 0.44 | 100.0 | 4.47 | 22.79 | 0.0444 | 0.0360 | 0.0490 |
| 0.44 - 0.43 | 100.0 | 4.69 | 21.72 | 0.0500 | 0.0376 | 0.0555 |
| 0.43 - 0.41 | 100.0 | 4.29 | 19.94 | 0.0525 | 0.0436 | 0.0623 |
| 0.41 - 0.40 | 100.0 | 4.20 | 19.43 | 0.0548 | 0.0432 | 0.0569 |
| 0.40 - 0.39 | 100.0 | 3.83 | 15.19 | 0.0650 | 0.0553 | 0.0616 |
| 0.39 - 0.38 | 99.5 | 3.50 | 14.39 | 0.0661 | 0.0585 | 0.0740 |
| 0.38 - 0.37 | 85.3 | 2.37 | 12.04 | 0.0779 | 0.0746 | 0.0750 |
| | | | | | | |
| 0.47- 0.37 | 97.6 | 3.95 | 18.51 | 0.0528 | 0.0440 | 0.0594 |
| Inf - 0.47 | 98.9 | 8.04 | 28.38 | 0.0565 | 0.0243 | 0.0589 |

35 K

| Resolution | %Complete | Multiplicity | Mean I/s | $R_{merge}$ | $R_{sigma}$ | $R_{rim}$ |
|---|---|---|---|---|---|---|
| Inf - 1.90 | 98.3 | 19.00 | 84.70 | 0.0378 | 0.0110 | 0.0398 |
| 1.90 - 1.23 | 100.0 | 23.69 | 78.72 | 0.0393 | 0.0094 | 0.0392 |
| 1.23 - 0.95 | 100.0 | 19.91 | 77.41 | 0.0375 | 0.0110 | 0.0382 |
| 0.95 - 0.83 | 100.0 | 15.61 | 61.73 | 0.0512 | 0.0138 | 0.0524 |
| 0.83 - 0.75 | 100.0 | 13.99 | 59.27 | 0.0550 | 0.0153 | 0.0538 |
| 0.75 - 0.69 | 100.0 | 12.16 | 55.07 | 0.0519 | 0.0164 | 0.0545 |
| 0.69 - 0.65 | 100.0 | 10.66 | 49.69 | 0.0601 | 0.0176 | 0.0620 |
| 0.65 - 0.61 | 100.0 | 9.15 | 47.66 | 0.0548 | 0.0177 | 0.0620 |
| 0.61 - 0.58 | 100.0 | 8.07 | 44.70 | 0.0568 | 0.0187 | 0.0558 |
| 0.58 - 0.56 | 100.0 | 6.72 | 37.35 | 0.0495 | 0.0201 | 0.0591 |
| 0.56 - 0.54 | 100.0 | 6.07 | 37.64 | 0.0491 | 0.0211 | 0.0539 |
| 0.54 - 0.52 | 100.0 | 5.73 | 32.42 | 0.0563 | 0.0239 | 0.0562 |
| 0.52 - 0.51 | 99.2 | 4.75 | 31.38 | 0.0484 | 0.0264 | 0.0571 |
| 0.51 - 0.49 | 100.0 | 4.74 | 28.01 | 0.0600 | 0.0294 | 0.0630 |
| 0.49 - 0.48 | 100.0 | 4.08 | 25.37 | 0.0542 | 0.0328 | 0.0654 |
| 0.48 - 0.47 | 100.0 | 3.32 | 25.63 | 0.0328 | 0.0317 | 0.0388 |
| 0.47 - 0.46 | 100.0 | 3.22 | 21.66 | 0.0382 | 0.0376 | 0.0452 |
| 0.46 - 0.45 | 99.1 | 2.95 | 21.11 | 0.0376 | 0.0376 | 0.0446 |
| 0.45 - 0.44 | 98.3 | 2.71 | 18.77 | 0.0437 | 0.0432 | 0.0501 |
| 0.44 - 0.43 | 91.4 | 2.28 | 15.96 | 0.0489 | 0.0510 | 0.0559 |
| | | | | | | |
| 0.53 – 0.43 | 98.4 | 3.58 | 23.67 | 0.0488 | 0.0343 | 0.0547 |
| Inf – 0.43 | 99.2 | 8.20 | 40.21 | 0.0429 | 0.0154 | 0.0446 |

35 K data integrated up to d = 0.40

| Resolution | %Complete | Multiplicity | Mean I/s | $R_{merge}$ | $R_{sigma}$ | $R_{rim}$ |
|---|---|---|---|---|---|---|
| Inf - 1.82 | 100.0 | 19.30 | 81.04 | 0.0375 | 0.0111 | 0.0393 |
| 1.82 - 1.17 | 100.0 | 23.56 | 81.55 | 0.0388 | 0.0096 | 0.0396 |
| 1.17 - 0.91 | 100.0 | 18.85 | 72.35 | 0.0406 | 0.0118 | 0.0399 |
| 0.91 - 0.79 | 100.0 | 14.91 | 58.61 | 0.0538 | 0.0145 | 0.0565 |
| 0.79 - 0.71 | 100.0 | 12.90 | 58.30 | 0.0520 | 0.0161 | 0.0537 |
| 0.71 - 0.66 | 100.0 | 11.08 | 50.16 | 0.0555 | 0.0169 | 0.0580 |
| 0.66 - 0.62 | 100.0 | 9.67 | 47.28 | 0.0585 | 0.0185 | 0.0620 |
| 0.62 - 0.58 | 100.0 | 8.22 | 45.68 | 0.0545 | 0.0183 | 0.0579 |
| 0.58 - 0.56 | 100.0 | 6.72 | 37.33 | 0.0495 | 0.0202 | 0.0531 |
| 0.56 - 0.54 | 100.0 | 6.07 | 37.59 | 0.0490 | 0.0212 | 0.0553 |
| 0.54 - 0.52 | 100.0 | 5.73 | 32.50 | 0.0560 | 0.0239 | 0.0568 |
| 0.52 - 0.50 | 99.6 | 4.84 | 30.08 | 0.0531 | 0.0270 | 0.0630 |
| 0.50 - 0.49 | 100.0 | 4.54 | 27.42 | 0.0621 | 0.0307 | 0.0652 |
| 0.49 - 0.47 | 100.0 | 3.69 | 25.70 | 0.0422 | 0.0319 | 0.0385 |
| 0.47 - 0.46 | 100.0 | 3.20 | 21.73 | 0.0382 | 0.0376 | 0.0449 |
| 0.46 - 0.45 | 99.0 | 2.97 | 21.36 | 0.0374 | 0.0371 | 0.0468 |
| 0.45 - 0.44 | 98.3 | 2.71 | 18.98 | 0.0435 | 0.0427 | 0.0559 |
| 0.44 - 0.43 | 91.8 | 2.28 | 16.18 | 0.0489 | 0.0502 | 0.0714 |
| 0.43 - 0.42 | 84.7 | 1.79 | 12.27 | 0.0603 | 0.0652 | 0.0778 |
| 0.42 - 0.41 | 61.6 | 0.96 | 11.60 | 0.0576 | 0.0748 | 0.0867 |
| 0.41 - 0.40 | 48.6 | 0.64 | 9.39 | 0.0628 | 0.0901 | 0.0393 |
| | | | | | | |
| 0.50 – 0.40 | 84.8 | 2.37 | 18.77 | 0.0462 | 0.0437 | 0.0536 |
| Inf – 0.40 | 92.7 | 6.88 | 36.43 | 0.0430 | 0.0164 | 0.0447 |

### 10.1.3  XD2006 Standard Refinement Strategy

| | | | |
|---|---|---|---|
| 1. | Scale factor | 22. | $U_{ij}$, xyz, M, D,     Q, O, H, kappa |
| 2. | M | 23. | $U_{ij}$, xyz, M, D,     Q, O, H, kappa     sigobs 2 |
| 3. | D, Q, O, H | 24. | $U_{ij}$, xyz, M, D,     Q, O, H, kappa     sigobs 1 |
| 4. | M, D, Q, O, H | 25. | $U_{ij}$, xyz, M, D,     Q, O, H, kappa     sigobs 0 |
| 5. | $U_{ij}$ | 26. | D, Q, O, H     NO SYM |
| 6. | M, D, Q, O, H | 27. | $U_{ij}$, xyz, M, D,     Q, O, H |
| 7. | $U_{ij}$, M, D,Q, O, H | 28. | $U_{ij}$, xyz, D,     Q, O, H, kappa |
| 8. | xyz | 29. | $U_{ij}$, xyz, M, D,     Q, O, H, kappa |
| 9. | xyz, M, D, Q, O, H | 30. | M     No CHEMCON |
| 10. | $U_{ij}$, xyz, M, D, Q, O, H | 31. | D, Q, O, H |
| 11. | kappa | 32. | $U_{ij}$, xyz, M, D,     Q, O, H |
| 12. | M | 33. | $U_{ij}$, xyz, D,     Q, O, H, kappa |
| 13. | M, kappa | 34. | xyz, $U_{ij}$, M, D,     Q, O, H, kappa |
| 14. | $U_{ij}$, xyz, M, D, Q, O, H | |     SHADE |
| 15. | kappa | 35. | xyz (hydrogen) $\sin\theta/\lambda$ 0.0 – 0.5 Å$^{-1}$ |
| 16. | $U_{ij}$, xyz, M, D, Q, O, H, kappa | 36. | $U_{ij}$, xyz, D, Q, O, H |
| 17. | xyz (hydrogen) $\sin\theta/\lambda$ 0.0 – 0.5 Å$^{-1}$ | 37. | xyz, $U_{ij}$, D, Q, O, H, kappa |
| 18. | $U_{ij}$, xyz, M, D, Q, O, H | 38. | xyz, $U_{ij}$, M, D, Q, O, H, kappa |
| 19. | $U_{ij}$, xyz, D, Q, O, H, kappa | 39. | kappa' |
| 20. | $U_{ij}$, xyz, M, D, Q, O, H, kappa | 40. | xyz, $U_{ij}$, M, D, Q, O, H, kappa |
| 21. | kappa' | | |

Scheme 12: Refinement strategy applied for paracyclophane.

1. Scale factor
2. D, Q, O, H
3. M
4. M, D, Q, O, H
5. *U*$_{ij}$
6. M, D, Q, O, H
7. *U*$_{ij}$, M, D, Q, O, H
8. Xyz
9. xyz, M, D, Q, O, H
10. xyz, *U*$_{ij}$, M, D, Q, O, H
11. κ
12. M
13. M, κ
14. xyz, *U*$_{ij}$, M, D, Q, O, H
15. κ

16. xyz, *U*$_{ij}$, M, D, Q, O, H, κ
17. xyz
18. xyz, *U*$_{ij}$, M, D, Q, O, H
19. xyz, *U*$_{ij}$, D, Q, O, H, κ
20. xyz, *U*$_{ij}$, M, D, Q, O, H, κ
21. κ'
22. D, Q, O, H
23. xyz, *U*$_{ij}$, M, D, Q, O, H, κ
24. xyz, *U*$_{ij}$, M, D, Q, O, H, κ     sigobs 1
25. xyz, *U*$_{ij}$, M, D, Q, O, H, κ     sigobs 0
26. xyz, *U*$_{ij}$, M, D, Q, O, H, weight
27. xyz, *U*$_{ij}$, D, Q, O, H, κ, weight
28. xyz, *U*$_{ij}$, M, D, Q, O, H, κ, weight
29. κ',weight
30. xyz, *U*$_{ij}$, M, D, Q, O, H, κ, weight

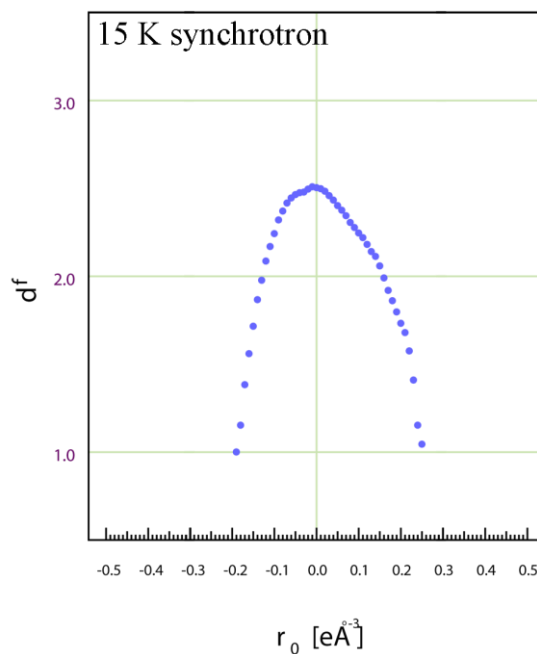## 10.1.4  Residual Density Analysis according to Henn & Meindl

### 10.1.4.1        Residual Density Analysis plots for Chapter 4.4.3

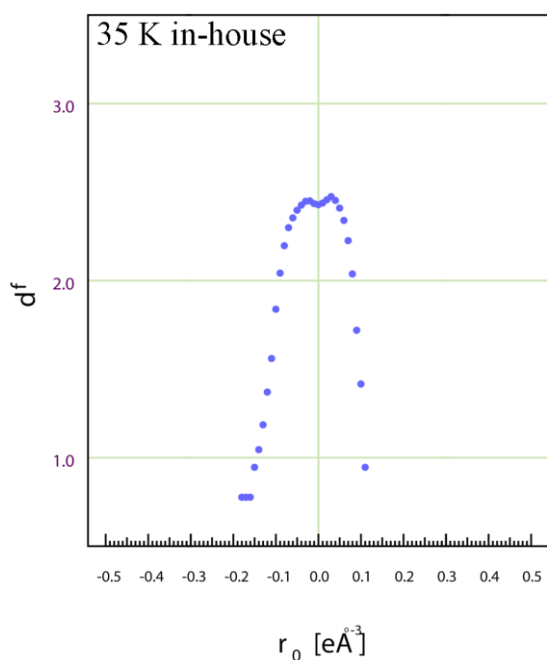Fractal dimension plots of the residual density calculated for the maximum resolution
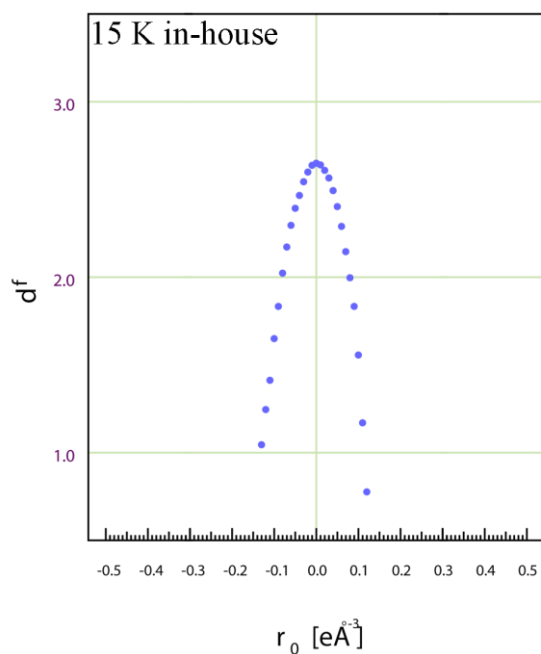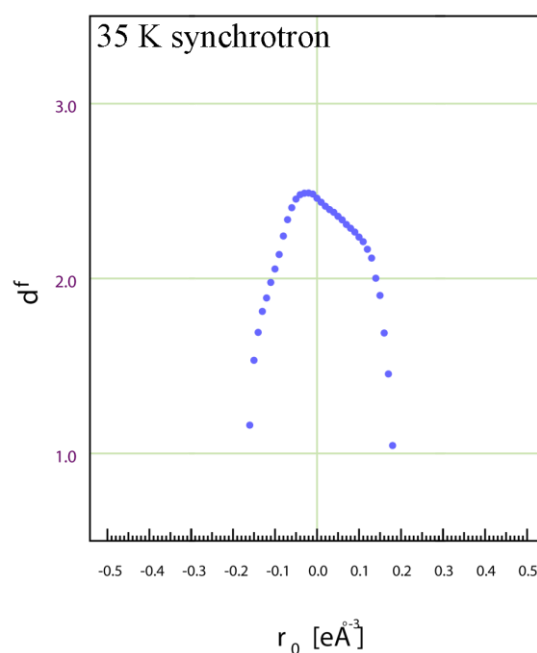


$d^f(0) = 2.6489$

$e_{gross} = 7.6100$

$d^f(0) = 2.5044$

$e_{gross} = 15.1038$



$d^f(0) = 2.4283$

$e_{gross} = 10.1920$

$d^f(0) = 2.4585$

$e_{gross} = 13.6089$

## 10.1.5 Bond lengths and angles after XD refinement in 4.4.4

Marked in red are the values deviating more than 3σ from the in-house values.

| Bond | 15 K in-house | 15 K synchrotron | 35 K in-house | 35 K synchrotron |
|---|---|---|---|---|
| C1-C2 | 1.40087(16) | 1.39869(15) | 1.40054(17) | 1.39859(18) |
| C1-C3 | 1.50901(15) | 1.50809(12) | 1.50907(15) | 1.50751(16) |
| C1-C4 | 1.40168(16) | 1.39991(15) | 1.40144(16) | 1.39934(18) |
| C2-C4 | 1.39515(14) | 1.39382(12) | 1.39523(14) | 1.39370(15) |
| C3-X7_C3 | 1.59465 | 1.59215 | 1.59336 | 1.59118 |
| C2-H2 | 1.07600(11) | 1.07600(10) | 1.07601(11) | 1.07600(12) |
| C3-H31 | 1.08500(12) | 1.08500(11) | 1.08500(13) | 1.08501(14) |
| C3-H32 | 1.08500(12) | 1.08500(11) | 1.08500(12) | 1.08500(15) |
| C4-H4 | 1.07600(11) | 1.07600(10) | 1.07600(11) | 1.07600(12) |

| Angle | 15 K in-house | 15 K synchrotron | 35 K in-house | 35 K synchrotron |
|---|---|---|---|---|
| C2-C1-C3 | 121.113(10) | 121.102(9) | 121.153(11) | 121.135(12) |
| C2-C1-C4 | 117.210(9) | 117.195(8) | 117.204(9) | 117.192(9) |
| C3-C1-C4 | 120.368(10) | 120.391(9) | 120.338(11) | 120.363(12) |
| C1-C2-C4 | 120.358(10) | 120.380(9) | 120.392(10) | 120.386(11) |
| C1-C2-H2 | 119.064(10) | 119.463(9) | 119.182(10) | 118.218(11) |
| C4-C2-H2 | 119.570(11) | 118.730(10) | 119.290(11) | 119.520(12) |
| C1-C3-H31 | 109.040(10) | 112.070(9) | 109.631(10) | 112.631(11) |
| C1-C3-H32 | 112.432(10) | 110.219(9) | 112.785(10) | 110.531(12) |
| H31-C3-H32 | 109.368(9) | 108.858(8) | 109.370(10) | 109.973(10) |
| C1-C4-C2 | 120.783(11) | 120.780(9) | 120.756(10) | 120.777(11) |
| C1-C4-H4 | 117.539(10) | 119.393(9) | 117.861(10) | 117.529(11) |
| C2-C4-H4 | 121.125(11) | 119.377(10) | 120.875(11) | 121.337(12) |

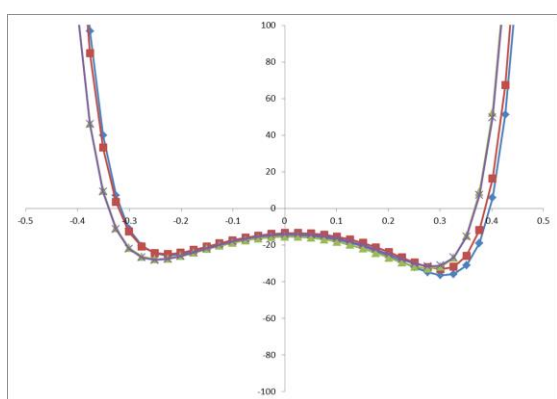## 10.1.6  Properties along the bond path for datasets discussed in 4.4.4

All four datasets have been summarized in the same plot to make the comparison easier.

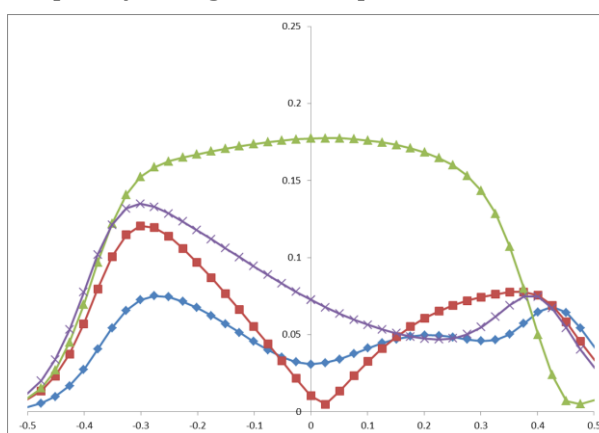The following color code has been used in all graphs.



15K_inhouse
35K_inhouse
15K_APS
35K_APS

C3 and C1

Laplacian along the bond path



Ellipticity along the bond path



C3 and X2_C3

Laplacian along the bond path



Ellipticity along the bond path



148

## C1 and C4
Laplacian along the bond path  Ellipticity along the bond path



## C2 and C4
Laplacian along the bond path  Ellipticity along the bond path



## C1 and C2
Laplacian along the bond path  Ellipticity along the bond path
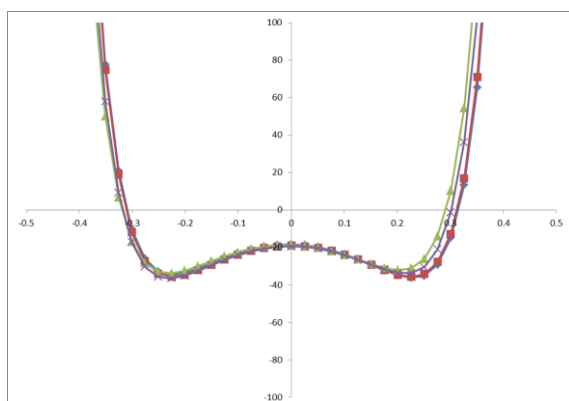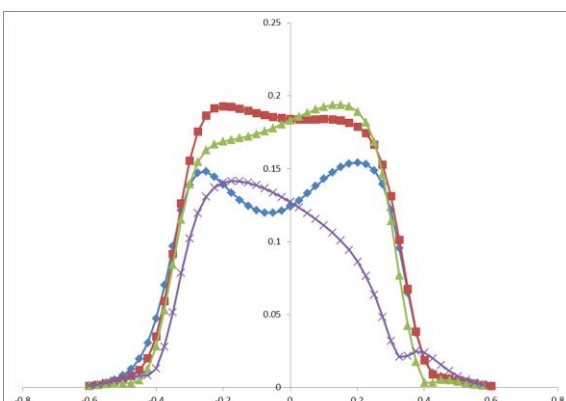
C2 and H2

Laplacian along the bond path
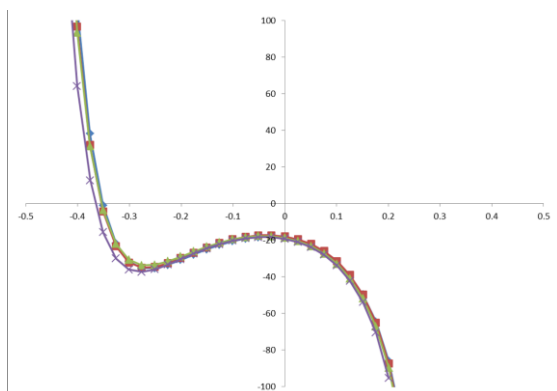
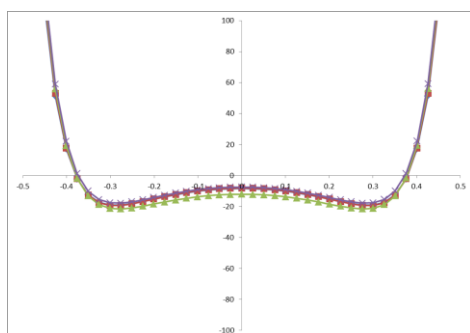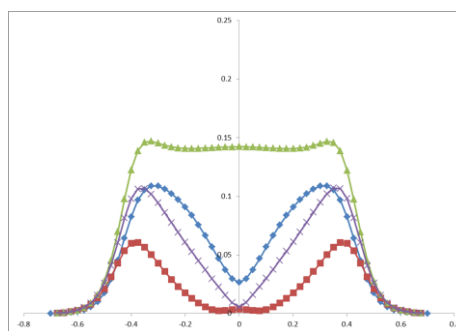Ellipticity along the bond path
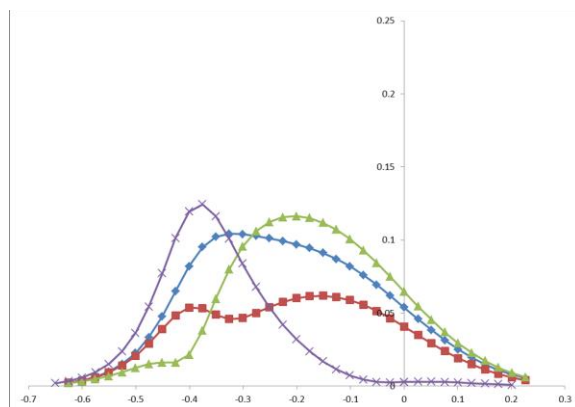


C3 and H31

Laplacian along the bond path

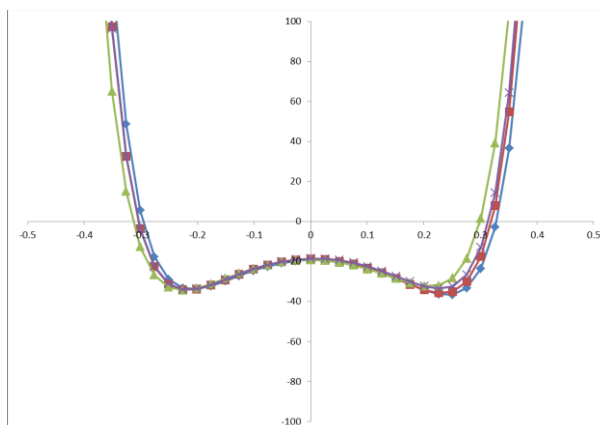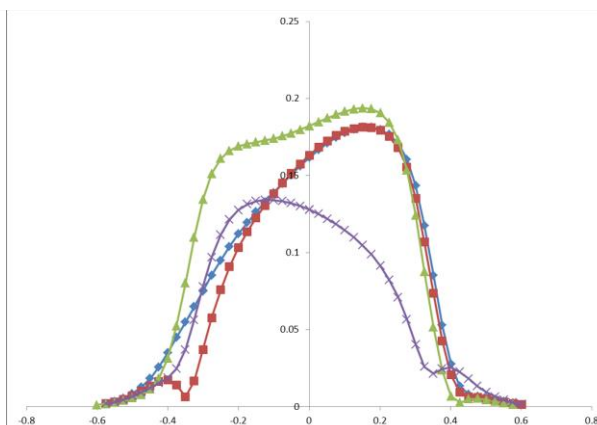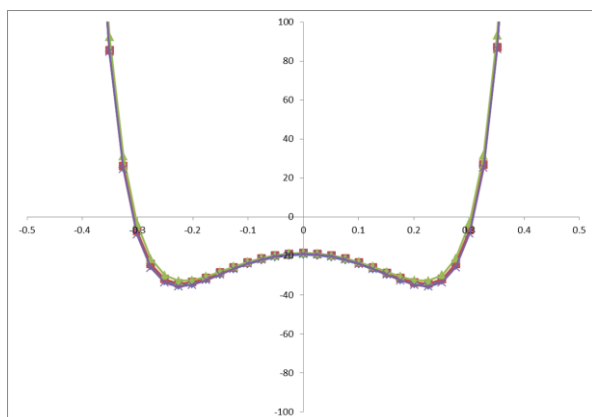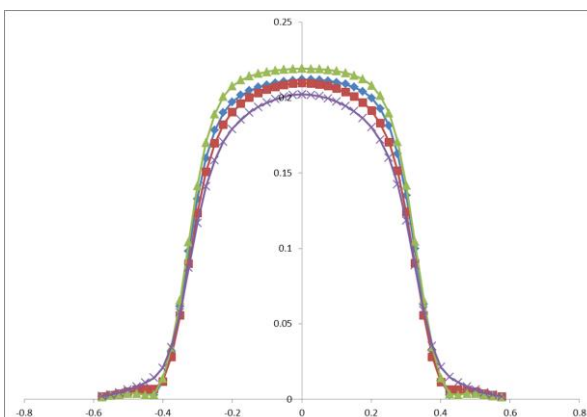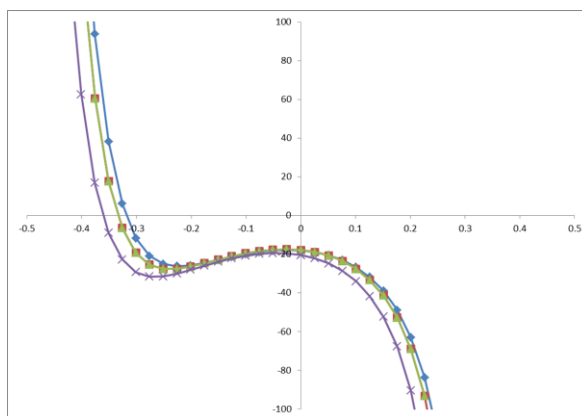Ellipticity along the bond path
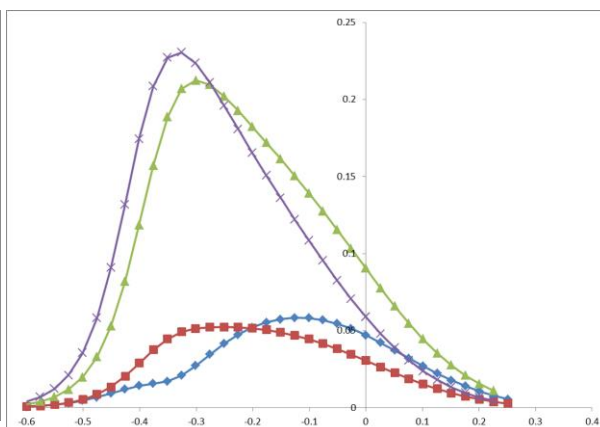


C3 and H32

Laplacian along the bond path
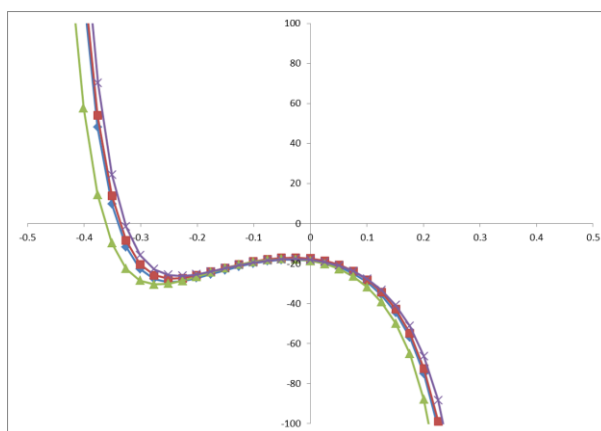
Ellipticity along the bond path
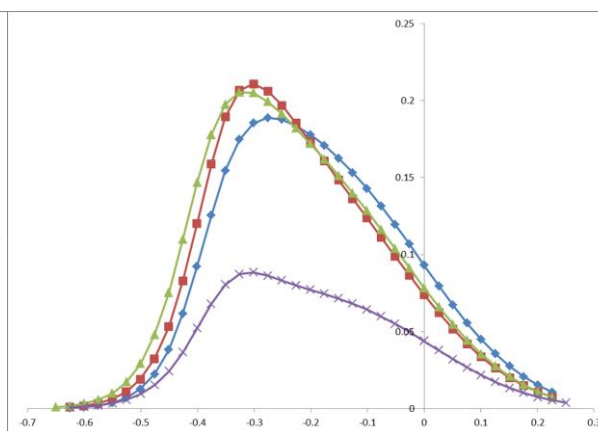
## C4 and H4

Laplacian along the bond path
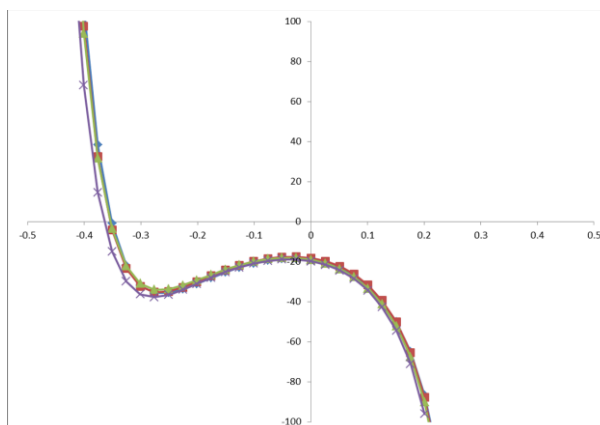
Ellipticity along the bond path
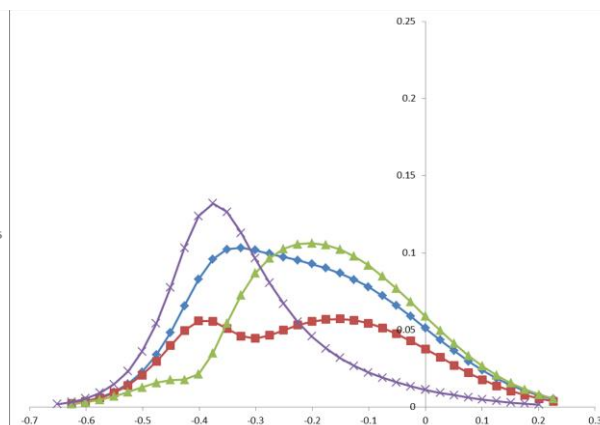
## 10.2   Additional information on TCNQ

### 10.2.1  Data collection strategy 100 K in-house

Image width: 0.3°                                          crystal size: 0.24 x 0.22 x 0.06 mm

Detector Distance: 5 cm

| run | exposure time | 2 theta value |
|-----|---------------|---------------|
| 1 | 2 | -24 |
| 2 | 2 | -24 |
| 3 | 2 | -24 |
| 4 | 2 | -24 |
| 5 | 20 | -40 |
| 6 | 20 | -40 |
| 7 | 20 | -40 |
| 8 | 20 | -40 |
| 9 | 100 | -80 |
| 10 | 100 | -80 |
| 11 | 100 | -80 |
| 12 | 100 | -80 |
| 13 | 1 | 0 |

### 10.2.2  Data collection strategy 100 K Bruker TXS

Image width: 0.5°                                          crystal size: 0.203 x 0.148 x 0.077 mm

Detector Distance: 4 cm

| run | exposure time | 2 theta value |
|-----|---------------|---------------|
| 1 | 60 | -72.50 |
| 2 | 90 | -107.50 |
| 3 | 90 | -107.50 |
| 4 | 10 | -15.00 |
| 5 | 90 | -102.50 |
| 6 | 90 | -90.00 |
| 7 | 30 | -37.50 |
| 8 | 10 | -7.50 |
| 9 | 60 | -72.50 |
| 10 | 60 | -82.50 |
| 11 | 90 | -110.00 |
| 12 | 10 | 10.00 |
| 13 | 10 | 25.00 |
| 14 | 90 | -102.50 |
| 15 | 90 | -102.50 |
| 16 | 90 | -105.00 |
| 17 | 90 | -107.50 |
| 18 | 90 | -110.00 |

| | | |
|---|---|---|
| 19 | 90 | -100.00 |
| 20 | 90 | -90.00 |
| 21 | 90 | -110.00 |

## 10.2.3  Data collection strategy APS 15 K and 31.5keV

Image width: 0.5°  crystal size: 0.130 x 0.127 x 0.030 mm

Detector Distance: 5 cm

| Run | exposure time | 2 theta value |
|---|---|---|
| 1 | 1.50 | -45 |
| 2 | 1.50 | -45 |
| 3 | 1.5 | -40 |
| 4 | 0.3 | 0 |
| 5 | 1.5 | -45 |
| 6 | 1.5 | -45 |
| 7 | 1.5 | -45 |
| 8 | 1.5 | -45 |
| 9 | 1.5 | -45 |
| 10 | 0.6 | 0 |
| 11 | 0.6 | 0 |
| 12 | 0.6 | 0 |
| 13 | 1.5 | -45 |

## 10.2.4 Data collection strategy APS 15 K and 30 keV

Image width: 0.5°                                        crystal size: unknown

Detector Distance: 5 cm

| run | exposure time | 2 theta value |
| --- | --- | --- |
| 1 | 0.5 | -25 |
| 2 | 0.5 | -25 |
| 3 | 0.5 | -25 |
| 4 | 0.5 | -25 |
| 5 | 0.5 | -25 |
| 6 | 0.5 | -25 |
| 7 | 0.5 | 0 |
| 8 | 0.5 | 0 |
| 9 | 0.5 | -25 |
| 10 | 0.5 | -25 |
| 11 | 0.5 | -25 |
| 12 | 0.5 | -25 |
| 13 | 0.5 | -25 |
| 14 | 0.5 | -25 |

## 10.2.5  XD2006 refinement strategy

| | | |
|---|---|---|
| 1. | Scale factor | |
| 2. | M | all atoms |
| 3. | D,Q,O,H | |
| 4. | M,D,Q,O,H | |
| 5. | $U_{ij}$ | all atoms |
| 6. | M, D, Q, O, H | |
| 7. | $U_{ij}$, M, D, Q, O, H | |
| 8. | XYZ | heavy atoms |
| 9. | XYZ, M, D, Q, O, H | |
| 10. | $U_{ij}$, XYZ, M, D, Q, O, H | XYZ heavy atoms |
| 11. | K | heavy atoms |
| 12. | M | |
| 13. | $\kappa$, M | $\kappa$ heavy atoms |
| 14. | $U_{ij}$, XYZ, M, D, Q, O, H | XYZ heavy atoms |
| 15. | $\kappa$ | heavy atoms |
| 16. | $U_{ij}$, XYZ, M, D, Q, O, H | XYZ heavy atoms |
| 17. | XYZ | hydrogen atoms $\sin\theta/\lambda = 0.0–0.5$ Å$^{-1}$ |
| 18. | $U_{ij}$, XYZ, M, D, Q, O, H | Reset |
| 19. | $U_{ij}$, XYZ, M, D, Q, O, H, $\kappa$ | $\kappa$ heavy atoms |
| 20. | $U_{ij}$, XYZ, D, Q, O, H | |

| | | |
|---|---|---|
| 21. | $\kappa'$ | heavy atoms |
| 22. | D,Q,O,H | |
| 23. | $U_{ij}$, XYZ, M, D, Q, O, H, $\kappa$ | $\kappa$ heavy atoms |
| 24. | $U_{ij}$, XYZ, M, D, Q, O, H, $\kappa$ | sigobs 2 |
| 25. | $U_{ij}$, XYZ, M, D, Q, O, H, $\kappa$ | sigobs 1 |
| 26. | $U_{ij}$, XYZ, M, D, Q, O, H, $\kappa$ | sigobs 0 |
| 27. | D, Q, O, H | NOSYM |
| 28. | $U_{ij}$, XYZ, M, D, Q, O, H | NOSYM |
| 29. | $U_{ij}$, XYZ ,D, Q, O, H, $\kappa$ | NOSYM |
| 30. | $U_{ij}$, XYZ, M, D, Q, O, H, $\kappa$ | NOSYM |
| 31. | $U_{ij}$, XYZ, M, D, Q, O, H | NOSYM; wght |
| 32. | $U_{ij}$, XYZ, D, Q, O, H, $\kappa$ | NOSYM; wght |
| 33. | $U_{ij}$, XYZ, M, D, Q, O, H, $\kappa$ | NOSYM; wght |
| SHADE | | |
| 34. | XYZ | hydrogen atoms $\sin\theta/\lambda = 0.0–0.5$ Å$^{-1}$ |
| 35. | $U_{ij}$, XYZ, M, D, Q, O, H | |
| 36. | $U_{ij}$, XYZ, D, Q, O, H, $\kappa$ | |
| 37. | $U_{ij}$, XYZ, M, D, Q, O, H, $\kappa$ | |

## 10.2.6  Residual Density Analysis
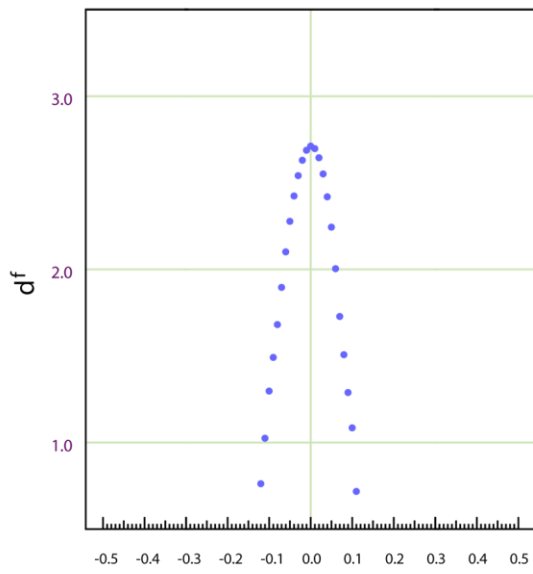


100 K in house     $r_0$ [eÅ$^{-3}$]

$d^f(0) = 2.7124$

$e_{gross} = 10.5553$ e
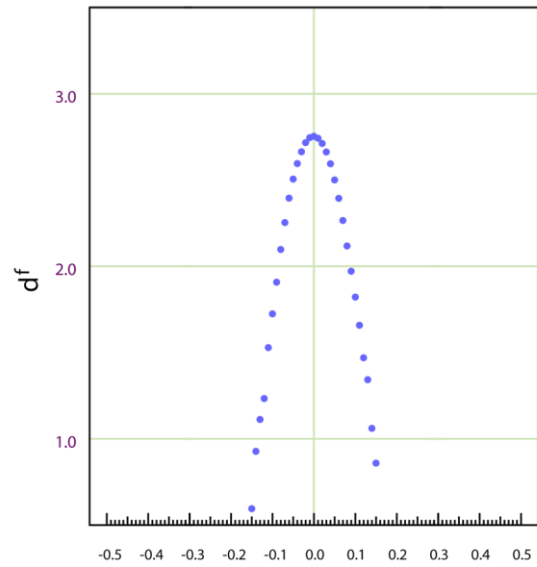


100 K Bruker     $r_0$ [eÅ$^{-3}$]

$d^f(0) = 2.7542$

$e_{gross} = 14.4647$ e
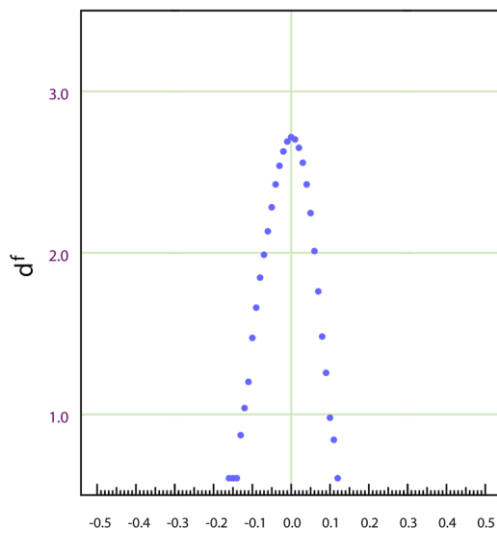


15 K APS 30 keV     $r_0$ [eÅ$^{-3}$]

$d^f(0) = 2.7160$

$e_{gross} = 10.5410$ e
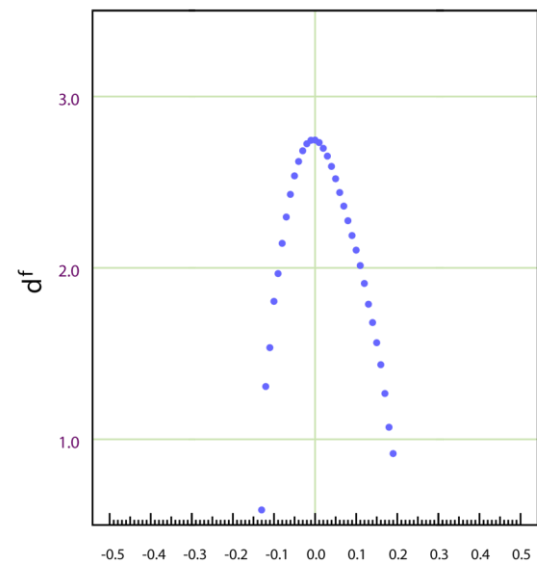


15 K APS 31.5 keV $r_0$ [eÅ$^{-3}$]

$d^f(0) = 2.7455$

$e_{gross} = 15.4869$ e

## 10.2.7  Multipole Populations for all four datasets

Values given in red differ more than 3σ from the numbers derived from the 100 K in-house data.

### 10.2.7.1        Pole Populations for N1/N2

|  | Invariom 100 K | 100 K Bub | 100 K Bruker | 15 K 30 keV | 15 K 31.5 keV |
|---|---|---|---|---|---|
| Pval | 5.036 | 5.058(23) | 5.107(20) | 4.985(12) | 5.071(16) |
| D11+ | 0.000 | -0.011(8) | -0.003(8) | 0.005(3) | -0.007(4) |
| D11- | 0.000 | -0.014(8) | 0.002(8) | -0.002(3) | 0.007(4) |
| D10 | -0.041 | -0.002(8) | 0.017(9) | -0.043(3) | -0.039(4) |
| Q20 | 0.217 | 0.209(6) | 0.213(6) | 0.199(3) | 0.206(4) |
| Q21+ | 0 | 0.002(5) | -0.001(5) | 0.000(3) | -0.010(3) |
| Q21- | 0 | 0.006(5) | -0.002(5) | 0.001(3) | -0.003(3) |
| Q22+ | 0 | 0.005(5) | 0.014(5) | 0.008(3) | -0.019(3) |
| Q22- | 0 | -0.006(4) | 0.001(5) | 0.006(2) | 0.008(3) |
| O30 | 0.031 | 0.050(6) | 0.051(6) | 0.040(3) | 0.034(4) |
| O31+ | 0 | 0.005(5) | 0.007(6) | 0.001(3) | -0.003(3) |
| O31- | 0 | 0.005(5) | 0.004(5) | 0.002(3) | 0.002(3) |
| O32+ | 0 | 0.002(5) | -0.005(6) | 0.001(3) | 0.003(3) |
| O32- | 0 | -0.002(5) | 0.002(5) | -0.001(3) | -0.002(3) |
| O33+ | 0 | 0.010(5) | 0.003(5) | -0.002(2) | -0.004(3) |
| O33- | 0 | -0.012(5) | -0.005(5) | -0.003(2) | -0.005(3) |
| H40 | -0.009 | 0.003(6) | 0.014(7) | 0.013(4) | -0.010(5) |
| H41+ | 0 | 0.010(5) | -0.007(6) | 0.004(3) | -0.007(4) |
| H41- | 0 | 0.010(6) | -0.012(6) | -0.008(3) | 0.007(4) |
| H42+ | 0 | 0.002(6) | 0.009(6) | 0.005(3) | -0.001(4) |
| H42- | 0 | 0.001(5) | -0.001(6) | 0.002(3) | -0.004(4) |
| H43+ | 0 | 0.006(5) | 0.008(6) | 0.005(3) | 0.005(4) |
| H43- | 0 | 0.004(5) | -0.001(6) | -0.004(3) | 0.003(4) |
| H44+ | 0 | 0.010(5) | 0.009(5) | 0.001(3) | -0.008(4) |
| H44- | 0 | -0.013(5) | -0.004(5) | 0.005(3) | -0.010(4) |

### 10.2.7.2 Pole Populations for C1/C2

| | Inavriom | 100K Bub | 100 K Bruker | 15 K 30kev | 15 K 31.5 kev |
|---|---|---|---|---|---|
| Pval | 3.978 | 3.995(29) | 3.968(26) | 4.081(17) | 4.006(21) |
| | | | | | |
| D11+ | 0 | 0.010(5) | 0.019(6) | 0.001(3) | -0.011(4) |
| D11- | 0 | 0.004(5) | 0.010(5) | -0.005(3) | -0.010(4) |
| D10 | -0.041 | 0.128(8) | 0.129(9) | 0.158(4) | 0.157(6) |
| | | | | | |
| Q20 | -0.172 | 0.302(8) | 0.302(9) | 0.317(4) | 0.337(5) |
| Q21+ | 0 | -0.003(6) | -0.008(6) | -0.001(3) | -0.017(4) |
| Q21- | 0 | -0.016(6) | -0.009(6) | -0.001(3) | 0.004(4) |
| Q22+ | 0 | -0.009(5) | -0.009(5) | -0.002(3) | -0.039(4) |
| Q22- | -0.036 | -0.003(4) | -0.002(5) | -0.001(3) | -0.019(4) |
| | | | | | |
| O30 | 0 | -0.057(7) | -0.063(8) | -0.041(5) | -0.048(6) |
| O31+ | 0 | 0.006(6) | 0.012(7) | 0.001(4) | 0.000(5) |
| O31- | 0.031 | 0.000(6) | 0.004(6) | 0.000(4) | 0.000(5) |
| O32+ | 0 | -0.029(5) | -0.022(6) | -0.010(3) | -0.015(5) |
| O32- | 0 | -0.010(6) | -0.005(6) | -0.001(3) | -0.007(5) |
| O33+ | 0.238 | -0.002(5) | -0.002(5) | 0.005(3) | 0.006(4) |
| O33- | 0.009 | 0.003(5) | -0.002(5) | -0.003(3) | 0.002(4) |
| | | | | | |
| H40 | -0.009 | 0.015(9) | 0.020(9) | 0.026(6) | 0.011(7) |
| H41+ | 0 | -0.011(8) | -0.008(8) | 0.003(5) | -0.008(6) |
| H41- | 0 | -0.018(8) | 0.003(8) | 0.014(5) | -0.015(7) |
| H42+ | 0 | -0.010(7) | -0.008(8) | 0.002(5) | -0.008(6) |
| H42- | 0 | 0.007(7) | 0.006(8) | -0.004(4) | -0.010(6) |
| H43+ | 0 | -0.002(7) | -0.008(7) | 0.009(4) | 0.005(6) |
| H43- | 0 | -0.012(7) | -0.002(7) | 0.009(4) | 0.000(6) |
| H44+ | 0 | -0.001(6) | 0.009(6) | -0.002(4) | -0.005(5) |
| H44- | 0 | 0.022(6) | 0.013(6) | -0.005(4) | 0.020(5) |

### 10.2.7.3    Pole Populations for C3

|        | Invariom | 100K Bub    | 100 K Bruker | 15 K 30kev  | 15 K 31.5 kev |
|--------|----------|-------------|--------------|-------------|---------------|
| Pval   | 3.983    | 4.150(40)   | 4.138(38)    | 4.042(25)   | 4.012(30)     |
|        |          |             |              |             |               |
| D11+   |          | 0.023(7)    | 0.006(8)     | -0.006(5)   | 0.011(6)      |
| D11-   |          | 0.003(6)    | 0.002(6)     | -0.003(4)   | -0.005(6)     |
| D10    | -0.001   | 0.124(9)    | 0.108(9)     | 0.081(6)    | 0.083(7)      |
|        |          |             |              |             |               |
| Q20    | 0.081    | 0.115(8)    | 0.111(8)     | 0.113(5)    | 0.119(6)      |
| Q21+   |          | 0.001(7)    | 0.001(7)     | -0.006(4)   | -0.033(5)     |
| Q21-   |          | -0.008(6)   | 0.018(6)     | 0.010(4)    | -0.004(5)     |
| Q22+   | -0.152   | -0.082(7)   | -0.089(7)    | -0.074(4)   | -0.106(5)     |
| Q22-   |          | 0.011(6)    | 0.007(6)     | 0.003(4)    | -0.013(5)     |
|        |          |             |              |             |               |
| O30    | 0.203    | 0.225(9)    | 0.232(10)    | 0.209(6)    | 0.192(7)      |
| O31+   |          | 0.014(8)    | 0.020(8)     | 0.001(5)    | 0.001(6)      |
| O31-   |          | -0.015(7)   | -0.001(7)    | 0.009(5)    | 0.007(6)      |
| O32+   | 0.147    | 0.183(8)    | 0.210(9)     | 0.193(5)    | 0.185(7)      |
| O32-   |          | 0.021(7)    | 0.007(7)     | 0.004(5)    | -0.009(6)     |
| O33+   |          | 0.003(7)    | 0.002(8)     | 0.000(5)    | -0.017(6)     |
| O33-   |          | 0.006(6)    | 0.004(6)     | 0.007(4)    | -0.006(5)     |
|        |          |             |              |             |               |
| H40    | 0.016    | 0.051(12)   | 0.024(13)    | -0.012(7)   | -0.011(10)    |
| H41+   |          | -0.008(10)  | 0.016(10)    | -0.005(6)   | -0.008(8)     |
| H41-   |          | 0.000(9)    | 0.001(9)     | 0.001(6)    | 0.000(8)      |
| H42+   | 0.002    | 0.014(10    | 0.005(12)    | -0.033(7)   | -0.011(9)     |
| H42-   |          | 0.020(9)    | -0.007(10)   | -0.020(6)   | 0.000(8)      |
| H43+   |          | 0.016(9)    | 0.035(10)    | -0.008(6)   | 0.022(8)      |
| H43-   |          | -0.010(8)   | 0.003(8      | -0.006(5)   | 0.006(7)      |
| H44+   | 0.009    | 0.034(9)    | 0.014(9)     | 0.019(6)    | 0.013(7)      |
| H44-   |          | 0.021(7)    | 0.009(7)     | -0.001(5)   | -0.003(6)     |

### 10.2.7.4 Pole Populations for C4

| | Invariom | 100K Bub | 100 K Bruker | 15 K 30kev | 15 K 31.5 kev |
|---|---|---|---|---|---|
| Pval | 4.028 | 3.831(39) | 3.811(38) | 3.894(25) | 3.907(31) |
| | | | | | |
| D11+ | | -0.004(6) | -0.003(6) | -0.004(4) | 0.003(5) |
| D11- | | 0.007(6) | 0.003(6) | 0.004(4) | -0.007(5) |
| D10 | 0.040 | -0.019(8) | -0.020(8) | -0.015(5) | 0.012(7) |
| | | | | | |
| Q20 | 0.045 | 0.080(7) | 0.075(8) | 0.096(4) | 0.126(6) |
| Q21+ | | 0.002(6) | 0.001(6) | -0.005(4) | -0.019(5) |
| Q21- | | 0.007(6) | -0.009(6) | -0.007(4) | 0.012(5) |
| Q22+ | -0.033 | -0.158(6) | -0.153(7) | -0.156(4) | -0.179(5) |
| Q22- | | -0.007(6) | -0.003(6) | -0.004(4) | 0.017(5) |
| | | | | | |
| O30 | 0.2 | 0.161(8) | 0.168(9) | 0.191(5) | 0.172(7) |
| O31+ | | -0.003(7) | 0.001(7) | 0.006(4) | -0.005(6) |
| O31- | | -0.011(6) | -0.009(7) | 0.000(4) | -0.009(6) |
| O32+ | 0.178 | 0.169(7) | 0.162(8) | 0.170(5) | 0.152(6) |
| O32- | | 0.007(7) | -0.008(8) | 0.004(5) | -0.015(6) |
| O33+ | | 0.002(6) | -0.003(6) | -0.002(4) | 0.004(5) |
| O33- | | 0.012(5) | 0.003(6) | -0.004(4) | -0.006(5) |
| | | | | | |
| H40 | -0.002 | 0.010(11) | -0.024(12) | -0.019(7) | 0.009(9) |
| H41+ | | -0.006(8) | 0.000(9) | -0.006(5) | -0.030(7) |
| H41- | | 0.009(8) | -0.002(8) | 0.004(6) | -0.007(7) |
| H42+ | -0.002 | 0.005(10) | -0.034(11) | -0.031(6) | 0.005(8) |
| H42- | | 0.017(9) | 0.007(11) | 0.003(6) | 0.015(8) |
| H43+ | | 0.017(7) | 0.011(8) | -0.010(5) | 0.002(7) |
| H43- | | 0.006(8) | -0.005(8) | 0.000(5) | -0.019(7) |
| H44+ | 0.014 | 0.033(8) | 0.019(8) | 0.013(5) | 0.021(7) |
| H44- | | 0.014(8) | 0.004(9) | 0.008(5) | -0.013(7) |

### 10.2.7.5       Pole Populations for C5/C6

|  | Invariom | 100K Bub | 100 K Bruker | 15 K 30kev | 15 K 31.5 kev |
|---|---|---|---|---|---|
| Pval | 4.014 | 4.131(21) | 4.101(20) | 4.109(10) | 4.091(17) |
|  |  |  |  |  |  |
| D11+ |  | -0.004(4) | -0.005(4) | 0.004(3) | 0.004(4) |
| D11- |  | 0.030(5) | 0.026(5) | 0.033(3) | 0.037(4) |
| D10 | 0.040 | 0.013(6) | 0.010(6) | 0.019(3) | 0.005(5) |
|  |  |  |  |  |  |
| Q20 | 0.296 | 0.101(5) | 0.105(5) | 0.106(3) | 0.124(4) |
| Q21+ |  | -0.010(4) | -0.004(4) | 0.001(3) | 0.004(3) |
| Q21- |  | -0.025(5) | -0.021(5) | -0.032(3) | -0.041(4) |
| Q22+ |  | -0.158(5) | -0.162(5) | -0.152(3) | -0.187(4) |
| Q22- |  | -0.011(4) | -0.003(4) | -0.003(3) | 0.007(3) |
|  |  |  |  |  |  |
| O30 | -0.069 | 0.240(5) | 0.245(6) | 0.243(3) | 0.247(5) |
| O31+ |  | -0.011(5) | -0.002(5) | 0.015(3) | -0.020(4) |
| O31- |  | 0.024(5) | 0.031(5) | 0.021(3) | -0.012(4) |
| O32+ |  | 0.139(5) | 0.144(5) | 0.142(3) | 0.142(4) |
| O32- |  | 0.006(5) | 0.004(5) | -0.007(3) | -0.002(4) |
| O33+ |  | -0.024(4) | -0.008(5) | 0.002(3) | 0.006(4) |
| O33- |  | 0.021(5) | 0.037(5) | 0.031(3) | 0.027(4) |
|  |  |  |  |  |  |
| H40 | -0.041 | -0.003(7) | 0.023(7) | 0.016(4) | 0.021(6) |
| H41+ |  | -0.007(5) | 0.005(5) | 0.011(3) | -0.005(5) |
| H41- |  | 0.029(6) | 0.014(6) | 0.002(4) | -0.005(5) |
| H42+ |  | -0.022(6) | -0.003(6) | -0.004(4) | -0.018(5) |
| H42- |  | 0.021(6) | 0.009(6) | -0.011(4) | 0.018(5) |
| H43+ |  | -0.012(6) | -0.002(6) | 0.002(4) | -0.007(5) |
| H43- |  | -0.008(6) | -0.016(6) | -0.006(4) | -0.010(5) |
| H44+ |  | 0.011(6) | 0.021(6) | 0.020(4) | 0.010(5) |
| H44- |  | 0.003(5) | -0.003(6) | 0.001(4) | -0.005(5) |

## 10.2.8 Laplacian and Ellipticity along the bond path for all four datasets
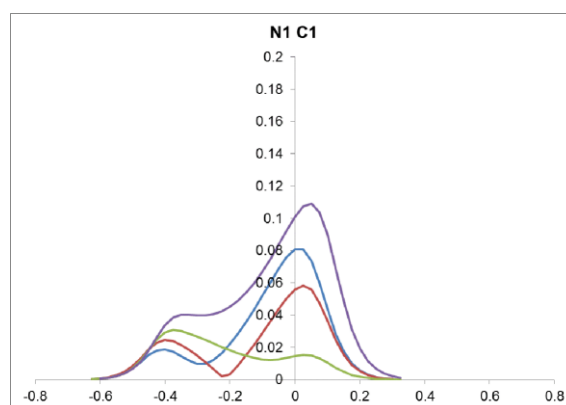
Colour coding:

━━ 100 K in house
━━ 100 K Bruker
━━ 15 K APS 30 keV
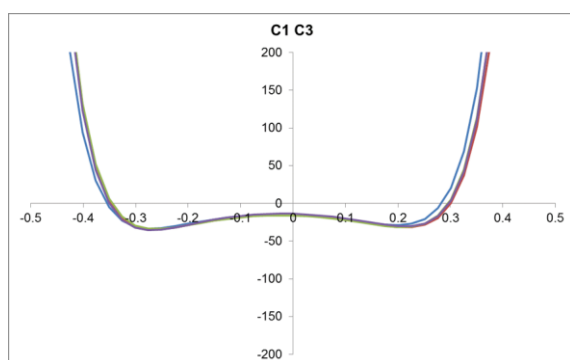━━ 15 K APS 31.5 keV

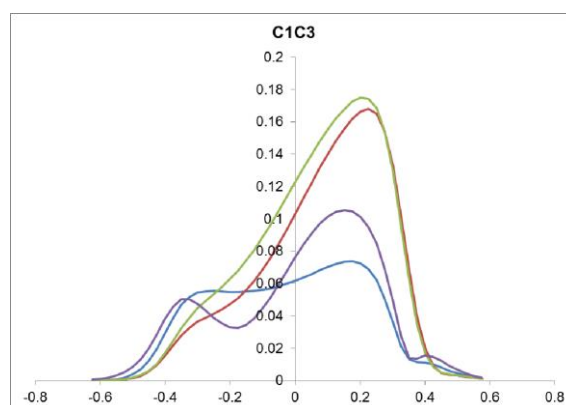N1 and C1

Laplacian
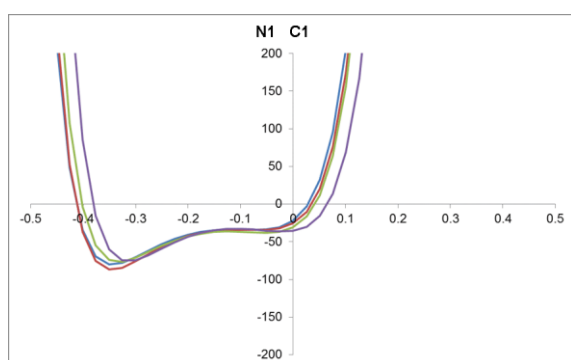
Ellipticity

C1 and C3
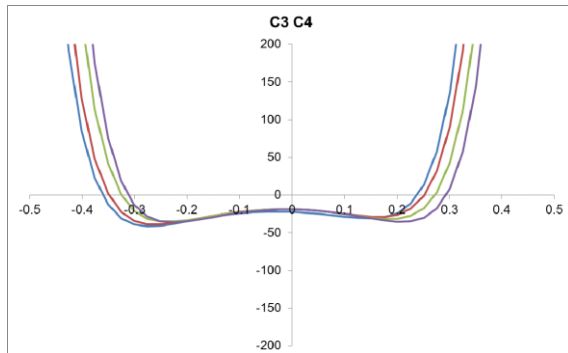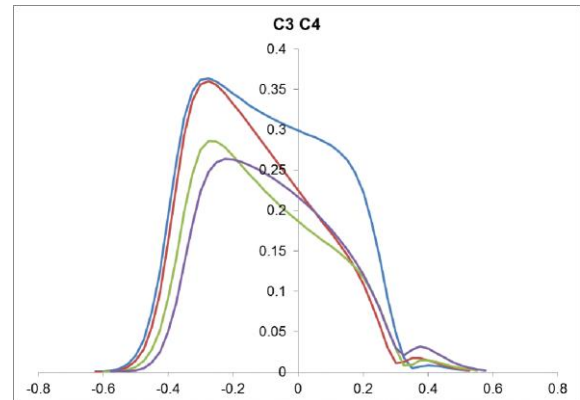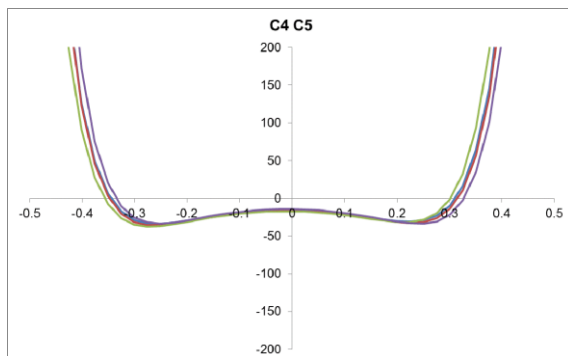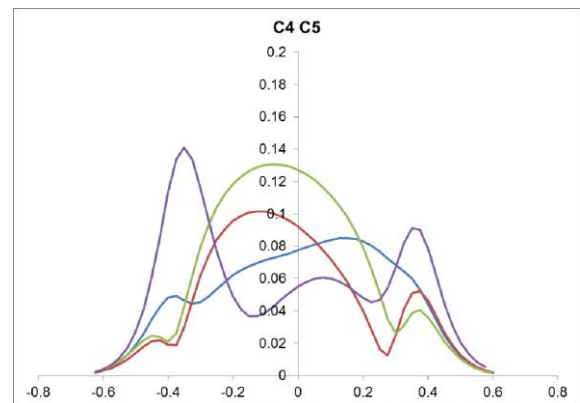
Laplacian

Ellipticity

## C3 and C4

Laplacian                                    Ellipticity



## C4 and C5

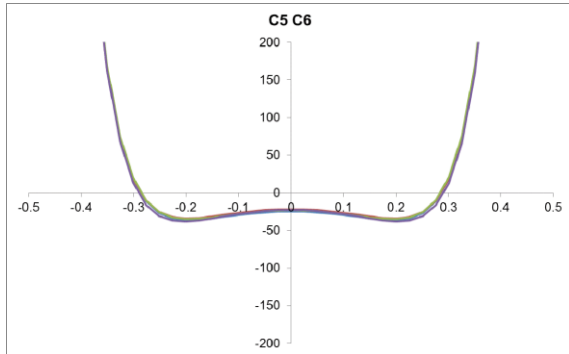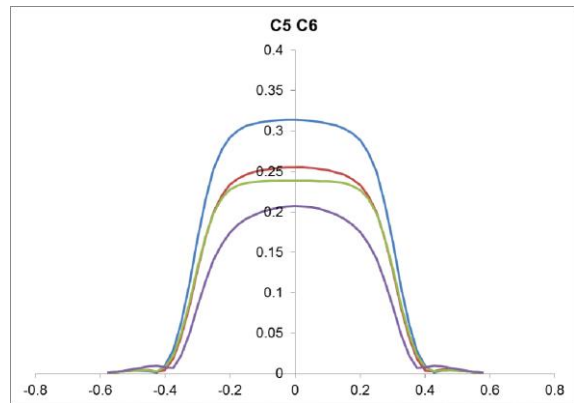Laplacian                                    Ellipticity

## C5 and C6

### Laplacian



### Ellipticity

# 11 REFERENCES

[1] W. Friedrich, P. Knipping, M. von Laue, *Sitzungsbericht der kaiserlich Akademischen Wissenschaften München* **1912**, 303-322.

[2] W. H. Bragg, W. L. Bragg, *Proc. R. Soc. Lond. A* **1913**, *88*, 428-438.

[3] W. L. Bragg, *Proc. R. Soc. Lond. A* **1913**, *89*, 248-277.

[4] G. M. Sheldrick, XS in SHELXTL v2013/1, WI, USA, Madison, **2012**.

[5] A. L. Spek, *Acta Cryst. A* **1990**, *46*, c34.

[6] E. Prince, I. U. o. Crystallography, *International Tables for Crystallography, Volume C: Mathematical, Physical and Chemical Tables*, Wiley**2004**.

[7] G. M. Sheldrick, SADABS 2014/1, Göttingen, **2014**.

[8] L. Krause, R. Herbst-Irmer, G. M. Sheldrick, D. Stalke, submitted, *J. Appl. Cryst.* **2014**.

[9] M. S. Schmøkel, L. Bjerg, F. k. Larsen, j. overgaard, S. Cenedese, G. K. H. Madsen, C. Gatti, E. Nishibori, K. Sugimoto, M. Takata, B. B. Iversen *Acta Cryst. A* **2013**, *69*, 570-582.

[10] M. S. Schmøkel, J. Overgaard, B. Brummerstedt Iversen, *Z. Anorg. Allg. Chem.* **2013**, *639*, 1922-1932.

[11] APEX2 v2.2012.2-0, WI, USA, Madison, **2012**.

[12] P. Müller, *Cryst. Rev.* **2009**, *15*, 57-83.

[13] J. Hey, Institute for Inorganic Chemistry, Georg-August-Universität (Göttingen), **2013**.

[14] D. Stalke, *Acta Cryst. B* **2014**, *70*, 781-782.

[15] M. R. V. Jørgensen, V. R. Hathwar, N. Bindzus, N. Wahlberg, Y.-S. Chen, J. Overgaard, B. B. Iversen, *IUCrJ* **2014**, *1*, 267-280.

[16] Bruker AXS Inc., SAINT v8.30C, WI, USA, Madison, **2013**.

[17] W. Kabsch, *Acta Cryst. D* **2010**, *66*, 125-132.

[18] SAINT+ Integration Engine Reference, Madison, WI, **2010**.

[19] N. K. Hansen, P. Coppens, *Acta Cryst. A* **1978**, *34*, 909-921.

[20] K. Diederichs, *Acta Cryst. D* **2010**, *66*, 733-740.

[21] K. Diederichs, P. A. Karplus, *Acta Cryst. D* **2013**, *69*, 1215-1222.

[22] G. M. Sheldrick, XPREP in SHELXTL 2014/2, WI, USA, Madison, **2014**.

[23] M. Weiss, *J. Appl. Cryst.* **2001**, *34*, 130-135.

[24] S. Parsons, H. Flack, *Acta Cryst. A* **2004**, *60*, s61.

[25] S. Parsons, H. D. Flack, T. Wagner, *Acta Cryst. B* **2013**, *69*, 249-259.

[26] S. Parsons, P. Pattison, H. D. Flack, *Acta Cryst. A* **2012**, *68*, 736-749, and references therein.

[27] R. Fleischer, D. Stalke, *Organometallics* **1998**, *17*, 832-838.

[28] B. Walfort, A. P. Leedham, C. R. Russell, D. Stalke, *Inorg. Chem.* **2001**, *40*, 5668-5674.

[29] D. Leusser, J. Henn, N. Kocher, B. Engels, D. Stalke, *J. Am. Chem. Soc.* **2004**, *126*, 1781-1793.

[30] R. F. Stewart, *J. Chem. Phys.* **1968**, *48*, 4882-4889.

[31] R. F. Stewart, *J. Chem. Phys.* **1969**, *51*, 4569-4577.

[32] R. F. Stewart, *J. Chem. Phys.* **1973**, *58*, 1668-1676.

[33] R. F. Stewart, *J. Chem. Phys. Lett.* **1979**, *65*, 5335.

[34] C. Jelsch, B. Guillot, A. Lagoutte, C. Lecomte, *J. Appl. Cryst.* **2005**, *38*, 38-54.

[35] A. Volkov, P. Macchi, L. J. Farrugia, C. Gatti, P. R. Mallinson, T. Richter, T. Koritsanszky, XD2006, A Computer Program Package for Multipole Refinement, Topological Analysis of Charge Densities and Evaluation of Intermolecular Energies from Experimental or Theoretical Structure Factors, **2006**.

[36] V. Petricek, M. Dusek, L. Palatinus, Jana2006. The crystallographic computing system., Czech Republik, Praha, **2006**.

[37] K. Meindl, J. Henn, *Acta Cryst. A* **2008**, *64*, 404-418.

[38] M. R. V. Jørgensen, H. Svendsen, M. S. Schmøkel, J. Overgaard, B. B. Iversen, *Acta Cryst. A* **2012**, *68*, 301 - 303.

[39] V. V. Zhurov, E. A. Zhurova, A. A. Pinkerton, *J. Appl. Cryst.* **2008**, *41*, 340-349.

[40] S. C. Abrahams, E. T. Keve, *Acta Cryst. A* **1971**, *27*, 157-165.

[41] L. Farrugia, *J. Appl. Cryst.* **2012**, *45*, 849-854.

[42] A. Stash, DRKplot for XD and SHELX, Moscow, **2007**.

[43] D. Stalke *Chem. – Eur. J.* **2011**, *17*, 9264-9278.

[44] U. Flierler, D. Stalke, L. J. Farrugia, in *Modern Charge-Density Analysis* (Eds.: C. Gatti, P. Macchi), Springer, Heidelberg, London, New York, **2012**, pp. 435-467.

[45] D. Stalke in *Electron density and chemical bonding II (Theoretical charge density studies) in Struct. Bonding, Vol. 147* (Eds.: D. Stalke), Springer, Berlin, New York, **2012**, pp. 143-192.

[46] R. F. W. Bader, P. M. Beddall, *J. Chem. Phys.* **1972**, *56*, 3320-3329.

[47] T. S. Koritsanszky, P. Coppens, *Chem. Rev.* **2001**, *101*, 1583-1628.

[48] R. F. W. Bader, *J. Phys. Chem. A* **2007**, *111*, 7966-7972.

[49] R. F. W. Bader, *J. Phys. Chem. A* **1998**, *102*, 7314-7323.

[50] R. F. W. Bader, *J. Phys. Chem. A* **2009**, *113*, 10391-10396.

[51] R. F. W. Bader, *Atoms in Molecules : A Quantum Theory*, Clarendon Press, Oxford; New York, **1990**.

[52] R. F. W. Bader, H. Essén, *J. Chem. Phys.* **1984**, *80*, 1943-1960.

[53] P. J. MacDougall, M. B. Hall, R. F. W. Bader, J. R. Cheeseman, *Can. J. Chem.* **1989**, *67*, 1842-1846.

[54] R. F. W. Bader, R. J. Gillespie, P. J. MacDougall, *J. Am. Chem. Soc.* **1988**, *110*, 7329-7336.

[55] J. Hey, D. M. Andrada, R. Michel, R. A. Mata, D. Stalke, *Angew. Chem.* **2013**, *125*, 10555-10559.; *Angew. Chem. Int. Ed.* **2013**, *52*, 10365-10369.

[56] L. J. Farrugia, C. Evans, D. Lentz, M. Roemer, *J. Am. Chem. Soc.* **2008**, *131*, 1251-1268.

[57] L. J. Farrugia, H. M. Senn, *J. Phys. Chem. A* **2010**, *114*, 13418-13433.

[58] J. Hey, D. Leusser, D. Kratzert, H. Fliegl, J. M. Dieterich, R. A. Mata, D. Stalke, *Phys. Chem. Chem. Phys.* **2013**, *15*, 20600-20610.

[59] R. F. W. Bader, T. S. Slee, D. Cremer, E. Kraka, *J. Am. Chem. Soc.* **1983**, *105*, 5061-5068.

[60] P. A. Karplus, K. Diederichs, *Science* **2012**, *336*, 1030-1033.

[61] A. T. Brünger, *Nature* **1992**, *355*, 472-475.

[62] A. T. Brünger, in *Methods Enzymol., Vol. Volume 277* (Eds.: R. M. S. Charles W. Carter Jr), Academic Press, **1997**, pp. 366-396.

[63] A. Paul, M. Kubicki, C. Jelsch, P. Durand, C. Lecomte, *Acta Cryst. B* **2011**, *67*, 365-378.

[64] S. Domagala, C. Jelsch, *J. Appl. Cryst.* **2008**, *41*, 1140-1149.

[65] J. Kleinschroth, H. Hopf, *Angew. Chem.* **1982**, *94*, 485-496.; *Angew. Chem. Int. Ed.* **1982**, *21*, 469-480.

[66] J. M. T. Vala, I. H. Hillier, S. A. Rice, J. Jortner, *J. Chem. Phys.* **1966**, *44*, 23-35.

[67] J. Spanget-Larsen, *Theoret. Chim. Acta* **1983**, *64*, 187-203.

[68] K. A. Doris, D. E. Ellis, M. A. Ratner, T. J. Marks, *J. Am. Chem. Soc.* **1984**, *106*, 2491-2497.

[69] D. Henseler, G. Hohlneicher, *J. Mol. Struc.* **2000**, *497*, 145-156.

[70] G. F. Caramori, S. E. Galembeck, *J. Phys. Chem. A* **2007**, *111*, 1705-1712.

[71] J. Pfister, C. Schon, W. Roth, C. Kaiser, C. Lambert, K. Gruss, H. Braunschweig, I. Fischer, R. F. Fink, B. Engels, *J. Phys. Chem. A* **2011**, *115*, 3583-3591.

[72] A. F. Murad, J. Kleinschroth, H. Hopf, *Angew. Chem.* **1980**, *92*, 388-389.; *Angew. Chem. Int. Ed.* **1980**, *19*, 389-390.

[73] P. J. Dyson, D. G. Humphrey, J. E. McGrady, D. M. P. Mingos, D. J. Wilson, *J. Chem. Soc., Dalton Trans* **1995**, *0*, 4039-4043.

[74] G. A. Papoyan, K. P. Butin, R. Hoffmann, V. I. Rozenberg, *Russ Chem Bull* **1998**, *47*, 153-159.

[75] K. A. Lyssenko, M. Y. Antipin, D. Y. Antonov, *ChemPhysChem* **2003**, *4*, 817-823.

[76] C. J. Brown, A. C. Farthing, *Nature* **1949**, *164*, 915 - 916.

[77] C. J. Brown, *J. Chem. Soc.* **1953**, 3265-3270.

[78] D. K. Lonsdale, H. J. Milledge, K. V. K. Rao, *Proc. R. Soc.* **1960**, *255*, 82-100.

[79]  A. Ron, O. Schnepp, *J. Chem. Phys.* **1962**, *37*, 2540-2546.

[80]  A. Ron, O. Schnepp, *J. Chem. Phys.* **1966**, *44*, 19-22.

[81]  J. T. S. Andrews, E. F. Westrum, *J. Phys. Chem.* **1970**, *74*, 2170-2174.

[82]  H. Hope, J. Bernstein, K. N. Trueblood, *Acta Cryst. B* **1972**, *28*, 1733-1743.

[83]  S. E. Walden, D. T. Glatzhofer, *J. Phys. Chem. A* **1997**, *101*, 8233-8241.

[84]  D. Henseler, G. Hohlneicher, *J. Phys. Chem. A* **1998**, *102*, 10828-10833.

[85]  T. Kottke, R. J. Lagow, D. Stalke, *J. Appl. Cryst.* **1996**, *29*, 465-468.

[86]  T. Kottke, D. Stalke, *J. Appl. Cryst.* **1993**, *26*, 615-619.

[87]  D. Stalke, *Chem. Soc. Rev.* **1998**, *27*, 171-178.

[88]  D. Leusser, Physikalisches Institut Julius-Maximilians-Universität (Würzburg), **1997**.

[89]  S. Grimme, *Chem.-Eur. J.* **2004**, *10*, 3423-3429.

[90]  H. Dodziuk, S. Szymański, J. Jaźwiński, M. Ostrowski, T. B. Demissie, K. Ruud, P. Kuś, H. Hopf, S.-T. Lin, *J. Phys. Chem. A* **2011**, *115*, 10638-10649.

[91]  A. Ron, M. Noble, E. K. C. Lee, *Chem. Phys.* **1984**, *83*, 215-219.

[92]  W. Goldacker, D. Schweitzer, K. P. Dinse, K. H. Hausser, *Chem. Phys.* **1980**, *48*, 105-111.

[93]  S. M. Bachrach, *J. Phys. Chem. A* **2011**, *115*, 2396-2401.

[94]  F. Hirshfeld, *Acta Cryst. A* **1976**, *32*, 239-244.

[95]  J. W. Edwards, G. L. Kington, R. Mason, *Trans. Faraday Soc.* **1960**, *56*, 660-667.

[96]  M. Walker, E. Pohl, R. Herbst-Irmer, M. Gerlitz, J. Rohr, G. M. Sheldrick, *Acta Cryst. B* **1999**, *55*, 607-616.

[97]  R. Marsh, *Acta Cryst. B* **1986**, *42*, 193-198.

[98]  R. Marsh, *Acta Cryst. B* **1981**, *37*, 1985-1988.

[99]  V. Schomaker, R. E. Marsh, *Acta Cryst. B* **1979**, *35*, 1933-1934.

[100]  C. V. Raman, *Indian J. Phys.* **1928**, *2*, 387-398.

[101]  P. W. Atkins, J. de Paula, *Physikalische Chemie*, Wiley-VCH Verlag GmbH, Weinheim, **2006**.

[102]  H. Haken, H. C. Wolf, *Molekülphysik und Quantenchemie* 5th ed., Springer-Verlag, Berlin Heidelberg New York, **2006**.

[103]  M. A. Adams, S. F. Parker, F. Fernandez-Alonso, D. J. Cutler, C. Hodges, A. King, *Appl. Spectrosc.* **2009**, *63*, 727-732.

[104]  P. H. Scudder, V. Boekelheide, D. Cornutt, H. Hopf, *Spectrochim. Acta A* **1981**, *37*, 425-435.

[105]  S. J. Clark, M. D. Segall, C. J. Pickard, P. J. Hasnip, M. J. Probert, K. Refson, M. C. Payne, *Z. Kristallogr. - New Cryst. Struct.* **2005**, *220*, 567-570.

[106]  K. Refson, P. R. Tulip, S. J. Clark, *Phys. Rev. B* **2006**, *73*, 155114.

[107]    W. Li, Z. Sui, H. Liu, Z. Zhang, H. Liu, *J. Phys. Chem. C* **2014**, *118*, 16028-16034.

[108]    M. S. Schmokel, L. Bjerg, S. Cenedese, M. R. V. Jorgensen, Y.-S. Chen, J. Overgaard, B. B. Iversen, *Chemical Science* **2014**, *5*, 1408-1421.

[109]    G. M. Sheldrick, *Acta Cryst. A* **2008**, *64*, 112-122.

[110]    C. B. Huebschle, G. M. Sheldrick, B. Dittrich, *J. Appl. Cryst.* **2011**, *44*, 1281-1284.

[111]    F. Allen, *Acta Cryst. B* **1986**, *42*, 515-522.

[112]    Z. Su, P. Coppens, *Acta Cryst. A* **1998**, *54*, 646-652.

[113]    L. Kissel, R. H. Pratt, *Acta Cryst. A* **1990**, *46*, 170-175.

[114]    A. Volkov, Y. A. Abramov, P. Coppens, *Acta Cryst. A* **2001**, *57*, 272-282.

[115]    A. Madsen, *J. Appl. Cryst.* **2006**, *39*, 757-758.

[116]    C. B. Huebschle, B. Dittrich, *J. Appl. Cryst.* **2011**, *44*, 238-240.

[117]    H. Wolf, D. Leusser, M. R. V. Jørgensen, R. Herbst-Irmer, Y.-S. Chen, E.-W. Scheidt, W. Scherer, B. B. Iversen, D. Stalke, *Chem. – Eur. J.* **2014**, *20*, 7048-7053.

[118]    R. Kaminski, S. Domagala, K. N. Jarzembska, A. A. Hoser, W. F. Sanjuan-Szklarz, M. J. Gutmann, A. Makal, M. Malinska, J. M. Bak, K. Wozniak, *Acta Cryst. A* **2014**, *70*, 72-91.

[119]    E. D. Stevens, P. Coppens, *Acta Cryst. A* **1976**, *32*, 915-917.

[120]    D. S. Acker, W. R. Hertler, *J. Am. Chem. Soc.* **1962**, *84*, 3370-3374.

[121]    T. L. Cairns, et al., see Supporting Information., *J. Am. Chem. Soc.* **1958**, *80*, 2775-2778.

[122]    W. J. Siemons, P. E. Bierstedt, R. G. Kepler, *J. Chem. Phys.* **1963**, *39*, 3523-3528.

[123]    L. R. Melby, R. J. Harder, W. R. Hertler, W. Mahler, R. E. Benson, W. E. Mochel, *J. Am. Chem. Soc.* **1962**, *84*, 3374-3387.

[124]    J. Ferraris, D. O. Cowan, V. Walatka, J. H. Perlstein, *J. Am. Chem. Soc.* **1973**, *95*, 948-949.

[125]    D. E. Schafer, F. Wudl, P. H. Schmidt, G. A. Thomas, J. P. Ferraris, D. O. Cowan, *Solid State Commun.* **1974**, *14*, 87-101.

[126]    C. D. Jaeger, A. J. Bard, *J. Am. Chem. Soc.* **1979**, *101*, 1690-1699.

[127]    R. Pauliukaite, A. Malinauskas, G. Zhylyak, U. E. Spichiger-Keller, *Electroanalysis* **2007**, *19*, 2491-2498.

[128]    P. A. Dowben, *Surf. Sci. Rep.* **2000**, *40*, 151-247.

[129]    D. Jérome, H. J. Schulz, *Advances in Physics* **2002**, *51*, 293-479.

[130]    S. Larsson, *Faraday Discuss.* **2006**, *131*, 69-77.

[131]    E. Espinosa, E. Molins, C. Lecomte, *Phys. Rev. B* **1997**, *56*, 1820-1833.

[132]    B. B. Iversen, F. K. Larsen, B. N. Figgis, P. A. Reynolds, *J. Chem. Soc., Dalton Trans.* **1997**, 2227-2240.

[133]   B. B. Iversen, F. K. Larsen, B. N. Figgis, P. A. Reynolds, A. J. Schultz, *Acta Cryst. B* **1996**, *52*, 923-931.

[134]   F. Larsen, *Acta Cryst. B* **1995**, *51*, 468-482.

[135]   P. Coppens, T. N. Guru Row, P. Leung, E. D. Stevens, P. J. Becker, Y. W. Yang, *Acta Cryst. A* **1979**, *35*, 63-72.

[136]   J. M. Cole, R. C. B. Copley, G. J. McIntyre, J. A. K. Howard, M. Szablewski, G. H. Cross, *Phys. Rev. B* **2002**, *65*, 125107.

[137]   R. E. Long, R. A. Sparks, K. N. Trueblood, *Acta Cryst.* **1965**, *18*, 932-939.

[138]   P. Macchi, *Crystallography Reviews* **2013**, *19*, 58-101.

[139]   G. M. Sheldrick, *Acta Cryst. A* **2014**, *70*, C1437.

[140]   K. Meindl, R. Herbst-Irmer, J. Henn, *Acta Cryst. A* **2010**, *66*, 362-371.

[141]   R. Herbst-Irmer, J. Henn, J. J. Holstein, C. B. Hübschle, B. Dittrich, D. Stern, D. Kratzert, D. Stalke, *J. Phys. Chem. A* **2012**, *117*, 633-641.

[142]   C. K. Johnson, H. A. Levy in *International Tables for X-Ray Crystallography,* (Eds.: Kynoch Press, Birmingham, **1974**.

[143]   L. J. Farrugia, A. D. Khalaji, *J. Phys. Chem. A* **2011**, *115*, 12512-12522.

[144]   K. N. Trueblood, H.-B. Bürgi, H. Burzlaff, J. D. Dunitz, C. M. Gramaccioli, H. H. Schulz, U. Shmueli, S. C. Abrahams, *Acta Cryst. A* **1996**, *52*, 770-781.

[145]   B. Dittrich, C. B. Hübschle, P. Luger, M. A. Spackman, *Acta Cryst. D* **2006**, *62*, 1325-1335.

[146]   C. B. Hübschle, P. Luger, B. Dittrich, *J. Appl. Cryst.* **2007**, *40*, 623-627.

[147]   B. Dittrich, C. B. Hübschle, J. J. Holstein, F. P. A. Fabbiani, *J. Appl. Cryst.* **2009**, *42*, 1110-1121.

[148]   V. V. Zhurov, E. A. Zhurova, A. I. Stash, A. A. Pinkerton, *J. Phys. Chem. A* **2011**, *115*, 13016-13023.

[149]   A. Fischer, D. Tiana, W. Scherer, K. Batke, G. Eickerling, H. Svendsen, N. Bindzus, B. B. Iversen, *J. Phys. Chem. A* **2011**, *115*, 13061-13071.

[150]   N. Bindzus, T. Straaso, N. Wahlberg, J. Becker, L. Bjerg, N. Lock, A.-C. Dippel, B. B. Iversen, *Acta Cryst. A* **2014**, *70*, 39-48.

[151]   D. Henseler, G. Hohlneicher, *J. Phys. Chem. A* **1999**, *103*, 1160-1161.

[152]   S. E. Walden, D. T. Glatzhofer, *J. Phys. Chem. A* **1999**, *103*, 1162-1163.

[153]   H. Hopf, *Isr. J. Chem.* **2012**, *52*, 18-19.

[154]   T. Van Regemorter, M. Guillaume, G. Sini, J. Sears, V. Geskin, J.-L. Brédas, D. Beljonne, J. Cornil, *Theor. Chem. Acc.* **2012**, *131*, 1-8.

[155]   K. Ueda, H. Morimoto, T. Sugimoto, N. Kanehisa, Y. Shibamoto, Y. Kai, *Mol. Cryst. Liq. Cryst.* **1996**, *279*, 123-132.

[156]   M. A. Dobrowolski, G. Garbarino, M. Mezouar, A. Ciesielski, M. K. Cyrański, *CrystEngComm* **2014**, *16*, 415-429.

[157]    H. Endres, H. J. Keller, W. Moroni, D. Nothe, *Acta Cryst. B* **1980**, *36*, 1435-1440.

[158]    E. Wenger, S. Dahaoui, P. Alle, P. Parois, C. Palin, C. Lecomte, D. Schaniel, *Acta Cryst. B* **2014**, *70*, 783-791.

[159]    J. Henn, A. Schonleber, *Acta Cryst. A* **2013**, *69*.

[160]    J. Henn, K. Meindl, *Acta Cryst. A* **2014**, *70*, 248-256.

[161]    Bruker AXS Inc., SAINT v7.68A, WI, USA, Madison, **2010**.

# Curriculum Vitae

**Name:** Hilke Wolf

**Adress:** Vor der Laakenbreite 6, 37075 Göttingen

**E-mail:** hilke.wolf@googlemail.de

**Telefone:** 0551-9004681

**Nationality:** German

**Date of Birth:** 19.11.1983

**Birthplace:** Leer/Ostfriesland

**Children:** Elin Hedda Wolf

(Date of Birth: 11.03.2010)

# Work and research experience

| | |
|---|---|
| since 2/2011 | Research assistent at the Georg-August University Goettingen, Institute for Inorganic Chemistry in the work group of Prof. Dr. D. Stalke **Key Responsibilities:**<ul><li>Maintenance and operation of Bruker D8 diffractometer</li><li>Single crystal X-ray diffraction structural analysis and its computerbased evaluation and analysis; specialised in high resolution diffraction experiments and charge density analysis</li><li>Planning and realisation of experiments abroad</li><li>Presentation of research results at national and international conferences</li><li>Tutoring new work group members in the use of diffractometers and data analysis</li><li>Tutoring students in lab courses and seminars</li></ul> |
| 4/2014 | Visit at the Rutherford Appleton Laboratories in Didcot, England; ISIS TOSCA beam-line; Inelastic Neutron Scattering and simultaneous Raman spectroscopy on a crystalline powder sample |

| | |
|---|---|
| 11-12/2013 | Visit at the Spallation Neutron Source in Oak Ridge, USA; Elastic neutron diffraction experiments on a single crystal (two weeks) |
| 10-11/2012 | Research exchange in Aarhus, Denmark at the Aarhus University in the work group of Prof. Dr. Bo B. Iversen (four weeks) |
| 7/2012 | Visit at the Advanced Photon Source in the Argonne National Laboratory, USA; planning and realisation of high resolution single crystal x-ray diffraction experiments (two weeks) |

## Academic Qualifications and Formal Education

| | |
|---|---|
| since 01/ 2011 | Dissertation at the Georg-August University Goettingen, Institute for Inorganic Chemistry in the work group of Prof. Dr. D. Stalke<br>Title of my thesis: „Charge Density Investigations on Fluorophors" |
| 01/2011 | Diploma exams in chemistry at the Georg-August University Goettingen (Mark: sehr gut) |
| 03-12/ 2010 | Birth of my daughter and parental leave |
| 05/2010- 10/2009 | Diploma thesis at the Georg-August University Goettingen in the work group of Prof. Dr. D. Stalke, Institute for Inorganic Chemistry<br>(Mark: sehr gut) |
| 04/2008- 10/2007 | Research stay at the University of Queensland School of Molecular and Microbial Science, Brisbane, Australia in the work group of Dr. C. Williams |
| 2006 | Vordiplom in chemistry at the Georg-August University Goettingen (Mark: gut) |
| 2011-2004 | Chemistry Studies at the Georg-August University Goettingen |

| | |
|---|---|
| 08/2004-08/2003 | Gap year in Australia within the work&travel programme |
| 2003-1996 | Abitur at Gymnasium am Kattenberge Buchholz in der Nordheide |
| | final mark :1.9 |
| | Focus subjects: Chemistry, History |

## Skills

| | |
|---|---|
| Language | English: fluent |
| | French and Latin (Basic: A1) |
| IT | MS Office, Origin, ChemDraw, Photoshop, TopSpin, ApexII, SHELX Suite, SADABS, SORTAV, SAINT |

## Extracurricular activities

| | |
|---|---|
| 08/2014 | Participated in the seminar: |
| | „Structural Determination at Large-Scale Facilities" |
| 06/2014 | Participated in the seminar: |
| | „Technologien rund um Funktionsmaterialien" |
| 03/2013 | Participated in the seminar: |
| | „Führungsexzellenz durch Diversity Management" |
| X-ray and other diffraction methods | Detailed knowledge in the analysis of problem crystal structures such as twins or split crystals; Maintenance and operation of Oxford Cryostream, Helijet und Bruker *Cryoflex* cooling devices |
| X-ray diffractometer | Maintenance of Bruker D8 goniometer equipped with either TXS or Incoatec Microfocus Source with Helios Mirror Optics (Filament change at the TXS, focussing and fine adjustment of the X-ray beam, maintenance of the detector cooling devices) |

comprehensive knowledge according to §5 Chem.Verbots.V.

Compulsory optional subject: Biomolecular Chemistry

# Personal Interests

Participation in the students council of chemistry (tutoring of first semester students; organisation of various activities) (2010-2004)

Elected member of the faculty council (Fakultaetsrat), the study commission (Studienkommission) as well as the students representative (2010-2004)

Long distance running, preferably outsides; books; travelling

# Participation at conferences and workshops

| 03/2014 | 8th CMC workshop, Goettingen; Participant |
| --- | --- |
| 06/2013 | Annual Meeting Center for Materials Chemistry, Aarhus, Denmark; oral presentation |
| 06/2013 | Gordon Research Conference on Electron Density and Chemical Bonding, Les Diablerets, Switzerland; Poster presentation |
| 11/2012 | 6th CMC workshop, Goettingen; oral presentation |
| 09/2012 | European Charge Density Meeting ECDM 6, High Tatras, Slovakia; Poster presentation |
| 11/2011 | 4th CMC workshop, Goettingen; Participant |

09/2011          Jaca International School on Charge Density, Jaca, Spain; Participant

11/2010          2nd CMC workshop, Goettingen ; Participant

10/2009          Bruker Users Meeting on NMR spectroscopy, Ettlingen, Germany; Participant

12/2007          Brisbane Biological and Organic Chemistry Symposium, Brisbane, Australien; Participant

## Publications

1.  <u>Hilke Wolf</u>, Nina Lock, Stewart Parker, Dietmar Stalke „Direct Spectrocopic Evidence of the Mechanism behind the Phase Transition of [2,2]-Paracyclophane"; *Chem. Eur. J.* **2014,** in print DOI:10.1002/chem.201405948

2.  <u>Hilke Wolf</u>, Mads R. V. Jørgensen, Regine Herbst-Irmer, Yu-Scheng Chen, Dietmar Stalke "Charge Density Investigations on [2,2]-Paracyclophane – In data we trust." *Acta Cryst. B* **2015**, *71*, 10-19.

3.  <u>Hilke Wolf</u>, Dirk Leusser, Mads R. V. Jørgensen, Regine Herbst-Irmer, Yu-Sheng Chen, Ernst–Wilhelm Scheidt, Wolfgang Scherer, Bo B. Iversen, Dietmar Stalke „Phase Transitions of [2,2]-Paracyclophane – An End to an Apparently Endless Story" *Chem. Eur. J.* **2014**, *20*, 7048–7053.

4.  Markus G. Scheibel, Isabel Klobsch, <u>Hilke Wolf</u>, Peter Stollberg, Dietmar Stalke, Sven Schneider „Thionitrosyl- and Selenonitrosyliridium Complexes" *Eur. J. Inorg. Chem.* **2013**, *22-23*, 3836-3839.

5.  Ramachandran Azhakar, Herbert W. Roesky, <u>Hilke Wolf</u>, Dietmar Stalke „On the Reactivity of the Silylene PhC(NtBu)$_2$SiNPh$_2$ toward Organic Substrates" *Z. Anorg. Allg. Chem.* **2013**, *639*, 934–938.

6.  Kartik C. Mondal, Herbert W. Roesky, Martin C. Schwarzer, Gernot Frenking, Benedikt Niepötter, <u>Hilke Wolf</u>, Regine Herbst-Irmer, Dietmar Stalke „ A Stable Singlet Biradicaloid Siladicarbene: (L:)$_2$Si" *Angew. Chem. Int. Ed.* **2013**, *52*, 2963–2967.

7.  Kartik C. Mondal, Herbert W. Roesky, Martin C. Schwarzer, Gernot Frenking, Igor Tkach, <u>Hilke Wolf</u>, Daniel Kratzert, Regine Herbst-Irmer, Benedikt Niepötter, Dietmar Stalke „Conversion of a Singlet Silylene to a stable Biradical" *Angew. Chem. Int. Ed.* **2013**, *52*, 1801–1805.

8.  Kartik C. Mondal, Prinson P. Samuel, Mykyta Tretiakov, Amit P. Singh, Herbert W. Roesky, A. Claudia Stückl, Benedikt Niepötter, Elena Carl, <u>Hilke Wolf</u>, Regine Herbst-Irmer, Dietmar Stalke „Easy Access to Silicon(0) and Silicon(II) Compounds" *Inorg. Chem.* **2013**, *52*, 4736–4743.

9.  Ramachandran Azhakar, Rajendra S. Ghadwal, Herbert W. Roesky, Ricardo A. Mata, <u>Hilke Wolf</u>, Regine Herbst-Irmer, Dietmar Stalke „Reaction of N-Heterocyclic Silylenes with Thioketone: Formation of Silicon-sulfur Three(S-C-

S)- and Five(Si-C-C-C-S)- Membered Ring Systems" *Chem. Eur. J.* **2013**, *19*, 3715–3720.

10. Ramachandran Azhakar, Herbert W. Roesky, <u>Hilke Wolf</u>, Dietmar Stalke „Metal free and selective activation of one C-F bond in a bound CF$_3$ group" *Chem. Commun.* **2013**, *49*, 1841–1843.

11. Ramachandran Azhakar, Herbert W. Roesky, <u>Hilke Wolf</u>, Dietmar Stalke „ Reactivity of Stable Heteroleptic Silylene PhC(N*t*Bu)$_2$SiNPh$_2$ towards Diazobenzene and

    *N*-Benzylidineaniline" *Organometallics* **2012**, *31*, 8608–8612.

12. Ramachandran Azhakar, Rajendra S. Ghadwal, Herbert W. Roesky, Hilke Wolf, Dietmar Stalke „Facile Access to Functionalized Silylenes PhC(N*t*Bu)$_2$SiX {X = PPh$_2$, NPh$_2$, NCy$_2$, N*i*Pr$_2$, NMe$_2$, N(SiMe$_3$)$_2$, O*t*Bu}" *Organometallics* **2012**, *31*, 4588–4592.

13. Ramachandran Azhakar, Rajendra S. Ghadwal, Herbert W. Roesky, <u>Hilke Wolf</u>, Dietmar Stalke „A début for base stabilized monoalkylsilylenes" *Chem. Commun.* **2012**, *48*, 4561–4563.

14. Martin Kuss-Petermann, <u>Hilke Wolf</u>, Dietmar Stalke, Oliver Wenger „Influence of donor-Acceptor Distance Varation on Photoinduced Electron and Proton Transfer in Rhenium(I)-Phenol Dyads" *J. Am. Chem. Soc.* **2012**, *134*, 12844–12854.

15. Ramachandran Azhakar, Rajendra S. Ghadwal, Herbert W. Roesky, <u>Hilke Wolf</u>, Dietmar Stalke „Stabilization of Low Valent Silicon Fluorides in the Coordination Sphere of Transition Metals" *J. Am. Chem. Soc.* **2012**, *134*, 2423–2428.